STUDY OF THE GROWTH AND INTERACTION OF COBALT OXIDES ON GRAPHITE AND OXIDES SURFACES

A thesis submitted in partial fulfillment for the degree of

DOCTOR IN ADVANCED MATERIALS AND NANOTECHNOLOGY

Author:
DANIEL DÍAZ FERNÁNDEZ

Advisor:
DR. LEONARDO SORIANO DE ARPE

Entregada en el Registro de la Universidad Autónoma de Madrid en marzo de 2015.
Director de la Tesis Doctoral: **Prof. Dr. Leonardo Soriano de Arpe**.

Composición del Tribunal de evaluación:

- Presidente: Prof. Dr. Carlos Palacio Orcajo (UAM)
- Secretario: Dr. Miguel Ángel Rodríguez Barbero (ICV-CSIC)
- Vocal 1: Dr. Juan Rubio Zuazo (ESRF)
- Vocal 2: Dr. Gonzalo García-Fuentes (AIN)
- Vocal 3: Dr. Francisco Yubero Valencia (ICMSE-CSIC)
- Suplente 1: Dr. Maurizio Sacchi (SOLEIL)
- Suplente 2: Prof. Dr. Amadeo López Vázquez de Parga (UAM)

Fecha de defensa de la Tesis Doctoral: 10 de abril de 2015.

daniel.diaz@uam.es

Grupo de Recubrimientos, Intercaras, Nanostructuras y Superficies
Departamento de Física Aplicada, Facultad de Ciencias
Universidad Autónoma de Madrid (UAM)

Escrito con LaTeX y JabRef 2.10.
Maquetado con TeXstudio 2.8.8.

Contents

List of acronyms

AEY	Auger Electron Yield
AFM	Atomic Force Microscopy
AM-AFM	Amplitude Modulation Atomic Force Microscopy
CRG	Collaborating Research Group
DFT	Density Functional Theory
EXAFS	Extended X-ray absorption fine structure
FWHM	Full width at half maximum
GIXRD	Grazing Incidence X-Ray Diffraction
HOPG	Highly Ordered Pyrolitic Graphite
IMFP	Inelastic mean free path
KPFM	Kelvin Probe Force Microscopy
LCA	Linear Combination Analysis
LEED	Low-Energy Electron Diffraction
MFM	Magnetic Force Microscopy
NEXAFS	Near-edge X-ray absorption fine structure
PES	Photoelectron Spectrocopy
PVD	Physical Vapor Deposition
RBS	Rutherford Backscattering Spectrometry

RGA . . . . . Residual Gas Analysis

SEM . . . . . Scanning Electron Microscopy

SPM . . . . . Scanning Probe Microscopy

STM . . . . . Scanning Tunneling Microscopy

TEY . . . . . Total Electron Yield

TIY . . . . . Total Ion Yield

UDOS . . . . . Unoccupied Density Of States

UHV . . . . . Ultra High Vacuum

XANES . . . . . X-ray absorption near-edge spectroscopy

XAS . . . . . X-Ray Absorption Spectroscopy

XPS . . . . . X-Ray Photoelectron Spectroscopy

XPS-IPSA . . . . . XPS inelastic peak shape analysis

XRD . . . . . X-Ray Diffraction

List of Figures

List of Tables

Acknowledgements

En primer lugar, mi agradecimiento personal y profesional a mi director de tesis, Leonardo Soriano de Arpe, por su paciencia en mis primeros pasos en la ciencia experimental, por preocuparse siempre de buscar contactos y técnicas con las cuáles pudiéramos explicar los resultados que se iban obteniendo, y por su consejo siempre sabio y experimentado, tanto profesional como personal. No sería la mitad de científico que soy hoy sin ser por él, sea cual sea esa cantidad.

En segundo lugar, a toda la gente del grupo GRIN: Oscar Bomatí, Alejandro Gutiérrez, Pablo Pernas, Iulian Preda, y a todos los jóvenes científicos que han pasado por aquí (Julián Parrilla, Carlos Morales, Davide Stefani...). Y en especial, a Guillermo Domínguez, amigo, hermano y compañero de tesis. Sin su apoyo moral y profesional durante tantas situaciones (y especialmente tantos sincrotrones) no estaría aquí, sin duda.

A toda la gente del departamento de Física Aplicada con la que he tenido el honor de colaborar o compartir charlas o cafés, sean catedráticos o técnicos: Carlos Palacio, Aurelio Climent, Pilar Prieto, Raquel Caballero, David Martín, Jose Antonio Rodríguez, Félix Mendoza... Extiendo un agradecimiento especial a mis compañeros becarios de este departamento, con los que tantos Bocata Seminar, comidas en la cafetería de Ciencias/Plaza Mayor de la UAM, charlas convertidas en terapias de grupo, y en general grandes momentos he compartido: Darío Gallach, Arancha Gómez, Eduard García, Noelia Benito, Esther Punzón, Chloe González, Rosalía Delgado, Valentin Nistor, Luis Antonio González, Sergio Pinilla...

A todos los colaboradores externos a la universidad que hemos tenido: Ángel Adolfo del Campo y Miguel Angel Rodríguez (ICV-CSIC), Francisco Yubero (ICMSE-CSIC), Rodrigo José Mossanek y Miguel Abbate, del departamento de Física de la Universidade Federal do Parana, Curitiba, Brasil (autores de los cálculos teóricos de XPS y XAS que se presentan en este trabajo); Jesús Chaboy, del ICMA-CSIC (espero que recuperes pronto de tus achaques); Francisco Javier Palomares (ICMM-CSIC), Antonio M. Márquez y Javier Fernández Sanz (US), a la gente del grupo ESISNA del ICMM-CSIC, y en especial a Javier Méndez, con quien tantas horas de AFM he compartido, y tantas charlas de gran valor científico y personal he tenido. Lo poco que sé de AFM es gracias a tí, sin duda. I extend my gratitude to all the people that has helped me in my synchrotron beamtimes: Maximilian Bauer, Ruslan Ovsyannikov, Maria Brzhezinskaya, Antje Vollmer and Heike Löchel from BESSY II, and Germán Castro, Juan Rubio, Enrique Salas, Álvaro García-Noval, Ana Gutiérrez and Pilar Ferrer from ESRF.

A todos mis amigos (Miguel, Raúl, Toño, Marga, María...) por ser el sostén de mi sanidad mental y mis psiquiatras personales durante tantos momentos.

Y por último, a mi familia y, sobre todo, a mis padres. A mi padre por enseñarme que la

paciencia y la tranquilidad son la clave del éxito en los momentos tensos, y a relativizar los momentos malos y a disfrutar de los buenos. Y a mi madre por enseñarme a no rendirme jamás, a seguir luchando a pesar de que todo parezca cuanto menos oscuro, y a perseguir mi vocación científica a pesar de que la situación, tanto personal como económica, no invitaba a ello. He llegado a una linea de meta importante en la carrera de un científico, y aunque no sé qué hay exactamente más adelante de esta bandera a cuadros, espero que os haya hecho sentir un poco orgullosos del camino recorrido hasta ahora. Con eso me basta.

Clarke's three laws:

1. When a distinguished but elderly scientist states that something is possible, he is almost certainly right. When he states that something is impossible, he is very probably wrong.
2. The only way of discovering the limits of the possible is to venture a little way past them into the impossible.
3. Any sufficiently advanced technology is indistinguishable from magi.

ARTHUR C. CLARKE
Profiles of the Future (1962)

Chapter 1

Introduction

SECTION 1.1

Transition metal oxides, oxide-oxide interfaces and cobalt oxides

The transition metal oxides field is one of the widest and most diverse in the materials science. Almost all of the interesting phenomena in condensed matter physics have been seen in these materials (Pauli paramagnetism, Mott transition, high-T_c superconductivity, ferromagnetism, antiferromagnetism, low-spin/high-spin transitions, ferroelectricity, antiferroelectricity, colossal magnetoresistance, charge ordering, bipolaron formation...), and although its study dates back to the beginnings of the 20th century, it is still currently one of the most active fields in materials science research [1–4]. The wide set of properties of these materials are caused by the great variety of crystal structures, polymorphs and geometric arrangements than can be found, but the most important factor for this variety is their complex electronic structure. It is governed by the *d*-*d* hybridization and correlation, but also influenced by effects related to metal-anion (*p*-*d*) hybridization, coordination geometry, spin configuration, sub-band filling, and other aspects. Many models have been proposed in order to try to find an unifying description of their properties, like the historically-relevant Mott-Hubbard model [5–7], or more recent models like the cluster model [8–10] or the ZSA scheme, proposed by Zaanen, Savatsky and Allen in 1985 [11]. While these models have been mostly successful in their unifying purpose, a lot of questions are still unanswered, specially on complex oxides, and a lot of work is still being made in brand new properties and applications of these materials.

But not only the oxides are interesting: as Herbert Kroemer said in his Nobel prize speech in 2000 [12], "the interface is the device". He coined this phrase referring to the success of devices based on thin semiconductor films for photonic and electronic applications, but since the oxide materials have such a wide set of properties, heterostructures based on oxide materials are also extremely interesting and well-researched. A lot of the most fascinating phenomena studied in recent years involve so-called "complex" oxides, usually with perovskite-like structures (such as the well-studied $SrTiO_3/LaTiO_3$ interface [13, 14], for example), but even with more simple and well-known oxides, the properties of these interfaces still yield unexpected and extraordinary features [15].

The cobalt oxides belong to this "simple and well-known" group of transition metal oxides: they have been extensively studied over the last century [16–18], and their applications (both the metal and their oxides) cover a wide range of fields: in biomedicine [19], as an essential component of superalloys for extreme work-conditions environments, such as gas turbines [20], in magnetic devices (such as the widely-used samarium-cobalt magnets, or alloyed in the magnetic layer of hard drive disk platters), gas sensors [21, 22] or catalysis [23, 24], aside from its historical use as colorants and pigments. Even after all these years of research, new applications are still found, such as their recent characterization as supercapacitors [25] or superconductors [26, 27]. For all of their interesting properties and its long research history, there are not a great number of characterization studies of the initial stages of the growth of this material. There is some work done on metal substrates [28–30], which are understandably easier to study (less substrate roughness and charge effects, possibility of using techniques like Scanning Electron Microscopy (SEM) or Low-Energy Electron Diffraction (LEED)), but

the characterization work on oxide substrates or graphite is even more scarce or just non-existent. The case of the growth of cobalt oxide on graphite is specially strange, given the well-known properties and technological importance of graphite, graphite oxide and, above all, graphene [31]; and the recently discovered properties of CoO_x/graphite composites [25, 32, 33]. Based on this lack of understanding of these interfaces, the previous experience of the GRIN research group on these kind of experiments [34–36] and the funding of the Consolider-Ingenio program (MINECO), this work was launched in 2009 as an attempt to shed some light into these hard to study, but technologically important interfaces.

SECTION 1.2

Aim and structure of this work

The general aim of this work is to properly characterize the growth, possible interface effects and stability of ultra-thin cobalt oxide grown on different substrates, and both the experiments and the scheme of this thesis have been structured around this goal. The results can be grouped in two general sets: characterization of the growth of CoO_x over diverse substrates, and the change of the adsorbate and its interaction with the substrate when these samples are subjected to different conditions. In the first set of results, the early, medium and final stages of the growth of cobalt oxides have been studied by performing successive evaporations of Co in a controlled O_2 atmosphere, with increasing evaporation times, over four substrates: three oxides (SiO_2, MgO and Al_2O_3) and Highly Ordered Pyrolitic Graphite (HOPG). The three oxides were chosen because of their different unit cells, lattice parameters and ionicities, as a way to find different behaviors and effects of the substrate parameters over the growth of the CoO_x layers. The HOPG substrate was initially chosen because of the expected low interaction with CoO and its terrace-like morphology, which should produce very different type of growths than those seen in the oxide substrates.

The other main focus of this work has been studied by selecting some coverages of these growths and subjecting them to room conditions and thermal oxidations conditions in controlled atmospheres. Both the changes in the properties already observed in the growths and the new features that could appear have been characterized and explained to the best of our knowledge and experimental possibilities. The main characterization techniques used to characterize all these experiments have been X-Ray Photoelectron Spectroscopy (XPS) (often performed in-situ, without taking the sample out of the vacuum chamber) and Atomic Force Microscopy (AFM), and depending on the results obtained, other techniques, such as X-Ray Absorption Spectroscopy (XAS), Raman spectroscopy or Rutherford Backscattering Spectrometry (RBS) have been used to acquire more information about the features and phenomena observed. The experimental information is also supported with adequate fittings and theoretical calculations wherever it has been possible, in order to have the most complete picture of the system available.

This thesis is structured in a similar way: after a description of both the experimental facilities and materials (chapter 2) and the characterization techniques used (chapter 3), the results are divided in two main blocks: one for the oxide substrates (chapter 4) and another for the HOPG substrates (chapter 5). Finally, the most important conclusions and open questions

for the future will be summarized in chapter 6.

SECTION 1.3

Bibliography

[1] H. Y. HWANG, Y. IWASA, M. KAWASAKI, B. KEIMER, N. NAGAOSA, and Y. TOKURA. "Emergent phenomena at oxide interfaces". *Nature materials* 11.2 (2012), pp. 103–113. DOI: 10.1038/nmat3223.

[2] P. YU, Y. H. CHU, and R. RAMESH. "Oxide interfaces: pathways to novel phenomena". *Materials Today* 15.7-8 (2012), pp. 320–327. DOI: 10.1016/S1369-7021(12)70137-2.

[3] J. MANNHART and D. G. SCHLOM. "Oxide Interfaces-An Opportunity for Electronics". *Science* 327.5973 (2010), pp. 1607–1611. DOI: 10.1126/science.1181862.

[4] S. JIN, T. H. TIEFEL, M. MCCORMACK, R. A. FASTNACHT, R. RAMESH, and L. H. CHEN. "Thousandfold Change in Resistivity in Magnetoresistive La-Ca-Mn-O Films". *Science* 264.5157 (1994), pp. 413–415. DOI: 10.1126/science.264.5157.413.

[5] N. F. MOTT. "The Basis of the Electron Theory of Metals, with Special Reference to the Transition Metals". *Proceedings of the Physical Society. Section A* 62.7 (1949), p. 416. DOI: 10.1088/0370-1298/62/7/303.

[6] N. F. MOTT. "The transition to the metallic state". *Philosophical Magazine* 6.62 (1961), pp. 287–309. DOI: 10.1080/14786436108243318.

[7] J. HUBBARD. "Electron Correlations in Narrow Energy Bands". *Proceedings of the Royal Society of London A: Mathematical, Physical and Engineering Sciences* 276.1365 (1963), pp. 238–257. DOI: 10.1098/rspa.1963.0204.

[8] S. ASADA and S. SUGANO. "Satellites in X-Ray photoelectron Spectra of Transition-Metal Compounds". *Journal of the Physical Society of Japan* 41.4 (1976), pp. 1291–1299. DOI: 10.1143/JPSJ.41.1291.

[9] S. LARSSON. "Theory of satellite excitations in inner shell X-ray photoelectron spectra of nickel and copper compounds". *Chemical Physics Letters* 32.3 (1975), pp. 401–406. DOI: 10.1016/0009-2614(75)85203-1.

[10] R. ZIMMERMANN, R. CLAESSEN, F. REINERT, P. STEINER, and S. HÜFNER. "Strong hybridization in vanadium oxides: evidence from photoemission and absorption spectroscopy". *Journal of Physics: Condensed Matter* 10.25 (1998), p. 5697. DOI: 10.1088/0953-8984/10/25/018.

[11] J. ZAANEN, G. A. SAWATZKY, and J. W. ALLEN. "Band gaps and electronic structure of transition-metal compounds". *Physical Review Letters* 55 (4 July 1985), pp. 418–421. DOI: 10.1103/PhysRevLett.55.418.

[12] H. KROEMER. "Nobel Lecture: Quasielectric fields and band offsets: teaching electrons new tricks". *Reviews of Modern Physics* 73 (3 Oct. 2001), pp. 783–793. DOI: 10.1103/RevModPhys.73.783.

[13] A. OHTOMO and H. Y. HWANG. "A high-mobility electron gas at the $LaAlO_3/SrTiO_3$ heterointerface". *Nature* 427.6973 (2004), pp. 423–426. DOI: 10.1038/nature02308.

[14] J. S. LEE, Y. W. XIE, H. K. SATO, C. BELL, Y. HIKITA, H. Y. HWANG, and C. C. KAO. "Titanium d_{xy} ferromagnetism at the $LaAlO_3/SrTiO_3$ interface". *Nature Materials* 12.8 (2013), pp. 703–706. DOI: 10.1038/nmat3674.

[15] A. TSUKAZAKI, S. AKASAKA, K. NAKAHARA, Y. OHNO, H. OHNO, D. MARYENKO, A. OHTOMO, and M. KAWASAKI. "Observation of the fractional quantum Hall effect in an oxide". *Nature Materials* 9.11 (2010), pp. 889–893. DOI: 10.1038/nmat2874.

[16] J. R. DAVIS and A. S. M. I. H. COMMITTEE. *Nickel, Cobalt, and Their Alloys*. ASM specialty handbook. ASM International, 2000. ISBN: 9780871706850.

[17] B. RAVEAU and M. SEIKH. *Cobalt Oxides: From Crystal Chemistry to Physics*. Wiley, 2012. ISBN: 9783527645541.

[18] T. TAKAMI. *Functional Cobalt Oxides: Fundamentals, Properties and Applications*. Pan Stanford Publishing, 2011. 180 pp. ISBN: 9789814463324.

[19] J. A. DISEGI, R. L. KENNEDY, and R. PILLIAR. *Cobalt-base Alloys for Biomedical Applications*. ASTM STP 1365 no. 1365. ASTM, 1999. ISBN: 9780803126084.

[20] D. COUTSOURADIS, A. DAVIN, and M. LAMBERIGTS. "Cobalt-based superalloys for applications in gas turbines". *Materials Science and Engineering* 88 (1987). Proceedings of the First International Symposium on High Temperature Corrosion of Materials and Coatings for Energy Systems and Turboengines, pp. 11–19. DOI: 10.1016/0025-5416(87)90061-9.

[21] M. X. MA, Z. Y. PAN, L. GUO, J. H. LI, Z. Y. WU, and S. H. YANG. "Porous cobalt oxide nanowires: Notable improved gas sensing performances". *Chinese Science Bulletin* 57.31 (2012), pp. 4019–4023. DOI: 10.1007/s11434-012-5363-0.

[22] H. J. NAM, T. SASAKI, and N. KOSHIZAKI. "Optical CO Gas Sensor Using a Cobalt Oxide Thin Film Prepared by Pulsed Laser Deposition under Various Argon Pressures". *The Journal of Physical Chemistry B* 110.46 (2006). PMID: 17107147, pp. 23081–23084. DOI: 10.1021/jp063484f.

[23] J. ROSEN, G. S. HUTCHINGS, and F. JIAO. "Ordered Mesoporous Cobalt Oxide as Highly Efficient Oxygen Evolution Catalyst". *Journal of the American Chemical Society* 135.11 (2013), pp. 4516–4521. DOI: 10.1021/ja400555q.

[24] W. ZHANG, H. L. TAY, S. S. LIM, Y. WANG, Z. ZHONG, and R. XU. "Supported cobalt oxide on MgO: Highly efficient catalysts for degradation of organic dyes in dilute solutions". *Applied Catalysis B: Environmental* 95.1-2 (2010), pp. 93–99. DOI: 10.1016/j.apcatb.2009.12.014.

[25] X. C. DONG, H. XU, X. W. WANG, Y. X. HUANG, M. B. CHAN-PARK, H. ZHANG, L. H. WANG, W. HUANG, and P. CHEN. "3D Graphene-Cobalt Oxide Electrode for High-Performance Supercapacitor and Enzymeless Glucose Detection". *ACS Nano* 6.4 (2012), pp. 3206–3213. DOI: 10.1021/nn300097q.

[26] K. TAKADA, H. SAKURAI, E. TAKAYAMA-MUROMACHI, F. IZUMI, R. A. DILANIAN, and T. SASAKI. "Superconductivity in two-dimensional CoO_2 layers". *Nature* 422.6927 (2003), pp. 53–55. DOI: 10.1038/nature01450.

[27] J. V. BADDING. "Superconducting materials: Cobalt oxide layers". *Nature Materials* 2.4 (2003), pp. 208–210. DOI: 10.1038/nmat868.

[28] L. GRAGNANIELLO, S. AGNOLI, G. PARTEDER, A. BAROLO, F. BONDINO, F. ALLEGRETTI, S. SURNEV, G. GRANOZZI, and F. P. NETZER. "Cobalt oxide nanolayers on Pd(100): The thickness-dependent structural evolution". *Surface Science* 604.21-22 (2010), pp. 2002–2011. ISSN: 0039-6028. DOI: 10.1016/j.susc.2010.08.012.

[29] W. MEYER, K. BIEDERMANN, M. GUBO, L. HAMMER, and K. HEINZ. "Surface structure of polar Co $_3O_4$ (111) films grown epitaxially on Ir(100)-(1 x 1)". *Journal of Physics: Condensed Matter* 20.26 (2008), p. 265011. DOI: 10.1088/0953-8984/20/26/265011.

[30] K. HEINZ and L. HAMMER. "Epitaxial cobalt oxide films on Ir(100)-the importance of crystallographic analyses". *Journal of Physics: Condensed Matter* 25.17 (2013), p. 173001. DOI: 10.1088/0953-8984/25/17/173001.

[31] K. S. NOVOSELOV, V. I. FAL, L. COLOMBO, P. R. GELLERT, M. G. SCHWAB, K. KIM, et al. "A roadmap for graphene". *Nature* 490.7419 (2012), pp. 192–200. DOI: 10.1038/nature11458.

[32] Z. C. YANG, C. H. TANG, Y. ZHANG, H. GONG, X. LI, and J. WANG. "Cobalt monoxide-doped porous graphitic carbon microspheres for supercapacitor application". *Scientific reports* 3 (2013), p. 2925. DOI: 10.1038/srep02925.

[33] X. YANG, K. FAN, Y. ZHU, J. SHEN, X. JIANG, P. ZHAO, S. LUAN, and C. LI. "Electric Papers of Graphene-Coated Co_3O_4 Fibers for High-Performance Lithium-Ion Batteries". *ACS Applied Materials & Interfaces* 5.3 (2013), pp. 997–1002. DOI: 10.1021/am302685t.

[34] L. SORIANO, G. G. FUENTES, C. QUIRÓS, J. F. TRIGO, J. M. SANZ, P. R. BRESSLER, and A. R. GONZÁLEZ-ELIPE. "Crystal-Field Effects at the TiO_2-SiO_2 Interface As Observed by X-ray Absorption Spectroscopy". *Langmuir* 16.17 (2000), pp. 7066–7069. DOI: 10.1021/la000330x.

[35] M. F. LÓPEZ, L. SORIANO, F. J. PALOMARES, M. SÁNCHEZ-AGUDO, G. G. FUENTES, A. GUTIÉRREZ, and J. A. JIMÉNEZ. "Soft x-ray absorption spectroscopy study of oxide layers on titanium alloys". *Surface and Interface Analysis* 33.7 (2002), pp. 570–576. DOI: 10.1002/sia.1422.

[36] L. SORIANO, I. PREDA, A. GUTIÉRREZ, S. PALACÍN, M. ABBATE, and A. VOLLMER. "Surface effects in the Ni 2p x-ray photoemission spectra of NiO". *Physical Review B* 75 (23 June 2007), p. 233417. DOI: 10.1103/PhysRevB.75.233417.

Chapter 1

Introducción

SECTION 1.1

Óxidos de metales de transición, intercaras óxido-óxido y óxidos de cobalto.

El campo de los óxidos de metales de transición es uno de los más amplios y diversos de toda la ciencia de materiales. Una gran parte de los fenómenos más interesantes de este campo de la física han sido vistos en estos materiales (paramagnetismo de Pauli, transiciones de Mott, superconductividad de alta T_c, ferromagnetismo, antiferromagnetismo, transiciones de spin bajo a spin alto, ferroelectricidad, antiferroelectricidad, magnetorresistencia gigante, orden de carga, formación de bipolarones...), y aunque se llevan estudiando desde principios del siglo 20, es todavía hoy uno de los campos más activos de la física de materiales [1–4]. Este amplio abanico de propiedades son causadas por la gran variedad de estructuras cristalinas, polimorfos y disposiciones geométricas que presentan, y sobre todo por su compleja estructura electrónica. Esta está principalmente regida por la hibridación de los orbitales *d*-*d*, pero también se ve influenciada por efectos de hibridación entre los orbitales *d* y *s* de anión y catión, diferentes coordinaciones, configuraciones de spin, sub-llenado de bandas y demás. A lo largo de la historia se han propuesto muchos modelos para intentar tener una descripción única de todas sus propiedades, como el modelo históricamente relevante de Mott-Hubbard [5–7], o intentos más recientes como el modelo de clusters [8–10] o el esquema ZSA, propuesto por Zaanen, Savatsky y Allen en 1985 [11]. A pesar de que estos modelos han tenido bastante éxito en su propósito unificador, todavía quedan muchos problemas sin responder, y muchos estudios se están realizando actualmente en nuevas propiedades y aplicaciones de estos materiales.

Pero no sólo los óxidos son interesantes por sí solos: como dijo Herbert Kroemer en su discurso de aceptación del premio Nobel de física en el año 2000 [12], "la intercara es el dispositivo". Cuando Kroemer pronunció esa frase, se estaba refiriendo específicamente a los dispositivos basados en láminas delgadas de semiconductores para aplicaciones fotovoltáicas y electrónicas, pero dado que los óxidos tienen tal variedad de propiedades, es lógico que las heteroestructuras basadas en estos materiales tengan también un gran interés y sean objeto de un gran número de estudios. Muchos de ellos se centran en heteroestructuras de óxidos considerados "complejos", como los que tienen estructura de perovskita (un buen ejemplo de esto es la intercara $SrTiO_3/LaTiO_3$ [13, 14]), pero intercaras basadas en óxidos más "simples" también han dado lugar a nuevas y fascinantes propiedades y aplicaciones [15].

Los óxidos de cobalto pertenecen a esa categoría de óxidos "simples y bien conocidos": han sido estudiados desde los inicios de la ciencia de materiales [16–18], y sus aplicaciones cubren un buen rango de campos: biomedicina [19], como componente esencial de superaleaciones para condiciones de trabajo extremas (por ejemplo, turbinas de gas) [20], en dispositivos magnéticos como los imanes de samario-cobalto, en forma de aleaciones en la capa magnética de discos duros, sensores de gases [21, 22] o como catalizadores [23, 24], además de su uso como pigmento a lo largo de la historia. Incluso después de tantos años de investigación en este material, nuevas propiedades de estos óxidos siguen siendo descubiertas, como su reciente aplicación en dispositivos supercapacitores [25] o superconductores [26, 27]. A pesar de esta cantidad de propiedades y aplicaciones, no existen muchos estudios de los primeros estadíos del

crecimiento de este material. Existe algo de trabajo sobre el crecimiento de óxidos de cobalto en sustratos metálicos [28–30], experimentos más fáciles de caracterizar (menor rugosidad del sustrato y efectos de carga, posibilidad de usar técnicas de caracterización como Scanning Electron Microscopy (SEM) or Low-Energy Electron Diffraction (LEED)), pero el trabajo de caracterización en sustratos de óxidos es muy escaso o no existente. El caso de la intercara CoO/grafito es especialmente extraño, dadas las excepcionales propiedades e importancia tecnológica del grafito y sobre todo, del grafeno [31]; y las propiedades recientemente descubiertas de compuestos de CoO_x/grafito [25, 32, 33]. Basándonos en la experiencia del grupo GRIN en este tipo de sistemas [34–36], y con la ayuda financiera del programa CONSOLIDER-Ingenio (MINECO), se inició este estudio para intentar arrojar un poco de luz en estas intercaras, que si bien son complejas de estudiar, tienen una gran importancia tecnológica.

SECTION 1.2

Objetivos y estructura de este trabajo.

El objetivo principal de este trabajo es caracterizar debidamente el crecimiento, los posibles efectos de intercara y la estabilidad de muestras de óxido de cobalto crecidas en diversos sustratos, y tanto los experimentos realizados como el esquema básico de esta tesis están estructurados alrededor de este objetivo. Los resultados de estos experimentos pueden ser agrupados en dos conjuntos generales: la caracterización del crecimiento de CoO_x en diversos sustratos, y el estudio del cambio de las propiedades vistas en el crecimiento cuando estas muestras son sometidas a condiciones distintas. Con respecto al estudio del crecimiento, este ha sido estudiado mediante un experimento de evaporaciones sucesivas de Co en una atmósfera controlada de O_2, con tiempos progresivamente mayores de deposición, sobre cuatro sustratos distintos: tres óxidos (SiO_2, MgO y Al_2O_3) y grafito pirolítico altamente orientado (HOPG). Los tres óxidos fueron escogidos por sus diferentes estructuras cristalinas, parámetros de red e ionicidades, para poder estudiar el efecto de los parámetros del sustrato en las capas crecidas encima de ellos. El HOPG fue escogido por su esperable baja interacción con el CoO, y por su morfología de terrazas planas, las cuáles deberían producir crecimientos muy distintos a los observados en los sustratos de óxidos.

El otro foco importante de esta tesis ha sido estudiado mediante el crecimiento de muestras con determinados recubrimientos sobre estos sustratos, y el estudio de estas después de ser sometidas a condiciones de presión atmosférica y a una reoxidación térmica. Los cambios de las propiedades de estas muestras con respecto a las recién crecidas han sido caracterizados y explicados lo mejor que nuestra capacidad experimental nos ha permitido. Las principales técnicas de caracterización usadas en todos los experimentos han sido XPS (muchas veces medido in-situ, es decir, sin sacar la muestra fuera de condiciones de ultra-alto vacío), y AFM, y dependiendo de los resultados obtenidos otras técnicas han sido empleadas para obtener más información de los fenómenos observados, como X-Ray Absorption Spectroscopy (XAS), espectroscopía Raman o Rutherford Backscattering Spectrometry (RBS). Además, cuando ha sido posible, estas observaciones experimentales han sido complementadas con cálculos teóricos, de cara a obtener la descripción más completa posible de estos resultados.

Esta tesis está estructurada de una manera similar: tras una descripción de las instalaciones,

equipamiento y materiales usados en estos experimentos (capítulo 2) y un resumen de las técnicas experimentales usadas (capítulo 3), los resultados son presentados en dos grandes capítulos: uno dedicado a los resultados sobre sustratos de óxidos (capítulo 4) y otro sobre los resultados en sustratos de HOPG (capítulo 6). Finalmente, las conclusiones más importantes obtenidas en este trabajo serán expuestas en el capítulo 6, además de las cuestiones abiertas que quedan para trabajos futuros.

SECTION 1.3

Bibliography

[1] H. Y. HWANG, Y. IWASA, M. KAWASAKI, B. KEIMER, N. NAGAOSA, and Y. TOKURA. "Emergent phenomena at oxide interfaces". *Nature materials* 11.2 (2012), pp. 103–113. DOI: 10.1038/nmat3223.

[2] P. YU, Y. H. CHU, and R. RAMESH. "Oxide interfaces: pathways to novel phenomena". *Materials Today* 15.7-8 (2012), pp. 320–327. DOI: 10.1016/S1369-7021(12)70137-2.

[3] J. MANNHART and D. G. SCHLOM. "Oxide Interfaces-An Opportunity for Electronics". *Science* 327.5973 (2010), pp. 1607–1611. DOI: 10.1126/science.1181862.

[4] S. JIN, T. H. TIEFEL, M. MCCORMACK, R. A. FASTNACHT, R. RAMESH, and L. H. CHEN. "Thousandfold Change in Resistivity in Magnetoresistive La-Ca-Mn-O Films". *Science* 264.5157 (1994), pp. 413–415. DOI: 10.1126/science.264.5157.413.

[5] N. F. MOTT. "The Basis of the Electron Theory of Metals, with Special Reference to the Transition Metals". *Proceedings of the Physical Society. Section A* 62.7 (1949), p. 416. DOI: 10.1088/0370-1298/62/7/303.

[6] N. F. MOTT. "The transition to the metallic state". *Philosophical Magazine* 6.62 (1961), pp. 287–309. DOI: 10.1080/14786436108243318.

[7] J. HUBBARD. "Electron Correlations in Narrow Energy Bands". *Proceedings of the Royal Society of London A: Mathematical, Physical and Engineering Sciences* 276.1365 (1963), pp. 238–257. DOI: 10.1098/rspa.1963.0204.

[8] S. ASADA and S. SUGANO. "Satellites in X-Ray photoelectron Spectra of Transition-Metal Compounds". *Journal of the Physical Society of Japan* 41.4 (1976), pp. 1291–1299. DOI: 10.1143/JPSJ.41.1291.

[9] S. LARSSON. "Theory of satellite excitations in inner shell X-ray photoelectron spectra of nickel and copper compounds". *Chemical Physics Letters* 32.3 (1975), pp. 401–406. DOI: 10.1016/0009-2614(75)85203-1.

[10] R. ZIMMERMANN, R. CLAESSEN, F. REINERT, P. STEINER, and S. HÜFNER. "Strong hybridization in vanadium oxides: evidence from photoemission and absorption spectroscopy". *Journal of Physics: Condensed Matter* 10.25 (1998), p. 5697. DOI: 10.1088/0953-8984/10/25/018.

[11] J. ZAANEN, G. A. SAWATZKY, and J. W. ALLEN. "Band gaps and electronic structure of transition-metal compounds". *Physical Review Letters* 55 (4 July 1985), pp. 418–421. DOI: 10.1103/PhysRevLett.55.418.

[12] H. KROEMER. "Nobel Lecture: Quasielectric fields and band offsets: teaching electrons new tricks". *Reviews of Modern Physics* 73 (3 Oct. 2001), pp. 783–793. DOI: 10.1103/RevModPhys.73.783.

[13] A. OHTOMO and H. Y. HWANG. "A high-mobility electron gas at the $LaAlO_3/SrTiO_3$ heterointerface". *Nature* 427.6973 (2004), pp. 423–426. DOI: 10.1038/nature02308.

[14] J. S. LEE, Y. W. XIE, H. K. SATO, C. BELL, Y. HIKITA, H. Y. HWANG, and C. C. KAO. "Titanium d_{xy} ferromagnetism at the $LaAlO_3/SrTiO_3$ interface". *Nature Materials* 12.8 (2013), pp. 703–706. DOI: 10.1038/nmat3674.

[15] A. TSUKAZAKI, S. AKASAKA, K. NAKAHARA, Y. OHNO, H. OHNO, D. MARYENKO, A. OHTOMO, and M. KAWASAKI. "Observation of the fractional quantum Hall effect in an oxide". *Nature Materials* 9.11 (2010), pp. 889–893. DOI: 10.1038/nmat2874.

[16] J. R. DAVIS and A. S. M. I. H. COMMITTEE. *Nickel, Cobalt, and Their Alloys*. ASM specialty handbook. ASM International, 2000. ISBN: 9780871706850.

[17] B. RAVEAU and M. SEIKH. *Cobalt Oxides: From Crystal Chemistry to Physics*. Wiley, 2012. ISBN: 9783527645541.

[18] T. TAKAMI. *Functional Cobalt Oxides: Fundamentals, Properties and Applications*. Pan Stanford Publishing, 2011. 180 pp. ISBN: 9789814463324.

[19] J. A. DISEGI, R. L. KENNEDY, and R. PILLIAR. *Cobalt-base Alloys for Biomedical Applications*. ASTM STP 1365 no. 1365. ASTM, 1999. ISBN: 9780803126084.

[20] D. COUTSOURADIS, A. DAVIN, and M. LAMBERIGTS. "Cobalt-based superalloys for applications in gas turbines". *Materials Science and Engineering* 88 (1987). Proceedings of the First International Symposium on High Temperature Corrosion of Materials and Coatings for Energy Systems and Turboengines, pp. 11–19. DOI: 10.1016/0025-5416(87)90061-9.

[21] M. X. MA, Z. Y. PAN, L. GUO, J. H. LI, Z. Y. WU, and S. H. YANG. "Porous cobalt oxide nanowires: Notable improved gas sensing performances". *Chinese Science Bulletin* 57.31 (2012), pp. 4019–4023. DOI: 10.1007/s11434-012-5363-0.

[22] H. J. NAM, T. SASAKI, and N. KOSHIZAKI. "Optical CO Gas Sensor Using a Cobalt Oxide Thin Film Prepared by Pulsed Laser Deposition under Various Argon Pressures". *The Journal of Physical Chemistry B* 110.46 (2006). PMID: 17107147, pp. 23081–23084. DOI: 10.1021/jp063484f.

[23] J. ROSEN, G. S. HUTCHINGS, and F. JIAO. "Ordered Mesoporous Cobalt Oxide as Highly Efficient Oxygen Evolution Catalyst". *Journal of the American Chemical Society* 135.11 (2013), pp. 4516–4521. DOI: 10.1021/ja400555q.

[24] W. ZHANG, H. L. TAY, S. S. LIM, Y. WANG, Z. ZHONG, and R. XU. "Supported cobalt oxide on MgO: Highly efficient catalysts for degradation of organic dyes in dilute solutions". *Applied Catalysis B: Environmental* 95.1-2 (2010), pp. 93–99. DOI: 10.1016/j.apcatb.2009.12.014.

[25] X. C. DONG, H. XU, X. W. WANG, Y. X. HUANG, M. B. CHAN-PARK, H. ZHANG, L. H. WANG, W. HUANG, and P. CHEN. "3D Graphene-Cobalt Oxide Electrode for High-Performance Supercapacitor and Enzymeless Glucose Detection". *ACS Nano* 6.4 (2012), pp. 3206–3213. DOI: 10.1021/nn300097q.

[26] K. TAKADA, H. SAKURAI, E. TAKAYAMA-MUROMACHI, F. IZUMI, R. A. DILANIAN, and T. SASAKI. "Superconductivity in two-dimensional CoO_2 layers". *Nature* 422.6927 (2003), pp. 53–55. DOI: 10.1038/nature01450.

[27] J. V. BADDING. "Superconducting materials: Cobalt oxide layers". *Nature Materials* 2.4 (2003), pp. 208–210. DOI: 10.1038/nmat868.

[28] L. GRAGNANIELLO, S. AGNOLI, G. PARTEDER, A. BAROLO, F. BONDINO, F. ALLEGRETTI, S. SURNEV, G. GRANOZZI, and F. P. NETZER. "Cobalt oxide nanolayers on Pd(100): The thickness-dependent structural evolution". *Surface Science* 604.21-22 (2010), pp. 2002–2011. ISSN: 0039-6028. DOI: 10.1016/j.susc.2010.08.012.

[29] W. MEYER, K. BIEDERMANN, M. GUBO, L. HAMMER, and K. HEINZ. "Surface structure of polar Co $_3O_4$ (111) films grown epitaxially on Ir(100)-(1 x 1)". *Journal of Physics: Condensed Matter* 20.26 (2008), p. 265011. DOI: 10.1088/0953-8984/20/26/265011.

[30] K. HEINZ and L. HAMMER. "Epitaxial cobalt oxide films on Ir(100)-the importance of crystallographic analyses". *Journal of Physics: Condensed Matter* 25.17 (2013), p. 173001. DOI: 10.1088/0953-8984/25/17/173001.

[31] K. S. NOVOSELOV, V. I. FAL, L. COLOMBO, P. R. GELLERT, M. G. SCHWAB, K. KIM, et al. "A roadmap for graphene". *Nature* 490.7419 (2012), pp. 192–200. DOI: 10.1038/nature11458.

[32] Z. C. YANG, C. H. TANG, Y. ZHANG, H. GONG, X. LI, and J. WANG. "Cobalt monoxide-doped porous graphitic carbon microspheres for supercapacitor application". *Scientific reports* 3 (2013), p. 2925. DOI: 10.1038/srep02925.

[33] X. YANG, K. FAN, Y. ZHU, J. SHEN, X. JIANG, P. ZHAO, S. LUAN, and C. LI. "Electric Papers of Graphene-Coated Co_3O_4 Fibers for High-Performance Lithium-Ion Batteries". *ACS Applied Materials & Interfaces* 5.3 (2013), pp. 997–1002. DOI: 10.1021/am302685t.

[34] L. SORIANO, G. G. FUENTES, C. QUIRÓS, J. F. TRIGO, J. M. SANZ, P. R. BRESSLER, and A. R. GONZÁLEZ-ELIPE. "Crystal-Field Effects at the TiO_2-SiO_2 Interface As Observed by X-ray Absorption Spectroscopy". *Langmuir* 16.17 (2000), pp. 7066–7069. DOI: 10.1021/la000330x.

[35] M. F. LÓPEZ, L. SORIANO, F. J. PALOMARES, M. SÁNCHEZ-AGUDO, G. G. FUENTES, A. GUTIÉRREZ, and J. A. JIMÉNEZ. "Soft x-ray absorption spectroscopy study of oxide layers on titanium alloys". *Surface and Interface Analysis* 33.7 (2002), pp. 570–576. DOI: 10.1002/sia.1422.

[36] L. SORIANO, I. PREDA, A. GUTIÉRREZ, S. PALACÍN, M. ABBATE, and A. VOLLMER. "Surface effects in the Ni 2p x-ray photoemission spectra of NiO". *Physical Review B* 75 (23 June 2007), p. 233417. DOI: 10.1103/PhysRevB.75.233417.

Chapter 2

Experimental details

SECTION 2.1

Sample growth: materials properties and evaporation technique

2.1.1 Materials: cobalt and substrates

In this section, the most important properties of the cobalt/cobalt oxides and the substrates used will be discussed. It is not the purpose of this section to give a complete and throughout description of them, since all these materials have been studied and well described throughout the last decades, and a lot of textbooks and articles can be found solely dedicated to them (two already cited and very insightful books about cobalt and cobalt oxides, which have been extensively consulted during the length of this work, are [1] and [2]); but it is good to display some of its most relevant properties for this study, so the results obtained can be better understood.

2.1.1.1 Cobalt: properties and technical details

Cobalt (symbol: Co, Z=27) is a chemical element which belongs to the transition metal group, like nickel, copper or iron, which main physical and structural properties are summarized in table 2.1. Cobalt is mainly found in Earth's crust in combination with other elements, but once it has been purified, it has a grey, sturdy and metallic appearance. Its name comes from the German *kobalt*, which means "goblin": this name was given by the miners that first tried to mine cobalt ores due to the difficulty in extracting pure metal from them, and because of the arsenic content in the primary cobalt ores, which caused the formation of the highly toxic arsenic oxide in the smelting process. Cobalt lumps (supplied by Goodfellow [3], 99.99+ % purity) have been used as precursor material throughout all the experiments of this work.

Parameter	**Co**
Standard atomic weight	58.933
Density (near room temperature)	8.90 g/cm^3
Atomic configuration	[Ar] 4s^2 3d^7
Structure (space group)	hcp (P63/mmc) & fcc (Fm3m)
Phase transition temperature	450 °C
Lattice (Å)	hcp: a=b=2.507, c=4.069. fcc: 3.54
Melting point	1495 °C
Boiling point	2927 °C

Table 2.1: Most important structural and physical parameters of cobalt.

2.1.1.2 Cobalt oxides: properties

Cobalt presents up to three oxidation states: Co^{2+}, Co^{3+} and Co^{4+}. Only two oxides are stable, though: Co_3O_4 and CoO. The first one is the most thermodinamically stable under room conditions [4], and it usually crystallizes in a spinel structure, with Co^{2+} cations tetrahedrally coordinated and Co^{3+} cations octahedrally coordinated with a ratio of 1:2. It dissociates into CoO if heated over 950 °C in air, and it is antiferromagnetic at low temperatures (T_N=40 K). The other stable oxide, CoO, usually crystallizes in an halite-type structure, with Co^{2+} ions octahedrally coordinated; but wurtzite [5] and zinc-blende [6] CoO structures have also been synthesized, although they are much rarer than the halite structure. It is antiferromagnetic (T_N=290 K), and if it is heated in air over 880 K, it oxidises to Co_3O_4. Their main physical and structural properties are summarized in table 2.2, and figures displaying their lattices are displayed in figure 2.1.

Parameter	**CoO**	**Co_3O_4**
Molar mass (g/mol)	74.93	240.80
Density (g/cm^3)	6.44	6.11
Crystal structures (point group)	Rock salt (Fm3m), zinc-blende ($F\bar{4}3m$), wurtzite ($P6_3mc$)	Cubic, spinel structure (Fd3m)
Lattice parameter (Å)	Rock salt: a=4.260; zincblende: a=3.245; wurtzite: a= 3.244, c=5.203	a=8.084
Melting point (°C)	1933	895

Table 2.2: Most important structural and physical parameters of cobalt oxides.

The cobalt oxides belong to the transition metal oxide group of materials. The bonding and stability of these compounds can be explained by Crystal Field Theory. First proposed by John Hasbrouck van Vleck and Hans Bethe in 1932 [11], it successfully describes many properties of these compounds, such as the splitting of the d orbitals to remove their degeneracy, their magnetism, colours, and hydration enthalpies.

In this model, the electric field created by the ligand electron pairs surrounding the central metal is approximated as point negative charges which repel and interact with the d-orbitals on the metal ion. The d-orbitals of an isolated metal ion have the same energy, and they conserve this degeneracy when they are surrounded by an isotropic negative density charge. However, when it is surrounded by isolated charges geometrically distributed around it, some of these charges experience more opposition from the d-orbital electrons of the metal ion than others based on the geometric structure of the molecule, and these interactions create a splitting due to the electrostatic environment: the value of this splitting is known as the crystal field splitting energy, of crystal field stabilization energy.

In order to understand this theory and its implications better, we need to study the geometry of the d-orbitals. Figure 2.2 shows a picture of them, along with the nomenclature usually adopted to distinguish them. The $d_{x^2-y^2}$ and d_{z^2} are aligned with the x, y and z axis, and are

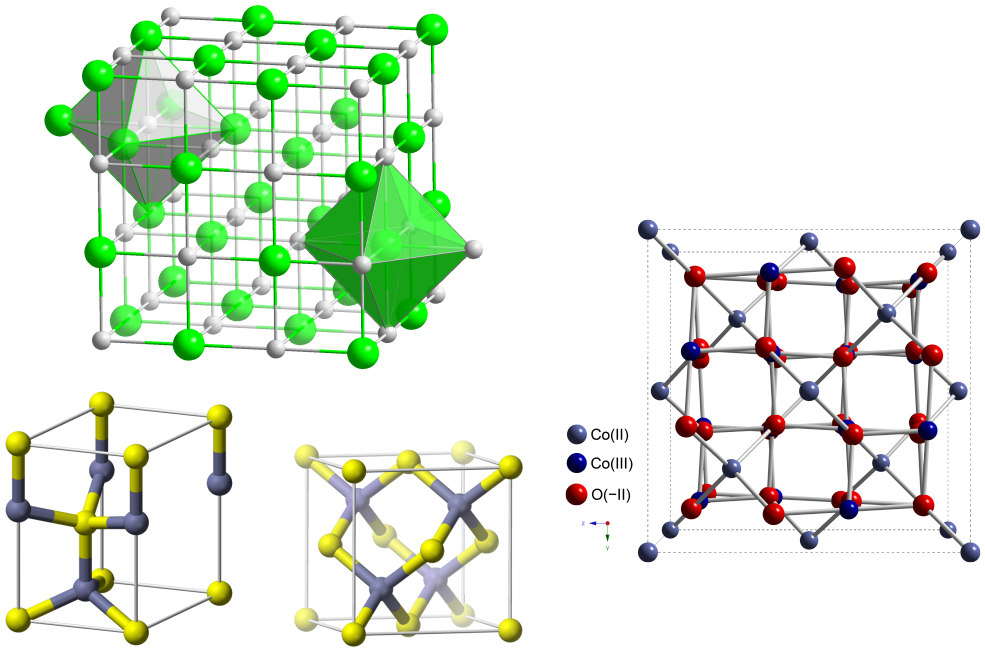

(a) CoO unit cells. Top: rock-salt, taken from [7]. Bottom left: wurtzite, taken from [8]. Bottom right: zincblende, taken from [9]

(b) Co_3O_4 spinel unit cell. Taken from [10]

Figure 2.1: Unit cells for the possible cobalt oxides structures commonly found

pointing at the negative charges when these are distributed in an octahedral symmetry; while the other three orbitals, d_{xy}, d_{yz} and d_{xz}, are not pointing at charges in this symmetry.

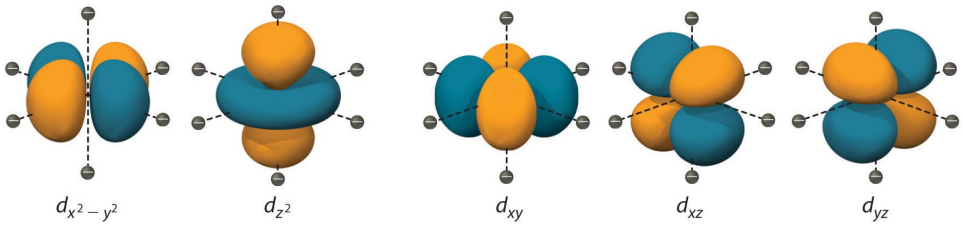

Figure 2.2: Spatial arrangement of the d-orbitals with respect to six ligand distributed in an octahedral symmetry. Picture taken from [12]

Two types of symmetries are going to be mentioned throughout this work: octahedral and tetrahedral. The splitting for the octahedral symmetry causes the $d_{x^2-y^2}$ and d_{z^2} orbitals to increase their energy, while the d_{xy}, d_{yz} and d_{xz} orbitals decrease their energy. Meanwhile, the tetrahedral symmetry causes the d_{xy}, d_{yz} and d_{xz} orbitals to increase their energy, while the $d_{x^2-y^2}$ and d_{z^2} orbitals energy is decreased. This is summarized in figure 2.3.

These ions can have a high-spin or low-spin character. When the spin-pairing energy is greater than the crystal field splitting energy, the electrons tend to occupy empty orbitals first,

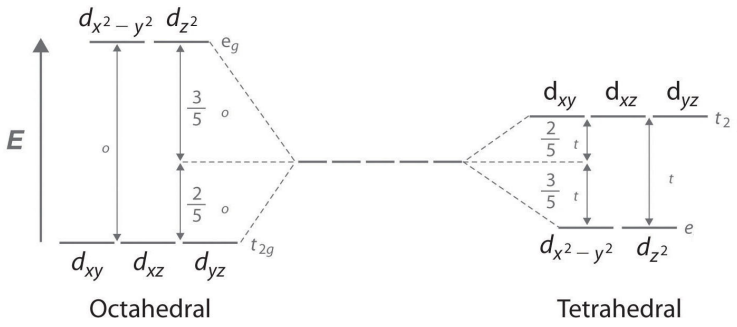

Figure 2.3: Separation of the *d*-orbitals in octahedral and tetrahedral symmetries. Picture taken from [12], minor modifications performed.

according to Hund's rule, giving way to high-spin complexes. On the other hand, when the crystal field splitting energy is greater than the spin-pairing energy, the electrons will tend to occupy the lower energy orbitals first, in accord to the Aufbau principle, giving way to low-spin complexes. In this work, the CoO is considered a high-spin octahedral complex, and the Co_3O_4 is a combination of Co^{2+} ions in high-spin tetrahedral configuration and Co^{3+} ions in low-spin octahedral configuration, adopting a normal spinel structure.

2.1.1.3 Substrates: properties and technical details

As it was stated in the introduction (page 22), four substrates have been used in this work: three oxides (SiO_2, Al_2O_3 and MgO) and Highly Ordered Pyrolitic Graphite (HOPG). The three oxides have been chosen because of their different unit cells, lattice parameters and ionicity values: they are all displayed in table 2.3 and figure 2.4. Single crystals (commercial, supplied by MTI [13]) were used instead of thermally grown oxides because of their lower roughness values. The HOPG was initially chosen as a standard support for the study of a non-interacting CoO_x growth, since the adsorbate-substrate interaction was initially supposed to be much lower than in the oxide substrate interfaces. Its most important parameters are displayed in table 2.4, and its unit cell can be see, along with the rest of the oxide substrates ones, in figure 2.4.

Before every experiment, the substrates were cleaned following these procedures:

- HOPG: scotch tape cleaving in atmosphere conditions, immediately before their introduction in vacuum conditions. Once in vacuum, a heating in vacuum conditions (T=400 °C, P$\sim 10^{-8}$ mbar, t=1 h) was made in order to remove possible contamination.

- Oxides: After introduced in vacuum, and if enough C and O contamination was detected, the substrates were heated (T=400 °C, P$\sim 10^{-8}$ mbar, t=1 h). If contamination was still present, cycles of a soft sputtering ($V_{discharge}$ =500 V, t=1 h, sputtering angle$\sim 10°$), followed by heating in an O_2 atmosphere(T=400 °C, P$\sim 10^{-3}$ mbar, t=1 h) were performed

	MATERIAL		
	SiO_2 (α-quartz)	**Al_2O_3**	**MgO**
Size (mm)		10x10x0.5	
Surface	<11-20> (X-cut)	<0001>	<110>
Structure (space group)	Trigonal ($P3_121$)	Hexagonal ($R\bar{3}c$)	Cubic ($Fm\bar{3}m$)
Lattice (Å)	a=4.91, c=5.40	a=4.76, c=12.99	a=4.21
Rq (nm)	0.3±0.03	0.27±0.05	0.25±0.06
Ionicity [14]	0.482	0.634	0.765

Table 2.3: Main parameters of the oxide substrates used in this work. All data, except the mean roughness, are taken from the supplier's web [13].

	BRAND		
	Goodfellow	**NT-MDT**	**Broker**
Size (mm)	10x10x2	10x10x1.5	12x12x1.2
Quality	ZYA	ZYA	ZYB
Mosaic spread (°)	0.4±0.1	0.4±0.3	0.8±0.2
Structure (space group)	Hexagonal ($P6_3/mmc$)		
Lattice (Å)	a=2.46, c=6.71		

Table 2.4: Most important parameters of the different HOPG substrates used in this work.

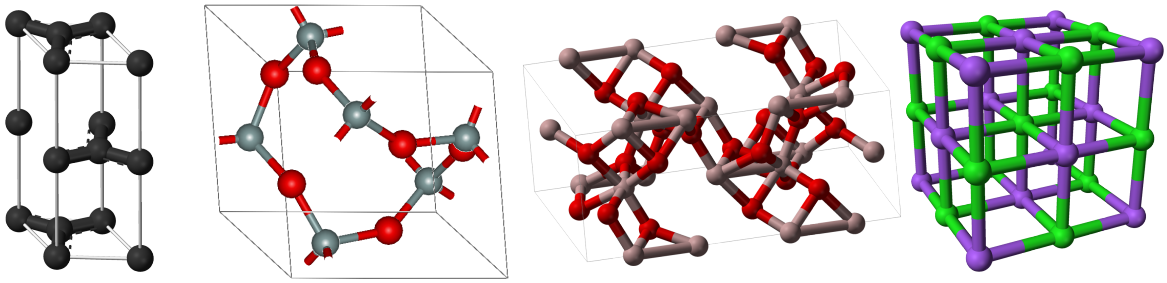

(a) HOPG (b) SiO_2 (c) Al_2O_3 (d) MgO

Figure 2.4: Unit cells diagrams for the substrates used in this work

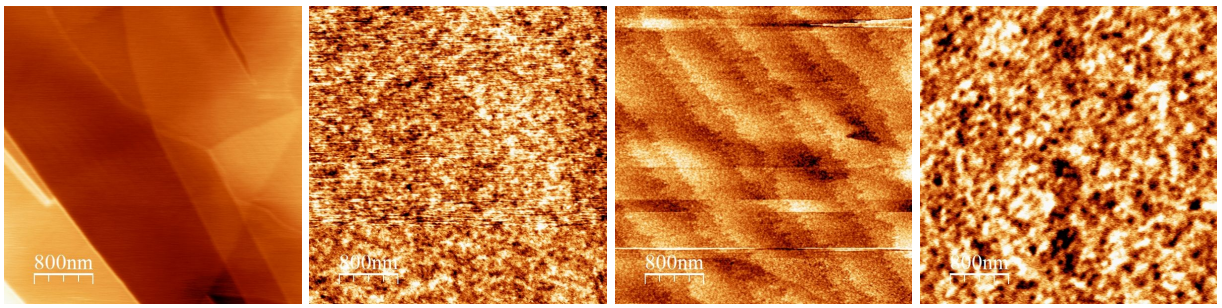

(a) HOPG (b) SiO_2 (c) Al_2O_3 (d) MgO

Figure 2.5: AFM topography images of the clean substrates. Size: 4 µm × 4 µm

until the C contamination was removed. This sputtering was only used in the growth experiments: for the rest of the samples, the substrates were only heated.

Figures 2.5 and 2.6 show AFM topography images and XPS survey spectra of the four clean substrates, respectively. Sometimes Ar contamination on the Al_2O_3 substrates (due to Ar implantation in the sputtering phase of the cleaning) and some traces of oxygen in the HOPG surveys are still visible, but they can be considered small enough for considering the substrates clean.

2.1.2 Evaporation technique: thermal evaporation

All the samples studied in this work have been grown through the thermal evaporation of cobalt in an O_2 atmosphere inside a vacuum chamber, so the experimental conditions could be carefully controlled and contaminations could be avoided as best as possible. This method has been chosen for this work because of both practical and experimental advantages: aside from being already available in the CLAM 4-Camaron setup, it allow us to have very low deposition rates and to ensure that the deposited material is directly in contact with the substrate, which is important in these kind of interface studies.

The thermal evaporation (also called thermal vaporization) belongs to the Physical Vapor Deposition (PVD) group of techniques, which share that only purely physical processes are implied in the coating of the substrate. In the thermal evaporation, a vapour is formed via the heating of a target material, which condenses on the substrate creating the material grown. The particles from the target arrive at the substrate with very low energies (∼0.1 eV [15]), so substrate damage is almost non-existent, and epitaxial layers are easily achieved through with method. Aside from liquid-gas evaporation, this vapour can also be formed from solid phases (via sublimation), depending on the melting point and vapour pressure of the target substance. The most important parameter that can be defined for this deposition technique, and the one determining the deposition rate in any thermal evaporation experiment, is the saturation or equilibrium vapour pressure, which is defined as the vapour pressure of the material in equilibrium with the solid or liquid surface in a closed container. The Antoine equation (which is derived from the well-known Clausius-Clayperon equation) establishes a relationship between temperature and vapour pressure:

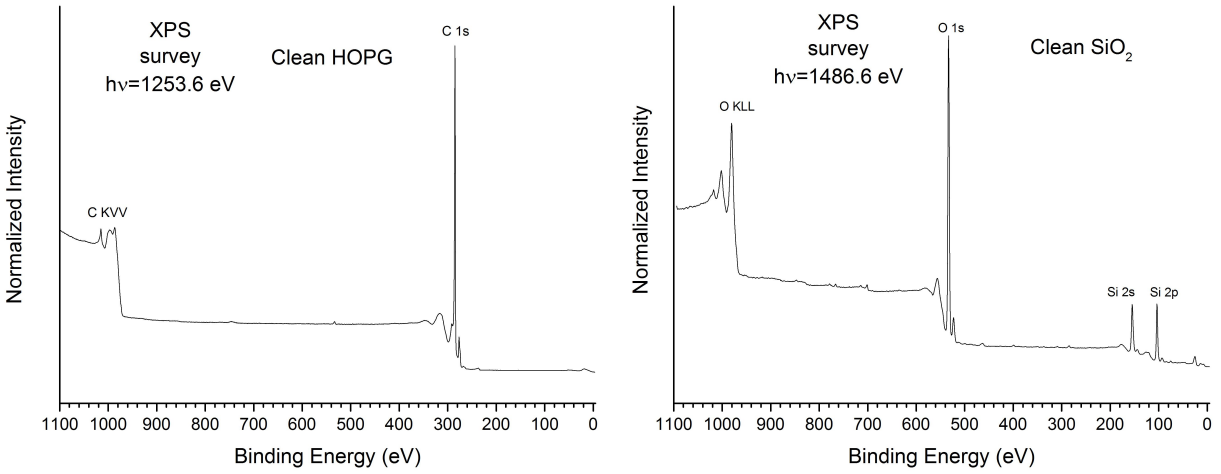

(a) HOPG

(b) SiO_2

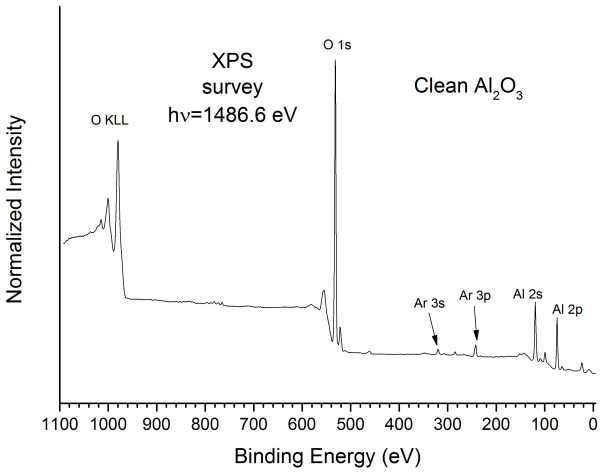

(c) Al_2O_3

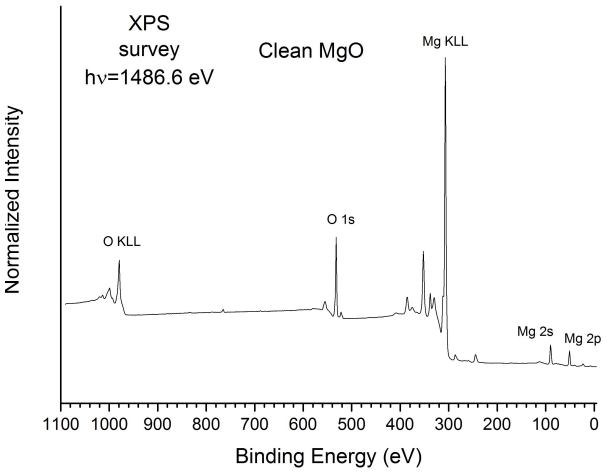

(d) MgO

Figure 2.6: XPS survey spectra of the clean substrates.

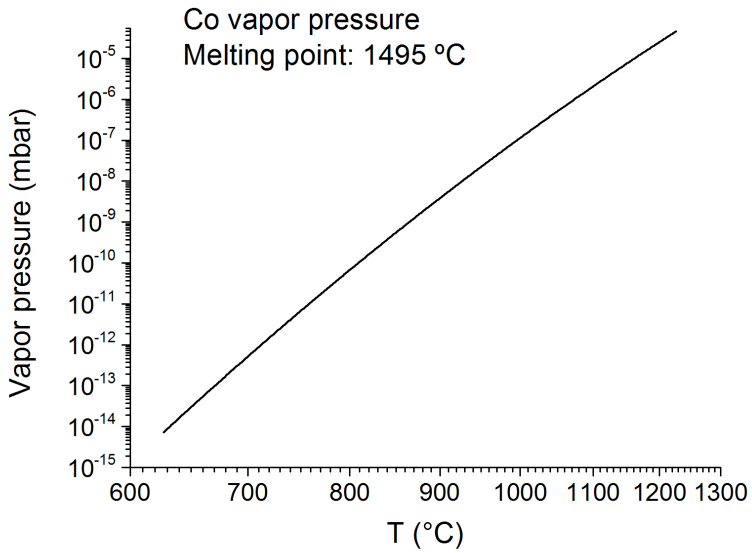

Figure 2.7: Cobalt vapor pressure. Data taken from [16]

$$\log_{10} P = A - \frac{B}{C+T}$$

, where P is the vapour pressure, T is the temperature, and A, B and C are material-related constants. Although these coefficients can be negative, they are calculated in such a way that the vapour pressure always increases with temperature. Figure 2.7 shows the equilibrium vapour pressure of cobalt for temperatures ranging from 600 to 1300 °C.

For low vaporization rates, like the ones used in this work, the flux of vaporized material follows a cosine distribution:

$$\frac{dm}{dA} = \left(\frac{E}{\pi r^2}\right) \cos\phi \cos\theta$$

, where $\frac{dm}{dA}$ stands for mass evaporated per area unit, E is the total mass evaporated, and r is the substrate-target distance.

2.1.3 Evaporating source

Figure 2.8 shows a scheme of the cobalt evaporation source used in all these experiments, whose design essentially resembles a Knudsen cell. The cobalt lumps are introduced inside the alumina crucible, which can be heated with the W coil that surrounds it, and it is covered with a Ta shield, in order to increase the energy efficiency of the evaporator and to avoid heat losses and possible contaminations (for example, evaporated W from the coil). A C-type thermocouple (W-5% Rh vs. W-26% Rh, 0 to 2320 °C) is placed in the crucible in order to measure its temperature. The oxygen is introduced via a gas line placed just aside this

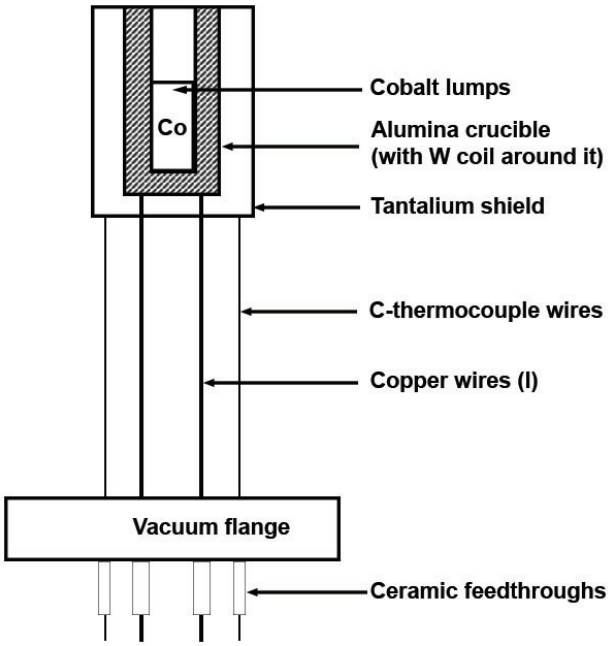

Figure 2.8: Basic scheme of the evaporating source used in this work.

evaporator, and once it has been installed at our vacuum chamber, the top of the evaporator has a fixed distance of ~ 10 cm from the sample.

SECTION 2.2

Experimental facilities

2.2.1 GRIN: CLAM 4-Camaron system

The CLAM 4-CAMARON system, which belongs to the GRIN research group, is a UHV chamber where samples can be grown in very controlled conditions and characterized by XPS in-situ (without having to take them out of the vacuum chamber). Almost all of the sample growths, along with a great deal of the XPS characterization, have been made in this system, which can be seen in figure 2.9.

This vacuum system is divided into three independent chambers, which can be communicated by opening the valves connecting them:

- Introduction chamber: in this part the samples are introduced from atmospheric conditions. It has a small volume, and it is connected to a Pfeiffer turbo-molecular pump (Pfeiffer TMU 071P, pump speed: 70 l/min), so its pressure can reach 10^{-7}-10^{-8} mbar in about an hour and a half.

- Preparation chamber: this part of the system is used for the growth and treatments of samples. The different flanges of this chamber are distributed in vertical planes, so

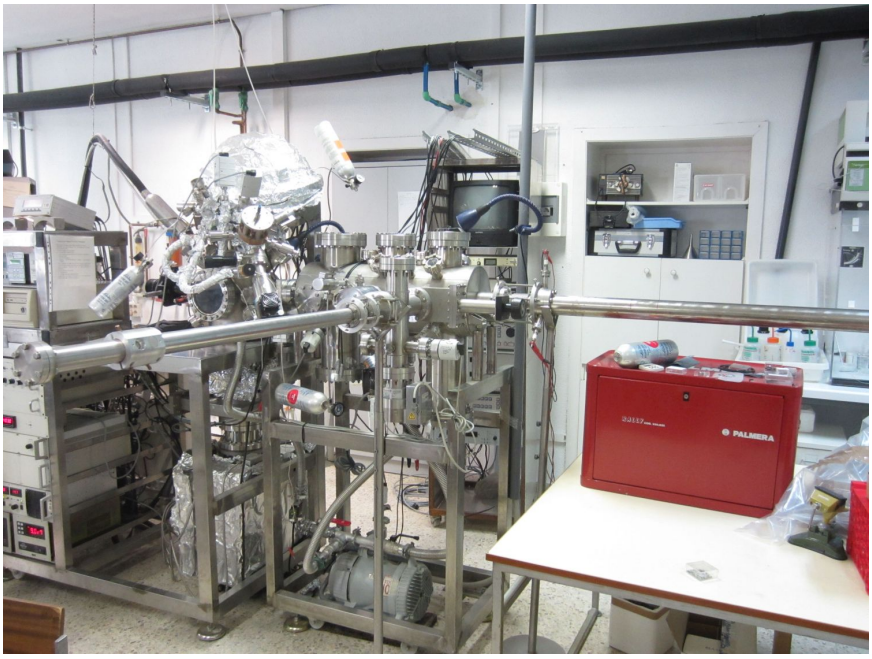

Figure 2.9: General view of the CLAM4-Camaron system.

various procedures and measurements can be made to a sample at the same time. Aside for the Co evaporator used for the growth of the samples studied in this work, it has an Penning ion gun (SPECS IQP 10/63), which is mainly used for sample cleaning; and a heating system, which consists on an halogen bi-pin lamp bulb (24 V, 275 W), being able to heat the samples to temperatures up to 400 °C or 600 °C, depending on the sample size and on the direct contact of the sample directly with the bulb. In the same vertical plane, a sapphire window is installed, which allows the use of an infrared pyrometer (Lumasense IMPAC IP140-LO, 100-700 °C). A quadrupole mass spectrometer (Pfeiffer PrismaPlus QMG 220 M, resolution: 0.5 a.m.u.) is also installed in this chamber, and it is routinely used for leak checks. This chamber is pumped by a Varian turbo-molecular pump (Varian TV301, pump speed: 300 l/min), and its base pressure is usually in the range of 10^{-8} mbar.

- Analysis chamber: in this chamber the XPS analyser and X-ray source are located. It is pumped by an ionic pump (Varian VacIon Plus 500, model 919-0106, pump speed: 410 l/min) and a titanium sublimation pump (Varian 916-0017, maximum sublimation rate: $9 \cdot 10^{-2}$ gr/h), and its working pressure is usually in the range of 10^{-10} mbar. Aside from the X-ray source, an ion gun, an electron gun (SPECS PU-EQ22) and a UV source (SPECS UVS300) for UPS measurements are also available, although they have not been use in this work due to technical problems. More details about the XPS analyser and the X-ray source are given on section 3.1.5 (page 66).

The movement of the sample throughout these three chambers is made via a magnetic linear translator rod. This system also allows the azimuthal rotation of the sample, which has been essential in the growth of all the samples.

2.2.2 Synchrotron facilities

Essentially, synchrotron radiation is the name given to the radiation emitted by a charged particle that is being accelerated radially ($\vec{a} \perp \vec{v}$). For non-relativistic velocities, the main properties of this radiation are essentially similar to the spectrum emitted by a dipole antenna, but when the velocity approaches the speed of light, its properties become extremely interesting for materials researchers: a broad and continuum spectrum (which enables the researchers to choose the wavelength required for their experiments), high flux, brilliance (number of photons per second, cross section, beam angular divergence and deviation from the central wavelength) and stability, pulsed emission, and the possibility of changing its polarization. More specific details about its properties can be found, for example, in [17–19].

For its production, the bunches of electrons are accelerated in boosters previous to the main storage ring (they can be more than one installed), which are usually linear or circular. Once they have acquired enough energy, they are injected into the main storage ring, which is composed of straight sectors separated by arcs, where magnets are placed in order to bend the charged particles towards the next straight sector and produce the synchrotron radiation (hence their name, bending magnets). In the straight sections, wigglers and undulators (arrangements of powerful magnets with different magnetization directions) are placed in order to focus the beam and increase its brilliance, aside from giving the beam a determined polarization. The beamlines are constructed after a bending magnet or an insertion device, and they are tangential to the synchrotron circumference, so the maximum amount of radiation can be used.

The measurements presented in this work have been made in two different european synchrotrons: BESSY II (acronym for “Berliner Elektronenspeicherring-Gesellschaft für Synchrotronstrahlung m. b. H.”, english: Berlin Electron Storage Ring Society for Synchrotron Radiation, now part of the Helmholtz-Zentrum Berlin für Materialien und Energie (HZB)), located at Berlin, Germany; and ESRF (European Synchrotron Radiation Facility), located at Grenoble, France. Their main characteristics are displayed at table 2.5.

Storage ring specifications	**BESSY II**	**ESRF**
Energy (GeV)	1.72	6
Current, top-up (mA)	300	200
Brilliance (photons/(s·mm^2· mrad^2· 0.1% BW))	10^{18}	10^{21}
Circunference radius (m)	240	844
Operative beamlines	46	28
Average beam lifetime (h)	10 (@ 300 mA)	10-50 (depending on filling mode)

Table 2.5: Most important beam characteristics of the BESSY and ESRF synchrotrons. Data taken from [20, 21].

2.2.2.1 PM4 Beamline SurICat/RAC-ARTOF (BESSY, Berlin, Germany)

The measurements presented at this work have been all made at the PM4 beamline. This is a photoemission endstation equipped with a Scienta SES100 analyser (used in this work for the PES measurements) and a Bruker fluorescence detector, aside from nanoamperimeters used to measure the sample drain current signal. It is also equipped with two preparation chambers (also usable as load locks), that are arranged in a way that the analyser chamber can be kept free of contaminating materials, and they both have heatable manipulators which provide temperature ranges from 80 K to 800 K. Its most relevant parameters are summarized at table 2.6:

Parameters	**SurICat, Optics beamline**
Monochromator	Plane grating, operated in collimated light (collimated PGM)
Energy range (eV)	20-2000 eV
Flux (photons/s)	10^9 - 10^{10}
Beam polarization	Horizontal
Focus size, hor. x vert. (mm)	3 x 1
Working pressure (mbar)	10^{10} (analyser), 10^8 (chambers)
I_0 measurement (XAS)	Clean Au (111) single crystal

Table 2.6: Most important parameters of the PM4 beamline of the BESSY synchrotron. (taken from [22])

2.2.2.2 SpLine (ESRF, Grenoble, France)

SpLine is a Spanish government-supported CRG (Collaborating Research Group) beamline of the ESRF synchrotron that started its operation in 2005, and is regulated by a contract between the MEC, responsible for the beamline operation and its accessibility to the Spanish scientific community, and the ESRF. It is a hard X-ray line, and it has two branches dedicated to high resolution X-ray diffraction (branch B) and X-ray absorption experiments (branch A), which operate in alternate mode. The most relevant parameters of both branches are displayed in table 2.7.

SECTION 2.3

Experimental methodology

2.3.1 Evaporator calibration

Before starting the growth of the samples, a calibration of the evaporator was performed, in order to find adequate current and voltage values for the low deposition velocities needed in this study. Two minute evaporations were initially made on a HOPG substrate with incrementally higher current and voltage values, until the Co 2p peaks started to be noticeable in the X-Ray

Parameters	SpLine, branches A and B
Monochromator	Pseudo channel-cut type
Energy range (eV)	5000-35000
Flux (photons/s)	10^{12}
Beam polarization	Horizontal
Focus size, hor. x vert. (mm)	0.1 x 0.1
Working pressure (mbar)	Atmospheric pressure (measurements)
I_0 measurement	Ionization chamber

Table 2.7: Most important characteristics, SpLine, branches A and B (ESRF) [23]

Photoelectron Spectroscopy (XPS) survey spectra. Once these values had been obtained, the substrate was cleaned again, and the growth of cobalt oxide on HOPG was started using these parameters. These values were slightly increased for the oxide growths, since the deposition velocity for the HOPG experiments was considered too low. All values are displayed at table 2.8.

Parameter	CoO/HOPG	CoO/oxides
Current (A)	9	10.5
Voltage (V)	18	22
T (°C)	900	1100
O_2 pressure (mbar)	$2 \cdot 10^{-5}$ (both)	
Angle (°)	0 (both)	

Table 2.8: O_2 pressure and evaporator power values and temperatures used in the depositions of the samples studied in this work.

2.3.2 Growths methodology

For the study of the growth of CoO on the oxide substrates, the first step was the proper cleaning of the substrates with the procedures explained in section 2.1.1.3 (page 40). Once they were measured and considered clean enough, the evaporator was initially degassed: with the sample out of the Preparation chamber (usually in the Introduction chamber), the evaporator power was increased in UHV conditions until they were slightly above the values shown in table 2.8. Once the evaporator temperature had stabilized, it was maintained at those values for 10 minutes, and then it was turned off. Also, the oxygen line was purged before every experiment, in order to avoid contamination. Once everything was properly cleaned, successive evaporations were made on each oxide substrate, with the evaporator current and voltage parameters displayed in table 2.8, but with increasingly larger times. The procedure followed for all the CoO growths made in this work is as follows:

CoO_x evaporation:

1. The initial pressure in the preparation chamber must be in the 10^{-8} mbar range.
2. The sample is placed on the evaporator plane of the chamber, facing in its opposite direction.
3. The evaporator is turned on, and the initial current value is set at $\sim$5 A.
4. The power values are slowly increased until the desired values are reached.
5. Once the temperature is stable, the oxygen leak valve is opened, and the oxygen pressure is regulated until it stabilizes around the desired values.
6. To begin the evaporation, the sample is turned 180°, so it faces the evaporator.
7. Once the desired evaporation time has finished, the evaporator power is slowly decreased until its temperature reaches 500 °C, so no more Co is being evaporated
8. The oxygen leak valve is closed.

After each step, in-situ XPS measurements were performed, and the experiment was continued until the substrate peaks could no longer be observed in the XPS survey spectrum, at which point the experiment was considered finished. The deposition rate and the coverage for each stage measured were then calculated, which are expressed throughout this work in equivalent monolayer units (Eq-ML or simply ML from now on): one ML is equivalent to the total quantity of material present in a single CoO layer with a constant height equal to its cell parameter (for the CoO: 1 ML→layer of h=2 Å, as it was stated in table 2.2, page 38). After these calculations and the analysis of these spectra were performed, samples with selected coverages were grown for the rest of the experiments performed in this work, like the AFM study of the morphology of these growths, XANES, RBS, GIXRD and EXAFS, were used as a way to understand better some of the key results obtained in this work.

2.3.3 Reoxidation methodology

As it was stated in the introduction, another big chunk of results of this thesis are based in the behavior of these ultra-thin CoO samples under thermal oxidation conditions. For these experiments, the following processes, with the conditions and order stated below, have been considered in this work:

Reoxidation, process 1 (Reox-P1 process)

1. The initial pressure in the preparation chamber must be in the 10^{-8} mbar range.
2. The sample is placed in the plane of the heating equipment of the preparation chamber, and the pyrometer is calibrated and positioned.
3. The sample is heated in UHV conditions (400 °C usually), until the sample temperature is constant.
4. The oxygen valve is opened until the desired pressure is attained ($2 \cdot 10^{-3}$ mbar usually). Once the pressure has reached this value, the timer is started.
5. Once the sample has stayed at this conditions for the desired time, the heating is stopped.
6. Once the temperature is below 100 °C (the minimum value measurable by the pyrometer), the oxygen valve is closed.

Reoxidation, process 2 (Reox-P2 process)

1. The initial pressure in the preparation chamber must be in the 10^{-8} mbar range.
2. The sample is placed in the plane of the heating equipment of the preparation chamber, and the pyrometer is calibrated and positioned.
3. The oxygen valve is opened until the desired pressure is attained ($2 \cdot 10^{-3}$ mbar usually)
4. Then, the sample is heated in this conditions (400 °C usually). Once the temperature is constant, the timer is started.
5. Once the sample has stayed at this conditions for the desired time, the heating is stopped.
6. When the temperature is below 100 °C (the minimum value measurable by the pyrometer), the oxygen valve is closed.

Heating

1. The initial pressure in the preparation chamber must be in the 10^{-8} mbar range.
2. The sample is placed in the plane of the heating equipment of the preparation chamber, and the pyrometer is calibrated and positioned.
3. The sample is heated in UHV conditions (400 °C usually). Once the sample temperature is constant, the timer is started.
4. Once the sample has stayed at this conditions for the desired time, the heating is stopped.

SECTION 2.4

Bibliography

[1] J. R. DAVIS and A. S. M. I. H. COMMITTEE. *Nickel, Cobalt, and Their Alloys*. ASM specialty handbook. ASM International, 2000. ISBN: 9780871706850.

[2] B. RAVEAU and M. SEIKH. *Cobalt Oxides: From Crystal Chemistry to Physics*. Wiley, 2012. ISBN: 9783527645541.

[3] *Goodfellow*. URL: http://www.goodfellow.com/.

[4] M. CHEN, B. HALLSTEDT, and L. J. GAUCKLER. "Thermodynamic assessment of the Co-O system". *Journal of Phase Equilibria* 24.3 (2003), pp. 212–227. ISSN: 1054-9714. DOI: 10.1361/105497103770330514.

[5] K. M. NAM, J. H. SHIM, D. W. HAN, H. S. KWON, Y. M. KANG, Y. LI, HY. SONG, W. S. SEO, and J. T. PARK. "Syntheses and Characterization of Wurtzite CoO, Rocksalt CoO, and Spinel Co3O4 Nanocrystals: Their Interconversion and Tuning of Phase and Morphology". *Chemistry of Materials* 22.15 (2010), pp. 4446–4454. DOI: 10.1021/cm101138h.

[6] J. DICARLO and A. NAVROTSKY. "Energetics of Cobalt (II) Oxide with the Zinc-Blende Structure". *Journal of the American Ceramic Society* 76.10 (1993), pp. 2465–2467. DOI: 10.1111/j.1151-2916.1993.tb03967.x.

[7] WIKIMEDIA COMMONS. *NaCl polyhedra*. File: NaCl_polyhedra.png. 2008. URL: http://upload.wikimedia.org/wikipedia/commons/c/c0/NaCl%5C_polyhedra.png.

[8] WIKIMEDIA COMMONS. *Wurtzite unit cell*. File: Wurtzite-unit-cell.png. 2007. URL: http://upload.wikimedia.org/wikipedia/commons/2/24/Wurtzite-unit-cell-3D-balls.png.

[9] WIKIMEDIA COMMONS. *Sphalerite unit cell-depth*. File: Sphalerite-unit-cell.png. 2007. URL: http://upload.wikimedia.org/wikipedia/commons/2/22/Sphalerite-unit-cell-depth-fade-3D-balls.png.

[10] WIKIMEDIA COMMONS. *Cobalt(II,III)-oxide-unit-cell*. File: Co3O4-unitcell. 2008. URL: http://upload.wikimedia.org/wikipedia/commons/8/8e/Cobalt(II,III)-oxide-unit-cell-2006-CM-perspective-3D-balls.png.

[11] J. VAN VLECK. "Theory of the Variations in Paramagnetic Anisotropy Among Different Salts of the Iron Group". *Phys. Rev.* 41 (2 July 1932), pp. 208–215. DOI: 10.1103/PhysRev.41.208.

[12] A. AWAN and R. J. LANCASHIRE. *Crystal Field Theory (Chemwiki)*. Ed. by DAVIS UNIVERSITY OF CALIFORNIA. URL: http://chemwiki.ucdavis.edu/Inorganic_Chemistry/Crystal_Field_Theory/Crystal_Field_Theory.

[13] *MTI Corporation*. URL: http://mtixtl.com.

[14] Y. Y. GUO, C. K. KUO, and P. S. NICHOLSON. "The ionicity of binary oxides and silicates". *Solid State Ionics* 123.1-4 (1999), pp. 225–231. DOI: 10.1016/S0167-2738(99)00083-1.

[15] D. M. MATTOX. "Chapter 6 - Vacuum Evaporation and Vacuum Deposition". *Handbook of Physical Vapor Deposition (PVD) Processing (Second Edition)*. Ed. by D. M. MATTOX. Second Edition. William Andrew Publishing, 2010, pp. 195–235. ISBN: 978-0-8155-2037-5. DOI: 10.1016/B978-0-8155-2037-5.00006-X.

[16] C. B. ALCOCK, V. P. ITKIN, and M. K. HORRIGAN. "Vapour Pressure Equations for the Metallic Elements: 298-2500 K". *Canadian Metallurgical Quarterly* 23.3 (1984), pp. 309–313. DOI: 10.1179/cmq.1984.23.3.309.

[17] P. WILLMOTT. *An Introduction to Synchrotron Radiation: Techniques and Applications*. Wiley, 2011. ISBN: 9781119972860.

[18] A. C. THOMPSON and D. VAUGHAN, eds. *X-Ray Data Booklet*. Jan. 2001.

[19] A. HOFMANN. *The Physics of Synchrotron Radiation*. Cambridge University Press, 2004. ISBN: 9781139451109.

[20] *Photon source BESSY II*. URL: http://www.helmholtz-berlin.de/quellen/bessy/index_en.html.

[21] *ESRF*. URL: http://www.esrf.eu/.

[22] *Optics Beamline (BESSY II)*. URL: https://www.helmholtz-berlin.de/pubbin/igama_output?modus=einzel&sprache=en&gid=1614&typoid=37587.

[23] *SpLine, branch A (ESRF)*. URL: http://www.esrf.eu/UsersAndScience/Experiments/CRG/BM25/BeamLine/SourceCharacteristics.

Chapter 3

Characterization techniques

SECTION 3.1

X-ray Photoelectron spectroscopy (XPS)

3.1.1 Introduction

X-Ray Photoelectron Spectroscopy (XPS) is a spectroscopic technique based on the study of the electrons emitted from a sample irradiated with X-rays. It gives compositional, chemical and sometimes morphological information about the surface (∼2-5 nm) of a sample. Its origins can be traced back to the beginnings of the 20th century, with the experiments of P. D. Ennis [1], but it was in the fifties, with the studies by Kal Sieghbahn [2], when it started to reach its actual status as one of the most important surface characterization spectroscopic techniques. When the X-ray source is not a commercial one, like in the case of synchrotron XPS measurements, it is also called Photoelectron Spectrocopy (PES). In this work, we will refer to this technique as Photoelectron Spectrocopy (PES) when the measurements are made in a synchrotron facility.

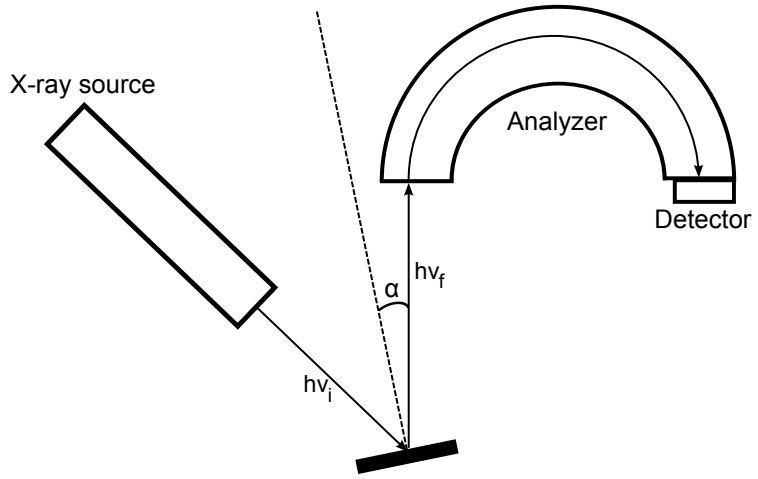

Figure 3.1: Scheme of a typical XPS experimental setup

A typical scheme of a XPS experimental setup can be seen in figure 3.1. The X-rays from the source arrive at the sample and induce the emission of electrons from the surface atoms, which are energetically separated by the analyser (which usually is a capacitor with a determined geometry) and counted in the detector. The angle between the sample surface normal and the analyser, labelled α on the scheme, is called the take-off angle, and it is important in determining the sampling depth of our measurement. Ultra-high vacuum conditions ($\sim 10^{-10}$ mbar) are commonly used so the electrons does not interact with themselves or other molecules in their path towards the analyser, but recent developments [3–6] have allowed this technique to be used in near-ambient pressure conditions.

XPS has been used in this study as our main chemical characterization technique because, aside from being available in our evaporation chamber, it has an impressive chemical sensitivity

(usually in the parts per thousand range), it allows us to easily distinguish between different oxidation states in transition metal oxides, and its sampling depth is adequate for the low coverages and interface studies presented in this work.

3.1.2 General features of an XPS spectra

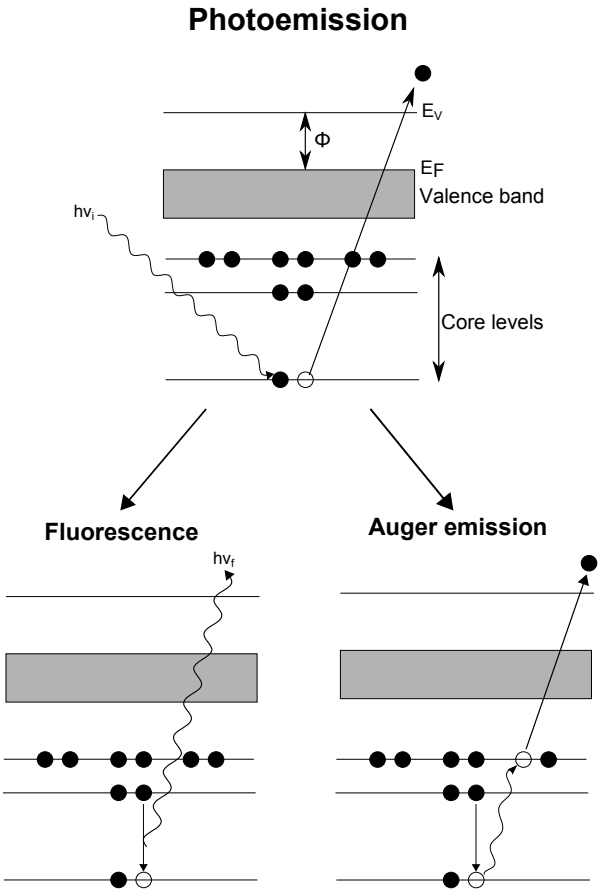

Figure 3.2: A basic scheme outlining two of the most important photoemission process that happens in an XPS measurement.

In a typical XPS spectra, the number of counts on the detector versus the energy (kinetic or binding) are represented. From the potential difference between the capacitor plates, the kinetic energy of the analysed electrons can be easily calculated, and the binding energy can be obtained from the following equation:

$$E_b = h\nu - E_k - \phi \tag{3.1}$$

, where E_b and E_k stand for binding and kinetic energy, $h\nu$ is the energy of the photons that are illuminating the sample, and ϕ stands for the sum of the sample and the spectrometer work functions. In this equation it is assumed that the first ionization energy of the orbital

involved in the photoemission process is equal to the negative of the binding energy of said orbital: in other words, the photoemission process does not change the binding energy of the orbital implied in it (Koopman's theorem [7]). This allows us to identify the orbitals of the elements present in the surface of our sample from the energy position of some of the peaks that appear in our spectrum. These peaks can be separated into several types:

- Photoemission lines: They come from a photoemission process (see figure 3.2), and are usually narrower than the rest. They will be better described in subsection 3.1.3, since they are usually the most important features of an XPS spectrum.

- Auger lines: These groups of lines are detected when a Auger process occurs (see figure 3.2), and are identified by three letters, which indicates the level of ionization, the level where the second electron involved in the transition comes from, and the level from which the Auger electron is emitted (K, L, N, O or V, the latter used when the final vacancies are in the valence band). They have constant kinetic energies, so they can be easily identifiable by changing the energy of the X-ray source, and checking for changes in their binding energy.

- Multiplet splitting: When an atom has unfilled shells with unpaired electrons in its valence bands, and a core electron vacancy is created, there can be coupling between the unpaired electron in the core and the unpaired electrons in the outer shell. This is manifested in the spectra as a structure with different peaks around the main photoelectron peak.

- Shake-up satellites: when the outgoing electron interacts with a valence electron and excites it to a higher energy level, it reduces the energy core electron, and gives rise to a satellite structure positioned a few eV above (in binding energy) the core level position.

- Shake-down satellites: when the outgoing electron not only interacts with a valence band electron, but it is also ejected from the atom. They are detectable in a XPS spectra as a broadening of a core level peak.

- Plasmons: the interaction of the ejected electron with the atoms can excite a resonance of the electronic plasma and produce a collective oscillation of its density, which quantization is called plasmon. They appear in an XPS spectrum as a series of equally spaced peaks with more binding energy than the main photoemission peak which originates them, and descending intensities.

- Ghost lines: when the anode of our X-ray source is not clean, other peaks appear in the emission from our source, which manifest in the spectra as small peaks corresponding to the most intense peaks, but displaced by a well known energy interval.

- X-ray satellites: even if the anode of the X-ray source is clean, its emission can be not entirely monochromatic, having small components aside from the main emission peak. This produces replicas of the peaks produced by the main emission line with a relative position and intensity that depends on the anode material.

Electrons that does not come from the upper layer of the sample will lose energy, which will be reflected as an general increase of the intensity of the spectra above the binding energy of said peaks. This feature is usually referred as the spectrum background, and it contains valuable information about the nature and morphology of our sample, as it will be discussed in section 3.1.3.2. It is continuous, since the scattering processes are random and multiple, and it also has a sizeable contribution from the Bremsstrahlung radiation from the X-ray source. Also, spin-orbit coupling effects will cause peaks coming from orbitals with azimuthal quantum number greater than 0 to appear twice in our spectra: this is known as the spin-orbit splitting effect. The peaks will have specific area ratios based on the degeneracy of each spin state, so the peaks coming from levels with greater total angular momentum quantum number will be more intense, and also will have lower binding energies.

3.1.3 Photoemission peaks and background

3.1.3.1 Profile of a photoemission peak

In the great majority of cases, the main objects of study in an XPS spectra are the photoemission peaks. Their shape is a combination of the physics involved in the ionization process and the distortions introduced by the experimental equipment. They have complex shapes, and even though they are usually symmetrical, they can also be asymmetrical. Their height is determined primarily by the photoemission cross section (the probability of an electron to be emitted from an atom), which depends on the X-ray energy and flux, and the orbital which is implicated in the photoemission process. Meanwhile, their full width at half maximum (FWHM) depends on the analyser resolution, our X-ray source bandwidth, and the lifetime of the core level implicated in the photoemission process.

Their position can change due to a lot of factors. The most interesting one from a researcher point of view is the chemical bonds between the elements of our sample (e.g., the binding energy of the Co $2p_{3/2}$ peak is different for metallic Co, CoO or Co_3O_4), but if the sample is an electrical insulator, the whole spectra is going to be displaced due to charge effects, even if the sample is connected to ground. This can easily corrected by checking the energy of a well known peak of our spectra (such as the C 1s peak, for example) and moving the whole spectra until the peak matches the expected value, a process that is called “energy calibration” or “charge correction”.

These peaks are usually modelled by the convolution of Gaussian and Lorentzian functions. The Gaussian curve is used to simulate any contribution made by the measurement process (such as x-ray line profile, Doppler and thermal broadening, or instrumental response, for example), while the Lorentzian shape simulates the lifetime broadening of the peak. The convolution of both shapes is called a Voigt profile (named after German physicist Woldemar Voigt), and does not have an analytical form [8]. Instead of a Voigt profile, other approximations are commonly used, such as Gaussian-Lorentzian sums and products.

The shape of these peaks can also be asymmetrical, something that can be due to a great variety of factors, like shake-up events in metallic samples, for example. In order to include this peak behaviour in the calculations, a tail modifier can be added to the Gaussian-Lorentzian shapes (usually just an exponential function with a piecewise condition), or a Doniach-Sunjic

function (named after the mathematicians Sebastian Doniach and Marijan Sunjic, who first proposed this function for asymmetrical peaks in 1970 [9]) can also be used. In this work, Gaussian-Lorentzian sums with exponential tail modifiers have been used for all the fittings of XPS asymmetrical peaks: its equations are displayed in figure 3.3, and a graph showcasing their differences can be seen in figure 3.4

$$G(E,\sigma) = \frac{e^{-(E-E_0)^2/(2\sigma^2)}}{\sigma\sqrt{2\pi}}$$

(a) Gaussian function

$$L(E,\gamma) = \frac{\gamma}{\pi\left((E-E_0)^2+\gamma^2\right)}$$

(b) Lorentz function

$$T(E,s,k,\sigma) = \begin{cases} s\exp\left[-k\dfrac{E-E_0}{\sigma}\right] & E \leq E_0 \\ 1 & E \geq E_0 \end{cases}$$

(c) Tail modifier

Figure 3.3: Equations of the peak shape functions used in this work to simulate the XPS photoemission peaks.

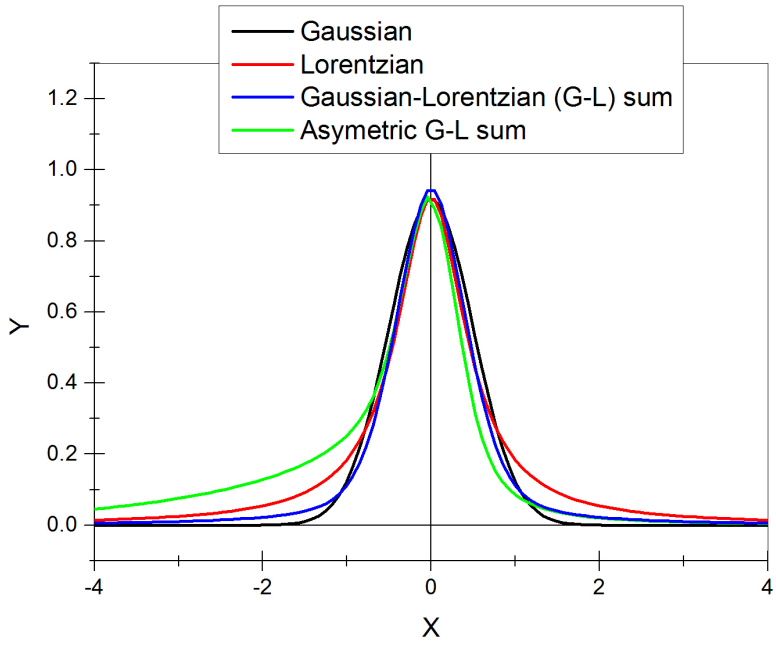

Figure 3.4: Gaussian, Lorentzian, G-L sum and modified G-L sum graphs. Width of Gaussian and Lorentzian functions: 1. The rest of the parameters have been modified for an easier comparison between them.

3.1.3.2 Inelastic background

For any successful quantitative calculation and fitting of an XPS spectra, an adequate removal of the background is mandatory, and if it is not well performed, it can alter peak intensities and distort any quantification attempt. From the various methods available for background removal, three of them (maybe the most used in XPS studies) are going to be considered in this section. The first one, called linear background method, consists in the removal of a linear background drawn between the first and the last points of a spectrum, and while it can work well in some cases, it is preferable to use another background removal method, since it is the most simple and least accurate of these methods. The other two will be explained in the following sections.

Shirley background One of the most popular methods for background removal was developed by David A. Shirley in 1972 [10], and, even if it can lead to significant errors if not used well [11], its ease of computation have made it one of the most used methods for background removal. It is an iterative method based on the idea that the background intensity at any energy point is proportional to the total spectral area to higher energies, or, in other words, that for each photoelectron at a particular energy there is a constant background to lower energies. If our background function is called $S_S(E)$, the algorithm for the Shirley background for an (E_{min}, E_{max}) energy interval is [12]:

$$S_{S,i}(E) = k \int_{E}^{+\infty} dE'(j(E') - S_{S,i-1}(E')) \tag{3.2}$$

, where $j(E')$ is the measured intensity at energy E', and k is the difference between the intensity values at E_{min} and E_{max}. The initial value $S_{S,0}$ is the one corresponding to a constant background, and the series usually converges after three or four iterations.

Tougaard background Another method for background calculation was developed by Sven Tougaard and colleagues almost twenty years ago [13–16]. We will not delve into too much details, since that is beyond the scope of this work, but some of the basics foundations of this method have to be explained, because they are important for understanding the methodology used in the calculations shown in chapters 4 and 5.

First, we start by making some definitions:

- $J(E, \Omega)$: measured intensity for energy E in a solid angle Ω.
- $F(E_0, \Omega_0, x)$: Flux of electrons excited at depth x, dx in an energy interval E_0, dE_0 into the solid angle Ω_0, $d^2\Omega_0$; that is, our primary atomic spectra.
- $G(E_0, R; E)$: Probability that an electron with initial energy E_0 has energy in the interval E, $E+dE$ after having travelled the path length R. It essentially gives the energy distribution of an electron as a function of the path length travelled in the solid.

- $Q(E_0, \Omega_0, x; R, \Omega)$: Probability that an electron excited with energy E_0 at depth x in direction Ω_0 will arrive at the surface in the direction Ω, $d^2\Omega$ after having travelled the path length R, dR.

The measured spectra $J(E, \Omega)$ will therefore be:

$$J(E,\Omega) = \int dE_0 \int d^2\Omega_0 \int dx\, F(E_0, \Omega_0, x) \times \int Q(E_0, \Omega_0, x; R, \Omega)\, G(E_0, R; E)\, dR \tag{3.3}$$

This method uses three main approximations:

1. The energy distribution at the point of excitation does not vary with depth: in other words, we can assume that the peaks that we are analysing comes from a zone of our sample that has an uniform composition.

2. The inelastic effects in the energy range that we are interested are predominant, so we can neglect the elastic scattering effects.

3. The total energy loss is small compared with the primary electron energy, which means that the inelastic cross section, $K(E, T)$, which should depend on the energy E and the distance interval that the electron travels while in the sample, T, will not depend on the energy.

The first approximation implies that we can separate the depth contribution from $F(E_0, \Omega_0, x)$:

$$F(E_0, \Omega_0, x) = f(x) \cdot F(E_0, \Omega_0) \tag{3.4}$$

, where $f(x)$ is now the concentration profile, the number of atoms at depth x. The second assumption allow us to simplify the equation (3.3):

$$J(E,\Omega) = \int dE_0\, F(E_0, \Omega) \int f(x)\, G(E_0, x/\cos\theta; E)\, dx \tag{3.5}$$

, where $G(E_0, x/\cos\theta; E)$ now depends on the depth and the angle of the path, and is primarily determined by the inelastic cross section $K(E, T)$, or the probability that an electron of energy E will lose energy in the interval T,$T + dT$ after having travelled a path length dR. Here is where the third approximation made earlier becomes useful, because it allowed Tougaard and his colleagues to give a rigorous solution to equation (3.5):

$$\begin{aligned} J(E,\Omega) &= \int dE_0\, F(E_0, \Omega) \int ds\, \exp^{-i2\pi s(E-E_0)} \times \int dx\, f(x) \exp^{-x\Sigma(s)\cos\theta} \\ \Sigma(s) &= \frac{1}{\lambda} - \int_0^\infty K(T)\, \exp^{-isT}\, dT \end{aligned} \tag{3.6}$$

The three important parameters that rule the behaviour of equation (3.6) are the IMFP (λ), the inelastic cross section ($K(T)$), and the concentration profile ($f(x)$). The first one can

be easily calculated with the so-called TPP-2 formula, derived by Shigeo Tanuma, Cedric J. Powell and David R. Penn [17]. For $K(T)$, the universal cross section, also developed by Sven Tougaard [18, 19], and which equation can be seen below, works reasonably well for most materials, and it is the one used in this work.

$$\lambda_i K(E,T) = \frac{BT^2}{(C+T^2)^2} \tag{3.7}$$

B and C are parameters that can be changed to yield better results, although the values $B = 1643\,\mathrm{eV}^2$ and $C = 3000\,\mathrm{eV}^2$ give reasonably good results for most types of materials. The third parameter, $f(x)$, is the most interesting from the point of view of this work, because it is directly related with the morphology of the sample, as it will be discussed in the next subsection.

3.1.4 Thickness/morphology quantification

Aside from elemental detection and chemical properties, XPS can also be used to estimate how much material we have grown on our substrate, and even to estimate the morphology of our deposition. In this section we are going to talk about the two methods used in this work to estimate this from our XPS spectra.

3.1.4.1 Infinitely thick layer model

The simplest model used for estimation of coverages is to consider that our material forms a layer that has a constant and uniform thickness across all the scanned area. The intensity of a peak corresponding to an infinitesimal slice of a layer with these characteristics, but an infinite thickness, is [20]:

$$dI = \Phi\,\sigma N k \exp\left(\frac{-x}{\lambda\cos(\theta)}\right)dx \tag{3.8}$$

, where I is the measured intensity, Φ is the photoionization cross section of the orbital corresponding to that peak, N is the number of atoms per volume unit, λ is the IMFP of the measured electrons, θ is the angle between the path of the escaping electrons and the surface normal (also called the take-off angle), and x is the depth where those electrons are ejected from. If we have a substrate that is covered with a layer of another material that has a thickness d, integrating equation (3.8) from 0 to d for the intensity of some peak that belongs to the substrate will give us the intensity from the material below the covering layer, and integrating from d to $+\infty$ for a peak that belongs to the layer above it will give us the intensity from said layer:

$$I_{\text{layer}} = \int_d^{+\infty} \Phi\sigma N k \exp\left(\frac{-x}{\lambda\cos(\theta)}\right)dx = \Phi\sigma N k \lambda_{\text{layer}}\cos(\theta)\left[1-\exp\left(\frac{d}{\lambda_{\text{layer}}\cos(\theta)}\right)\right] \tag{3.9}$$

$$I_{\text{bulk}} = \int_0^{d} \Phi\sigma N k \exp\left(\frac{-x}{\lambda\cos(\theta)}\right)dx = \Phi\sigma N k \lambda_{\text{bulk}}\cos(\theta)\exp\left(\frac{d}{\lambda_{\text{bulk}}\cos(\theta)}\right) \tag{3.10}$$

In our experiments, $\theta = 0$, so $\cos(\theta) = 1$, Also, if the measured series of spectra all have the same take-off angle, all the factors preceding both integrals can be grouped into a single constant:

$$I_\infty \equiv \Phi\sigma N k \lambda_{\text{layer}} \cos(\theta)$$

, and equations (3.9) and (3.10) can be simplified:

$$I_{\text{layer}} = I_\infty \left[1 - \exp\left(\frac{d}{\lambda_{\text{layer}}}\right)\right] \tag{3.11}$$

$$I_{\text{bulk}} = I_\infty \exp\left(\frac{d}{\lambda_{\text{bulk}}}\right) \tag{3.12}$$

If we have a series of spectra for different coverages that have been measured in the same conditions, (in our case, same analyser-sample-X-ray source distances), and we know the IMFP of the ejected electrons (which, as we said in page 64, can be calculated), we can fit the measured intensities of a peak of the deposited layer with equation (3.11), and find values for the thickness d of the layer. Obviously, if the material does not grow with this morphology, the results will not be precise, but since the area measured by XPS is usually much larger than the width of the structures that the deposited material is conforming on the substrate, it is valid as a first approximation of the total material quantity grown on the substrate.

3.1.4.2 XPS inelastic peak shape analysis (XPS-IPSA) (Tougaard background correction method)

As we said in page 63, the background calculated by the Tougaard formula depends on the concentration profile $f(x)$. This means that, if we have a calculated background, and we know the rest of parameters involved in said formula, we can determine the concentration profile from which that background came from: in other words, we can, to some extent, extract morphological information from the inelastic background of our XPS spectra. One way that we can achieve this is by calculating the peak shapes using equation (3.6). Another way of obtaining $f(x)$ is solving equation (3.6) for the primary excitation spectra $F(E,\Omega)$ [13, 21]:

$$\begin{aligned} F(E,\Omega) &= \frac{1}{P_1}\left[J(E,\Omega) - \int dE' J(E,\Omega) \times \int ds \exp^{\left[i2\pi s\left(E'-E\right)\right]}\left(1 - \frac{P_1}{P(s)}\right)\right] \\ P(s) &= \int d(x) f(x) \exp\left(-\frac{x}{\cos\theta}\Sigma(s)\right) \\ P_1 &= \int d(x) f(x) \exp\left(-\frac{x}{\lambda\cos\theta}\right) \end{aligned} \tag{3.13}$$

Since the most probable energy loss for electrons moving in solids is, in general, between 10 and 30 eV above (in binding energy) the main photoemission peak [19], the intensity measured from 30 eV above the main photoemission peak (in binding energy) once the background

has been removed should be equal to zero. This gives us a good strategy for estimating the morphology of our sample: we can calculate $F(E,\Omega)$, and then change $f(x)$ until this constraint is fulfilled. If we have access to a pure sample of the material which peaks are being studied, we can use it as a reference, and make variations on $f(x)$ until we end up with a calculated spectrum with the same absolute intensity and peak shape as the reference spectrum: this is the approach that has been used in this work.

To conclude this part, we have to note that, while this is a powerful method, it also has obvious limitations, mostly due to the approximations made (uniform composition, for example), and the experimental limitations (maximum probing depth of XPS, for example). Still, they are all within the range of the characteristics of our samples, and while they do not allow us to use it on the lowest or highest coverage ranges explored, it is enough to obtain interesting morphological data and correlations with other techniques.

3.1.5 Experimental details

The XPS measurements showed in this work have been made at the Group of Coatings, Interfaces and Nanostructures at the Applied Physics Department of the Universidad Autónoma de Madrid, at the vacuum chamber described in section 2.2, with a 9 channeltron hemispherical analyzer (model CLAM-4, ThermoVG Scientific) with a resolution of 0.7 eV at a 20 eV pass energy. The surveys were made with a 50 eV pass energy and a step of 1 eV, while the rest of the regions were made with a step of 0.1 eV and a 20 eV pass energy. The source used is a twin-anode source (model number: XR3E2), with Mg and Al anodes (Mg Kα =1253.6 eV, Al Kα =1486.6 eV) radiations. The Mg anode was used for all the CoO_x/HOPG experiments, while the Al anode was used in the oxide substrate experiments, in order to avoid a possible overlapping of the Co 2p and O KLL peaks, which could distort the result of the low coverage samples measurement.

The PES measurements were made in the SurICat (Surface Investigation and Catalysis) station of the Optics Beamline SurICat/RAC-ARTOF beamline of the BESSY synchrotron (Berlin, Germany), with a high resolution electron energy analyser Scienta SES100. Two configurations were used for the O 1s and C 1s regions: one which would probe the maximum depth available ($h\nu = 1000$ eV, T-off angle=0°), and another that would be as superficial as possible. For the low sampling depth configurations, the angle was set at (60°), and the $h\nu$ energy was chosen so the kinetic energy of the outgoing photoelectrons would be between 50-100 eV. The most important beam parameters have been described in section 2.2.2.1 (page 48), and the energy resolutions for the used beam energies, angles and slit configurations are displayed in table 3.1.

The charge correction has been made using the substrate peaks, with the values displayed in table 3.2. Since the resolution of our spectrometer is not enough to resolve the 2p doublet in the oxide substrates, the peak used is the general 2p peak resulting from the sum of the $2p_{1/2}$ and $2p_{3/2}$ peaks. For fittings, the software XPSPeak [22] was used, and Originlab Origin versions 8.5 and 9.0 [23] have been used to plot and perform basic analysis on all the XPS spectra, aside from a good deal of the rest of the graphs shown in this work. For the XPS-IPSA calculations, the software QUASES-Analyze, developed by Sven Tougaard and Francisco

Region	hν (eV) (T-off angle)	Resolution (meV)	Sampling depth (Å)
Survey	1000 (0°)	310	-
Co 2p	1000 (0°)	210	7
O 1s (0°)	1000 (0°)	210	11
C 1s (0°)	1000 (0°)	210	14
O 1s (60°)	600 (60°)	140	3
C 1s (60°)	380 (60°)	70	3

Table 3.1: Resolution for the main regions measured on the PES experiments performed at the SurICat endstation in the BESSY synchrotron.

Substrate	Reference peak	Energy (eV)	Reference
HOPG	C 1s	284.3	[26]
SiO_2	Si 2p	103.4	[27]
MgO	Mg 2p	54	[28]
Al_2O_3	Al 2p	74.4	[29]

Table 3.2: Peak energies used as reference in the charge correction of the XPS and PES spectra.

Yubero [24] has been used, and the inelastic mean free paths were calculated with the free (for non-commercial use) program QUASES-IMFP-TPP2M [25].

SECTION 3.2

Atomic Force Microscopy (AFM)

Atomic Force Microscopy (AFM) is a microscopy technique which belong to the Scanning Probe Microscopy (SPM) techniques group, like Scanning Tunneling Microscopy (STM) or Magnetic Force Microscopy (MFM). It was developed by Gerd Binnig, Christoph Gerber and Calvin Quate in 1986 [30], five years later than the development of STM [31], also by Gerd Binnig and Heinrich Hohrer, for which they received the Nobel prize in 1986.

In AFM, we approach a very thin tip (also called “probe”) to the surface of a sample, mounted in a flexible cantilever, and close enough (typically a few nm) to be affected by forces produced by its interaction with the sample, like electrostatic repulsion, Van Der Waals forces, capillarity forces, and so on. A tip parameter (for example, tip-sample distance) is then fixed with a feedback loop, and an area of the sample is scanned while the variations on the deflection of the cantilever are registered, using the reflection of a laser with the back of the cantilever, which movement is registered by a photodiode matrix.

Depending on the probe-sample distance, different modes of operation, based on the sample-tip interaction type, can be distinguished, as shown in figure 3.5. Also, depending on the tip composition, the electric and magnetic fields applied between the tip and the sample, and even the tip harmonic mode used, a myriad of techniques can be distinguished. In this

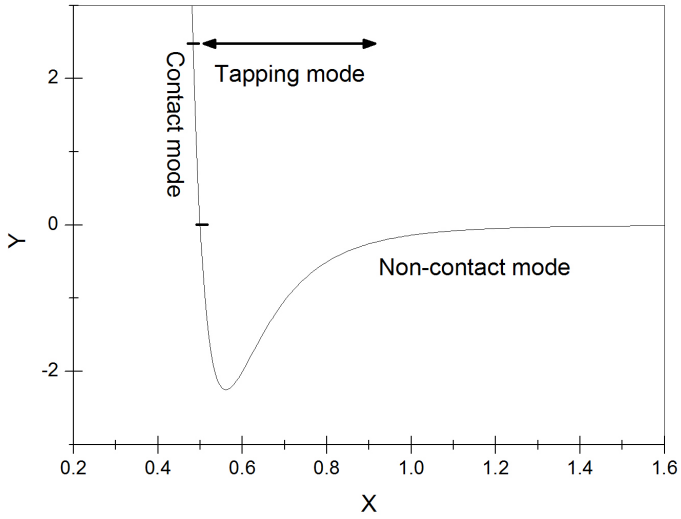

Figure 3.5: Approximate range of the imaging modes in AFM, imposed over a Lennard-Jones sample-tip potential

section we are going to focus only in the imaging mode used in this work: dynamic non-contact (amplitude modulated) mode.

3.2.1 Amplitude modulation atomic force microscopy (AM-AFM)

This imaging mode tries to attain the lateral resolution of the contact mode without approaching the tip as close to the surface, in order to avoid lateral forces and sample damage. Its basic principle is that the cantilever is set to a distance in which it does not interact with the sample (non-contact regime), but it is excited at a fixed frequency, which is usually at or slightly below its free resonance frequency, so the tip ends up interacting with the sample, but a lot less than in contact mode. The amplitude is then used as a feedback channel (hence the name), and the variations in amplitude and phase are registered, which end up conforming different images.

Several models have been developed to describe the tip-cantilever system and its interaction with the sample, both analytical [32–34] and numerical [35–37]. One of the most successful, developed by Ricardo García and others [38–40], will be explained with more detail in the next paragraphs, in order to illustrate the information that can be extracted from the different type of images obtained in a measurement. We start by approximating the tip-sample system as a point-mass spring system:

$$m\frac{\partial^2 z}{\partial t^2} + \frac{m\omega_0}{Q}\frac{\partial z}{\partial t} + kz = F_{ts} + F_0\cos(\omega t) \tag{3.14}$$

, where m and z are the mass and vertical position of the cantilever-tip system, and ω_0, Q and k are its angular resonance frequency, quality factor (a dimensionless parameters which

in essence characterizes a resonator's bandwidth relative to its centre frequency) and force constant. F_0 and ω are the amplitude and the frequency of the external force applied to the cantilever-tip system, and F_{ts} are the sample-tip interaction forces, which can be Van der Waals forces, adhesion forces, capillary forces and short-range repulsive forces. The steady state of the solution of the equation (3.14) can be safely approximated as a sinusoidal function:

$$z(z_c, t) = z_0(z_c) + A(z_c)\cos[\omega t - \phi(z_c)] \tag{3.15}$$

, where z_c is the equilibrium tip position when no external force is applied to the cantilever, and z_0, ω and ϕ are the mean amplitude, frequency and phase of the oscillation. Álvaro San Paulo and Ricardo García showed [38] that, applying the virial theorem at $\omega = \omega_0$, and assuming that the tip-sample power dissipation is negligible and the contact time is small (<0.2 T), the amplitude of the oscillation can be approximated as:

$$A \approx A_0 \left[1 - 4 \left(\frac{\left\langle F_{ts,c} \right\rangle}{F_0} \right)^2 \right]^{1/2} \tag{3.16}$$

, where A_0 and F_0 are the values of the free oscillation amplitude and external force, $F_{ts,c}$ are the conservative tip-sample forces, and the rest of the symbols have appeared before. This equation implies that the variations in the amplitude of the recorded signal are proportional only to the conservative tip-sample interactions, such as electrostatic forces, Pauli repulsion and Van Der Waals forces, which are also responsible for the topography image in contact mode, making both images essentially similar.

The phase changes in the recorded signal also carry important information. From the calculations for the equation (3.16), Javier Tamayo and Ricardo García have shown [41] that there is a relation between phase change and energy dissipation:

$$E_{dis} = E_{ext} - E_{med} = \frac{\pi k A A_0 \sin\phi}{Q} - \frac{\pi k A^2 \omega}{Q \omega_0}$$

, which was deduced considering that, in the steady state, the energy per cycle supplied by the external force (E_{ext}) must be converted either into hydrodynamic damping in the medium (E_{med}) and/or energy dissipated in the sample (E_{dis}). The above equation can be rewritten into a more practical form for $\omega = \omega_0$:

$$\sin\phi = \frac{A}{A_0}\left(1 + \frac{E_{dis}}{E_{med}}\right) \tag{3.17}$$

Equation (3.17) tells us something remarkable about phase changes: they only depend on inelastic processes, such as changes in the adhesion, viscoelasticity and such; and therefore are independent of the topography, giving us information about changes in the sample related to things as composition and adhesion changes, for example.

3.2.2 Experimental details

The AFM measurements were made in a Nanotec Cervantes Microscope with a Dulcinea electronic control unit at the Instituto de Ciencia de Materiales de Madrid, using Si tips from Nanosensors (PPP-NCHR and SSS-NCHR models, f∼300 kHz, k∼30 N/m) and Si tips coated with Au nanoparticles, made by Yves Huttel (patent P201030712). All the images were taken in tapping mode, and were processed with the WSxM software [42]. The feedback parameters used were the amplitude and the phase, using Nanotec's integrated Phase-Locking Loop (PLL) characteristics.

SECTION 3.3

Confocal Micro-RAMAN spectroscopy

The RAMAN spectroscopy is a spectroscopic technique based on the measurement of the inelastic photon scattering produced by the illumination of a sample with light. It was predicted theoretically by Adolf Smekal in 1923 [43], but it was first observed experimentally in 1928 by C. V. Raman and K. S Krishnan in solids [44] and G. Landsberg and L. I. Mandelstam in liquids [45]. It shares its effectiveness in distinguishing molecules and molecular groups that have very similar compositions (being particularly effective in distinguishing organic molecules) with FT-IR ot NIRS, but since the Raman effect manifests itself in the light scattered by the sample instead of the light that absorbs, it requires less sample preparation than the techniques mentioned, and it can be applied on liquids, gases, or samples in transparent containers, like glass or quartz.

A typical experimental setup for this technique usually implies the illumination of the sample with a monochromatic laser, in order to be able to resolve the narrow Raman peaks of our spectrum as best as possible; and the recording of the scattered signal with a spectrometer or a CCD camera. Since the Raman scattering is usually between three and six orders of magnitude weaker than elastic scattering, filters are usually used in order to cut all the signal coming from it before it enters the spectrometer. In order to improve both lateral and depth resolution, confocal setups can be equipped in the laser part of the experimental scheme. A microscope or an AFM probe are also sometimes available in these setups, in order to make detailed mappings of an area of the substrate with greatly improved resolutions in comparison with non-confocal setups (100 nm of lateral resolution). A basic scheme of a confocal Raman spectrometer can be seen in figure 3.6.

3.3.1 Theory and Raman spectra

The object of this section is not to offer a complete theoretical description of the Raman effect, but to give a brief summary of the theoretical foundations of this spectroscopy than can be useful to understand the results obtained in this work. More detailed information can be found elsewhere: [46] and [47] are two good reviews of the most important details of this spectroscopy, and have been extensively consulted for this work. Therefore, we are going to study the simplest system in which this effect can be studied, a diatomic molecule excited

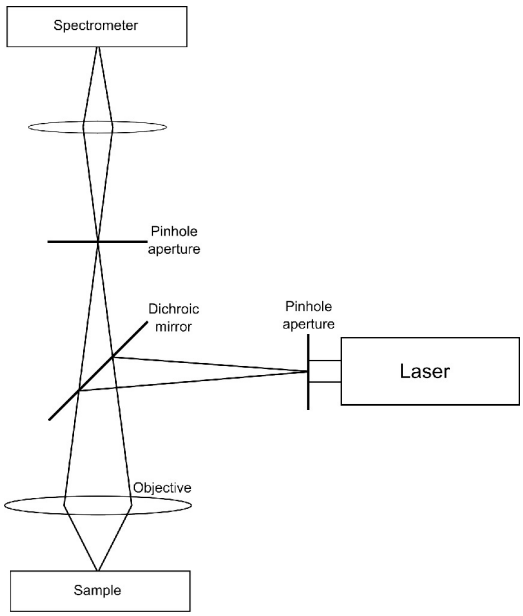

Figure 3.6: Diagram of a typical experimental setup for a confocal Raman spectrometer.

by an external electromagnetic wave, and only the classical effects of the interaction will be considered. The expression of the induced dipole moment in the molecule by the external electromagnetic sinusoidal wave is:

$$P = \alpha E_0 \cos(2\pi \nu_0 t) \tag{3.18}$$

, where α is the polarizability of the material, and ν_0 is the frequency of the incident electromagnetic wave. The molecular bond confine the atoms into discrete vibrational energy levels, with an energy:

$$E_{\text{vib}} = \left(j + \frac{1}{2}\right) h \nu_{\text{vib}}$$

, where $j = 0, 1, 2, ...$ is the vibrational quantum number, and ν_{vib} and h are the frequency of the vibrational mode and the Planck constant. In order to simplify the calculations, we can considerate this vibrations to be harmonic, and express the displacement of the atoms about their equilibrium position as:

$$dQ = Q_0 \cos(2\pi \nu_{\text{vib}} t) \tag{3.19}$$

Since the total displacement for a diatomic molecule is typically about 10% of the total molecular bond length, we can safely approximate the polarizability α by taking the first term of its Taylor expansion:

$$\alpha = \alpha_0 + \frac{\partial \alpha}{\partial Q} dQ \tag{3.20}$$

Substituting (3.19) into (3.20) gives:

$$\alpha = \alpha_0 + \frac{\partial \alpha}{\partial Q} Q_0 \cos(2\pi \nu_{\text{vib}} t) \tag{3.21}$$

, and substituting (3.21) into (3.18) gives:

$$P = \alpha_0 E_0 \cos(2\pi \nu_0 t) + \frac{\partial \alpha}{\partial Q} Q_0 \cos(2\pi \nu_{\text{vib}} t) E_0 \cos(2\pi \nu_0 t)$$

, which can be rewritten into the more convenient form:

$$P = \alpha_0 E_0 \cos(2\pi \nu_0 t) + \left[\frac{\partial \alpha}{\partial Q} \frac{Q_0 E_0}{2} \right] \{ \cos[2\pi (\nu_0 - \nu_{\text{vib}}) t] + \cos[2\pi (\nu_0 + \nu_{\text{vib}}) t] \} \tag{3.22}$$

The first term of equation (3.22) represents the elastic scattering of the incident wave, while the two other terms represents inelastic scattering, with the final vibrational frequency of the dipole being $\nu_0 - \nu_{\text{vib}}$ (Stokes scattering) or $\nu_0 + \nu_{\text{vib}}$ (Anti-Stokes scattering). These two terms depends on $\frac{\partial \alpha}{\partial Q}$, and represents the most important condition for the Raman scattering to appear: the vibrational displacement of atoms *must* produce a change in the polarizability.

In a typical Raman spectrum, the intensity of the measured peaks (usually called Raman bands) is plotted against the Raman shift (the difference between the wavenumbers of the measured excitation and the laser source). The Raman shift position of the bands measured depend mainly on the mass of the atoms and the bond strength of the molecule studied. The chemical environment affects the intensity of these bonds, and it also plays a significant factor in the Raman shift of the bands. Their intensity depends on the concentration and polarizability of the molecule studied, and the source parameters (both intensity and frequency). Of all these parameters, the most interesting for us is the polarizability, since its changes are related to the structure of the molecule studied (bond length, strength and type, atomic or molecular size, molecular orientation, and so on).

3.3.2 Experimental details

The Raman measurements were obtained using a confocal Raman microscopy coupled with and atomic force microscopy (AFM) instrument (Witec ALPHA 300RA) with laser excitation at 532 nm and a 100X objective lens (NA = 0.9). Power calibrations were performed in order to determine a safe laser power which would not change the oxidation state of the samples. The results (figure 3.7) yielded that the oxidation state of the CoO samples changed if the laser power was above 25 mW, so the laser power was set to 5 mW for all the measurements shown in this work. The optical diffraction resolution of the confocal microscope was limited to about 200 nm laterally and 500 nm vertically. Raman spectral resolution of the system was down to 0.02 cm^{-1}. The samples were mounted in a piezo-driven scan platform having 4 nm lateral and 0.5 nm vertical positioning accuracy. The piezoelectric scanning table allows three-dimensional displacements in steps of 3 nanometers (0.3 nm in vertical direction), giving a very high spatial resolution for both the AFM and confocal Raman microscopy. The microscope base was also equipped with an active vibration isolation system, active 0.7-1000 Hz. The system allows studying the same area of the sample by selecting the adequate objective of the microscope. Collected spectra were analysed by using Witec Control Plus software.

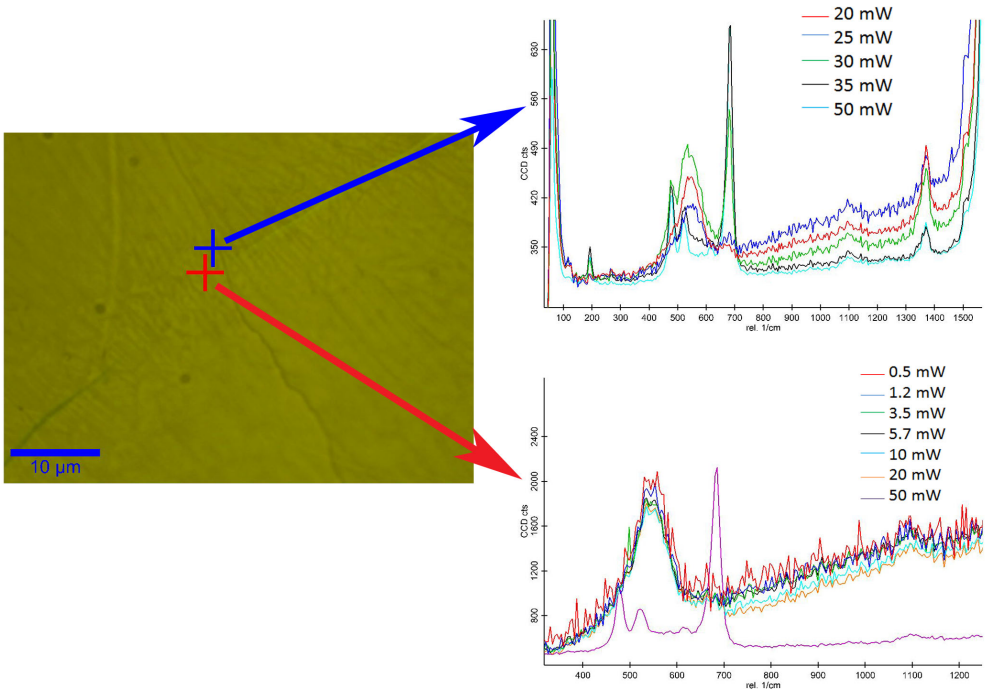

Figure 3.7: Raman measurements of a 40 ML sample of CoO on HOPG with different laser power values.

SECTION 3.4

X-ray Absorption Spectroscopy (XAS)

X-Ray Absorption Spectroscopy (XAS) is a spectroscopic technique in which a sample is illuminated with X-rays, as we do in XPS, but instead of measuring what is being emitted from the sample, we measure the absorption of the sample. It gives chemical and structural information in local ranges, and is therefore adequate for analyzing samples that do not have a long range order, like solutions or amorphous phases. It was used as our main structural technique for the CoO/oxides experiments because amorphous layers were expected, given the room temperature and other experimental conditions used in this work. Its theoretical origins can be traced back to the studies of the fine structure of the X-ray absorption lines made in the end of the nineteenth century by Karl Wilhelm Stenström [48], and its importance for materials science was first acknowledged by Walther Kossel in the 1920s [49]. However, its application as a characterization technique started to become relevant in the eighties, when synchrotron radiation facilities gave the researchers beams with enough brilliance and resolution for this technique to be useful, and the number of publications have risen every year since then.

A typical scheme of a XAS experiment can be seen in figure 3.8. The incident energy is varied around the value of an X-ray absorption line of some element that is present in our sample (which makes this technique element-selective), and the result of the excitations and desexcitations of the sample (photons, photoelectrons, and even ions) are measured. Even though the basic process is similar to the one that rules photoemission spectroscopy,

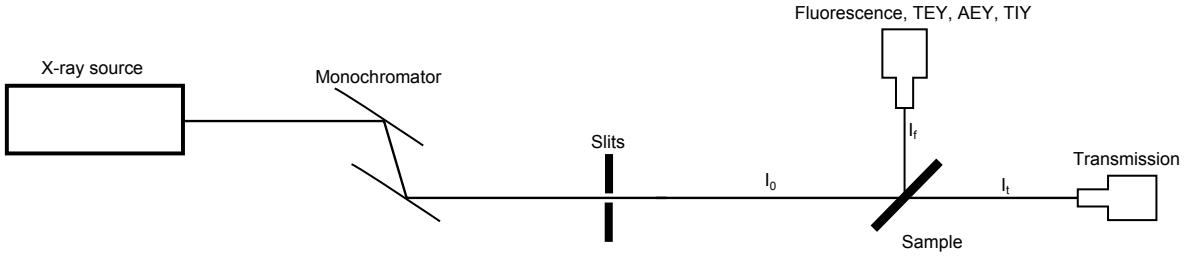

Figure 3.8: Basic scheme of a typical XAS experimental setup.

the information extracted from it is quite different: in photoemission spectroscopy, only the initially ejected photoelectron is measured, while in XAS, the fluorescent photon or Auger electron or an inelastically scattered photoelectron may also be measured. This means that the final state of the photoelectron may be a bound state, since the photoelectron itself need not be detected, Also, the interaction of the ejected photoelectrons is going to be modified by its local environment, usually creating interferences between the outgoing and scattered waves, and that will be reflected in our absorption spectrum, which is why this spectroscopy can also give structural information. Depending on what and how these desexcitations are measured, several modes can be distinguished. Their main characteristics are summarized in table 3.3:

Mode	**Measured quantity**	**Probing depth**
Transmission	Transmitted intensity	Full sample thickness
Fluorescence yield	Emitted photons	$>$ 0.1-10 μm [50]
Total electron yield	Emitted electrons	3-10 nm [51]
Partial electron yield	Emitted electrons (fixed energy)	$<$ 1 nm [52]
Total ion yield	Emitted ions	$<$ 1 nm [53]

Table 3.3: Different measurement modes in XAS spectroscopy and their main characteristics

A typical XAS spectra is displayed in figure 3.9, where the number of counts or the absorption coefficient of the sample is plotted versus the photon energy. A spectrum usually shows a more intense line, also called “edge” or “white line”, which represents the absorption threshold of the orbital that is being studied. Depending on the energy range around this edge, two main regions can be distinguished:

- X-ray absorption near-edge spectroscopy (XANES): the part of the spectra ∼50 eV below and above the edge. This region covers both the edge and the pre-edge features below it.
- Extended X-ray absorption fine structure (EXAFS): the part of the spectra above the XANES region.

The energy boundary between these two regions is approximate, since the transition between them is gradual, but they carry significantly different information: XANES carry chemical

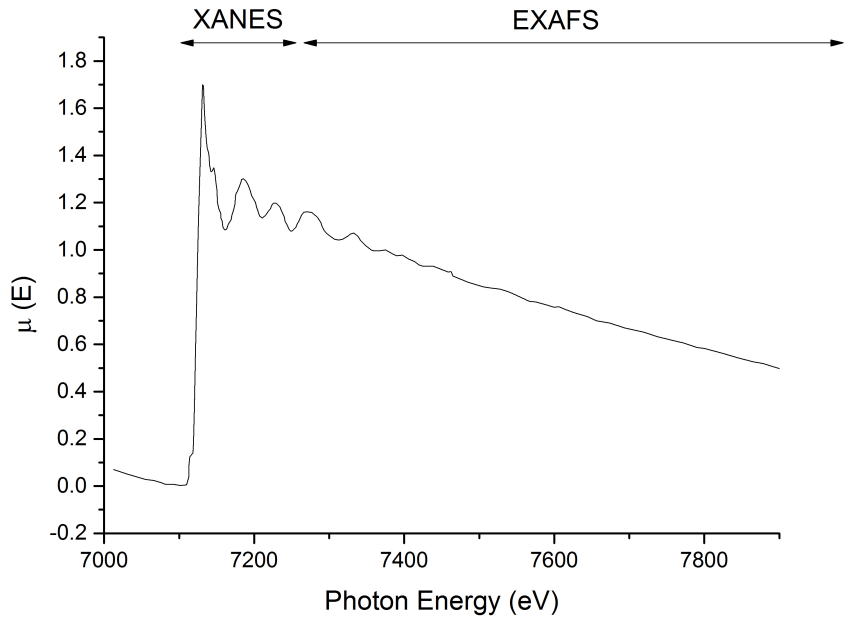

Figure 3.9: Fe K spectra coming from a Fe_3O_4 foil which shows the approximate energy range of XANES and EXAFS regions.

information, while EXAFS carry short-range structural information. We will talk about these regions and the information that can be extracted from them in the next two subsections.

3.4.1 Extended X-ray absorption fine structure (EXAFS)

The EXAFS region covers all the XAS part of the spectrum from, approximately, 50-150 eV above the main absorption line, and it is usually measured with hard X-rays, so all the possible oscillations created by the interferences between the outgoing and scattered waves can be measured. The lower energy limit of this regime means that the excited photoelectrons have a high kinetic energy, so its backscattering amplitude is going to be quite low, and their interaction with the surrounding atoms while is getting out from the sample is going to be dominated by single backscattering processes.

The main object of analysis in this region is the corrected absorption coefficient from an isolated atom, $\chi(E)$, which represents the fractional change in the absorption coefficient due to the neighbour atoms.

$$\chi(E) = \frac{\mu - \mu_0}{\Delta\mu_0} \tag{3.23}$$

Before we can begin to extract information from it, a correct normalization of the data must be made, something that usually implies the calibration of any possible shifts due to the beamline, and subtraction of a pre-edge (usually just a straight line) and a post-edge background (approximated with a cubic spline polynomial fitting). Once the data has been

properly normalized, a Fourier transform is applied to work in the wavelengths space. An equation for the behaviour of the absorption coefficient in this space can be calculated using some approximations:

1. A Gaussian atomic distribution around the absorber atom at R_i distances is assumed.
2. The scattered and outgoing waves are approximated by plane waves
3. Only single-electron processes are considered
4. The potential of the surrounding atoms is approximated as spheres with a zero region between them (muffin-tin approximation)

Within these approximations (detailed information about its calculation can be found, for example, in [54]), equation (3.24), called the "EXAFS equation", can be obtained for every scattering process that can happen in our analysed structure (usually called "scattering paths"). The data obtained experimentally can be fitted against this equation in order to extract the information that we are looking for:

$$\begin{gathered}\chi_i(k) = \frac{N_i S_0^2}{kR_i^2}\sin(2kR_i + \phi(k))\exp(-2\sigma_i k^2)\exp\left(\frac{2R_i}{\lambda(k)}\right) \\ R_i = R_0 + \Delta R \\ k^2 = \frac{2m(E-E_0)}{\hbar}\end{gathered} \tag{3.24}$$

The meaning of the parameters of equation (3.24) are:

- $F_i(k)$: Effective scattering amplitude.
- $\phi(k)$: Phase shift
- $\delta(k)$: Mean free path
- R_0: Initial path length
- N_i: Degeneracy of the path.
- S_0: Passive electron reduction factor
- σ_i^2: Mean-squared displacement (also called Debye-Waller factor)
- E_0: Energy shift
- ΔR: change in half-path length

The first four parameters can be calculated theoretically: specialized software like FEFF or IFFEFIT [55, 56] can be used to calculate the scattering paths from the structure of the material. The rest of these parameters have to be obtained from the fittings: once the scattering paths have been obtained from the original structure, variations on these parameters are made until the experimental data is properly fitted.

3.4.2 X-ray absorption near-edge spectroscopy (XANES)

As it was stated before, the XANES region of a XAS spectra covers between 50 and 150 eV above the white line. Since the kinetic energy of the electrons ejected from the atom is low (5-150 eV), the photoelectron backscattering amplitude by neighbour atoms is very large, and multiple scattering events become dominant, as opposed to EXAFS, where the high kinetic energy of the ejected electrons causes single scattering events to be more dominant. These regime has, therefore, a more defined contribution by chemical effects than EXAFS.

As in the case of Raman spectroscopy, only the most basic theoretical elements of this spectroscopy will be touched, and more information can be found elsewhere [57]. The absorption of the sample is given by the photoionization cross section (σ), which, for an incident electromagnetic field with a vector potential $A(\vec{r},t)$, polarization direction $\hat{\epsilon}$ and frequency ω ($A(\vec{r})$ can be safely considered as a classical wave of polarization, so $\hat{\epsilon} \perp \vec{k}$, and $A(\vec{r},t) \cong \hat{\epsilon} A_0 e^{i\vec{k}\cdot\vec{r}}$). σ is given by Fermi's golden rule:

$$\sigma \propto \sum_f |\langle f | A(\vec{r},t) \cdot \vec{p} \, | i \rangle|^2 \delta\left(E - E_f\right) \propto \sum_f |\langle f | \, \hat{\epsilon} \cdot \vec{p} e^{i\vec{k}\cdot\vec{r}} \, | i \rangle|^2 \delta\left(E - E_f\right) \tag{3.25}$$

, where $|i\rangle$, $|F\rangle$, E_i, and E_f denote the initial and final states and their energies, $\vec{k}$ stands for the wave vector of the incident beam, and $\vec{p}$ stands for the sum of the linear momenta of the electrons in the atom. The Taylor expansion of $\hat{\epsilon} \cdot \vec{p} e^{i\vec{k}\cdot\vec{r}}$ is:

$$\hat{\epsilon} \cdot \vec{p} e^{i\vec{k}\cdot\vec{r}} \simeq \hat{\epsilon} \cdot \vec{p}\left(1 + i\vec{k} \cdot \vec{r}\right) + \ldots \tag{3.26}$$

If we take only the first term of this expansion, the result is said to take the dipole approximation, and the resulting transition probabilities can only have an orbital momentum change of $\Delta l = \pm 1$ between their initial and final states. Calculations that also take the second term into account are said to take the quadrupolar approximation ($\Delta l = \pm 2$), and while their transition probability is much lower than the dipolar ones (between two and three orders of magnitude), they can be seen in pre-white line features, usually due to structural distortions, orbital hybridization, and so on. All of these transitions end up implicating non-occupied states, which is why XAS is called a "non occupied states spectroscopy".

3.4.3 Experimental details

The EXAFS and XANES measurements of the Co 1s region were carried out at the BM25-SpLine beamline at the ESRF synchrotron (Grenoble, France):, while the XANES measurements of the Co 2p, O 1s and C 1s regions were performed at the PM4 Beamline of the BESSY synchrotron (Berlin, Germany). The technical details of both beamlines have been outlined at section 2.2.2.

For the data treatment and fitting of the EXAFS Co 1s measurements, the software suite Demeter [58] was used. The normalization of the data was performed with the software Athena, and the fittings were carried out with the software Artemis, both inside the Demeter suite. For the fittings, a full CoO structure was calculated from a basic .cif file with the ATOMS software, and FEFF6 was used to calculate the theoretical scattering paths for said structure

Shell	Complete path	Degeneracy	R_{eff} (Å)	Rank (%)
First	$[Co]_{abs}$-$[O]^1$	6	2.133	100
Second	$[Co]_{abs}$-$[Co]^2$	12	3.013	83

Table 3.4: Paths used in the EXAFS calculations, as computed by FEFF for a CoO cluster. $[Co]_{abs}$ refers to the absorber atom that emits the photoelectron, and the exponent of the second atom refers to the neighbour number (of the two inter-penetrated fcc lattices)

(both programs are included in the Artemis suite). From all the scattering paths obtained, the ones displayed in table 3.4 were chosen: the main criteria used for this choice was that they were the only scattering paths with an effective radius below the one analysed in our spectra.

The measurements at the SuriCat beamline were carried in Total Electron Yield (TEY) mode, measuring the sample drain current with a Keithley 6485 picoammeter, and recorded in ASCII mode with a custom-made BESSY software called EMP/2; while the measurements at SpLine (ESRF, Grenoble) were made in fluorescence mode with a multi-element solid state detector. All these measurements were performed in ultra-high vacuum conditions, and the configuration slits and approximate resolution values of the regions measured are given in table 3.5:

Region	Slits (μm)	Resolution (meV)
Co 2p	50	120
O 1s	50	60
C 1s	50	30

Table 3.5: Slits configurations and approximate resolution values for the XANES measurements made in the PM4 beamline. Resolution change in the energy interval measured: ∼5%.

SECTION 3.5

Rutherford Backscattering Spectrometry (RBS)

Rutherford Backscattering Spectrometry (RBS) is an spectroscopic technique that measures the retrodispersed ions (usually He^{2+} or protons) that are accelerated towards a sample: the resulting counts-energy spectrum gives both compositional information and depth distribution of said components (depth resolution: $\sim 50\,Å$, maximum sampling depth: $\sim 2\,\mu m$ [59]). It is considered a non-destructive technique, although the high energy of the ions (2-3 MeV) can induce damages and modifications to some samples. Its history can be traced back to the historical Geiger-Marsden series of experiments of 1909-1914, supervised and interpreted by Ernest Rutherford, and which led to the famous atomic model named after him [60]. It was not considered a materials analysis technique until the 1957 experiments by Sylvan Rubin, Thomas O. Passell and L. Evan Bailey [61]. Although its depth resolution is out of the thickness ranges explored in this work, RBS has been used in the CoO/HOPG reoxidation experiments

as a way to try to measure diffusion effects in those samples due to the thermal treatment.

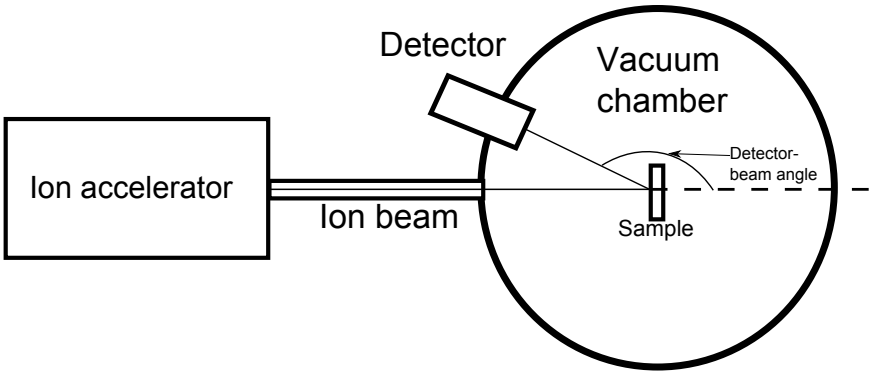

Figure 3.10: Basic experimental scheme for an RBS measurement

A typical setup for an RBS experiment can be seen at figure 3.10. The detector-beam angle (also called scattering angle) is an important parameter The measurements must be made in high or ultra-high vacuum conditions because of the short mean free path of the accelerated ions at room conditions.

3.5.1 Theoretical background

For a basic theoretical foundation of this technique, we are going to start by assuming the following approximations:

- The projectile energy is much larger than the binding energy of the target atoms.
- Nuclear reactions are considered to be non-existent.
- The physics of the collisions can be described by pure Coulomb repulsion.

The collision between the ion and an atom of the sample can be considered as a classical elastic (hard-sphere) collision, with the energy of the retrodispersed ion (E_1) with respect to its original energy (E_0) equal to:

$$E_1 = kE_0$$
$$k = \left(\frac{M_1 \cos\theta \pm \sqrt{M_2^2 - M_1^2 (\sin\theta)^2}}{M_1 + M_2} \right)^2$$

, where k (called the kinematic factor) depends on the original particle (subindex 1), the target nucleus (subindex 2) and the scattering angle with respect to the laboratory frame (θ). The probability of observing a retrodispersing event is going to be given by the retrodispersion differential cross section, which can be expressed, in the center-of-mass reference, by the Rutherford's formula:

$$\left(\frac{d\sigma}{d\Omega}\right)_c = \left[\frac{Z_1 Z_2 e^2}{4E_c \sin^2(\theta_c/2)}\right]^2$$

When $M_1 \ll M_2$, this expression is also valid for the laboratory frame of reference, but when this condition is not met, the complete expression is as follows:

$$\frac{d\sigma}{d\Omega} = \left(\frac{Z_1 Z_2 e^2}{4E}\right)^2 \frac{4}{\sin^4\theta} \frac{\left\{\sqrt{[1-(M_1/M_2)^2 \sin\theta]^2} + \cos\theta\right\}^2}{\sqrt{[1-(M_1/M_2)^2 \sin\theta]^2}}$$

Aside from the $\frac{Z_1 Z_2 e^2}{4E}$ prefactor, the main dependencies of both the kinematic factor and the differential cross section are the masses of both the accelerated ions, the target nucleus, and the scattering cross section, which enables us to obtain compositional information. The information about the depth distribution of our elements comes from another two important definitions: the energy loss and the stopping cross section.

The energy loss concept comes from the fact that every energetic particle that impacts on the sample will penetrate a certain depth into it. If a layer of uniform and known composition is defined, and the change in energy and depth are defined as ΔE and Δx, respectively, the energy loss per unit length can be defined as:

$$\lim_{\Delta x \to 0} \frac{\Delta E}{\Delta x} dx(E)$$

The energy at some point of that layer with depth x will therefore be:

$$E(x) = E_0 - \int_0^x \frac{dE}{dx} dx$$

There is a problem for the evaluation of this integral: the energy loss is defined as a function of E, not of x. This can be resolved if we define this integral as it follows:

$$dx = \frac{dx}{dE}(E) \cdot dE \rightarrow x = \int_{E_0}^{E} \left(\frac{dE}{dx}\right)^{-1} dE \tag{3.27}$$

This integral is not exactly valid for a real experiment, since it only involves individual particles and target nucleus. In this case, a stopping cross section is defined as follows:

$$\epsilon = \left(\frac{1}{N}\right)\left(\frac{dE}{dx}\right) \tag{3.28}$$

This equation, coupled with 3.27, is what it gives us the possibility to extract depth distribution of our components across all the sampling depth range of RBS. All the codes and algorithms used in these calculations uses approximations or previously obtained values for ϵ and $\frac{dE}{dx}$, but a more extensive explanation of this or other features of RBS are beyond the scope and use given to this technique in this work, and can be found elsewhere (two excellent manuals consulted for this section are [59] and [62])

3.5.2 Experimental details

The RBS measurements were made at the Centro de Microanálisis de Materiales (CMAM), which belongs to the Universidad Autónoma de Madrid. It has a 5 MV terminal voltage tandem accelerator, designed and manufactured by High Volteng Europe Engineering, and produces highly collimated beams of a 1 mm^2 size. More technical details about the characteristics of this accelerator can be found elsewhere [63, 64]. The measurements were made with He^{++} ions at a 165° scattering angle (IBM configuration), and two beam energies were used: 1800 keV (for the large coverage samples) and 3045 keV (for the low coverage samples, in order to maximize the O signal). The condition of the detector was not optimal, and therefore some resolution was lost, which further increased the difficulty in the simulation and interpretation of the low coverage samples results. For its analysis and the spectra simulations, the software SIMNRA 6.06 [65] was used. The analysis of the 3045 keV spectra used non-Rutherford cross sections for the fittings of the O peaks (Feng et al, 1994, private communication).

SECTION 3.6

Surface X-ray diffraction

3.6.1 Introduction

X-Ray Diffraction (XRD) is a structural characterization technique based on the (usually) angular measurement of the X-rays diffracted from a sample. The intensity and angular distribution of the reflected X-rays are related to the crystal structure of their components via the well-known structure factor of the crystal lattice and the Laue equations, and they give information about the crystallographic structure of the sample (given that is ordered enough for this technique to be useful), possible different phases inside the sample, crystallite sizes, and even strains and lattice parameter values. When the crystal has a well-defined three-dimensional symmetry, the shape of the diffracted peaks are usually points distributed across the reciprocal space (the Fourier distribution of the spatial lattice of the crystal), but when one of the Laue equations is removed (as in the case of a crystal surface), the diffraction pattern becomes a 2D lattice of rods, sharp in both directions parallel to the plane where the Laue equations that remains are still valid, and diffuse (or continuous) in the out-of-plane direction (more information about the details of this technique can be found, for example, in [66]). These rods can be explored maintaining a very low X-ray beam-sample angle (so the penetration length is as small as possible), and performing scans along the free Miller index of that specific rod.

3.6.2 Experimental details

The measurements were made at the optical branch B of the BM25 beamline of the ESRF (Grenoble, France), which main optical characteristics have been outlined at table 2.7 (page 49). The energy was set at 14.7 keV (λ=0.85 Å), and for the measurements, a six-circle diffractometer in vertical geometry was used, which, in addition to the standard circles for orienting

the sample and the detector, had additional motions to align the surface normal along predefined directions (vertical or horizontal), which is needed in this experiments. The energy resolution of these measurements is $\Delta E/E = 1.5 \cdot 10^{-4}$.

SECTION 3.7

Bibliography

[1] P. D. INNES. "On the Velocity of the Cathode Particles Emitted by Various Metals under the Influence of Rontgen Rays, and Its Bearing on the Theory of Atomic Disintegration". *Proceedings of the Royal Society of London. Series A* 79.532 (1907), pp. 442–462. DOI: 10.1098/rspa.1907.0056.

[2] K. SIEGBAHN and K. EDVARSON. "X-Ray spectroscopy in the precision range of 1 : 105". *Nuclear Physics* 1.8 (1956), pp. 137–159. DOI: 10.1016/S0029-5582(56)80022-9.

[3] M. SALMERON and R. SCHLÖGL. "Ambient pressure photoelectron spectroscopy: A new tool for surface science and nanotechnology". *Surface Science Reports* 63.4 (2008), pp. 169–199. DOI: 10.1016/j.surfrep.2008.01.001.

[4] A. JÜRGENSEN, N. ESSER, and R. HERGENRÖDER. "Near ambient pressure XPS with a conventional X-ray source". *Surface and Interface Analysis* 44.8 (2012), pp. 1100–1103. DOI: 10.1002/sia.4826.

[5] F. F. TAO. "Design of an in-house ambient pressure AP-XPS using a bench-top X-ray source and the surface chemistry of ceria under reaction conditions". *Chemical Communications* 48 (32 2012), pp. 3812–3814. DOI: 10.1039/C2CC17715C.

[6] J. SCHNADT, JA. KNUDSEN, J. N. ANDERSEN, H. SIEGBAHN, A. PIETZSCH, F. HENNIES, N. JOHANSSON, N. MÅRTENSSON, G. ÖHRWALL, S. BAHR, S. MÄHL, and O. SCHAFF. "The new ambient-pressure X-ray photoelectron spectroscopy instrument at MAX-lab". *Journal of Synchrotron Radiation* 19.5 (Sept. 2012), pp. 701–704. DOI: 10.1107/S0909049512032700.

[7] T. KOOPMANS. "Über die Zuordnung von Wellenfunktionen und Eigenwerten zu den Einzelnen Elektronen Eines Atoms". *Physica* 1 (1-6 1934), pp. 104–113. DOI: 10.1016/S0031-8914(34)90011-2.

[8] S. EVANS. "Curve synthesis and optimization procedures for X-ray photoelectron spectroscopy". *Surface and Interface Analysis* 17.2 (1991), pp. 85–93. DOI: 10.1002/sia.740170204.

[9] S. DONIACH and M. SUNJIC. "Many-electron singularity in X-ray photoemission and X-ray line spectra from metals". *Journal of Physics C: Solid State Physics* 3.2 (1970), p. 285. DOI: 10.1088/0022-3719/3/2/010.

[10] D. A. SHIRLEY. "High-Resolution X-Ray Photoemission Spectrum of the Valence Bands of Gold". *Physical Review B* 5 (12 June 1972), pp. 4709–4714. DOI: 10.1103/PhysRevB.5.4709.

[11] S. TOUGAARD and B. JØRGENSEN. "Inelastic background intensities in XPS spectra". *Surface Science* 143.2-3 (1984), pp. 482–494. DOI: 10.1016/0039-6028(84)90554-5.

[12] J. VÁGH. "The Shirley background revised". *Journal of Electron Spectroscopy and Related Phenomena* 151.3 (2006), pp. 159–164. DOI: 10.1016/j.elspec.2005.12.002.

[13] S. TOUGAARD. "Quantitative analysis of the inelastic background in surface electron spectroscopy". *Surface and Interface Analysis* 11.9 (1988), pp. 453–472. DOI: 10.1002/sia.740110902.

[14] S. TOUGAARD. "Formalism for quantitative surface analysis by electron spectroscopy". *Journal of Vacuum Science & Technology A: Vacuum, Surfaces, and Films* 8.3 (1990), pp. 2197–2203. DOI: 10.1116/1.577037.

[15] S. TOUGAARD and H. S. HANSEN. "Non-destructive depth profiling through quantitative analysis of surface electron spectra". *Surface and Interface Analysis* 14.11 (1989), pp. 730–738. DOI: 10.1002/sia.740141109.

[16] S. TOUGAARD. "Inelastic background correction and quantitative surface analysis". *Journal of Electron Spectroscopy and Related Phenomena* 52 (1990), pp. 243–271. DOI: 10.1016/0368-2048(90)85022-2.

[17] S. TANUMA, C. J. POWELL, and D. R. PENN. "Calculations of electron inelastic mean free paths. V. Data for 14 organic compounds over the 50-2000 eV range". *Surface and Interface Analysis* 21.3 (1994), pp. 165–176. DOI: 10.1002/sia.740210302.

[18] S. TOUGAARD. "Universality Classes of Inelastic Electron Scattering Cross-sections". *Surface and Interface Analysis* 25.3 (1997), pp. 137–154. DOI: 10.1002/(SICI)1096-9918(199703)25:3<137::AID-SIA230>3.0.CO;2-L.

[19] S. TOUGAARD. "Low energy inelastic electron scattering properties of noble and transition metals". *Solid State Communications* 61.9 (1987), pp. 547–549. DOI: 10.1016/0038-1098(87)90166-9.

[20] D. BRIGGS and M. P SEAH. *Practical Surface Analysis: Auger and X-ray photoelectron spectroscopy*. Vol. 1. John Wiley and sons, 1996. ISBN: 9780471262794.

[21] S. TOUGAARD and P. SIGMUND. "Influence of elastic and inelastic scattering on energy spectra of electrons emitted from solids". *Physical Review B* 25 (7 Apr. 1982), pp. 4452–4466. DOI: 10.1103/PhysRevB.25.4452.

[22] R. KWOK. *XPSPeak 4.1*. 2000. URL: http://www.uksaf.org/xpspeak41.zip.

[23] ORIGINLAB CORPORATION. *Origin 8.5*. 2010. URL: http://www.originlab.com.

[24] S. TOUGAARD and F. YUBERO. *QUASES-Analyze, version 4.4*. 2001. URL: http://www.quases.com/home/.

[25] S. TOUGAARD. *QUASES-IMFP-TPP2M, version 2.1*. 2000. URL: http://www.quases.com/products/quases-imfp-tpp2m/.

[26] M.J. WEBB, P. PALMGREN, P. PAL, O. KARIS, and H. GRENNBERG. "A simple method to produce almost perfect graphene on highly oriented pyrolytic graphite". *Carbon* 49.10 (2011), pp. 3242–3249. DOI: 10.1016/j.carbon.2011.03.050.

[27] J. F. MOULDER, W. F. STICKLE, P. E. SOBOL, and K. D. BOMBEN. *Handbook of X-ray Photoelectron Spectroscopy*. Ed. by JILL CHASTAIN. Perkin-Elmer Corporation, 1992. ISBN: 0855012080.

[28] R. HOOGEWIJS, L. FIERMANS, and J. VENNIK. "Electronic relaxation processes in the KLL' auger spectra of the free magnesium atom, solid magnesium and MgO". *Journal of Electron Spectroscopy and Related Phenomena* 11.2 (1977), pp. 171–183. DOI: 10.1016/0368-2048(77)85108-6.

[29] E. PAPARAZZO. "XPS analysis of oxides". *Surface and Interface Analysis* 12.2 (1988), pp. 115–118. DOI: 10.1002/sia.740120210.

[30] G. BINNIG, C. F. QUATE, and CH. GERBER. "Atomic Force Microscope". *Physical Revew Letters* 56 (9 Mar. 1986), pp. 930–933. DOI: 10.1103/PhysRevLett.56.930.

[31] G. BINNIG, H. ROHRER, CH. GERBER, and E. WEIBEL. "Surface Studies by Scanning Tunneling Microscopy". *Physical Review Letters* 49 (1 July 1982), pp. 57–61. DOI: 10.1103/PhysRevLett.49.57.

[32] L. NONY, R. BOISGARD, and J. P. AIME. "Nonlinear dynamical properties of an oscillating tip–cantilever system in the tapping mode". *The Journal of Chemical Physics* 111.4 (1999), pp. 1615–1627. DOI: 10.1063/1.479422.

[33] K. SCHRÖTER, A. PETZOLD, T. HENZE, and T. THURN-ALBRECHT. "Quantitative Analysis of Scanning Force Microscopy Data Using Harmonic Models". *Macromolecules* 42.4 (2009), pp. 1114–1124. DOI: 10.1021/ma8024464.

[34] L. WANG. "Analytical descriptions of the tapping-mode atomic force microscopy response". *Applied Physics Letters* 73.25 (1998), pp. 3781–3783. DOI: 10.1063/1.122893.

[35] J. LEGLEITER. "The effect of drive frequency and set point amplitude on tapping forces in atomic force microscopy: simulation and experiment". *Nanotechnology* 20.24 (2009), p. 245703. DOI: 10.1088/0957-4484/20/24/245703.

[36] R. GARCÍA and A. SAN PAULO. "Dynamics of a vibrating tip near or in intermittent contact with a surface". *Physical Review B* 61 (20 May 2000), R13381–R13384. DOI: 10.1103/PhysRevB.61.R13381.

[37] Y. ZHANG and Y. ZHAO. "Nonlinear dynamics of atomic force microscopy with intermittent contact". *Chaos, Solitons & Fractals* 34.4 (2007), pp. 1021–1024. DOI: 10.1016/j.chaos.2006.03.125.

[38] A. SAN PAULO and R. GARCÍA. "Tip-surface forces, amplitude, and energy dissipation in amplitude-modulation (tapping mode) force microscopy". *Physical Review B* 64 (19 Oct. 2001), p. 193411. DOI: 10.1103/PhysRevB.64.193411.

[39] J. R. LOZANO and R. GARCÍA. "Theory of Multifrequency Atomic Force Microscopy". *Physical Review Letters* 100 (7 Feb. 2008), p. 076102. DOI: 10.1103/PhysRevLett.100.076102.

[40] J. R. LOZANO and R. GARCIA. "Theory of phase spectroscopy in bimodal atomic force microscopy". *Physical Review B* 79 (1 Jan. 2009), p. 014110. DOI: 10.1103/PhysRevB.79.014110.

[41] J. TAMAYO and R. GARCIA. "Relationship between phase shift and energy dissipation in tapping-mode scanning force microscopy". *Applied Physics Letters* 73.20 (1998), pp. 2926–2928. DOI: 10.1063/1.122632.

[42] I. HORCAS, R. FERNANDEZ, J. M. GOMEZ-RODRIGUEZ, J. COLCHERO, J. GOMEZ-HERRERO, and A. M. BARO. "WSXM: A software for scanning probe microscopy and a tool for nanotechnology". *Review of Scientific Instruments* 78.1, 013705 (2007), p. 013705. DOI: 10.1063/1.2432410.

[43] A. SMEKAL. "Zur Quantentheorie der Dispersion". German. *Naturwissenschaften* 11.43 (1923), pp. 873–875. DOI: 10.1007/BF01576902.

[44] C. V. RAMAN. "A new radiation". *Indian Journal of Physics* (1928). Ed. by INDIAN ASSOCIATION FOR THE CULTIVATION OF SCIENCE, pp. 387–398.

[45] G. LANDSBERG and L. MANDELSTAM. "Eine neue Erscheinung bei der Lichtzerstreuung in Krystallen". German. *Naturwissenschaften* 16.28 (1928), pp. 557–558. DOI: 10.1007/BF01506807.

[46] P. VANDENABEELE. *Practical Raman Spectroscopy: An Introduction*. Analytical techniques in the sciences. Wiley, 2013. ISBN: 9781119961901.

[47] A. JORIO, M. S. DRESSELHAUS, R. SAITO, and G. DRESSELHAUS. *Raman Spectroscopy in Graphene Related Systems*. Wiley, 2011. ISBN: 9783527643905.

[48] W. STENSTRÖM. "Experimentelle Untersuchungen der Röntgenspektra. M-Reihe". *Annalen der Physik* 362.21 (1918), pp. 347–375. DOI: 10.1002/andp.19183622103.

[49] W. KOSSEL. "Zum Bau der Röntgenspektren". German. *Zeitschrift für Physik* 1 (1 1920), pp. 119–134. DOI: 10.1007/BF01881031.

[50] A. J. ACHKAR, T. Z. REGIER, H. WADATI, Y.-J. KIM, H. ZHANG, and D. G. HAWTHORN. "Bulk sensitive x-ray absorption spectroscopy free of self-absorption effects". *Phyical Review B* 83 (8 Feb. 2011), p. 081106. DOI: 10.1103/PhysRevB.83.081106.

[51] M. ABBATE, J. B. GOEDKOOP, F. M. F. DE GROOT, M. GRIONI, J. C. FUGGLE, S. HOFMANN, H. PETERSEN, and M. SACCHI. "Probing depth of soft x-ray absorption spectroscopy measured in total-electron-yield mode". *Surface and Interface Analysis* 18.1 (1992), pp. 65–69. DOI: 10.1002/sia.740180111.

[52] D. C. QI, W. CHEN, and A. T. S. WEE. "NEXAFS Studies of Molecular Orientations at Molecule-Substrate Interfaces". *The Molecule-Metal Interface*. Wiley-VCH Verlag GmbH & Co. KGaA, 2013, pp. 119–151. ISBN: 9783527653171. DOI: 10.1002/9783527653171.ch5.

[53] C. D. CAPPA, J. D. SMITH, K. R. WILSON, and R. J. SAYKALLY. "Revisiting the total ion yield x-ray absorption spectra of liquid water microjets". *Journal of Physics: Condensed Matter* 20.20 (2008), p. 205105. DOI: 10.1088/0953-8984/20/20/205105.

[54] B. K. TEO. *EXAFS: basic principles and data analysis*. Inorganic chemistry concepts. Springer-Verlag, 1986. ISBN: 9783540158332.

[55] UNIVERSITY OF WASHINGTON. *The FEFF project*. URL: http://feffproject.org/.

[56] B. RAVEL. *IFEFFIT*. URL: http://cars9.uchicago.edu/ifeffit/.

[57] J. STÖHR. *NEXAFS Spectroscopy*. Springer Series in Surface Sciences. Springer, 1992. ISBN: 9783540544227.

[58] B. RAVEL. *Demeter 0.9.20*. URL: http://bruceravel.github.io/demeter/.

[59] W. K. CHU, J. W. MAYER, and M. A. NICOLET. *Backscattering spectrometry*. Academic Press, 1978. ISBN: 9780121738501.

[60] E. RUTHERFORD. "LXXIX. The scattering of α and β particles by matter and the structure of the atom". *Philosophical Magazine Series 6* 21.125 (1911), pp. 669–688. DOI: 10.1080/14786440508637080.

[61] S. RUBIN, T. O. PASSELL, and L. E. BAILEY. "Chemical Analysis of Surfaces by Nuclear Methods". *Analytical Chemistry* 29.5 (1957), pp. 736–743. DOI: 10.1021/ac60125a001.

[62] M. MAYER. *SimNRA's User Guide*. Report IPP 9/113. Max-Planck-Institut für Plasmaphysik, Garching, Germany, 1997.

[63] A. GOTTDANG, D. J. W. MOUS, and R. G. HAITSMA. "The novel HVEE 5 MV Tandetron™". *Nuclear Instruments and Methods in Physics Research Section B: Beam Interactions with Materials and Atoms* 190.1-4 (2002), pp. 177–182. DOI: 10.1016/S0168-583X(02)00458-5.

[64] D. J. W. MOUS, A. GOTTDANG, R. G. HAITSMA, G. GARCIA LOPEZ, A. CLIMENT-FONT, F. AGULLÓ-LÓPEZ, and D. O. BOERMA. "Performance and Applications of the first HVE 5MV Tandetron™ at the University of Madrid". *AIP Conference Proceedings* 680.1 (2003), pp. 999–1002. DOI: 10.1063/1.1619877.

[65] M. MAYER. *SIMNRA 6.06*. 2011. URL: http://home.rzg.mpg.de/~mam/.

[66] I. K. ROBINSON and D. J. TWEET. "Surface X-ray diffraction". *Reports on Progress in Physics* 55.5 (1992), p. 599. DOI: 10.1088/0034-4885/55/5/002.

Chapter 4

Interaction of Cobalt oxides with other oxide substrates

SECTION 4.1

Introduction

This chapter will be dedicated to the results obtained in the study of the growth and interaction of CoO_x on the oxide substrates. The results about the study of the growth are presented in section 4.2: the chemistry of the growth is studied by means of XPS and XANES in section 4.2.1, and then the more quantitative aspects of the growth, such as coverage determination and its morphology, are discussed in subsection 4.2.2. The analysis of the CoO/oxide interface will be presented in 4.3, where theoretical cluster calculations of the XPS Co $2p_{3/2}$ spectra will allow us to study the size and support effects produced in the growth of these samples. Finally, the results of the study of the stability of the layers, both under room conditions and after a thermal oxidation process, will be presented in section 4.4.

These results have been extracted from multiple experiments, performed during the last five years. All the XPS spectra come from three in-situ growths of CoO on the three oxide substrates: in this experiments, CoO was grown for incrementally larger times, and measured in-situ after each stage by XPS, without taking the sample out of the vacuum chamber. Data from other techniques were measured ex-situ: samples with chosen coverages were grown in our preparation chamber, and then measured with the corresponding technique as soon as they were taken out of it. All of these experiments, aside from being very time consuming (each complete growth experiment took more than a month to be completed, and the correct growth of a single sample could take a full day or more), are not easy to perform and analyse, and a lot of experimental problems had to be resolved. For example, the sputtering used in the vacuum cleaning of the substrates before starting the growth experiments introduces a lot of defects, and will surely imply a severe modification of the crystallinity of their surfaces. The energy calibration of the XPS spectra is also not trivial, since both the substrate and the deposited layers are electrical insulators, and when the substrate peaks were no longer visible, other peaks, such as the oxygen peaks of the cobalt oxide layers, had to be used. Also, the AFM measurements suffered a lot of resolution changes, because they were performed at room conditions, and therefore the sample absorbs a lot of contamination. This contamination sometimes ends up sticking on the tip, leading to changes in the resolution. Nevertheless, repetition of the samples and measurements, aside from a careful control of all the experimental parameters, ended up leading to reproducible results, which are presented in this chapter.

SECTION 4.2

Study of the growth of Co oxides on oxide substrates

4.2.1 Chemical analysis of the growth

4.2.1.1 Survey XPS spectra

For the analysis of the chemistry involved during the growths, we first present in figure 4.1 the XPS survey spectra of the growth of CoO on the three oxide experiments. The energies

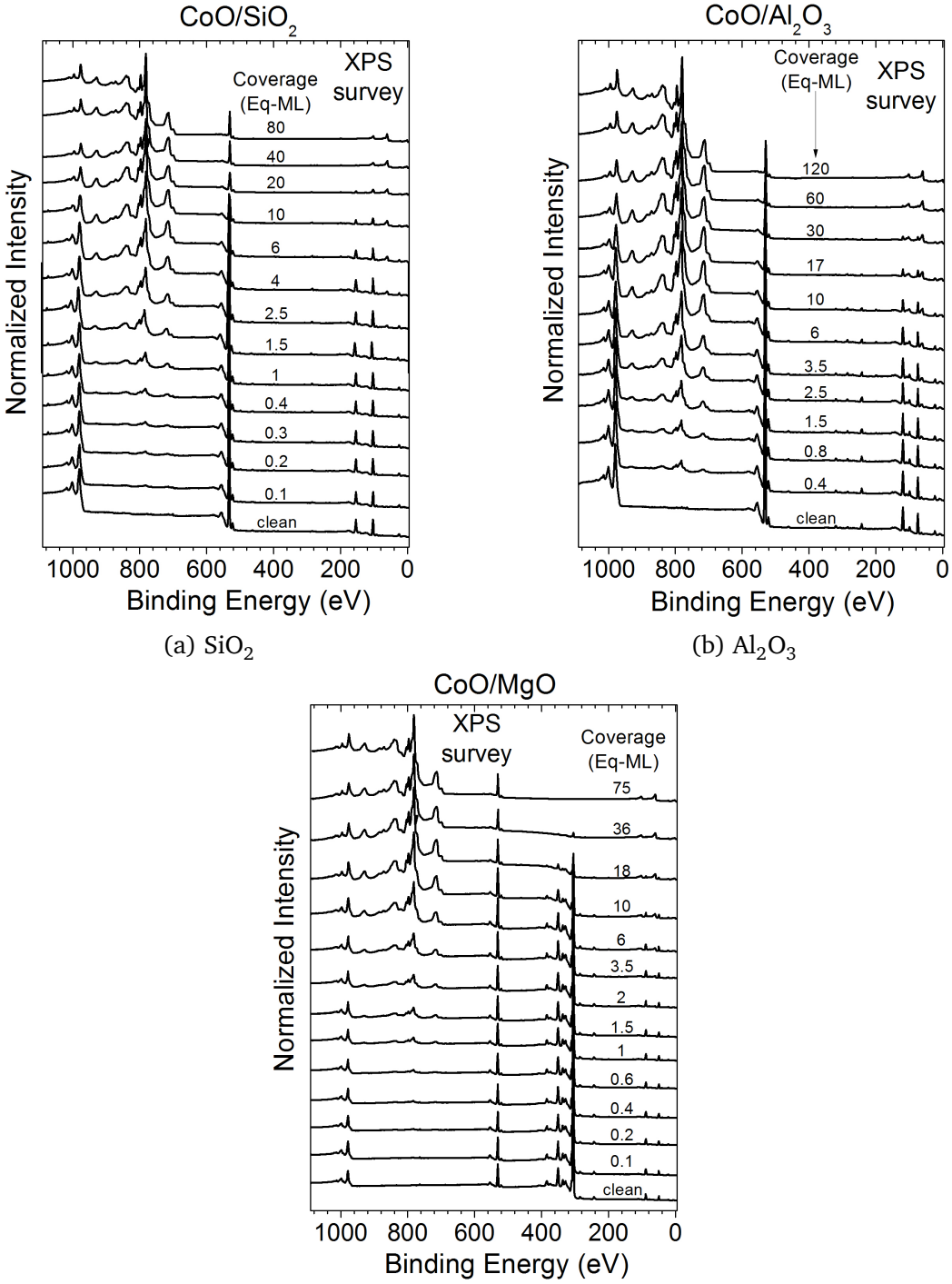

(a) SiO_2

(b) Al_2O_3

(c) MgO

Figure 4.1: XPS survey spectra for all the measured stages of the growth of cobalt oxides on the three oxides substrates. Coverage and substrate as labelled.

Peak	Energy (eV)		
	SiO_2	Al_2O_3	MgO
O LMM (Al Kα)	979-976	976	977
Co 2s	929	929	929
Co 2p	781-780	780-779	781-780
Co LMM (Al Kα)	714	714	715
O 1s	533-530	532-530	531-530
Ar 3s	-	320	-
C 1s	-	285	-
Ar 3p	-	240	-
Co 3s	103	102	103
Co 3p	61	60	61
(Substrate) 2s	154 (Si 2s)	119 (Al 2s)	88.7 (Mg 2s)
(Substrate) 2p	103.4 (Si 2p)	74.4 (Al 2p)	54 (Mg 2p)

Table 4.1: Energies of the most important peaks seen in the XPS survey spectra of the growth of cobalt oxides on the three oxide substrates.

of the most important peaks that appear in these spectra are summarized in table 4.1. The coverages of these samples (more information about their calculation will be given in section 4.2.2.1, page 96) are given in equivalent monolayers (Eq-ML or simply ML from now on) units: this unit measures the total quantity of material grown as if it was distributed in a uniform layer with a height of an atomic monolayer of the material analysed. In this work, it was chosen that 1 ML is equivalent to a layer with a height of roughly 2 Å, which is the distance between the Co and O ions in the CoO lattice.

The evolution of the spectra with the coverage shows the expected features of the growth of cobalt oxides on a substrate. The peaks that correspond to the substrate (the O 1s and metal 2s and 2p core levels of the oxide substrates) are the only ones visible for the early coverages. Once the grown cobalt oxide is thick enough, the peaks belonging to the deposited material (Co 2p, Co LMM, Co 3s and so on) start being visible, while the intensity of the substrate features decreases. For the largest coverages deposited, only cobalt oxides features are visible, and these growth experiments were considered finished at that point. Aside from this, their most significant feature is the small (or even absence) quantity of contaminants, like nitrogen (N 1s peak, 400 eV), carbon (C 1s peak, 285 eV), or tungsten (W 4f peak, 34 eV) for instance. Still, some carbon can be seen at the CoO/Al_2O_3 experiments, in addition to some traces of argon (Ar 3s and Ar 3p, 320 eV and 238 eV respectively). The Al_2O_3 substrate had more initial contamination than the others, so that it was subjected to more sputtering/heating cycles, and therefore, it is the one where is more probable that some small quantity of argon could get implanted. This cleaning was not perfect, because some carbon can still be seen at the clean substrate, but its quantity was considered small enough to start the growth experiment. Also, the intensity of the C 1s peak does not increase with the coverage, so it is safe to assume that the evaporating equipment (evaporator and gas line) was clean throughout all the depositions.

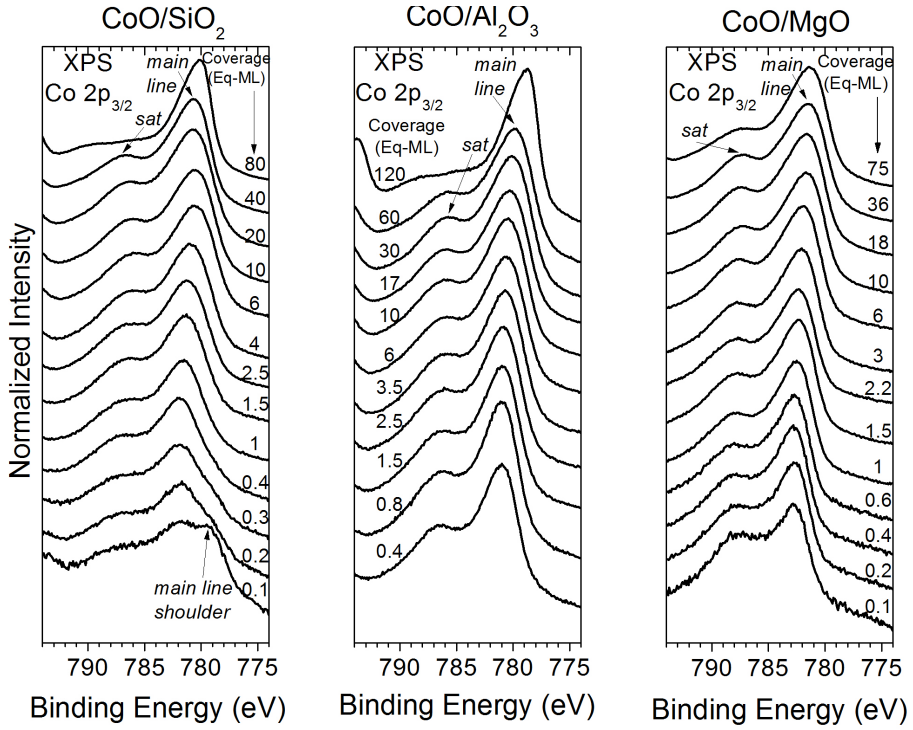

(a) SiO_2 (b) Al_2O_3 (c) MgO

Figure 4.2: XPS Co $2p_{3/2}$ spectra of all the measured stages of the growth of cobalt oxides on the three oxides substrates. Coverage and substrate as labelled.

4.2.1.2 Co $2p_{3/2}$ XPS spectra

The Co $2p_{3/2}$ region spectra are shown in figure 4.2, and the energies of the most important peaks seen at first glance are displayed in table 4.2. Almost all of the spectra have a similar shape, showing a main peak located at a binding energy of ∼781.0 eV (in the following as "*main line*") and a satellite peak at ∼787.0 eV (in the following as "*sat*"). For coverages above 40 ML of the growth on SiO_2 and Al_2O_3, this peak structure changes: the intensity of the *sat* peak decreases, and there is a change in the shape and energy of the *main line* peak. Also another contribution, located at ∼779 eV, appears as a shoulder in the shape of the *main*

Peak	Energy (eV)		
	SiO_2	Al_2O_3	MgO
main line	781.8-780.5	781.0-778.8	781.7-780.2
sat	797.5-796.4	796.5-795.6	797.5-796.4
main line shoulder	779.3	-	-

Table 4.2: Energies of the most important peaks found in the XPS Co $2p_{3/2}$ spectra of the growth of cobalt oxides on the three oxide substrates.

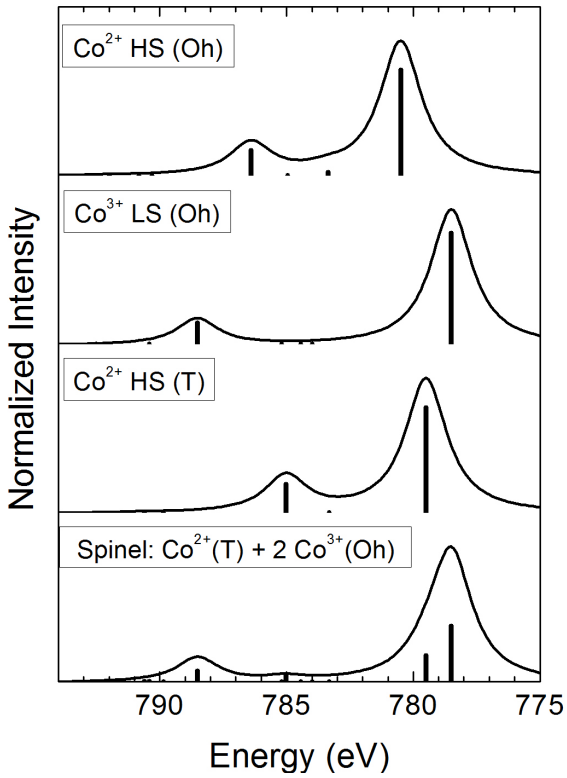

Figure 4.3: Theoretical calculations of the XPS Co $2p_{3/2}$ region for different Co oxidation states and coordinations. Top spectrum corresponds to the CoO structure, while the bottom spectrum corresponds to the Co_3O_4 spinel structure, which is a combination of the second and third spectrum shown.

Parameter	Co^{2+}	Co^{3+}
Δ	5.5	4.0
U	5.2	5.0
pdσ	1.3	1.9
10 Dq	0.70	1.0
B	0.14	0.15
C	0.54	0.60

Table 4.3: Cluster model parameters for the cluster model calculations shown in figure 4.3. All values are given in eV.

line peak for the lowest coverages of the growth on SiO_2, (labelled in table 4.2 as "*main line* shoulder").

For the assignment of the Co species found during the growth, theoretical cluster calculations of the Co $2p_{3/2}$ region were performed. The cluster consisted of a Co ion surrounded by oxygen ions in octahedral (CoO_6) or tetrahedral (CoO_4) symmetries. The main parameters of this model were the d-d Coulomb interaction U, the charge transfer energy Δ and the p-d hybridization $pd\sigma$. The cluster was solved with the configuration interaction scheme [1], where the ground and final states are expanded in configuration of the type $3d^{n+k}\underline{L}^k$, where $\underline{L}$ denotes a hole in the oxygen band. Each configuration is further split into different multiplets, which are given in terms of the Racah parameters B and C and the crystal field 10 Dq: these parameters are shown in table 4.3, and they are all in agreement with previous works [2]. The cluster model is then solved with exact diagonalization, and the spectral weight is calculated using the sudden approximation.

The results are presented in figure 4.3, and the parameters used in these calculations are shown in table 4.3: the energy positions of the different final states are related to the position

of the main peak in the Co^{2+} HS O_h spectrum. The top spectrum of figure 4.3 shows the calculations for the CoO structure (conformed by Co^{2+} ($3d^7$) ions in high spin configuration and octahedral symmetry (HS Oh)), which is composed by three peaks: the already discussed *main line* (main photoemission line) and *sat* (shake-up satellite) peaks, and a less intense third peak, labelled as *mult*, which is caused by multiplet effects. The spectrum for the Co_3O_4 structure (bottom) is a combination of the second and third spectra shown, which correspond to Co^{3+} ($3d^6$) ions in low spin configuration and octahedral symmetry (Co^{3+} LS (Oh)), and Co^{2+} ($3d^7$) ions in high spin configuration and tetrahedral symmetry (Co^{2+} (HS T)), respectively. The two biggest differences between this and the CoO spectrum is the loss in intensity of the satellite features, and the shift of the mainline peak towards lower binding energies: these features can be used to distinguish between both cobalt oxides at a first glance. Based on this theoretical calculations and the information found in the bibliography [3–6], we can conclude that the main species found in the growth of cobalt oxides on these substrates are:

- CoO/SiO_2:
  - $<$ 30 ML: CoO
  - $>$ 40 ML: Co_3O_4
  - $<$ 1 ML: some unoxidized Co
- CoO/Al_2O_3:
  - $<$ 40 ML: CoO
  - $>$ 40 ML: Co_3O_4
- CoO/MgO:
  - CoO for all the coverages explored.

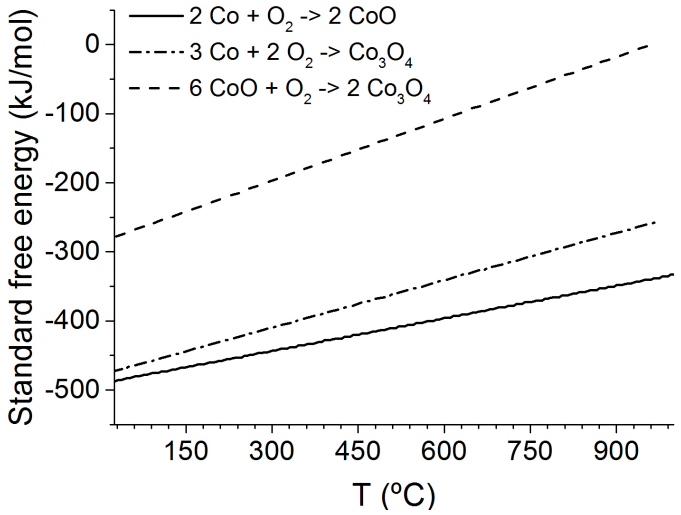

Figure 4.4: Free energy diagrams of the two possible cobalt oxidation reactions, and the oxidation of CoO to Co_3O_4. Data taken from [7]

These compositions can be explained in terms of the free energy diagrams of the Co-O oxidation reaction, which are displayed in figure 4.4. They show that the most favourable reaction is the oxidation of Co to CoO, just what we are obtaining in these experiments, and the oxidation state that is most consistent with the low energy of the evaporated Co atoms and the relatively low oxygen conditions of the growth. The loss of intensity of the satellite structure of the Co $2p_{3/2}$ region suggests that the growth of Co_3O_4 starts earlier in the SiO_2 substrate than in the other two substrates. Also, the lower coverages of the growth on SiO_2 show some unoxidized Co. Two hypothesis for this Co appearance are suggested: the differences in lattice parameters, structures and coordination of the CoO and SiO_2 lattices, and the presence of oxygen vacancies on the SiO_2 surface [8].

4.2.1.3 O 1s XPS spectra

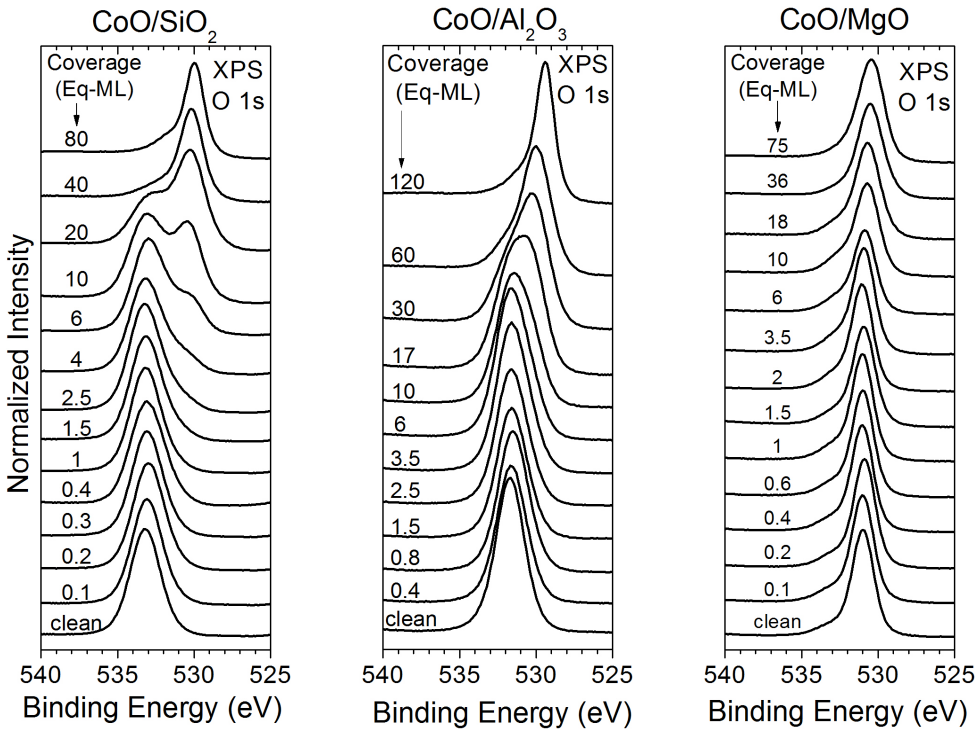

(a) SiO_2 (b) Al_2O_3 (c) MgO

Figure 4.5: XPS O 1s spectra for all the measured stages of the growth of cobalt oxides on the three oxide substrates. Coverage and substrate as labelled.

The O 1s XPS spectra are displayed in figure 4.5. All three spectra series are mainly composed of two peaks, one corresponding to the O 1s core level for CoO (∼530.5 eV), and another that is assigned to O 1s of the corresponding oxide substrate: 533.2 eV for SiO_2, 531.6 eV for Al_2O_3, and 530.9 eV for MgO [9–11]. The binding energy of the O 1s core levels of the substrate changes in accordance with their ionicity: the peak corresponding to MgO has a lower binding energy due to the more ionic character of their Mg-O bonds, while the peak corresponding to

SiO_2 has a higher binding energy because of the high covalent character of the Si-O bonds. The shift seen in the CoO peak for the final coverages is attributed to the already commented oxidation state change of the deposited material from CoO to Co_3O_4 for large coverages.

4.2.2 Quantitative analysis

4.2.2.1 Analysis of the XPS intensities

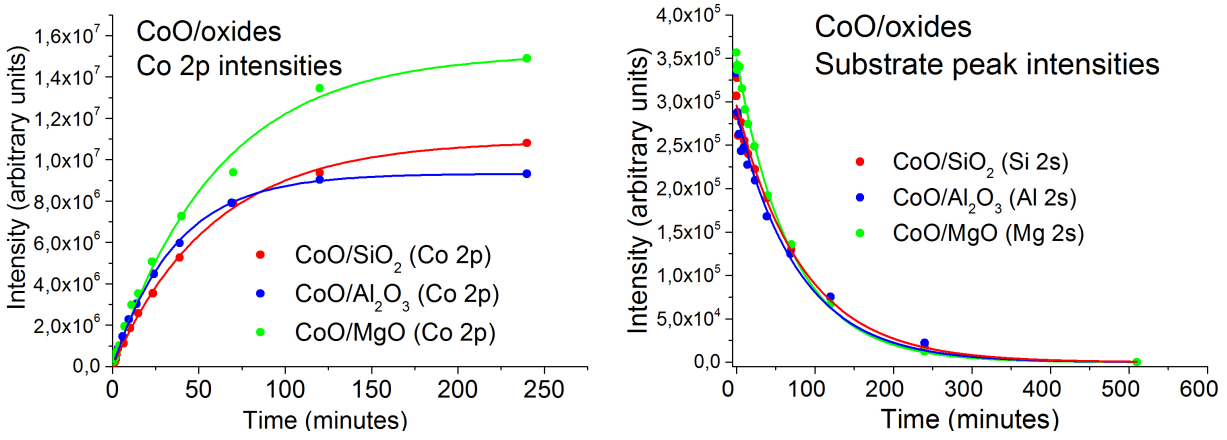

(a) Intensities of the Co 2p peaks

(b) Intensity of the substrate peaks

Figure 4.6: Variation of the XPS Co 2p and substrate region peak intensities using the infinitely thick layer model for the growth of cobalt oxides on the three oxide substrates.

To determine the coverage of the growth of CoO on the oxide substrates, the XPS spectra obtained during the growth experiments were used. Both the Co 2p peaks and adequate substrate peaks (chosen as they would not overlap with any cobalt oxide features) were selected, and then a Shirley background was subtracted. Then, they were integrated, and the infinitely thick layer model (see section 3.1.4.1, page 64) was used in order to obtain both the coverage for each evaporation and the deposition rate. Figure 4.6 shows the fitted curves for the three growth experiments, and table 4.4 shows the values obtained in these calculations, along with the most important parameters used, like the region analysed and the IMFP of the electrons coming from the analysed orbital. In the bottom row of this table, the R^2 coefficients for each fitting are shown: this parameter is also known as the coefficient of determination, and it measures the proportion of response variation "explained" by the independent variables in the model. In this case, the closer to 1, the better the fit is.

4.2.2.2 AFM study of the growth

Now we will present the results of the characterization of these growths by AFM. The measurements were made ex-situ, and the samples were measured just after being taken out of the vacuum chamber, in order to minimize their contamination. Although the technical details of these measurements have been displayed in section 3.2.2 (page 70), it is important to

	CoO/SiO_2	CoO/Al_2O_3	CoO/MgO
IMFP (Å)	13.93 (Co 2p) 36.36 (Si 2s)	13.93 (Co 2p) 31.96 (Al 2s)	13.93 (Co 2p) 28.08 (Mg 2s)
v (ML/min)	0.24 ± 0.01 (Co 2p) 0.22 ± 0.02 (Si 2s)	0.38 ± 0.01 (Co 2p) 0.25 ± 0.02 (Al 2s)	0.22 ± 0.02 (Co 2p) 0.20 ± 0.01 (Mg 2s)
v_{med} (ML/min)	$\mathbf{0.23 \pm 0.02}$	$\mathbf{0.31 \pm 0.07}$	$\mathbf{0.21 \pm 0.02}$
R^2 value	0.99897 (Co 2p) 0.98410 (Si 2s)	0.99878 (Co 2p) 0.97033 (Al 2s)	0.99388 (Co 2p) 0.99771 (Mg 2s)

Table 4.4: Deposition rate calculations obtained with the infinitely thick layer method for the growth of cobalt oxides on the three oxide substrates. The IMFP of the peaks used in the calculations and the R^2 values of the fittings are also presented in this table.

remind that the tip vibration amplitude and the sample-tip distance were set as low as possible, in order to maximize the resolution and avoid the displacement of material by the tip. As a way to check this possibility, increasingly bigger images were routinely taken without changing their centre coordinates. The resulting images never showed typical signs of displacement of material by the tip, like vertical marks that could correspond with the borders of smaller images taken in that area, so we can be sure that no material has been displaced by the tip in the images displayed in this work.

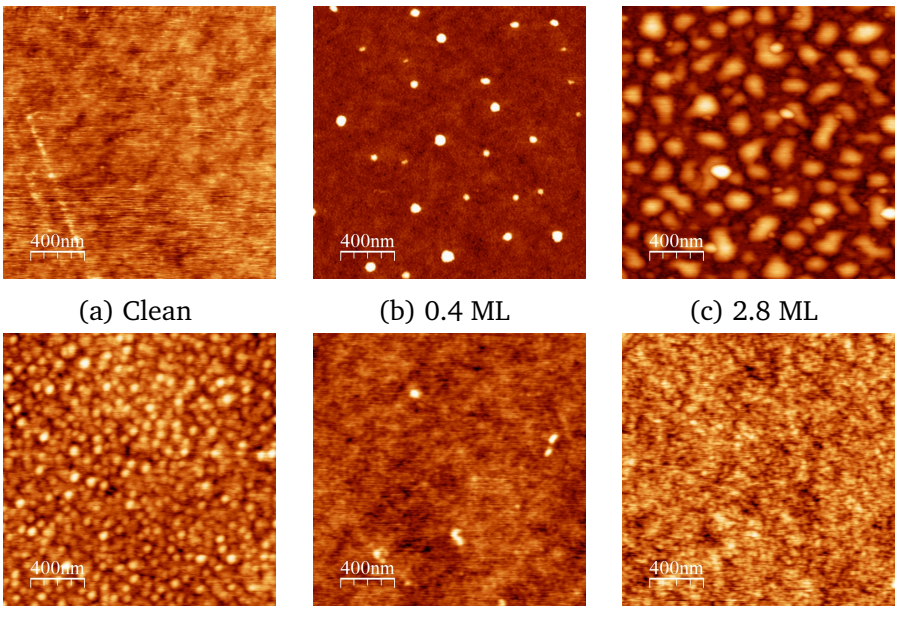

(a) Clean (b) 0.4 ML (c) 2.8 ML

(d) 4 ML (e) 9.5 ML (f) 22 ML

Figure 4.7: AFM topography images for selected coverages of the growth of CoO on SiO_2, plus an image of the clean substrate. CoO coverage as labelled. Size of the images: $2\,\mu m \times 2\,\mu m$.

The AFM images taken for the growth of CoO on SiO_2 (figure 4.7) show an island type of growth: a first layer of islands with a height of 8-12 Å starts covering the SiO_2, and after a good portion of the substrate has been covered, a second layer of islands with a lower mean height ($\sim$ 4 Å) starts growing on top of the first layer. The images for larger coverages show a completely flat surface, so it can be assumed that the rest of the growth happens in a layer-by-layer way.

Meanwhile, the AFM images taken for the growth on MgO and Al_2O_3 (figures 4.8 and 4.9) show no change when compared to the morphology of the substrate, which means that the growth of cobalt oxide on these substrates is produced in a layer-by-layer way. This is specially visible in the CoO/Al_2O_3 images, where the typical Al_2O_3 stepped structure [12] is visible even in the 10 ML sample.

Table 4.5 shows an estimation of the roughness of the samples as given by the R_q coefficient, which is defined as the square root of the sum of the squares of the individual heights and depths of the measured image. These values were calculated with the software WSxM, using the mean of the R_q values obtained for three different 5 μm × 5 μm AFM topography images for each sample. These roughness measurements were also tried on the maximum-sized images taken (10 μm), but this size is very close to the maximum available movement of the piezoelectric used, causing a lot of distortions around the edges of the extracted images. To correct this, harsher filters had to be used, leading to the distortion of the height values obtained. The AFM measurement of these samples is difficult, and a lot of contamination can be picked by the tip, thus changing its resolution and the R_q values obtained: nevertheless, the first conclusion that can be extracted is that they are very low for the three growths. They show increasing values for coverages between 1 and 5 ML, and a decrease when the coverage gets to 10 ML, approaching the original substrate roughness. This effect is more evident on the growth on SiO_2 and more subtle on the rest of the growths, which agrees with the morphology seen in the AFM images of the growths.

SiO_2		**Al_2O_3**		**MgO**	
Coverage (ML)	R_q (nm)	Coverage (ML)	R_q (nm)	Coverage (ML)	R_q (nm)
clean	0.18±0.02	clean	0.13±0.01	clean	0.15±0.01
0.4	0.11±0.02	1	0.16±0.01	1	0.23±0.05
2.8	0.21±0.01	2	0.21±0.03	2	0.21±0.01
4	0.59±0.06	4	0.18±0.04	4	0.34±0.03
9.5	0.20±0.02	10	0.10±0.02	10	0.15±0.02

Table 4.5: R_q values obtained in the analysis of the AFM images of the growth of cobalt oxides on the three substrates.

To summarize, we have observed two different morphologies fo the growth of cobalt oxides on these three substrates. The growth of CoO on SiO_2 show a Volmer-Weber (i.e. islands formation) way of growth, where adatom-adatom interactions are stronger than the adatom-surface interaction. However, the growth of CoO on MgO and Al_2O_3 shows a Frank-van der Merwe (i.e., layer-by-layer) way of growth, where adatoms attach preferentially to surface sites.

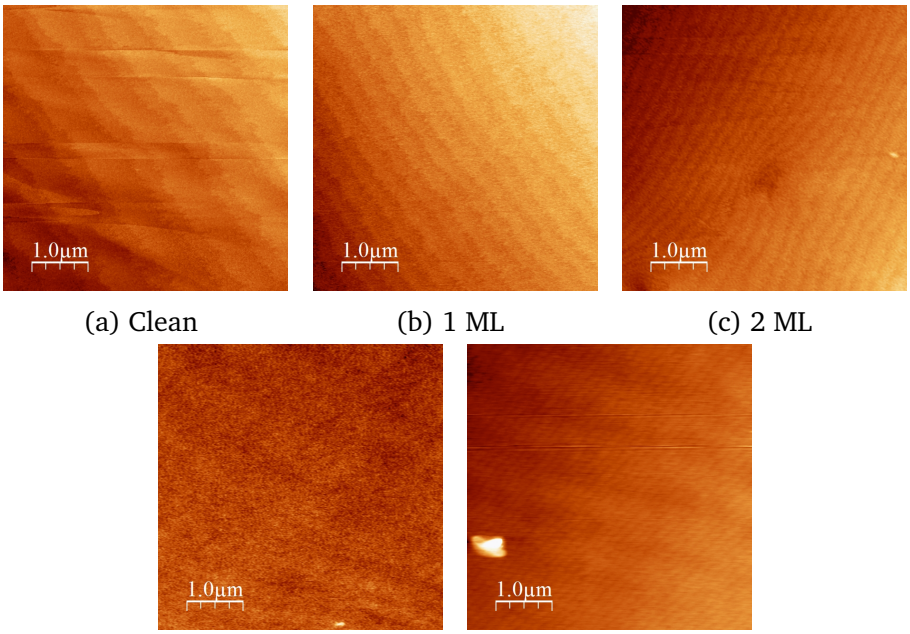

(a) Clean (b) 1 ML (c) 2 ML

(d) 4 ML (e) 10 ML

Figure 4.8: AFM topography images for selected coverages of the growth of CoO on Al_2O_3, plus an image of the clean substrate. CoO coverage as labelled. Size of the images 5 μm × 5 μm.

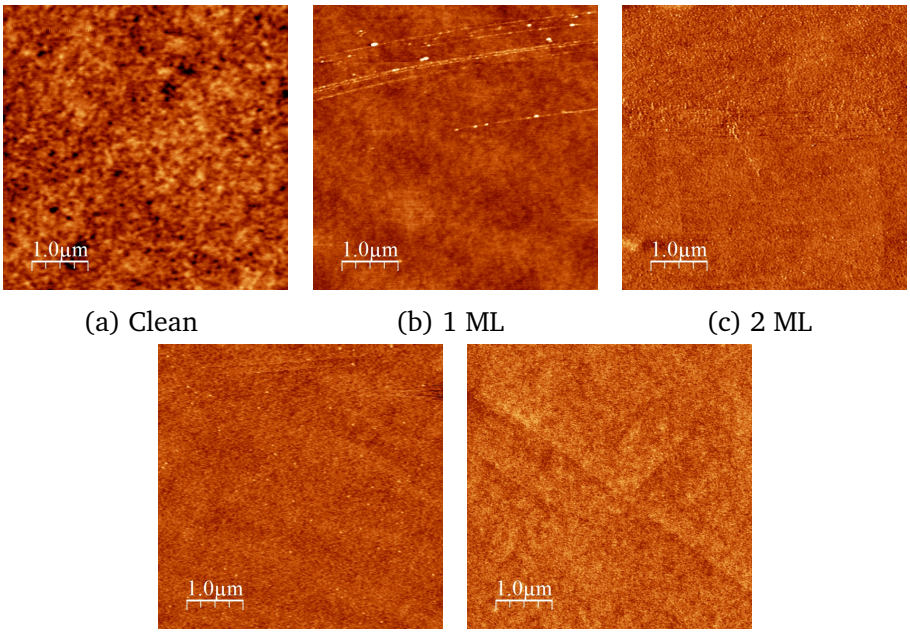

(a) Clean (b) 1 ML (c) 2 ML

(d) 4 ML (e) 10 ML

Figure 4.9: AFM topography images for selected coverages of the growth of CoO on MgO, plus an image of the clean substrate. CoO coverage as labelled. Size of the images 5 μm × 5 μm.

The morphologies observed above can be explained in terms of the lattice parameters and structures of the substrates and the deposited CoO. In the growth on SiO_2, there are huge differences in the lattice parameter (the lattice mismatch of both structures is ∼15 %) and the crystal structure of the CoO and the SiO_2(rocksalt for the CoO, trigonal for the SiO_2), so it makes sense that the initial stages of that growth are in the form of islands. The CoO and MgO have the same crystal structure (rocksalt) and almost the same lattice parameter (the lattice mismatch of both structures is 0.01 %), so it is logical that the growth of CoO on that substrate happens in a layer-by-layer way.

The differences in the lattice parameter (12 %) and crystal structure (rocksalt vs. hexagonal) in the growth of CoO on Al_2O_3 could lead us to think that the morphology should be closer to that found in the growth on SiO_2. Theoretical DFT calculations of the initial stages of the growth of cobalt oxides on this substrate, made by Zayed et al [13], show that the initial CoO layers grow oriented in the fcc-type cubic (1 1 1) planes instead of the (1 0 0) face, in order to minimize the lattice mismatch between both structures. These calculations also showed that the preferred growth mode will be layer-by-layer, which agrees with our results on the morphology.

4.2.2.3 XPS-Inelastic Peak Shape Analysis (XPS-IPSA) and comparison with AFM data

The first step for the study of the morphology of the growth by means of the XPS-IPSA method is the selection of the peaks to be studied. The main criteria used is that the inelastic background region of the peak being studied (∼ 50-100 eV) has to be free of contributions coming from other peak structures. Table 4.6 shows the regions chosen, along with the most important parameters for the XPS-IPSA calculations. Once the peaks and regions were chosen, a spectra of that same region from a bulk sample was selected as reference. For the growths on SiO_2 and Al_2O_3, 40 and 60 ML coverages were chosen, respectively, since they were the largest coverages where the shake-up satellite structure of the CoO seemed clearly conserved. For the MgO sample, a spectrum from a clean MgO substrate was used as reference.

Substrate	**Peak**	**KE (eV)**	**IMFP (Å)**	Region (KE, eV)	hν (eV)
SiO_2	Co 2p	706	13.96	525-735	1486.6
Al_2O_3	Co 2p	706	13.96	525-735	1486.6
MgO	Mg KLL	1180	24.58	975-1195	1486.6

Table 4.6: Peaks used for the XPS-IPSA calculations of the growth of cobalt oxides on the three oxide substrates, their kinetic energies and IMFP, and the lower and higher bounds of regions analysed.

After trying different concentration profiles, it was found that the models showing the best fittings to the experimental data were as follows:

- **CoO/SiO_2**: two island model, with a first layer of islands with a constant height of 8 Å, and a second layer of islands with a constant height of 4 Å. This second layer starts growing

when the first layer has covered around 70% of the substrate (coverages between 2 and 3 ML).

- **CoO/Al_2O_3, CoO/MgO**: layer-by-layer model, which completely covers the substrate from the first deposited monolayer. In the case of the CoO/MgO experiment, this model is called "“buried layer model", since the material studied is the substrate, which is being buried by the deposited CoO layer.

Figures 4.10 to 4.12 show the XPS-IPSA results (labelled as QUASES in the graphs) for all the measurements of the in-situ growth of CoO on the oxide substrates. These figures show both the height and total coverage values obtained in the XPS-IPSA calculations and the comparison between the coverage obtained with XPS-IPSA and AFM/XPS (infinitely thick layer method). Aside from the results of the fittings, all height-total coverage graphs have dashed lines representing the different morphologies for fixed coverages values, as a way to easily detect the coverages grown in each sample analysed. The XPS-IPSA data from the growth of CoO on SiO_2 is compared with the cluster dimensions and coverage data extracted from the AFM images, since the way of growth of CoO on this substrate allowed for cluster dimensions measurements and coverage calculations via flooding analysis. The data from the growth on MgO and Al_2O_3 cannot be compared in this way, since the growth is layer-by-layer, so the coverage data extracted from the XPS-IPSA calculations is compared with the coverage data obtained with the analysis of the XPS intensities shown previously.

In all three cases, these calculations agree not only with the morphology and height values observed by AFM, but also with the total CoO coverage calculated by the flooding analysis of the AFM images (for the CoO/SiO_2 experiment) and the XPS infinitely thick layer model (in the other two cases).

4.2.3 Summary

The chemistry and morphology of the growth of cobalt oxides on the three oxide substrate has been characterized by multiple techniques. The chemistry of the growth has been studied with in-situ XPS measurements, and has yielded that the major cobalt species found throughout the coverage range explored is CoO, while Co_3O_4 has been observed for coverages above 40 ML on the growths on SiO_2 and Al_2O_3. Some unoxidized Co has been detected for the lower coverages of the growth of cobalt oxides on SiO_2, which has been attributed to differences in the lattice parameter and structure between the SiO_2 and the CoO, although the effect of possible oxygen vacancies in the substrate surface cannot be ruled out without additional experiments.

The morphology of the growth of CoO on these substrate has been studied with AFM and conformed by XPS-IPSA. Two different ways of growth have been detected in these experiments: a Volmer-Weber (i.e, island growth) growth mode for the growth of CoO on SiO_2, and a Frank-Van Der Merwe growth mode (i.e., layer-by-layer growth) for the growth of CoO on MgO and Al_2O_3. The morphologies seen in the growths on SiO_2 and MgO have been rationalized in terms of the differences in crystal structure and lattice parameter between them. The morphology observed in the growth of CoO on Al_2O_3 has confirmed previous theoretical calculations made

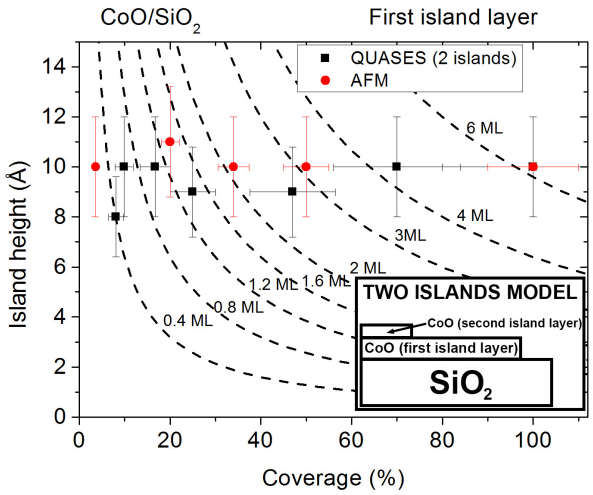

(a) Comparison of the information for the first layer of islands, as given by the AFM quantitative analysis (red dots) and XPS-IPSA using the two islands concentration profile (black squares).

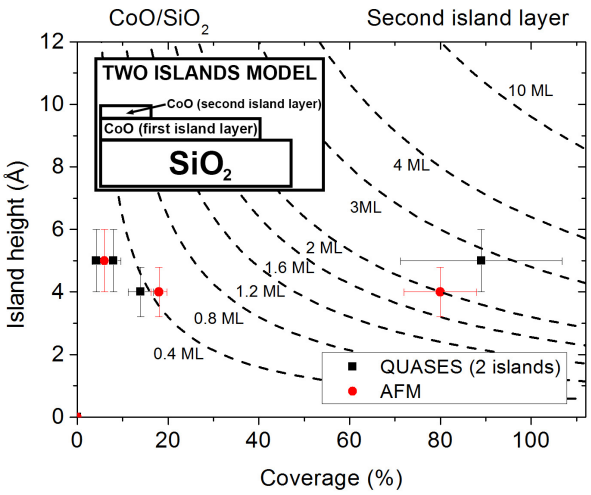

(b) Comparison of the information for the second layer of islands, as given by the AFM quantitative analysis (red dots) and XPS-IPSA using the two islands concentration profile (black squares)

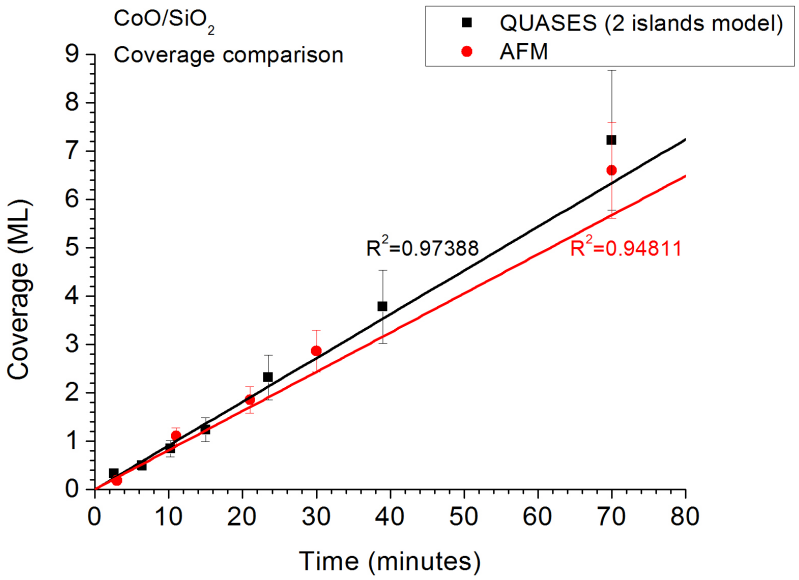

(c) Comparison of the total amount of deposited material as a function of the growth time given by AFM (red dots) and XPS-IPSA (black squares).

Figure 4.10: XPS-IPSA calculations for the two islands model applied to the growth of CoO on SiO_2, and comparison with AFM dimensions and coverage data. The insets on (a) and (b) shows the two islands concentration profile used in the XPS-IPSA calculations.

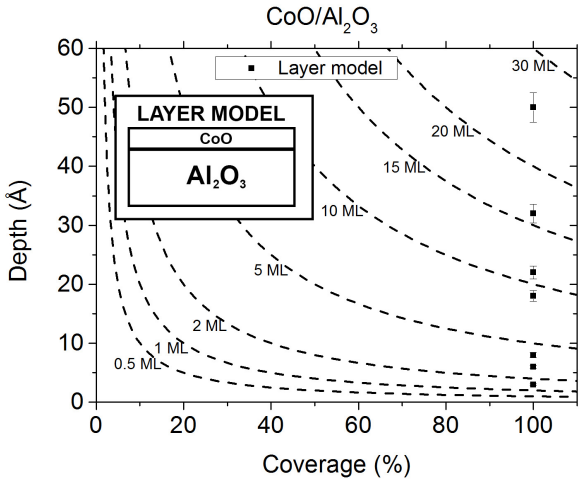

(a) Summary of the XPS-IPSA calculations using the layer concentration profile

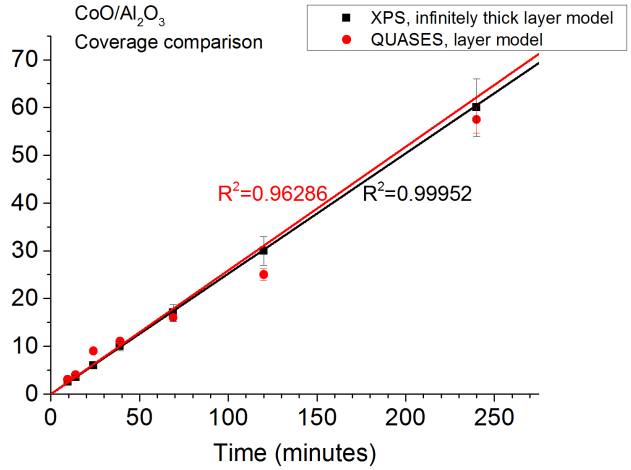

(b) Comparison of the total amount of deposited material as a function of the growth time given by the fitting of the XPS Co 2p intensities (red dots) and XPS-IPSA (black squares)

Figure 4.11: XPS-IPSA calculations for the layer model applied to the growth of CoO on Al_2O_3. The inset on (a) shows the concentration profile used.

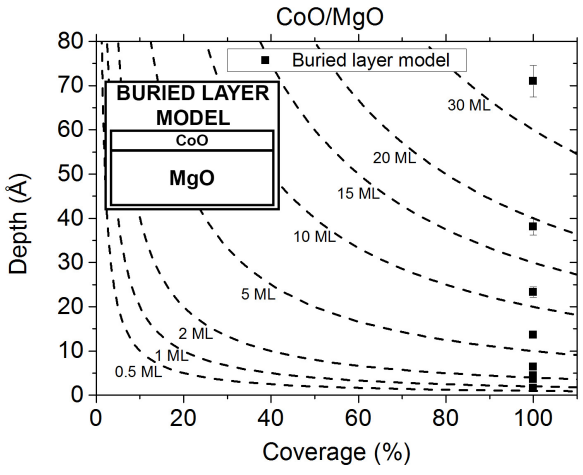

(a) Summary of the XPS-IPSA calculations using the buried layer concentration profile

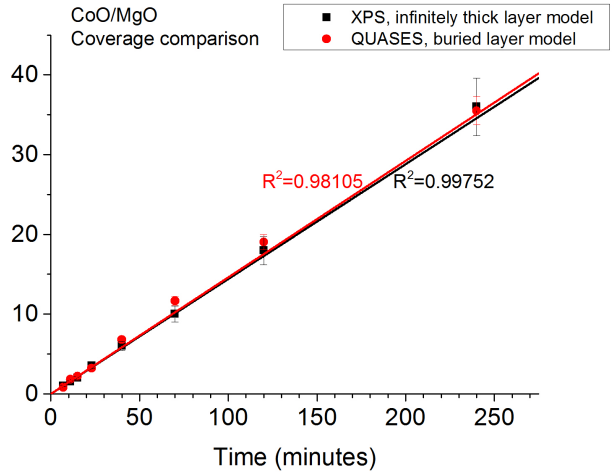

(b) Comparison of the total amount of deposited material as a function of the growth time given by the fitting of the XPS Co 2p intensities (red dots) and XPS-IPSA (black squares)

Figure 4.12: XPS-IPSA calculations for the buried layer model applied to the growth of CoO on MgO. The inset on (a) shows the concentration profile used.

for the first stages of this growth, where it was shown that the initial CoO layers grow oriented in the fcc-type cubic (1 1 1) planes instead of the (1 0 0) planes.

SECTION 4.3

Study of the CoO/oxide interfaces: size and support effects

The analysis of the CoO/oxide interfaces has been done with the Co $2p_{3/2}$ spectra of the in-situ XPS measurements of the growth of CoO on the three substrates. As we have already seen in the theoretical calculations for different Co ions, the complex electronic configuration of the cobalt oxides (d^7 oxide) gives rise to a complex Co $2p_{3/2}$ spectrum, which is very sensitive to the local symmetry of the Co atoms. In order to study the local symmetry of the Co atoms at the interface we present new cluster calculations for a CoO_6 cluster, where the pdσ parameter, which accounts for the O 2p-Co 3d orbitals overlap, has been varied in order to simulate different local environments of the Co atoms. Since this parameter is correlated with the 10 Dq (crystal field) parameter, both have to be varied simultaneously.

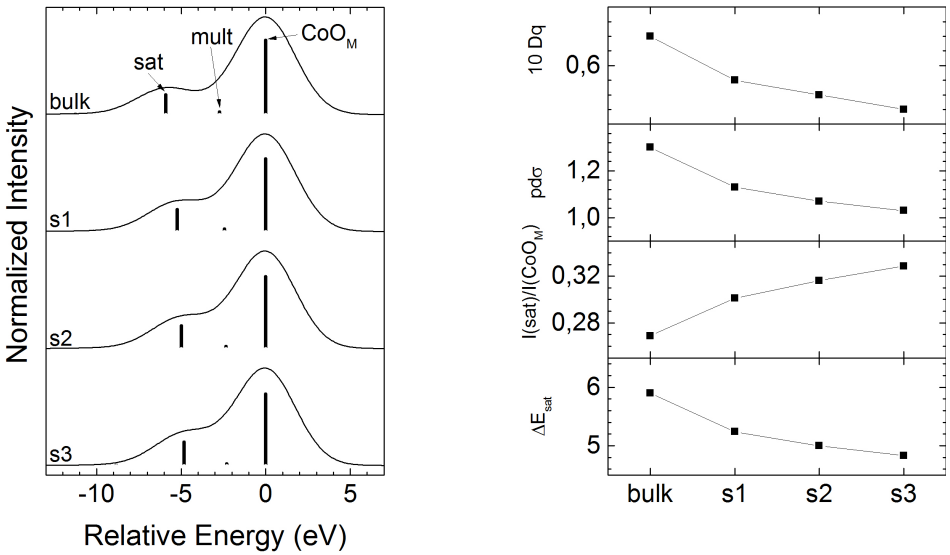

(a) XPS Co $2p_{3/2}$ spectra calculations of a CoO structure for three different 10 Dq and $pd\sigma$ values

(b) Satellite separation and relative intensity with respect to the main peak

Figure 4.13: Cluster calculations of the XPS Co $2p_{3/2}$ spectra for a CoO structure, and trends in the relative energy and position of the *sat* peak (with respect to the *main line* peak)

The results are shown in figure 4.13. They yield that if the value of the pdσ parameter is decreased, the intensity ratio between the *sat* and *main line* peaks increases, and the relative distances between these two peaks decreases. This means that changes in the relative energy and position of the *sat* peak (with respect to the *main line* peak) can give us an idea about

changes in the ionic-covalent character of the bonds of the grown CoO layers, due, for instance, to loss of coordination, disorder, bidimensionality, etc.

With these trends in mind, fittings of the XPS Co $2p_{3/2}$ spectra were made. The region lower end was set at ∼774 eV, and the three peaks already discussed (*main line*, *sat* and *mult*) were used. Changes in the relative distance and intensity of the *sat* peak were allowed, and the relative position and intensity of the *mult* peak were left as constant, since the calculations show almost no variation of these parameters throughout all the pdσ range explored. All the peaks used were given symmetric Gaussian-Lorentzian sums shapes, and the Gaussian-Lorentzian parameter was set at 20% for all the peaks used in the fittings. Only fittings for coverages below 20 ML were performed, since these fittings seek interface effects, which will not be visible for coverages larger than those explored. The fittings for the lowest coverages of the growth on SiO_2 also include a fourth peak in order to represent unoxidized Co: the same shape, asymmetry and Gaussian-Lorentzian parameter was used for this peak. Figure 4.14 displays fittings for four different coverages of the growth of CoO on the three oxide substrates as a way to show the good agreement between experimental data and fitted spectra.

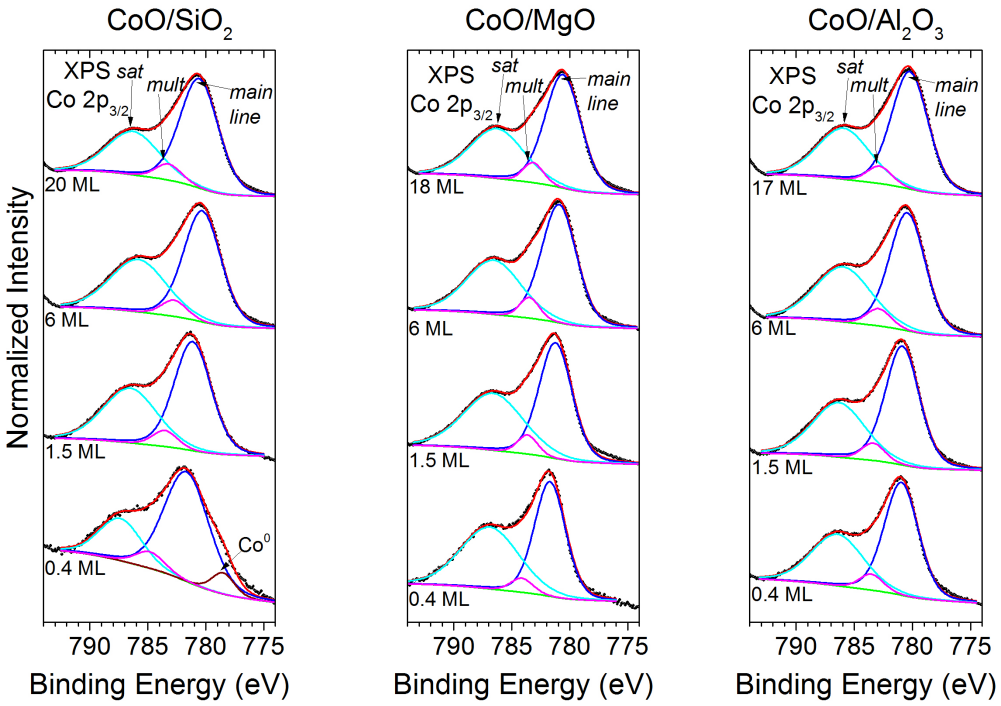

(a) SiO_2 (b) MgO (c) Al_2O_3

Figure 4.14: Fittings of the XPS Co $2p_{3/2}$ spectra of four selected coverages of the growth of CoO on the three oxide substrates. Coverages, peaks used and substrates as labelled.

Figures 4.15 and 4.16 show the variation in the binding energy of the *main line* peak and changes in the relative position and intensity of the *sat* peak (labelled as ΔE_{sat} and I_{sat} from now on), as extracted from these fittings. We start commenting the variations in the energy position of the *main line* peak (figure 4.15).

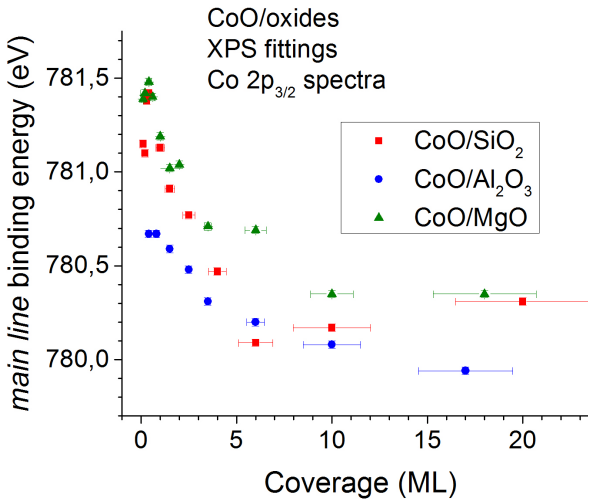

Figure 4.15: Binding energy of the *main line* peak as a function of the total deposited coverage, as extracted from the fittings of the XPS Co $2p_{3/2}$ spectra of the growth of CoO on the three oxide substrates.

The first feature observed is a shift towards lower binding energies for coverages below 5 ML on the three substrates. This shift for very low coverages seems to be due to extra-atomic relaxation effects caused by the small size of the structures analysed. This has been observed in metallic and oxide nanoparticles and ultra-thin layers [14–16]. The binding energy of the *main line* peak ends up stabilizing around 780.4 eV for the largest coverages of the growth on MgO and SiO_2 explored with these fittings, which is in excellent agreement with the values observed in the bibliography for bulk CoO samples (780.5 eV). The binding energy for the growth on SiO_2 shows a minimum value of 780.1 eV for the 6 ML coverage, and then approaches the aforementioned final value of 780.5 eV. This behaviour can be attributed to the morphology change of this growth for the coverages between 4 and 10 ML. Indeed, the AFM images of this growth (figure 4.7) showed a change in the way of growth in this coverage range. Nevertheless, this minimum could be also be caused by experimental errors, and more coverages below and above this point should be studied to verify this.

The binding energy position for the growth on Al_2O_3 has a similar behaviour, but the *main line* peak shows a global energy shift of about 0.8 eV with respect to the growths on the other two substrates, energy values that are also lower than the binding energy observed in this peak for the growth on HOPG (subsubection 5.4.1.1, page 137). Possible errors in the energy calibration of the spectra were checked with the energy of the O 1s and Al 2p peaks, and they were ruled out. In order to explain it, we need to come back to the already mentioned theoretical Density Functional Theory (DFT) calculations of this interface [13]. Aside from determining the CoO face grown on Al_2O_3, they found an electron density transfer of about 1 eV from the topmost O layer of the substrate to the first two CoO nanolayers. In this picture, the electric dipole moment created at the interface makes the photoelectrons gain kinetic energy, thus shifting them towards lower binding energies. This feature in the binding energy of the *main line* peak of the growth of CoO on Al_2O_3 can be considered an experimental proof

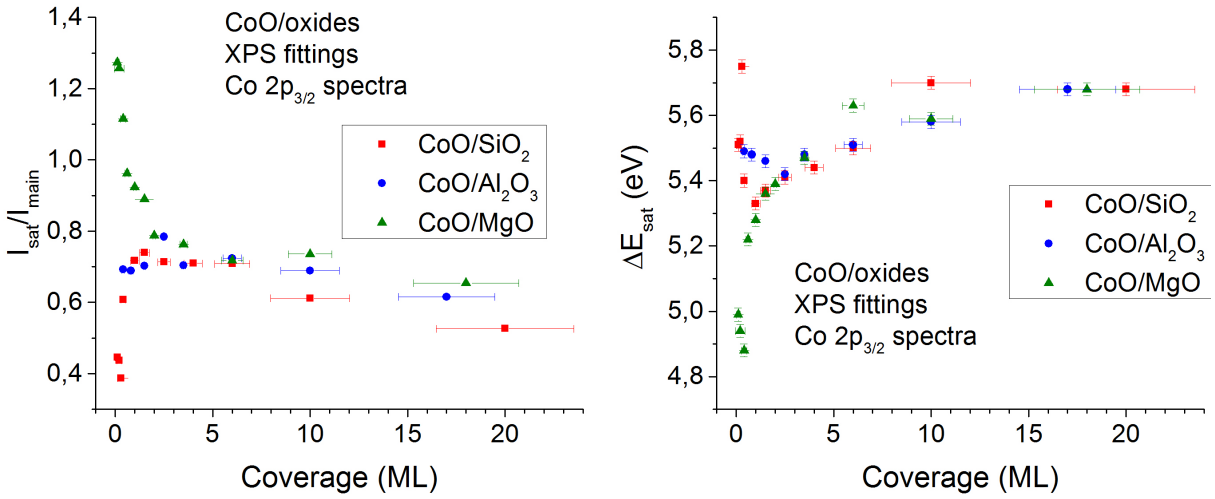

(a) Relative intensity of the *sat* peak with respect to the *main line* peak (labelled as I_{sat}/I_{main})

(b) Energy separation between the *sat* and *main line* peaks (labelled as ΔE_{sat})

Figure 4.16: Variation of the relative position and intensity of the *sat* peak (in relation to the *main line* peak) as a function of the total deposited coverage, as extracted from the fittings of the XPS Co $2p_{3/2}$ spectra of the growth of CoO on the three oxide substrates.

of this theoretical prediction.

Now we are going to focus on the changes of I_{sat} and ΔE_{sat} with the coverage: figure 4.16 shows the values of both quantities obtained from the fittings. The first thing that it is noticeable is that the behaviour of the I_{sat} for any of the three growths is the opposite of the ΔE_{sat} behaviour, which is consistent with what was observed in the theoretical calculations. Since they give the same information, we are going to comment only the ΔE_{sat} graph from now on.

The three experiments show different trends for low coverages: the growth on MgO shows a gradual increase, the growth on Al_2O_3 maintains more stable values, and the growth on SiO_2 shows an initial decrease that hits a minimum value around the 2 ML coverage value, and from there it increases back. Starting from the 3 ML coverage, the values of the ΔE_{sat} have the same behaviour for the three growths, and end up stabilizing around ∼5.7 eV, a value that is reasonably close to the predicted 6 eV value for the bulk CoO structure in the theoretical calculations.

In previous experiments made in our group of deposition of ultra-thin transition metal oxide layers on these substrates with conditions similar as in this experiments [17, 18], it was seen that the most covalent substrates reduced the covalency of the deposited transition metal oxide layers. The trends seen here suggest just the opposite: there is a less covalent oxide grown on the most ionic of the substrates explored (MgO), and a more initial covalent oxide in the most covalent of the three substrates (SiO_2). This allows us to state that the covalency of the substrate does not affect the growth of CoO layers as our previous experience with similar experiments suggested: these effects have a different origin.

Our hypothesis for this behaviour is based on the morphology of the deposited CoO layers,

which also depends on the morphology and crystalline properties of the oxide substrates, as we have already observed. The MgO layer grows in a very epitaxial way, which means that, for 1 ML, only half of the complete CoO layer will be formed (Co-O instead of Co-O-Co). This means that a complete Co^{6+} coordination octahedron will not be formed, and therefore the character of the bonds of this layer will be less covalent. The coverage increase will end up completing this coordination octahedron, increasing the covalency of the bonds in the grown layer. The morphology of the Al_2O_3 layer would suggest a similar behavior and explanation, but the aforementioned charge transfer, the (1 1 1) face grown and the magnetic effects seen in the DFT calculations could affect its trends in a significant way.

Finally, the trends seen in the growth on SiO_2 can also be explained in terms of the morphology of the growth. For the lowest coverages (<2 ML) we do not have continuous layers, but CoO nanoparticles with a constant height of ∼8 Å. This means two things: they can form bulk-like CoO structures from the beginning, and they have a higher surface energy. These nanoparticles become more like extended islands for coverages around 3 ML (they grow in width, but not on height), and from there the growth progresses in a layer-by-layer growth mode for coverages above 4 ML, so it makes sense that the initial ΔE_{sat} values of the nanoparticles formed at lower coverages will gradually approach those seen in the growth on the other two substrates. Our conclusion is that these initial nanoparticles have higher values of covalency due to their surface energy, and once this morphology is lost, and it becomes similar to the one seen in the other two growths, the ΔE_{sat} values behave in the same way as the growths on MgO and Al_2O_3.

SECTION 4.4

Stability of the CoO layers

4.4.1 Stability upon air exposure

4.4.1.1 XPS Co $2p_{3/2}$ spectra

Since the above study of the cobalt oxide layers have been performed for samples grown "in-situ" under UHV conditions, now we intend to study the stability of those layers upon air exposure and even submitted to aggressive conditions.

The first study of the stability of these ultra-thin layers consisted of the exposure of 3 and 20 ML CoO/oxide samples to room conditions. Samples with these coverages were separately grown, taken out of the vacuum chamber, and left exposed to room conditions for one month. Then they were introduced again in the vacuum chamber and measured by XPS, with no extra treatment. Again, only the Co $2p_{3/2}$ region will be shown, since it provides most of the important information. Figure 4.17 shows the XPS Co $2p_{3/2}$ region measurements of 3 and 20 ML samples before and after being exposed to atmospheric conditions for 1 month. All the spectra are presented with a Shirley background removed, being normalized for a better comparison.

After one month exposed to air, the Co $2p_{3/2}$ XPS spectra of the 3 ML samples show a decrease in the relative position and an increase of the relative intensity of the *sat* peak (with

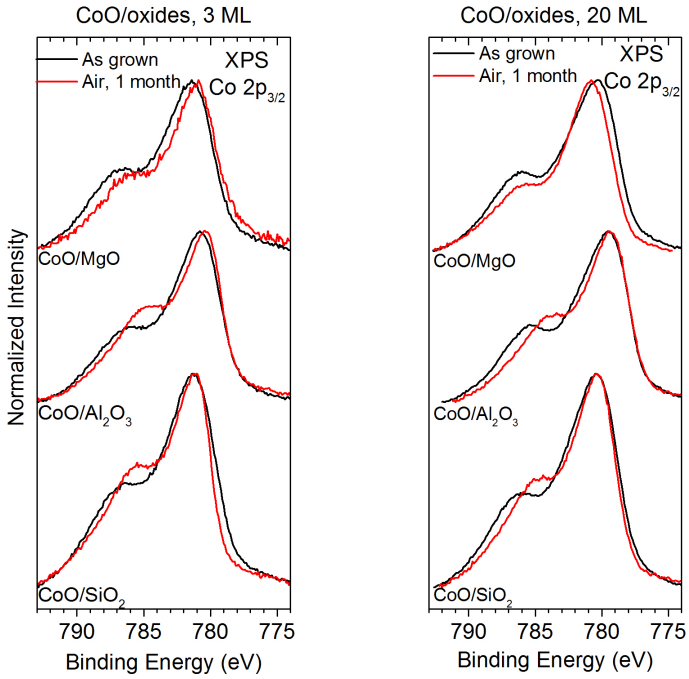

(a) 3 ML (b) 20 ML

Figure 4.17: XPS Co $2p_{3/2}$ spectra of CoO samples grown on the three oxide substrates, measured as grown (black line) and after being exposed to atmospheric conditions for 1 month (red line). Coverage and substrates as labelled.

respect to the *main line* peak) in the samples grown on SiO_2 and Al_2O_3, and a narrowing of the *main line* peak for the samples grown on SiO_2, while the spectrum of the sample grown on MgO stay mostly unchanged. All of this could be explained by the appearance of cobalt hydroxide, which has a lower ΔE_{sat} value, a narrower *main line* peak, and a slightly higher satellite intensity value [6]. The narrowing of the main line and the satellite intensity increase in the samples grown on SiO_2 sample suggests that this is the less stable of these interfaces under atmospheric conditions, while the other two are more stable, specially the samples grown on MgO.

Meanwhile, all the 20 ML samples suffer changes after exposure to air: the spectra of the samples grown on SiO_2 and Al_2O_3 show a narrowing of the *main line* peak and a shift of the *sat* peak towards lower binding energies. This could also be explained by the aforementioned growth of cobalt hydroxide on the surface of these samples. The spectrum of the sample grown on MgO has a less intense satellite intensity after the exposition to air, which suggests that a little quantity of its surface could be transformed into Co_3O_4. Nonetheless, the apparent lack of cobalt hydroxide on both coverages allows us to conclude that the samples grown on MgO are the most stable under room conditions.

4.4.1.2 XRD powder diffractograms

The 20 ML samples were also measured after being exposed for three months to room conditions by XRD at the branch B of the SpLine beamline of the ESRF synchrotron (λ=0.885 Å, E=14 keV). The results obtained are displayed in figure 4.18. Their analysis was carried out with an evaluation version of the Match! software [19]: the results of the peak assignations can be seen in table 4.7. Except for the 22.4° peak seen in the MgO sample, all the rest of the peaks cannot be assigned to reflections corresponding to CoO or Co_3O_4, and even in the case of the MgO sample, the intensity of that peak is very small: this means that these samples are highly amorphous. These are powder diffractograms, so reflections coming from the orientation of the single crystal substrates are not expected: the fact that the rest of the peaks seen in them can be assigned to substrate features means that either the substrates are not as well oriented as expected, or that the atmosphere and/or the cobalt oxide depositions are inducing small modifications to their surface. Nevertheless, the small crystallinity observed in the MgO sample is another argument in favour of their greater stability when compared with the samples grown on the other two substrates.

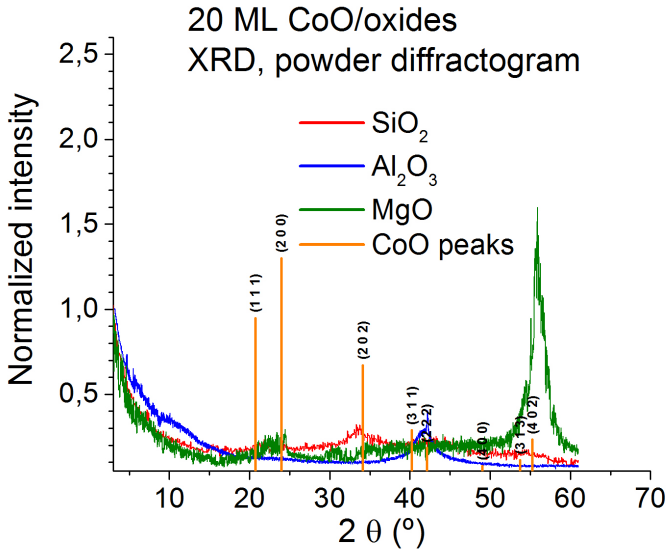

Figure 4.18: Powder diffractograms for the 20 ML samples of CoO grown on the three different oxides, after three months of exposure to room conditions. The orange lines indicate the expected positions of the peaks for a CoO structure.

Substrate	Peak (°)	Assignation
SiO_2	33.7	SiO_2, (1 2 1) reflection.
Al_2O_3	42	Gibbsite ($Al(OH)_3$), multiple reflections.
MgO	24.4	CoO, (2 0 0) reflection.
	56	MgO, (4 0 2) reflection.

Table 4.7: Results of the peak assignation of the powder diffractograms shown in figure 4.18.

4.4.1.3 XANES Co 1s spectra

In the next two subsubsections, the results of the XAS measurements of the Co 1s region for samples grown on the three oxide substrates will be presented. It was chosen as our main structural characterization technique because of the amorphous structure seen in the XRD diffractograms presented in the last subsubsection: as it was stated in section 3.4 (page

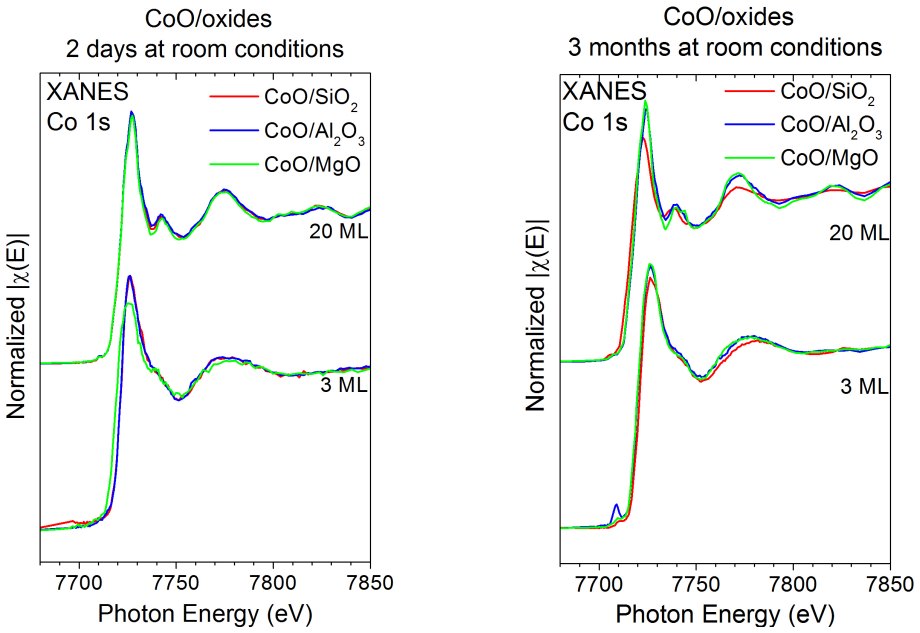

(a) Samples exposed for 2 days at room conditions.

(b) Samples exposed for 3 months at room conditions.

Figure 4.19: XANES spectra of the 3 and 20 ML samples of CoO grown on the three oxide substrates, after being exposed for (a) 2 days and (b) two months to room conditions.

73), this technique is ideal to study samples with this level of amorphization. Samples with coverages of 3 and 20 ML were exposed to room conditions for 2 days and three months. The measurements were performed in two different beamtimes at the BM 25 beamline of the ESRF synchrotron (Grenoble, France): more details about these measurements can be found in subsection 3.4.3 (page 77). All the samples were grown at the GRIN laboratory: the samples exposed for two days were kept in low vacuum conditions until the measurements, while the samples exposed for three months were left at room conditions since they were grown.

Figure 4.19 shows the XANES spectra taken for both sets of samples. All the 20 ML spectra have roughly the same shape and features reported in the bibliography for bulk CoO [20]: a main line at 7726 eV, a very small prepeak at ∼7710 eV, and a structure composed by defined oscillations for energies above the main line. The spectra show important changes from the 3 to the 20 ML samples: the oscillations above the main line appear broader and less defined. This difference is attributed to the low dimensionality of the analysed material, something that has also been observed in previous studies of NiO made by our group [21]. In the case of NiO, those spectra also showed similar differences depending on the coverage: theoretical multiple scattering calculations [22, 23] allowed us to simulate the experimental spectra with lower size clusters, giving a very good agreement with the experimental NEXAFS spectra.

Now we will focus on the evolution of the Co 1s XANES spectra with the air exposure time. Although the majority of the samples do not show great changes at a first glance, there are two samples that need to be commented. The spectrum corresponding to the 20 ML sample of CoO grown on SiO_2 shows a lessening of the oscillations intensity after the main line with

the exposure time, which is related to possible changes in the structure or the composition of these layers. Meanwhile, the spectrum corresponding to the 3 ML sample grown on Al_2O_3 shows the appearance of a prepeak at ~7710 eV in the sample exposed to air for three months, with roughly the same energy than that of the bulk CoO, but with a much higher intensity. This high intensity of the prepeak has been assigned in the literature to Co atoms tetrahedrally coordinated [24, 25] in the spectra for $CoAl_2O_4$. According to this, XANES seems to indicate the formation of $CoAl_2O_4$ at the CoO/Al_2O_3 interface. It is important to note that Co atoms in both CoO and $CoAl_2O_4$ are in the form of Co^{2+}, thus the XPS spectra have been only able to observe the cobalt atoms that has this oxidation state, without differentiating between CoO or $CoAl_2O_4$ (we remind the reader that a small percentage of cobalt hydroxide was also detected in the XPS analysis of these samples), whereas the high sensitivity to the local symmetry of XANES has allowed to detect the formation of the binary oxide at the CoO/Al_2O_3 interface. Therefore we can conclude that air exposure somehow promotes the formation of $CoAl_2O_4$ at the CoO/Al_2O_3 interface, while similar binary oxides have not been detected at the interfaces of the other 3 ML samples. However, it is important to stress out that this is a hypothesis, and more measurements are necessary to confirm it.

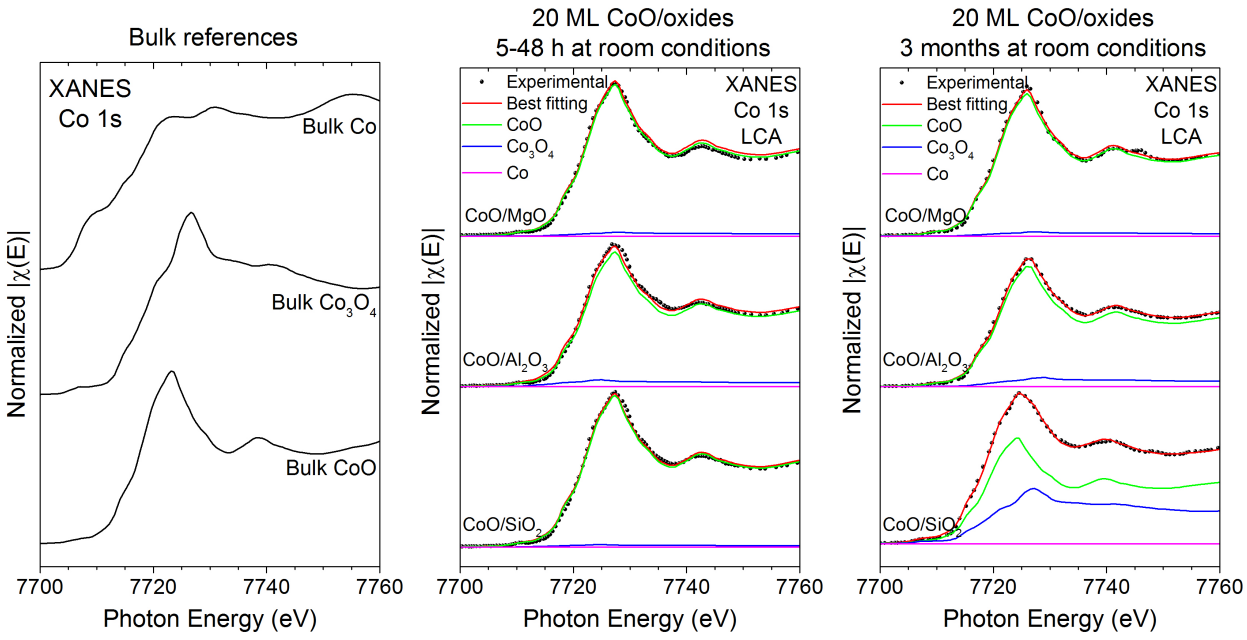

(a) CoO, Co_3O_4 and Co reference spectra

(b) Samples exposed for 2 days at room conditions.

(c) Samples exposed for 3 months at room conditions.

Figure 4.20: Results of the linear combination of the XANES Co 1s spectra of the 3 and 20 ML samples of CoO grown on the three substrates: (a) bulk CoO, Co_3O_4 and Co spectra used in these calculations. After being exposed for (b) 2 days and (c) two months exposed to room conditions.

The composition of the 20 ML samples was checked with linear combinations of three reference XANES spectra of the Co 1s region for bulk CoO, Co_3O_4 and Co samples, displayed in figure 4.20a. Linear combinations were made in order to fit the experimental data as best

Room conditions time	Substrate	% CoO	% Co_3O_4	% Co
2 days	SiO_2	97.94	2.06	0
	Al_2O_3	94.07	5.93	0
	MgO	97.08	2.92	0
3 months	SiO_2	62.46	37.54	0
	Al_2O_3	92.04	7.96	0
	MgO	96.60	3.40	0

Table 4.8: Compositions found in the LCA analysis of the XANES Co 1s spectra of the 20 ML samples of CoO grown on the three oxide substrates.

as possible. The XANES Co 1s spectra of bulk cobalt hydroxide was not used because of its similarities with the CoO spectra [26]. The results of these calculations are shown in figures 4.20b and 4.20c, and table 4.8 displays the compositions found with this analysis for all the samples. These calculations were not made on the 3 ML samples because of the changes in these spectra caused by the low dimensionality of the grown CoO samples.

All the samples show a majority of CoO, with varying percentages of Co_3O_4 depending on the substrate and the exposition time. The samples grown on SiO_2 have only a 3 % of Co_3O_4 after two days, but this percentage grows up to a 37 % after three months, which means that the samples grown on this substrate are not very stable after being exposed to room conditions for long times. The changes in the composition of this sample seen by XPS and XANES can be explained by two factors: the different air exposition time of the samples measured by both techniques, and the different sampling depth of XPS ($\sim$2 nm) and XANES ($\sim$0.1-10 μm in fluorescence mode). The results obtained by both techniques suggests that cobalt hydroxide grows initially on the sample surface, and after a longer exposition time, Co_3O_4 starts appearing throughout the whole volume of the sample.

Meanwhile, the samples grown on the other two substrates do not show a great change in their composition after three months: the percentage of Co_3O_4 on the sample grown on Al_2O_3 increases from a 6 to an 8 %, while the sample grown on MgO has almost the same 3 % of Co_3O_4 content for the two times explored. The lower Co_3O_4 content of the sample grown on MgO, in addition to its slower growth over time, confirms our previous hypothesis that this substrate is the most suitable to grow stable CoO samples.

4.4.1.4 EXAFS spectra of the Co 1s region, two days of exposure to air

The full range of the EXAFS signal was also measured for the 3 and 20 ML samples exposed to air conditions during 48 hours, in order to have some structural information about these layers: they are shown in figure 4.21, with the EXAFS region highlighted. The spectra corresponding to the 3 ML samples do not meet enough statistics to perform a successful analysis, due to the low amount of material deposited to obtain a good signal to noise ratio in fluorescence mode, and an analysis of the EXAFS signal will be only performed in the 20 ML samples spectra.

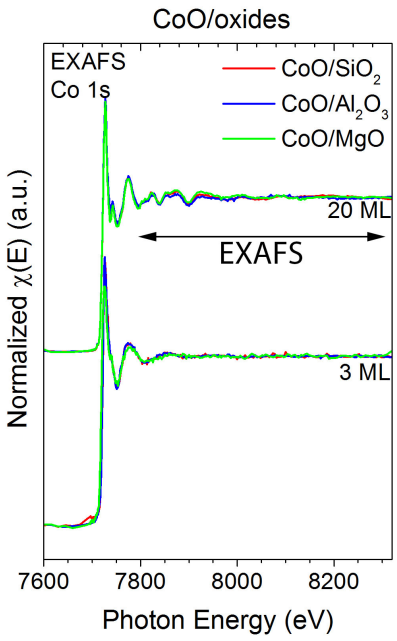

Figure 4.21: XAS Co 1s spectra for the 3 and 20 ML samples of CoO grown on the three oxide substrates after being exposed to room conditions for 48 hours. The EXAFS part of the spectra is highlighted.

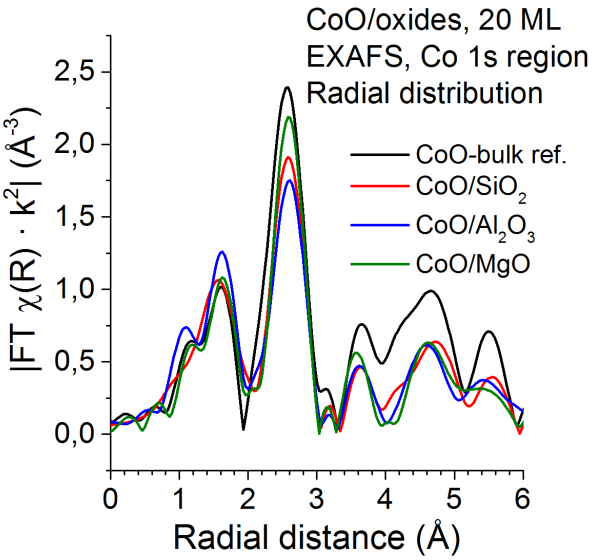

Figure 4.22: Radial distribution of the EXAFS signal obtained in the measurement of the 20 ML samples of CoO grown on the three oxide substrates. The distribution is weighted to k^2 order.

Figure 4.22 shows the radial distribution (i.e., the Fourier transform of $\chi(E)$) of the 20 ML samples: the CoO reference spectra has also been plotted as a reference. The region until ∼3.2 Å belongs to the single-scattering paths described in table 3.4 of section 3.4.3 (page 78): all the rest of the peaks above it belong to multiple-scattering paths, and will not be studied in this work. In the spectra, a first set of peaks can be clearly distinguished, located roughly at ∼1.6 Å: they correspond to Co-O bonds. A second and more intense peak, located at ∼2.6 Å, corresponds to Co-Co bonds: they have a larger intensity with respect to the first set because of the higher degeneracy of the second shell (12 Co atoms in the second shell versus 6 O atoms in the first shell). These spectra show an interesting trend at a first glance: the intensity of the peaks corresponding to the CoO/MgO sample is closer to that of the CoO bulk reference than those coming from the other two oxide substrate samples (this is specially noticeable in the 2.6 Å peak). The intensity of these peaks is related to the degeneracy/coordination number and the Debye-Waller factor, so we can expect a variation of the main parameters of the fittings that follows this trend.

We will now discuss the result of the EXAFS fittings, which are displayed in figure 4.23. These fittings were made in the region belonging to the two first coordination shells, and using the two single-scattering paths shown in table 3.4 (page 78). The noise of the experimental data was considered low, so analysis with more paths and a wider window can be performed,

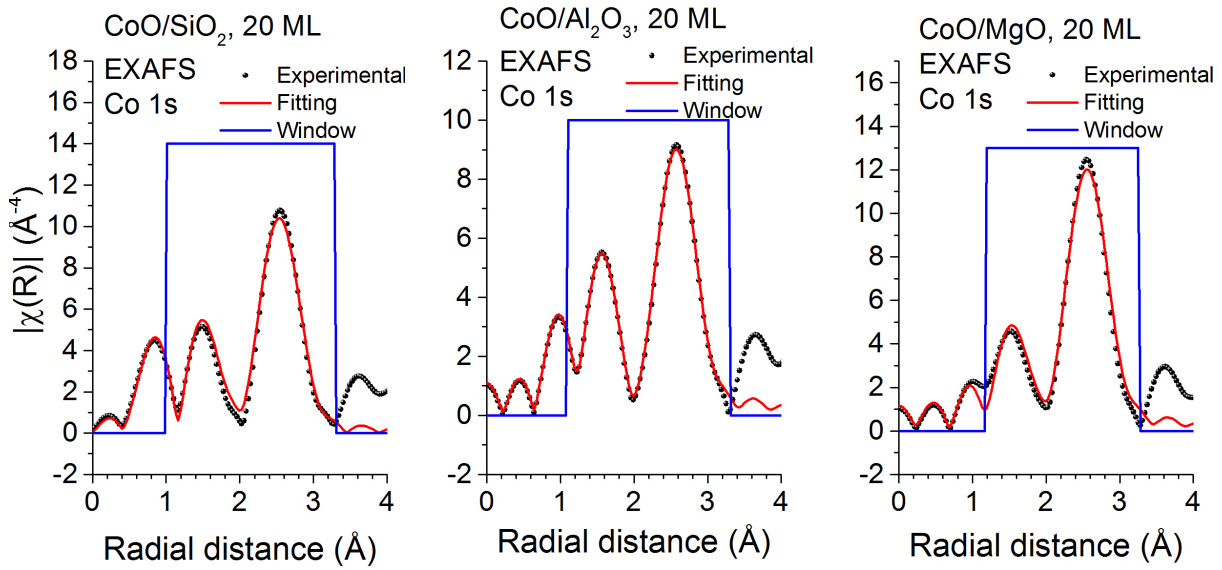

(a) CoO/SiO_2 (b) CoO/Al_2O_3 (c) CoO/MgO

Figure 4.23: Fittings of the radial distribution of the EXAFS signal obtained in the measurement of the 20 ML samples of CoO grown on the three oxide substrates.

	N		ΔR (Å)		σ^2 (Å^3)	
Sample	1st	2nd	1st	2nd	1st	2nd
CoO/SiO_2	7.87± 0.06	10,04±0.08	2,129±0.005	2,99±0.02	0,011±0.001	0,013±0.001
CoO/Al_2O_3	6,87±0.09	8,36±0.05	2,098±0.008	3,01 ±0.01	0,009±0.001	0,012±0.002
CoO/MgO	6,50±0.04	10,52±0.08	2,13±0.01	3,011±0.007	0,009±0.001	0,012±0.001
CoO-ref.	6	12	2.133	3.017	0.007	0.011

Table 4.9: EXAFS parameters obtained in the fittings of the 20 ML samples of CoO on the oxide substrates. 1st and 2nd refers to the values obtained for the first and second coordination shells, respectively.

but at this time only these relatively simple analysis with single-scattering paths have been completed: a more in-depth analysis remain as an open problem for the future.

The parameters obtained in these fittings are displayed in table 4.9. These parameters confirm our previous assumptions about their behaviour: the sample with parameters closer to the CoO reference is the 20 ML CoO/MgO sample, while the other two samples parameters have higher deviations with respect to the reference. The Debye-Waller parameter is higher on the CoO/SiO_2 sample, which is logical if we take into account that the initial morphology of this growth was clustered, and therefore, more disordered. However, the most important feature that these fittings reveal is an oxygen excess on the first shell of coordination, and a Co defect on the second one. As a way to check the origin of this disagreement, the compositions obtained on the linear combination of the XANES spectra can be used to estimate the number of oxygen ions coming only from the cobalt oxides deposited, considering that each Co ion has six oxygen first neighbours in the CoO structure, and eight on the Co_3O_4. This calculation, along with the values obtained in the EXAFS fittings and the compositions calculated in the linear combination of the XANES spectra, are shown in table 4.10.

Substrate	**Composition**		**1st oxygen neighbours**	
	% CoO	**% Co_3O_4**	**EXAFS**	**XANES**
SiO_2	97.94	2.06	7.87	6.04
Al_2O_3	94.07	5.93	6.87	6.11
MgO	97.08	2.92	6.50	6.05

Table 4.10: Comparison between the number of oxygen neighbours in the 1st shell of coordination, as obtained from the EXAFS fittings, and the calculation from the composition of the samples obtained in the linear combination of the XANES spectra.

The comparison between these values tell us that this oxygen excess can not be explained only with the formation of Co_3O_4. This means that this excess oxygen is not bonded to cobalt forming either one of the cobalt oxides, so it can be assumed that it is somehow free inside or in-between the CoO structure. The values obtained for this oxygen excess are smaller for the MgO and Al_2O_3 than for the SiO_2 substrate, something that is in agreement to the oxidation state change seen in the in-situ XPS measurements of the growth: the spectra for coverages around 75 ML (the highest coverage deposited on MgO) showed a shape similar to the one assigned to the CoO grown on the MgO and Al_2O_3 substrates, while the spectra of the growth on SiO_2 clearly showed the features of Co_3O_4. This result is also congruent with the small crystallinity of the sample grown on MgO seen in the XRD powder diffractograms: if these samples have a small percentage of crystallinity, they will admit less extra oxygen in their structure, and the number of first neighbours will be closer to that of the stochiometric CoO. All of these evidences lead us to propose this oxygen excess as the reason behind the oxidation state change seen in the in-situ study of the growth for coverages larger than 40 ML. Indeed, if we are depositing oxygen at the same time as cobalt oxide in our samples, the total quantity of oxygen will grow with the coverage and deposition time, until the oxygen quantity will be too large for the CoO structure to be stable, thus provoking the growth of Co_3O_4 instead of CoO.

4.4.2 Stability upon thermal annealing

The second study of the stability of these samples was done by growing some CoO samples with different coverages on the three substrates, and then, thermally oxidizing them by the Reox-P1 process (section 2.3.3, page 51), measuring them before and after this process by XPS and AFM. For the morphological characterization of the possible changes of these samples after the Reox-P1 process, 2 and 10 ML CoO coverages (considered low and high enough coverages, given all the phenomena observed in the study of the growth of CoO) were grown on the three substrates and measured by AFM after Reox-P1: the results are displayed in figure 4.24, and their roughness given by the R_q values are displayed in table 4.11.

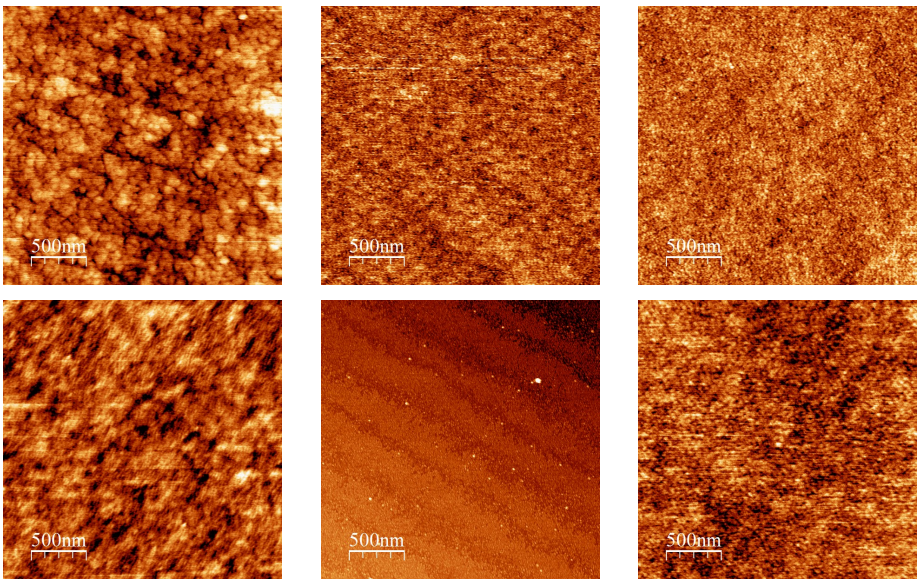

(a) SiO_2 (b) Al_2O_3 (c) MgO

Figure 4.24: AFM topography images of the CoO samples grown on the three substrates after the Reox-P1 process. Substrate as labelled. Coverages: top row, 2 ML; bottom row, 10 ML. Size of all the images: 2.5 µm × 2.5 µm.

Substrate	Coverage (ML)	R_q (nm)
SiO_2	2	0.30±0.05
	10	0.24±0.04
Al_2O_3	2	0.22±0.07
	10	0.88±0.05
MgO	2	0.4±0.1
	10	0.25±0.03

Table 4.11: R_q values obtained in the analysis of the AFM images of the 2 and 10 ML samples of CoO grown on the three oxide substrates after the Reox-P1 process.

All samples grown on MgO and Al_2O_3 show morphologies similar to their non-reoxidized partners: layers that seem to respect the substrate morphology. The 10 ML CoO/SiO_2 sample also has this morphology, but the image of the 2 ML sample shows clusters that have an average height of ∼4 Å. The R_q values are a little higher than their corresponding as-grown coverage partners, although they are still very low.

We studied by XPS the possibility of some loss of material after the Reox-P1 process, either because of desorption or diffusion into the substrate. Figure 4.25 shows the surveys for 2 ML samples before and after this process, and the insets shows the normalized (with respect to the minimum value) Co 2p region spectra. They show roughly the same global intensity of the Co peaks observed for all the samples, which means that no cobalt is being desorbed of diffused into the substrate structure as a result of the treatment.

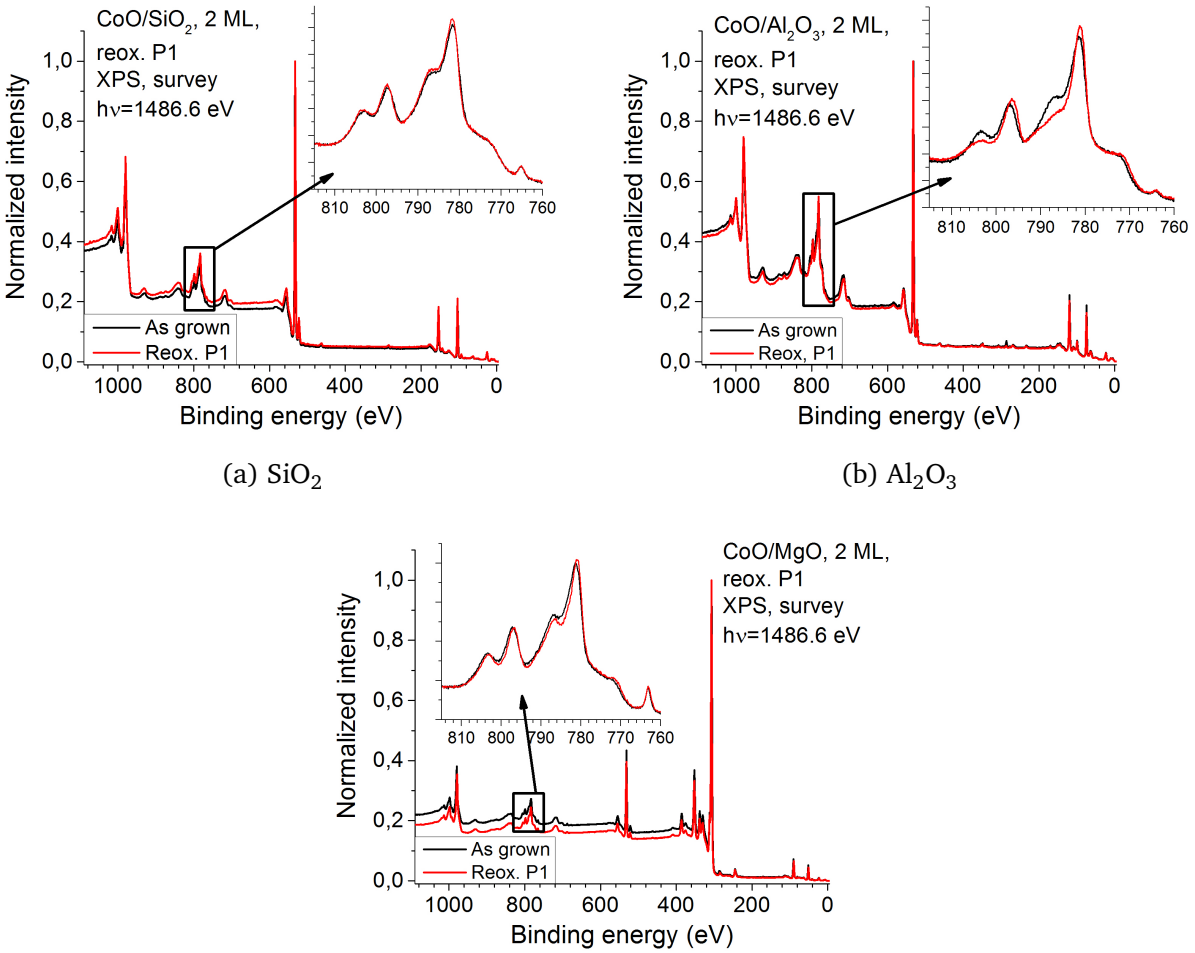

(a) SiO_2

(b) Al_2O_3

(c) MgO

Figure 4.25: Normalized XPS survey spectra of 2 ML samples of CoO grown on the three oxide substrates, before (black line) and after (red line) the Reox-P1 process. Inset shows the Co 2p region spectra, normalized with respect to the value at 760 eV. Substrate as labelled.

The XPS measurements of samples with coverages from 1 to 10 ML after being subjected to the Reox-P1 process are shown in figure 4.26. From the satellite structure and peak energies, it can be concluded that the samples grown on MgO keep the Co^{2+} oxidation state in its majority for coverages up to 4 ML, the samples grown on SiO_2 keep it up to 2 ML, and those grown on Al_2O_3 change to Co_3O_4 from the first coverage explored.

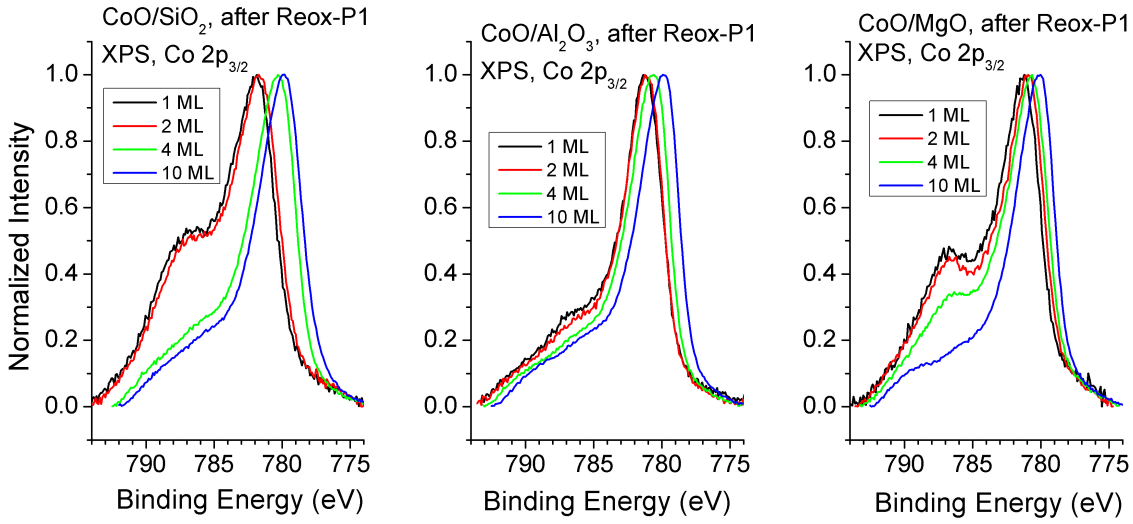

(a) SiO_2 (b) Al_2O_3 (c) MgO

Figure 4.26: Normalized XPS Co $2p_{3/2}$ spectra of CoO samples grown on the three oxide substrates after the Reox-P1 process. A Shirley background has been removed in all of them. Coverages and substrates as labelled.

This changes in the oxidation state with the coverage and the substrate can be explained in terms of the morphology and crystal structure of the CoO and the substrates. As in the case of the room conditions stability, it makes sense that the samples grown on MgO are the most stable after the Reox-P1 process, since the lattice mismatch between the CoO and MgO lattices is the lowest of all the interfaces studied in this work, the CoO deposits have a small percentage of crystallinity, and it has already been proven that they are the most stable under room conditions. Meanwhile, the data extracted from the room exposure study of the samples grown on Al_2O_3 has shown that they are not as stable as the samples grown on MgO, so it is logical that under more aggressive conditions, these samples change their oxidation state.

Meanwhile, the stability of the samples with coverages below or equal to 2 ML grown on SiO_2 can be explained in terms of their morphology. For coverages below or equal to this, the samples are nanoparticles, which have a higher surface energy, and are therefore more resistant to oxidation state changes. This is supported by the AFM images of the 2 ML coverages, which showed that the samples still conserve their original nanostructured morphology: this proves that the surface energy of these nanoparticles is a very important factor in their stability. For higher coverages, this morphology changes to extended islands or even layers, and the reduction of the surface energy causes this samples to lose their stability, changing their oxidation state to Co_3O_4 after the Reox-P1 process.

4.4.3 Summary

The study of the stability of these samples under air conditions and after a thermal oxidizing process has given us two major conclusions. The first one is that the most suitable substrate to grow stable CoO samples is MgO: the samples grown on this substrate show the less growth of Co_3O_4 and cobalt hydroxide over time, they do not reoxidize to Co_3O_4 after the thermal reoxidation process (labelled as Reox-P1) if their coverage is below 4 ML, and they are the only samples that show a small percentage of crystallinity in the 20 ML XRD powder diffractograms. The crystal structures of CoO and MgO are equal, and their lattice parameters only have a 0.01 % of mismatch, so it is logical that the more resistant layers are grown on this substrate. It has also been shown that the layers grown on the Al_2O_3 do not show a great percentage of Co_3O_4 growth over time, but they are not so stable as the samples grown on MgO. First, the CoO grown on this substrate reoxidizes to Co_3O_4 after the Reox-P1 process; and second, a prepeak appears after three months at room conditions, which it has been interpreted as the appearance of $CoAl_2O_4$ at the CoO/Al_2O_3 interface. Finally, the study of the samples grown on SiO_2 have given signs of the growth of cobalt hydroxide after a month at room conditions, and have also shown the greater growth of Co_3O_4 when exposed for three months (37 % after three months for the 20 ML coverage), but the samples with coverages below or equal to 2 ML have been shown to be stable after the thermal oxidation process. This has been interpreted in terms of the morphology of these samples: the AFM images for coverages below 2 ML showed that the material was distributed in the form of nanoparticles, which have a great surface energy, and gives them more resistance to oxidation state changes. Once this morphology is lost (for coverages above 2 ML, the material grows as more extended islands), this surface energy is lower, and the samples lose their stability.

The other major conclusion has been extracted from the study of the EXAFS signal for the 20 ML samples exposed to room conditions for two days. An oxygen excess has been detected in the first sphere of coordination, which has been proven not to come from the growth of Co_3O_4. It has been proposed that this oxygen is being deposited at the same time as the CoO, and that it is the key behind the oxidation state change for high coverages seen in the in-situ study of the growth of cobalt oxides: the structure of the deposited samples will accumulate oxygen until its quantity is too large for the CoO to be stable, and will trigger the appearance of Co_3O_4.

SECTION 4.5

Conclusions

In this chapter, we have presented all the results obtained in this work about the growth and chemical stability of ultra-thin cobalt oxide samples deposited on oxides substrates with different covalent/ionic ratios (SiO_2, Al_2O_3 and MgO). The chemical analysis of the growth has been characterized by in-situ XPS measurements, and has revealed that, on all substrates, the material starts growing as CoO (Co^{2+}) up to coverages of about 40 ML, while larger coverages give rise to the formation of Co_3O_4 on the growth on SiO_2 and Al_2O_3. Some unoxidized cobalt has also been found in the lowest coverages of the growth on SiO_2, which has been explained in

terms of the different coordination of CoO and SiO_2, and the possible presence of O_2 vacancies on the SiO_2 substrate. The study of the morphology of the growth by AFM and XPS-IPSA has revealed two main ways of growth: the material follows a Volmer-Weber (i.e. islands formation) growth mode in the SiO_2 substrate, whereas for Al_2O_3 and MgO the growth follows a Frank-Van der Merwe (i.e. layer-by-layer) mode. From this, it has been concluded that CoO adatoms have stronger interaction with Al_2O_3 and MgO surfaces than with SiO_2. The mismatch of the lattice parameter between the CoO deposits and those of the substrate has been proposed to be the main reason behind the two different growth modes seen on SiO_2 and MgO, while the growth of CoO samples oriented on the fcc-(1 1 1) planes (as seen in theoretical DFT calculations) has been proposed to be the reason behind the layer-by-layer growth of CoO on Al_2O_3.

The CoO/oxide interfaces have been studied by fittings of the XPS Co $2p_{3/2}$ spectra. The analysis of the variation of the binding energy of the main photoemission line peak has revealed a general shift for coverages below 5 ML, which has been attributed to extra-atomic relaxation effects. Also, a shift of $\sim$0.7 eV has been seen for the growth on Al_2O_3: previously published theoretical calculations of this interface predicted a charge transfer from the substrate to the CoO nanolayers, and this shift constitutes an experimental proof of this theoretical prediction. The variations on the relative intensity and position of the shake-up satellite peak (with respect to the main line photoemission peak) have also been studied, since theoretical cluster calculations of the XPS Co $2p_{3/2}$ spectra for different pdσ values have linked them to variations the ionic-covalent character of the CoO bonds. It has been demonstrated that the ionicity of the substrates is not the relevant factor in these variations: the morphology of the deposited materials, which is mainly dictated by the structural parameters of the substrates, has been shown to be the key factor in the changes of the ionic-covalent character of the bonds in the deposited CoO samples.

Finally, the chemical and morphological stability of these CoO layers has been tested in two different environments: room conditions and after a thermal oxidation process (labelled as Reox-P1). Aside from the growth of Co_3O_4 and $Co(OH)_x$ after room exposure, this study has yielded two major conclusions: MgO is the most suitable substrate to grow stable CoO nanolayers, and an oxygen excess has been detected in the 20 ML CoO samples after 2 days at room conditions, which has been proposed to be the reason behind the oxidation state change seen for large coverages in the in-situ measurements of the growth.

SECTION 4.6

Bibliography

[1] A. FUJIMORI and F. MINAMI. "Valence-band photoemission and optical absorption in nickel compounds". *Physical Review B* 30 (2 July 1984), pp. 957–971. DOI: 10.1103/PhysRevB.30.957.

[2] J. VAN ELP, J. L. WIELAND, H. ESKES, P. KUIPER, G. A. SAWATZKY, F. M. F. DE GROOT, and T. S. TURNER. "Electronic structure of CoO, Li-doped CoO, and $LiCoO_2$". *Physical Review B* 44 (12 Sept. 1991), pp. 6090–6103. DOI: 10.1103/PhysRevB.44.6090.

[3] K. OKADA and A. KOTANI. "Complementary Roles of Co 2 p X-Ray Absorption and Photoemission Spectra in CoO". *Journal of the Physical Society of Japan* 61.2 (1992), pp. 449–453. DOI: 10.1143/JPSJ.61.449.

[4] V. M. JIMÉNEZ, J. P. ESPINÓS, and A. R. GONZÁLEZ-ELIPE. "Control of the stoichiometry in the deposition of cobalt oxides on SiO_2". *Surface and Interface Analysis* 26.1 (1998), pp. 62–71. DOI: 10.1002/(SICI)1096-9918(199801)26:1<62::AID-SIA349>3.0.CO;2-R.

[5] S. C. PETITTO, E. M. MARSH, G. A. CARSON, and M. A. LANGELL. "Cobalt oxide surface chemistry: The interaction of CoO(1 0 0), Co_3O_4(1 1 0) and Co_3O_4(1 1 1) with oxygen and water". *Journal of Molecular Catalysis A: Chemical* 281.1-2 (2008), pp. 49–58. DOI: 10.1016/j.molcata.2007.08.023.

[6] M. C. BIESINGER, B. P. PAYNE, A. P. GROSVENOR, L. W.M. LAU, A. R. GERSON, and R. ST.C. SMART. "Resolving surface chemical states in XPS analysis of first row transition metals, oxides and hydroxides: Cr, Mn, Fe, Co and Ni". *Applied Surface Science* 257.7 (2011), pp. 2717–2730. DOI: 10.1016/j.apsusc.2010.10.051.

[7] DISSEMINATION OF IT FOR THE PROMOTION OF MATERIALS SCIENCE (DOITPOMS), UNIVERSITY OF CAMBRIDGE. *The interactive Ellingham diagram*. URL: http://www.doitpoms.ac.uk/tlplib/ellingham_diagrams/interactive.php.

[8] V. A. GUBANOV, A. F. ZATSEPIN, V. S. KORTOV, S. P. FREIDMAN, and G. B. CHERLOV. "Electronic structure of oxygen-vacancy defects in silicon dioxide". English. *Journal of Applied Spectroscopy* 49.1 (1988), pp. 741–745. DOI: 10.1007/BF00662917.

[9] J. F. MOULDER, W. F. STICKLE, P. E. SOBOL, and K. D. BOMBEN. *Handbook of X-ray Photoelectron Spectroscopy*. Ed. by JILL CHASTAIN. Perkin-Elmer Corporation, 1992. ISBN: 0855012080.

[10] E. PAPARAZZO. "XPS analysis of oxides". *Surface and Interface Analysis* 12.2 (1988), pp. 115–118. DOI: 10.1002/sia.740120210.

[11] R. HOOGEWIJS, L. FIERMANS, and J. VENNIK. "Electronic relaxation processes in the KLL' auger spectra of the free magnesium atom, solid magnesium and MgO". *Journal of Electron Spectroscopy and Related Phenomena* 11.2 (1977), pp. 171–183. DOI: 10.1016/0368-2048(77)85108-6.

[12] F. CUCCUREDDU, S. MURPHY, I. V. SHVETS, M. PORCU, H. W. ZANDBERGEN, N. S. SIDOROV, and S. I. BOZHKO. "Surface morphology of c-plane sapphire (α-alumina) produced by high temperature anneal". *Surface Science* 604.15-16 (2010), pp. 1294–1299. DOI: 10.1016/j.susc.2010.04.017.

[13] A. ZAYED, A. M. MÁRQUEZ, and J. F. SANZ. "Nanosized CoO Films on the α-Al_2O_3 (0001) Surface: A Density Functional Study". *The Journal of Physical Chemistry C* 117.44 (2013), pp. 22714–22722. DOI: 10.1021/jp406016z.

[14] Y. WU, E. GARFUNKEL, and T. E. MADEY. "Initial stages of Cu growth on ordered Al_2O_3 ultrathin films". *Journal of Vacuum Science & Technology A: Vacuum, Surfaces, and Films* 14.3 (May 1996), pp. 1662–1667. DOI: 10.1116/1.580315.

[15] J. A. RODRIGUEZ, R. A. CAMPBELL, and D. W. GOODMAN. "Interaction of ultrathin films of copper with rhodium(100) and ruthenium(0001): an XPS study". *The Journal of Physical Chemistry* 95.6 (1991), pp. 2477–2483. DOI: 10.1021/j100159a068.

[16] M. B. LEE, J. H. LEE, Y. H. LEE, J. H. LEE, and S. H. HAHM. "Extra-Relaxation Effects in Ultra-Thin Al2O3 Films on Metal Substrates". *Journal of the Korean Physical Society* 35.6 (1999), pp. 482–491. DOI: 10.3938/jkps.35.482.

[17] L. SORIANO, M. SÁNCHEZ-AGUDO, R. J. O. MOSSANEK, M. ABBATE, G. G. FUENTES, P. R. BRESSLER, L. ALVAREZ, J. MÉNDEZ, A. GUTIÉRREZ, and J. M. SANZ. "Interface effects in the electronic structure of TiO_2 deposited on MgO, Al_2O_3 and SiO_2 substrates". *Surface Science* 605.5-6 (2011), pp. 539–544. DOI: 10.1016/j.susc.2010.12.013.

[18] I. PREDA, A. GUTIÉRREZ, M. ABBATE, F. YUBERO, J. MÉNDEZ, L. ALVAREZ, and L. SORIANO. "Interface effects in the Ni 2p X-ray photoelectron spectra of NiO thin films grown on oxide substrates". *Physical Review B* 77 (7 Feb. 2008), p. 075411. DOI: 10.1103/PhysRevB.77.075411.

[19] CRYSTAL IMPACT GBR. *Match! Phase identification from powder diffraction.* URL: http://www.crystalimpact.com/match/.

[20] G. PELECKIS, X. L. WANG, R. S. LIU, and S. X. DOU. "Co valence by K-edge X-ray absorption spectroscopy, magnetic properties, and structure of polycrystalline bulk $Zn_{1-x}Co_xO$". *Magnetics, IEEE Transactions on* 41.10 (Oct. 2005), pp. 2727–2729. DOI: 10.1109/TMAG.2005.854689.

[21] I. PREDA, L. SORIANO, D. DÍAZ-FERNÁNDEZ, G. DOMÍNGUEZ-CAÑIZARES, A. GUTIÉRREZ, G. R. CASTRO, and J. CHABOY. "X-ray absorption study of the local structure at the NiO/oxide interfaces". *Journal of Synchrotron Radiation* 20.4 (2013), pp. 635–640. DOI: 10.1107/S0909049513012417.

[22] M. BENFATTO and S. DELLA LONGA. "Geometrical fitting of experimental XANES spectra by a full multiple-scattering procedure". *Journal of Synchrotron Radiation* 8.4 (July 2001), pp. 1087–1094. DOI: 10.1107/S0909049501006422.

[23] M. BENFATTO, J. A. SOLERA, J. CHABOY, M. G. PROIETTI, and J. GARCÍA. "Theoretical analysis of x-ray absorption near-edge structure of transition-metal aqueous complexes in solution at the metal *K* edge". *Physical Review B* 56 (5 Aug. 1997), pp. 2447–2452. DOI: 10.1103/PhysRevB.56.2447.

[24] A. M. BEALE and G. SANKAR. "Understanding the Crystallization of Nanosized Cobalt Aluminate Spinel from Ion-Exchanged Zeolites Using Combined in Situ QEXAFS/XRD". *Chemistry of Materials* 18.2 (2006), pp. 263–272. DOI: 10.1021/cm050797z.

[25] M. O. FIGUEIREDO, T. P. SILVA, and J. P. VEIGA. "A {XANES} study of cobalt speciation state in blue-and-white glazes from 16th to 17th century Chinese porcelains". *Journal of Electron Spectroscopy and Related Phenomena* 185.3-4 (2012), pp. 97–102. DOI: 10.1016/j.elspec.2012.02.007.

[26] R. MA, Z. LIU, K. TAKADA, K. FUKUDA, Y. EBINA, Y. BANDO, and T. SASAKI. "Tetrahedral Co(II) Coordination in α-Type Cobalt Hydroxide: Rietveld Refinement and X-ray Absorption Spectroscopy". *Inorganic Chemistry* 45.10 (2006). PMID: 16676955, pp. 3964–3969. DOI: 10.1021/ic052108r.

Chapter 5

Interaction of Cobalt oxides with graphite

SECTION 5.1

Introduction

This chapter is dedicated to the results obtained in the study of the growth and interaction of Co oxides on HOPG. This substrate was chosen because of its near-planar topography, surface long-range order and expected lower interaction with cobalt oxides (in comparison to the oxide substrates). It was also chosen because of the outstanding relevance of graphite and graphene-related studies, as it has been adequately stated in the introduction of this thesis.

This chapter will be structured in a similar way as the previous chapter: both, the growth of CoO and the stability under thermal oxidation conditions, will be analysed. The first sections will be dedicated to the study of the chemistry, morphology and interface effects of the as-grown samples. A good amount of these results will be extracted from in-situ measurements, like the XPS spectra of the growth experiment performed at the GRIN laboratory, or the PES and XAS spectra of the experiments made at the PM4 beamline of the BESSY synchrotron: the AFM images were taken ex-situ. Section 5.5 will be dedicated to the most relevant group of results of this whole thesis, where it will be seen that the thermal treatment of these as-grown samples creates a nanopatterning on the HOPG surface. It will be shown that our process has a higher efficiency than similar experiments performed in the last 30 years, and the reason behind this enhanced efficiency will be studied and explained. Finally, the stability on air conditions of the as-grown and reoxidized samples will be studied in section 5.6.

SECTION 5.2

Chemical analysis of the growth of cobalt oxides on graphite by XPS

5.2.1 Survey XPS spectra

The chemistry of the growth of CoO on HOPG has been studied with XPS and PES. The results of the XPS measurements performed in-situ at the GRIN lab will be the main source of information, while the PES measurements of the O 1s region (also performed in-situ) will give information about the origin of the peaks seen in those spectra.

Figure 5.1 shows the XPS survey spectra for all the steps explored in the successive evaporations experiment made in the GRIN laboratory. The energies of the most important peaks are summarized in table 5.1. These spectra show the expected features for the growth of cobalt oxides on HOPG. For the first coverages, only peaks that correspond to the substrate (C 1s and C KVV) are visible. Once the coverage is high enough, peaks belonging to the deposited material (Co 2p, Co LMM, O 1s, Co 3s and so on) start being noticeable, while the intensity of the substrate features decreases. For the largest coverage deposited (80 ML), only peaks that belong to cobalt oxides are visible, and the growth experiment was considered as finished after this stage. Aside from this, the most important conclusion about these spectra is that they do not show peaks that can be attributed to contamination. Stochiometry calculations have also been tried here, but wrong concentration ratios (Co/O relations of 2.1 for the 10 ML

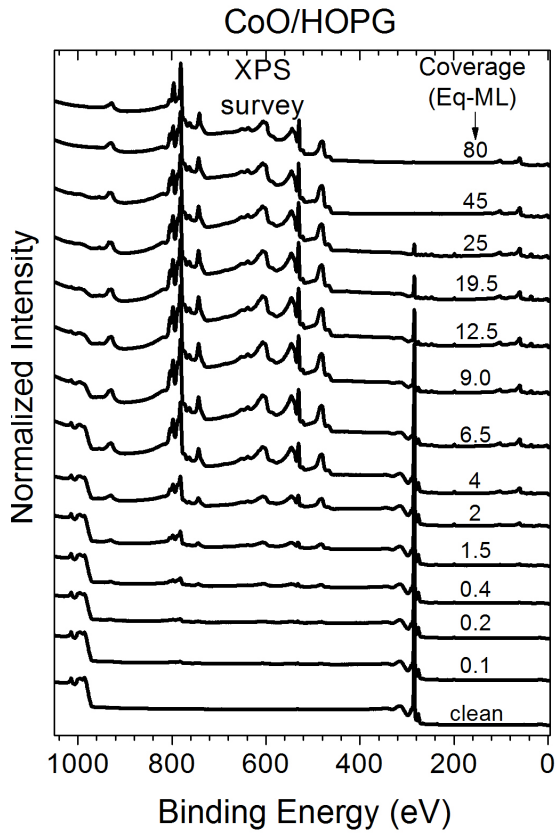

Figure 5.1: XPS survey spectra of the growth of cobalt oxides on HOPG. Coverage and substrate as labelled.

Peak	Energy (eV)
C KVV	990
Co 2s	928
Co 2p	781-779
O 1s	532-530
Co LMM	482
C 1s	284
Co 3s	103
Co 3p	60

Table 5.1: Binding energy of the most important peaks visible in the XPS survey spectra of the growth of cobalt oxides on HOPG.

sample, for example) were obtained for all the spectra analysed. Our explanation for this error lies in the proximity of the auger O KLL and Co 2p peaks, which causes shape and intensity distortions to the cobalt peaks.

5.2.2 Co $2p_{3/2}$ XPS spectra

The XPS Co $2p_{3/2}$ spectra for all the stages of the in-situ growth of cobalt oxides on HOPG are shown in figure 5.2. The spectra have roughly the same features as those obtained in the growths on oxide substrates. For almost all the coverages, they are composed by two peaks, one at ∼781 eV (labelled as "*main line*") and another at ∼787 eV (labelled as "*sat*"). The lowest coverages spectra show a main line shoulder at ∼778 eV, and the higher coverages feature a shape change of the *sat* peak and a shift of the *main line* peak towards lower binding energies. The comparison of these spectra with the theoretical cluster calculations for different Co oxidation states shown in chapter 4 allow us to state that the major oxidation states found in this growth are:

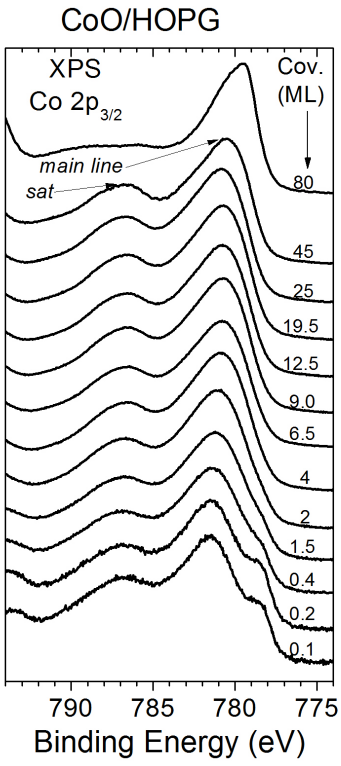

Figure 5.2: XPS Co $2p_{3/2}$ spectra for all the measured stages of the growth of CoO_x on HOPG.

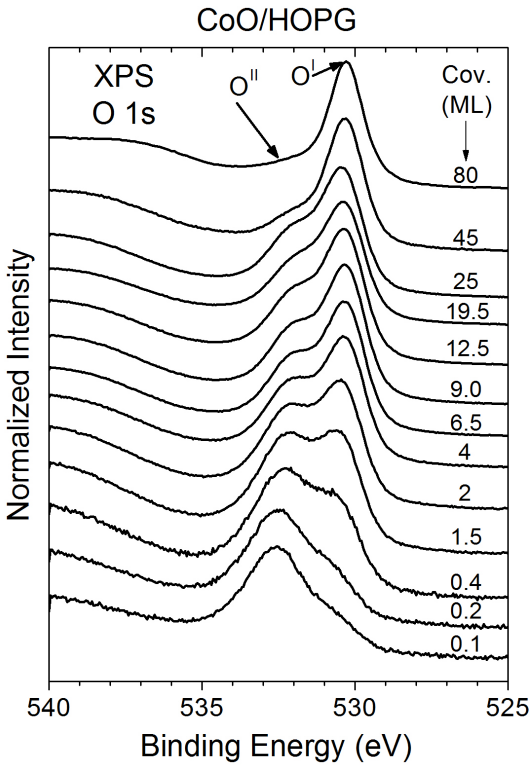

Figure 5.3: XPS O 1s spectra for all the measured stages of the growth of CoO on HOPG.

- <40 ML: CoO
- >40 ML: Co_3O_4
- <1 ML: Some percentage of unoxidized Co is also detected

The main results and the experimental conditions are similar to those in the growth on oxide substrates. Therefore, the reasoning made in subsubsection 4.2.1.2 (page 92) for the oxidation states found in those growths is also applicable here. The unoxidized Co seen in the lowest coverages can be attributed to the different coordinations of substrate and CoO, but it can also be caused by the reduction of CoO by the substrate. The graphite has a reducing behaviour with respect to the metal oxides, so it is plausible that some of the CoO can be reduced by the graphite [1].

5.2.3 O 1s XPS and PES spectra

The XPS O 1s spectra for the growth of cobalt oxides on HOPG are shown in figure 5.3. The spectra for all the coverages explored are formed by two peaks. The first one is located

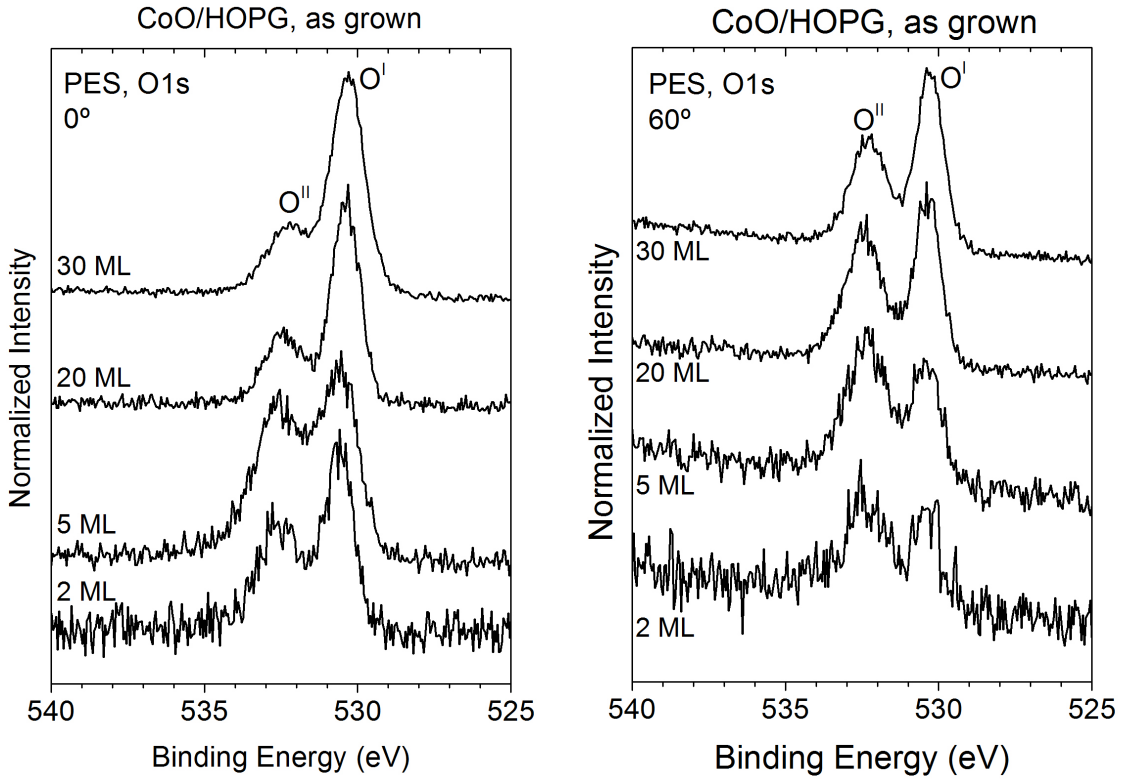

(a) Take-off angle=0°, $h\nu$=1000 eV.

(b) Take-off angle=60°, $h\nu$=600 eV

Figure 5.4: PES O 1s spectra of the growth of CoO on HOPG made in the PM4 beamline of BESSY synchrotron. Take-off angles and incident photon energies as labelled. The spectra marked with an asterisk have less resolution than the others.

at 530.5 eV (labelled as O^{I}), and belongs to the oxygen from the CoO bulk lattice. The second peak is located at 532.5 eV (labelled as O^{II}), and its intensity decreases with the coverage.

The O 1s region was also measured by PES in two beamtimes granted at the PM4 Beamline of the BESSY synchrotron. For these experiments, four samples of CoO were grown on HOPG with the same deposition rate used in the growths made in our laboratory, and then measured in-situ. As explained in subsection 3.1.5 (page 66), the PES measurements were made with two basic configurations in mind: one where the bulk effects would be more prominent (take-off angle=0°, $h\nu$=1000 eV) and another where only the most superficial layers would be probed (take-off angle=60°, $h\nu$=600 eV). All the important experimental data of these measurements, including their sampling depth, have been displayed in table 3.1 (page 67).

The results of the PES measurements of the O 1s spectra are shown in figure 5.4. The spectra are composed of the same O^{I} and O^{II} peaks seen in the XPS spectra, and it can be seen that the intensity of the 532.5 eV peak decreases with the coverage, but it is higher in the 60° spectra.

The origin of the O^{I} peak is clear, but the assignment of the O^{II} is not so apparent. Similar

results have been obtained in previous XPS measurements of NiO growths on HOPG [2], where this peak was assigned to the most superficial oxygen atoms at the NiO surface. In this case for CoO, the binding energy of this peak, its evolution with the coverage and the crystal lattice are similar, so it seems reasonable to make the same assignment for the O^{II} peak, since the intensity changes of the O^{II} peak with the take-off angle in the PES spectra confirm its superficial nature. However, other explanations for this peak, such as absorbed oxygen on top of the CoO surface, cannot be discarded without additional experiments.

5.2.4 Summary

The study of the chemistry of the growth of cobalt oxides on HOPG has been performed by means of in-situ XPS and PES measurements. The comparison of the XPS Co $2p_{3/2}$ region spectra with the cluster calculations made for different Co ions has yielded that the main cobalt oxide found during the growth is CoO. Co_3O_4 is found for coverages above 40 ML, and some unoxidized cobalt has also been found for coverages below 1 ML. The origin of this unoxidized cobalt has been explained in terms of the different coordinations of substrate and CoO and the reducing character of the substrate. The O 1s spectra are composed by two peaks. The first one, located at 530.5 eV, has been assigned to the CoO lattice. The second one is located at 532.5 eV, and it has been assigned to the most superficial O atoms of the CoO lattice, although more experiments are necessary in order to confirm this hypothesis.

SECTION 5.3

Quantitative analysis

5.3.1 Analysis of the XPS intensities

The same procedure used in the chapter of the oxide substrates (see page 96) has been used in the calculations of the deposition rate for the growth of CoO on HOPG. The results of these calculations for the Co 2p and C 1s peaks are shown in table 5.2 and figure 5.5. The deposition rate for this experiment is different than what was obtained in the oxide substrates

	CoO/HOPG
IMFP (Å)	10.95 (Co 2p) 28.67 (C 1s)
v (ML/min)	0.10 ± 0.01 (Co 2p) 0.07 ± 0.01 (C 1s)
v_{med} (ML/min)	$\mathbf{0.08 \pm 0.01}$

Table 5.2: Deposition rates obtained with the infinitely thick layer method for the growth of cobalt oxides on HOPG.

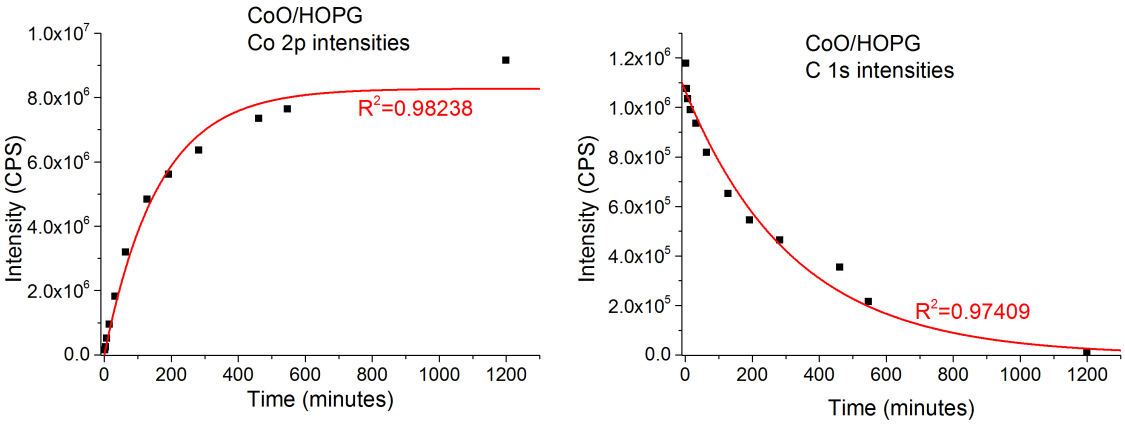

Figure 5.5: Variation of the XPS Co 2p and C 1s peak intensities using the infinitely thick layer model for the growth of cobalt oxides on HOPG.

growths because the evaporator power values used in this growth were lower (table 2.8, page 49).

5.3.2 AFM study of the growth

The study of the morphology of the growth by AFM was made by growing six samples with different coverages, which were measured as soon as they were taken out of the vacuum chamber. The results are summarized in figure 5.6.

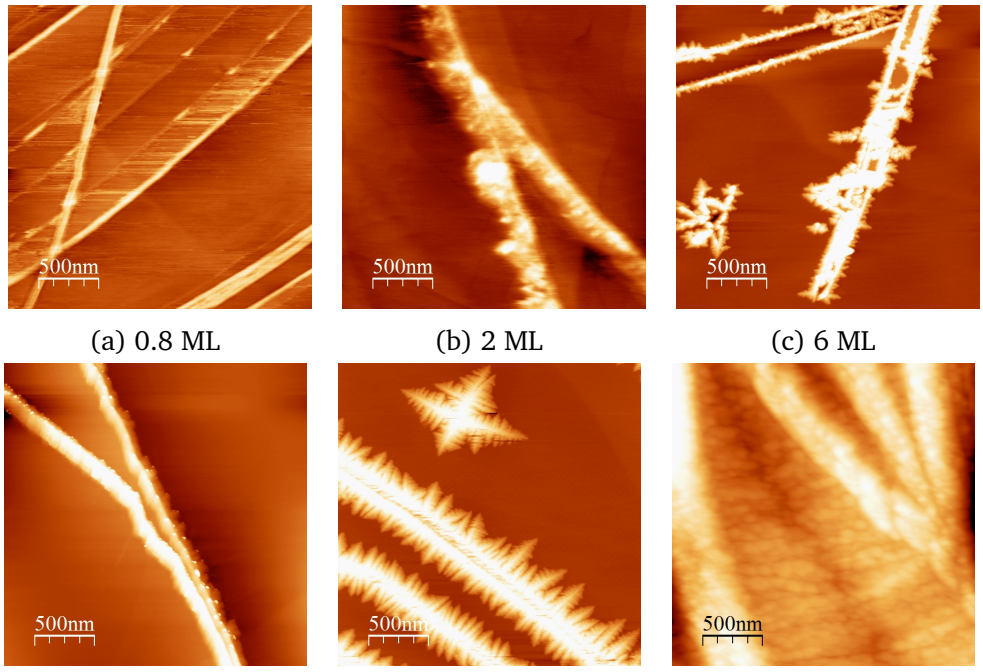

(a) 0.8 ML (b) 2 ML (c) 6 ML

(d) 11 ML (e) 22 ML (f) 80 ML

Figure 5.6: AFM topography images of different stages of the growth of CoO on HOPG. Size of the images: 2.5 µm × 2.5 µm. CoO coverage as labelled.

For the early stages of growth, CoO particles appear agglomerated at the steps of the HOPG surface, leading to the formation of structures along the steps of up to 100 Å in height. Once the steps have been completely filled in, dendritic structures starts growing at the material accumulated at the steps (with clear 90° angular distributions), and islands start growing on the HOPG terraces. These islands are also decorated with dendritic ramifications, having heights ranging from 20-50 Å (for the early stages of growth), to 70-80 Å for the intermediate stages: the profiles of these structures (figure 5.7) yield that they mostly have a triangular structure. For coverages around 80 ML, full coverage of the substrate is observed.

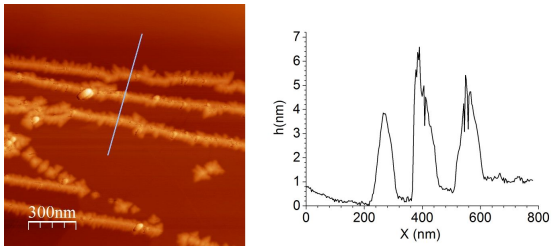

(a) Coverage: 6 ML. AFM topography image size: 1.5×1.5 μm

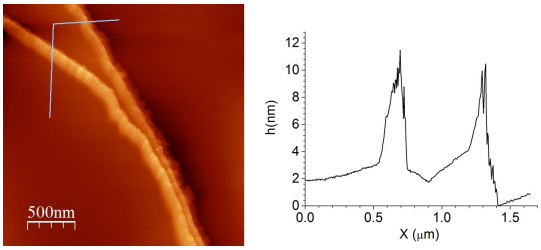

(b) Coverage: 11 ML. AFM topography image size: 2.5×2.5 μm

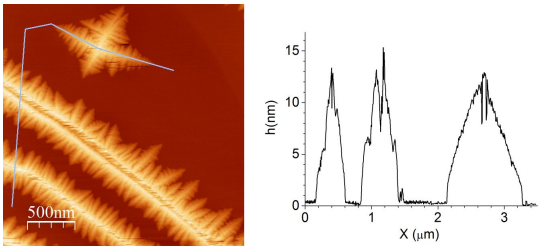

(c) Coverage: 22 ML. AFM topography image size: 2.5×2.5 μm

Figure 5.7: AFM topographic profiles of the steps and islands accumulations of material taken for different CoO coverages grown on HOPG. CoO coverage and AFM topography image size as labelled.

After a careful examination of the measured AFM images, the formation of a wetting layer has also been observed: some examples of its appearance are shown in figure 5.8. This layer does not appear in the vicinity of an island, as it can be seen in the flat areas surrounding the islands in figure 5.8c. Figure 5.8a shows a border separating two different regions with a step of approximately 4 Å, as depicted in the profile. The lack of agglomerated islands on this border discards the possibility that this could be one of the HOPG steps. The height of the wetting layer given by the topographic profile agrees with the formation of one unit cell thick layer of CoO, which accounts for 2 ML in height. Similar images could easily be detected for samples with total coverage between 3 and 15 ML. Figure 5.8b shows a detail of the wetting layer for a coverage of about 11 ML, where CoO domains grow following the three possible directions as dictated by the hexagonally arranged HOPG substrate. This preferential arrangement of the CoO atoms on the HOPG substrate suggests that CoO clusters autoassemble on the HOPG surface.

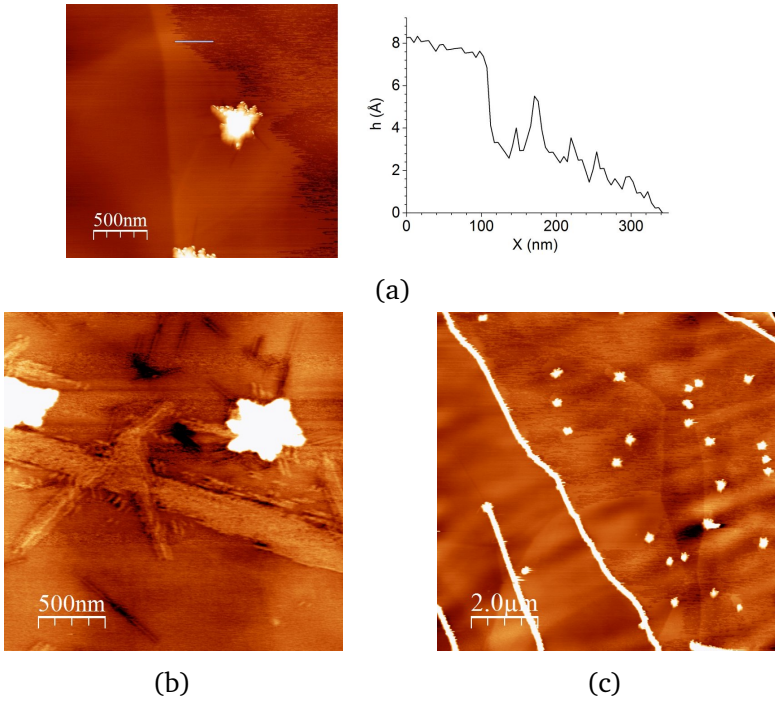

Figure 5.8: AFM images of 11 ML samples of CoO on HOPG where the wetting layer is clearly observable. Sizes of the images: (a) and (b), 2.5 µm× 2.5 µm; (c), 10 µm× 10 µm. (a) also includes a topological profile of the wetting layer.

According to these results, we can conclude that, after the filling of the HOPG steps by small CoO nanoclusters, cobalt oxide grows on HOPG following a Stranski-Krastanov growth mechanism [3] with the formation of 2 CoO ML (1 unit cell) thick wetting layer followed by the growth of CoO islands on top. The CoO deposits show a strong diffusion along the HOPG surface towards the steps, allowing the formation of an ultrathin CoO wetting layer by autoassembling, and the growth of the dendritic structures decorating the edges of the CoO step structures and islands.

5.3.3 XPS Inelastic Peak Shape Analysis (XPS-IPSA) and comparison with AFM

The XPS-IPSA calculations for the growth of cobalt oxides on HOPG have been made using the same procedure followed in subsubsection 4.2.2.1 (page 96) for the growths on the oxide substrates. The main parameters of the region chosen for these calculations are displayed in table 5.3.

The evidences found in the AFM study of the growth led us to choose two different concentration profiles for these calculations that could take into account the triangular distributions of material at the steps and the wetting layer. The first one considers the CoO deposits as distributed in a set of triangular islands with equal maximum heights between each other, while the second one considers part of the substrate covered by a wetting layer of fixed thickness,

Peak	Co 2p
KE (eV)	450
z **IMFP (Å)**	10.96
Region (KE, eV)	355-500
hν (eV)	1253.6

Table 5.3: Peak used for the XPS-IPSA calculations of the growth of CoO on HOPG, and its kinetic energy and IMFP

and a fraction of this wetting layer covered by planar islands. Both models are depicted as insets in their respective calculation graphs.

The calculations for the triangular islands concentration profile are shown in figure 5.9, along with the dimensions and coverage data taken from the analysis of the AFM images. In the triangular islands model, no height or coverage parameters were taken from the topography images, and the fittings give a good agreement with the mean dimensions of the material at the steps and islands observed by AFM. The calculated quantity of deposited material, shown in figure 5.9b, is close to that coming from the XPS-IPSA fittings, although a slight difference between them can be appreciated.

The results of the calculations using the wetting layer + planar islands model are shown in figure 5.10. The height of the planar islands was taken from the AFM topography images and the rest of the parameters were left free, as a way to reduce the number of parameters to fit and the error of the calculations. Figure 5.10a shows the variation of the percentage of substrate covered only by the wetting layer (labelled as "Cov_W"). It shows that this percentage initially increases linearly with the coverage, goes through a maximum at ∼12-15 ML, and then drops off for larger deposits. This indicates that for 0-5 ML, the growth consists primarily in an increase of the extension of the wetting layer and in the range 5-12 ML, the islands start to grow on top of the wetting layer while the wetting layer is still expanding on the surface. At ∼15 ML the wetting layer covers the complete surface and for larger deposits, the islands continue to grow and cover ∼65% (=100-35% in figure 5.10a) of the surface at 20 ML. The total coverage as a function of the evaporation time is shown in figure 5.10b. The results from the AFM data are also shown, and the agreement between the two techniques is better than in the case of the triangular islands model, which gives confidence in the proposed way of growth.

5.3.4 Summary

The most quantitative aspects of the growth, such as the deposition rate calculations and the study of its morphology, have been presented in this section. The analysis and fitting of the XPS intensities of the Co 2p and C 1s regions have yielded lower deposition rates than for the oxide growths: they have been explained as due to the lower evaporation power values used in this growth. The study of the morphology of the growth by AFM has yielded a Stranski-Krastanov way of growth. The CoO starts growing at the steps of the substrate, and once these steps have been filled, a wetting layer starts covering the terraces of the substrate, followed

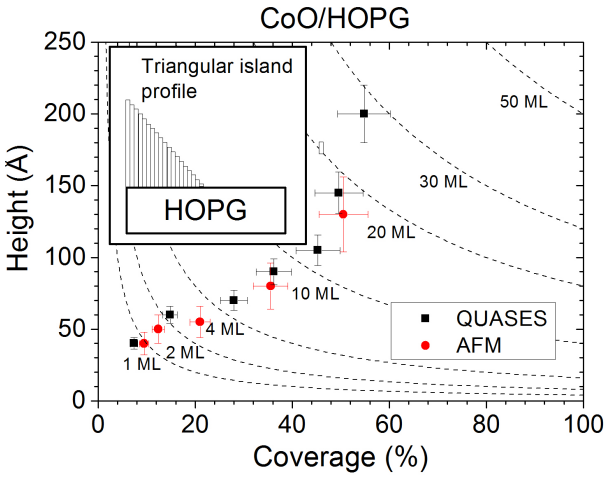

(a) Comparison of the quantitative analysis given by AFM (red dots) and XPS-IPSA using the triangular islands concentration profile (black squares).

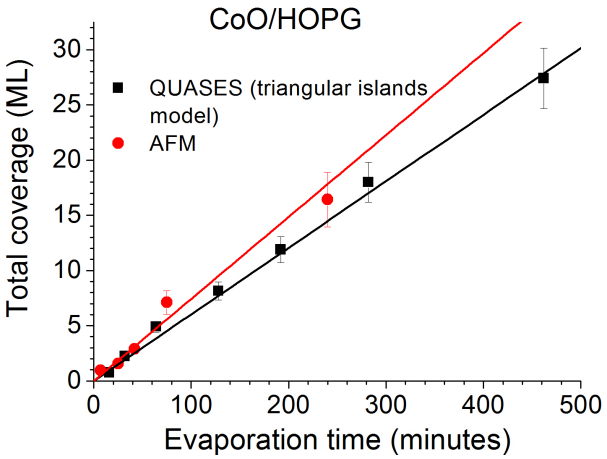

(b) Comparison of the total amount of deposited material as a function of the growth time given by AFM (red dots) and XPS-IPSA (black squares)

Figure 5.9: XPS-IPSA calculations for the triangular islands model applied to the growth of CoO on HOPG, and comparison with AFM dimensions and coverage data. The inset on (a) shows the triangular islands concentration profile used in the XPS-IPSA calculations.

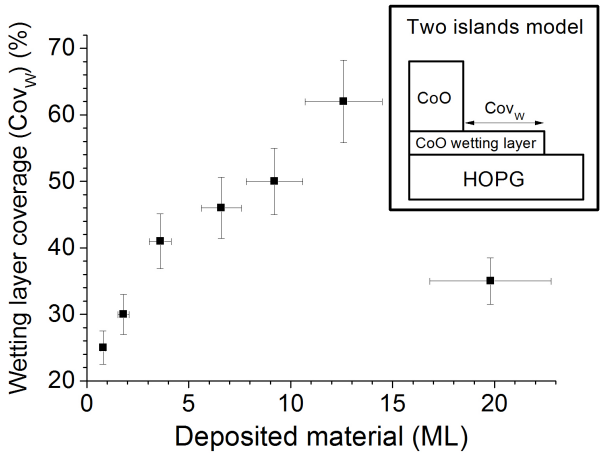

(a) Percentage of uncovered wetting layer as a function of deposited material given by XPS-IPSA

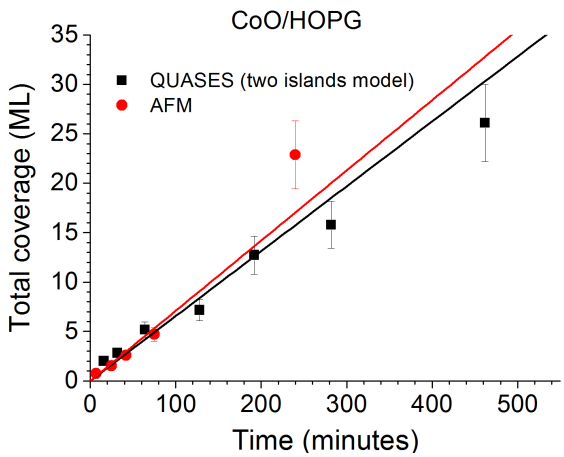

(b) Comparison of the total amount of deposited material as a function of the growth time given by AFM (red dots) and XPS-IPSA (black squares).

Figure 5.10: XPS-IPSA calculations for the wetting layer+planar islands model applied to the growth of CoO on HOPG, and comparison with AFM dimensions and coverage data. The inset on graph (a) shows the wetting layer+planar islands concentration profile used in the XPS-IPSA calculations.

by the growth of CoO islands on top of it. The material accumulated at the steps and islands have triangular shapes and show dendritic ramifications, and the wetting layer shows signs of autoassembling and ordering along the crystallographic directions of the substrate. The full coverage of the substrate is observed at 80 ML. This morphology has been confirmed by XPS-IPSA calculations using two different concentration profiles: one with triangular islands, and another with planar islands on top of a wetting layer.

SECTION 5.4

Interaction of Co oxides with graphite surfaces

Once the chemistry and morphology of the growth has been properly characterized, the interaction of these CoO layers with the substrate will be studied. The results obtained are divided in two subsections: effects seen on the regions related to the deposited CoO (Co 2p and O 1s), and effects seen on the regions related to the substrate (C 1s). The effects on the CoO clusters have been studied with two techniques: XPS and XAS. The experimental data is supported by theoretical cluster model calculations of the Co $2p_{3/2}$ XPS spectra, atomic multiplet calculations for the Co 2p XAS spectra, and density of states calculations for the O 1s XAS spectra. The XPS calculations will give information about effects caused by the size of the deposited material and the ionic-covalent character of the CoO bonds, while the XAS spectra will give information about possible changes in the structure of the CoO deposits.

Meanwhile, the modifications made to the substrate will be studied with the measurements of the C 1s region by XPS, PES and XAS. All the PES and XAS spectra come from the aforementioned in-situ growths made in the PM4 beamline of the BESSY synchrotron, while the XPS spectra are extracted from the measurements of the original in-situ growth experiment made in the GRIN laboratory. The geometry of the experimental conditions will be a useful tool in this section: in the PES spectra, it will allow us to distinguish between bulk and surface effects, while in the XAS spectra, the linear polarization of the x-ray beam will excite transitions depending on the orientation of the bonds, allowing us to extract information about structural anisotropies.

5.4.1 Study of the CoO overlayer

5.4.1.1 Co $2p_{3/2}$ XPS spectra

The theoretical XPS Co $2p_{3/2}$ spectra presented in chapter 4 (figure 4.3, page 93) can also be used here to explore changes in the ionic-covalent character of the bonds of the grown CoO samples, and give information about size and support effects. The same three peaks used in those fittings (labelled as "*main line*", "*mult*" and "*sat*") have also been used here. The main parameters of these peaks, such as their FWHM, or the relative position of the *sat* and *mult* peaks with respect to the *main line* peak, have been maintained with respect to those used on the fittings of the growths on oxide substrates. As in the case of the oxide growths, only coverages lower than 20 ML have been fitted, since we can be sure that only CoO is going to be found on them, and also because these size-related effects are expected to be observed only

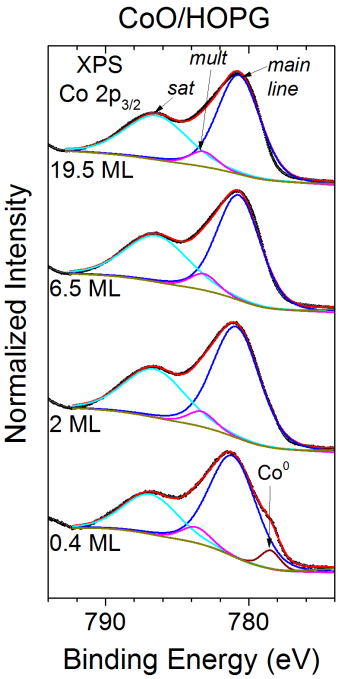

Figure 5.11: Fittings for the XPS Co $2p_{3/2}$ spectra of some selected coverages of the growth of CoO on HOPG.

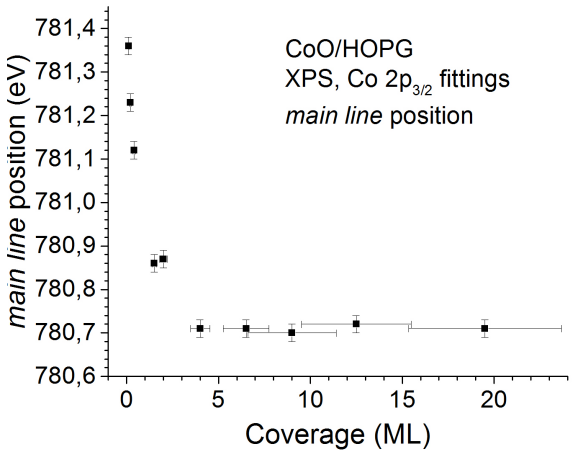

Figure 5.12: Evolution of the "*main line*" peak with the coverage, as extracted from the fittings of the XPS Co $2p_{3/2}$ spectra of the growth of CoO on HOPG.

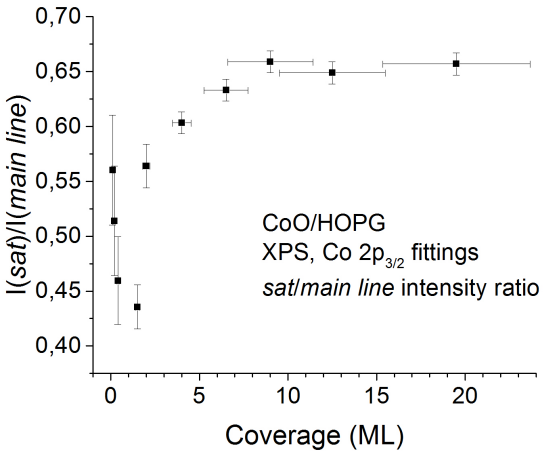

(a) I(*sat*)/I(*main line*) ratio

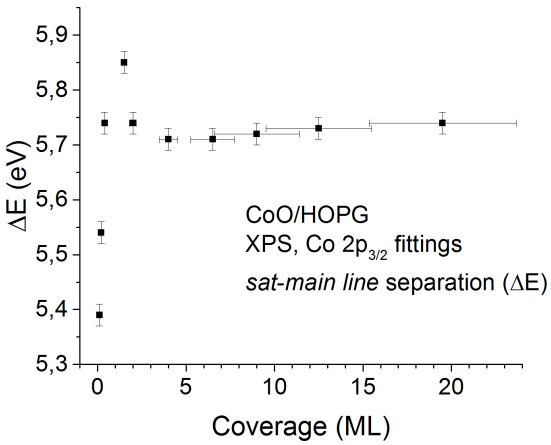

(b) Energy separation between the *sat* and *main line* peaks

Figure 5.13: Evolution of the relative intensity and position of the *sat* peak (with respect to the *main line*), as extracted from the fittings of the XPS Co $2p_{3/2}$ spectra of the growth of CoO on HOPG

for low coverages. Figure 5.11 shows some examples of these fittings for the whole coverage range explored.

The evolution of the binding energy of the "*main line*" peak with the coverage is shown in figure 5.12. It shows similar shifts as those seen in the growth on oxide substrates. For coverages below 4 ML, there is a shift of the peak position towards lower binding energies, and once the coverage has reached 4 ML, a constant value of 780.7 eV is observed. This low coverage shift can be explained as extra-atomic relaxation effects, as in the case of the growths on the oxide substrates. The final "*main line*" binding energy value is ∼780.7 eV, which is roughly the same that was found in the growths on SiO_2 and MgO, and close to that predicted for the bulk CoO structure in the theoretical calculations.

The results for the relative position and intensity of the "*sat*" peak are shown in figure 5.13. They show inverted trends when compared against each other, which agrees with the trends for these parameters seen in the theoretical calculations. The relative energy position shows an initial increase from a value below the bulk-like value, a slight decrease in the 1.5-4 ML region, and a final stabilization for larger coverages around ∼5.8 eV. This final value is in excellent agreement with the bulk CoO value obtained in the calculations (6 eV).

We suggest that this change in the trend seen for coverages larger than 2 ML can be attributed to the morphology of the sample. It has been shown in the AFM results of subsection 5.3.2 that, for the 2 ML coverage, a 30% of the substrate is covered by a wetting layer of ∼8 Å, which means that ∼60% of the deposited material has this morphology. This layer shows some kind of ordering, so its crystalline structure should be more ordered and closer to the bulk structure than that of the deposits formed at the steps. Therefore, the effects happening on this wetting layer will be predominant with respect to those of the material located at the steps for coverages below 2 ML: since the wetting layer also grows with the coverage, the general ionic-covalent character of the bonds seen in the XPS spectra will also increase. For coverages larger than 2 ML, the size and percentage of deposited material at the steps increases, and islands start appearing in the terraces already covered by the wetting layer: this causes the effects belonging to the material located at the steps and islands to become more important. Since the material deposited at the steps and islands grows in a more disordered way, the ionic-covalent character of its bonds will be smaller, so the general covalence trend will experience a decrease. For coverages larger than 4 ML, the effects of the material at the steps and islands will be completely dominant, and the relative position of the *sat* peak will stay constant. This result, together with the data obtained in the growths on oxide substrates, reinforces the idea that these changes of the ionic-covalent character of the CoO bonds are not caused by the covalency of the substrate, but because of the morphology of the grown samples.

5.4.1.2 Co 2p XAS spectra

The XAS Co 2p spectra for coverages ranging from 2 to 30 ML are shown in figure 5.14: they were measured in-situ in the same beamtimes already commented in section 5.2.3. The spectra marked with an asterisk (5 and 30 ML) have less resolution than the others due to experimental problems in the beamtime where they were grown and measured. The grating used in these experiments was different than that used in the other beamtime, and the photon energy used for the 0° measurements of this region in the 2 and 20 ML samples (1000 eV) was

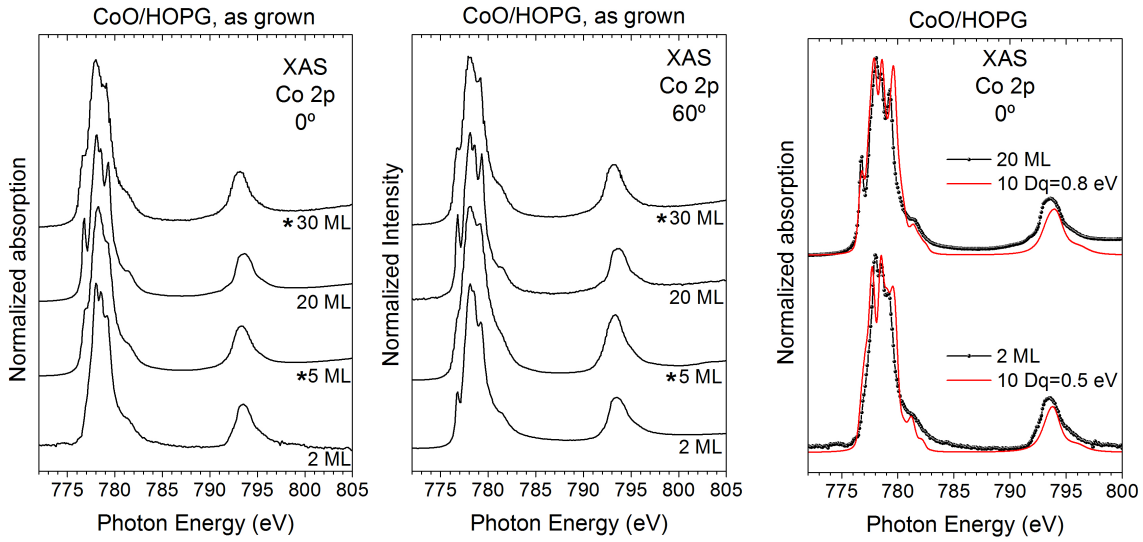

(a) Co 2p region, incident angle: 0°.

(b) Co 2p region, incident angle: 60°

Figure 5.14: XAS Co 2p spectra of different coverages of the growth of CoO on HOPG. Incident angles: 0° and 60°. The 5 and 30 ML spectra have less resolution due to the aforementioned changes in the cff constant of the monochromator.

Figure 5.15: XAS Co 2p spectra of different coverages of the growth of CoO on HOPG (black line with points, incident angle: 0°), and comparison with atomic multiplet calculations (red line).

outside its operative range. The only solution to perform these measurements was to change the cff constant of the monochomator [4], which resulted in a loss of resolution. The Co 2p XAS spectra are dominated by multiplet effects, and their peaks are very narrow, so this loss of resolution will be specially noticeable in these spectra.

The spectra show two main groups of peaks at ∼778 and 794 eV, which correspond to the Co $2p_{3/2}$ and Co $2p_{1/2}$ levels, separated by spin-orbit coupling. There are changes in these spectra related to the multiplet structure at ∼778 eV: if we compare the 2 and 20 ML spectra, the 2 ML 0° spectrum does not show the 776.7 eV peak, and these multiplet features are less defined in the 2 ML 0° spectra when compared to the 60° spectra.

The fine structure and positions of both levels, which has been extensively studied and modelled over the years [5–7], can be used to determine the oxidation state of the sample at a first glance. The first conclusion that can be extracted is that these spectra confirm the main oxidation state conclusions found in the XPS Co $2p_{3/2}$ spectra, since the shape of the spectra is closer to that found in the bibliography for CoO.

In order to explore the changes seen with the coverage and the beam angle, theoretical multiplet calculations of the Co 2p absorption edge of CoO were performed for different 10 Dq

(crystal field) values. Figure 5.15 shows the result of these calculations for 10 Dq values of 0.5 and 0.8 eV, and their comparison with the Co 2p XAS spectra taken at normal incidence for the 2 and 20 ML samples. The theoretical spectrum with 10 Dq=0.5 eV do not show the 776.7 eV peak, which agrees with the experimental 2 ML spectrum. This means that the loss of structure in our spectra can be explained as due to the low 10 Dq values of our samples, which can be directly linked to their low dimensionality. This result is consistent with the results of the study of the XPS Co 2p $_{3/2}$ spectra, which also showed changes related to the low dimensionality of the samples for the lower coverages.

The changes in the 2 ML spectra with the sample-beam angle suggests some sort of distortion on the Co coordination octahedron, which could be explained by the appearance of some sort of interaction between the grown cobalt oxide and the substrate. Since the material deposited at the steps should have grown at least in an amorphous or polycrystalline way, our guess is that the wetting layer is the one that it is interacting. This assumption is supported by the previously shown AFM images of this wetting layer (figure 5.8, page 134), which showed how it distributed itself in the crystallographic directions of the substrate.

5.4.1.3 O 1s XAS spectra

The O 1s XAS spectra are shown in figure 5.16. According to bibliography, and more specifically to De Groot's work on XAS O K-edge spectra interpretation [6, 8], the O 1s spectra of 3d-transition metal oxides can be divided in two regions. The first region, located near the absorption threshold, is related to O 2p-metal 3d hybridized bands, and is composed of two peaks, related to the metal t_{2g} and e_g sub-bands, and separated by a crystal field splitting. The other region is located 5-10 eV above it, has a broader structure, and is related to O 2p-metal 4sp hybridized bands. These spectra are directly related to the unoccupied density of states (UDOS) of O p-character orbitals, so Density Functional Theory (DFT) calculations can be used to simulate these spectra.

The spectra of the 20 and 30 ML samples have the same structure, and do not show significant changes with the coverage or the beam angle. However, the 0° spectra of the 2 and 5 ML samples show different t_{2g}/e_g band intensity ratio with respect to the bulk signal, and the O 2p-Co 4sp region shows much broader features than in the higher coverage samples.

Direct comparison of these spectra with previous studies [5, 6, 9] yield more or less the same characteristics of bulk CoO spectra for the 20 and 30 ML samples, which further confirms the cobalt oxide species found in other measurements. In order to study the coverage and angle changes seen in the 2 and 5 ML samples, DFT calculations for CoO slab and bulk configurations were performed: the results are shown in figure 5.17). They show this loss of features for the slab configuration, which means that the different features seen in the low-coverage samples are caused by the low dimensionality of the samples. Meanwhile, the changes in the 2 and 5 ML spectra with the angle seem to suggest the same conclusions made in the Co 2p XAS spectra: there is a strong interaction of the deposited CoO with the substrate.

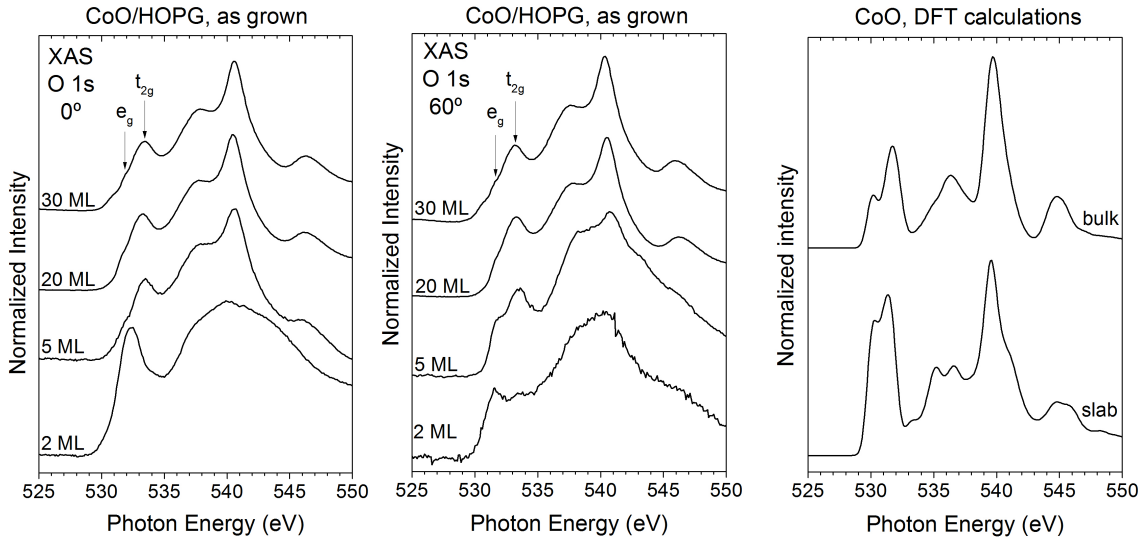

(a) Incident angle: 0°. (b) Incident angle: 60°

Figure 5.16: XAS O 1s spectra of different coverages of the growth of CoO on HOPG. Incident angles: 0° (figure 5.16a) and 60° ((figure 5.16b).

Figure 5.17: DFT calculations of the XAS O 1s spectra of CoO for slab and bulk configurations.

5.4.2 Study of the HOPG substrate

5.4.2.1 C 1s XPS and PES spectra

Figure 5.18 shows the in-situ XPS C 1s spectra of the growth of cobalt oxides in HOPG made in the GRIN laboratory. For the majority of the coverages grown, only one asymmetrical peak can be seen at 284.2 eV (labelled as "sp^2 peak" from now on), which is assigned to the HOPG sp^2 bonds [10]. The asymmetry of this peak is usually attributed to neutralization by conduction electrons of the holes created during photoionization, and it is a consequence of the conductive character of graphite [11]. The two largest CoO coverage spectra show a broadening of this peak and the appearance of two new contributions at 285.6 eV and 288.5 eV. Their relative distances with respect to the main sp^2 peak allow us to relate them to C-O and C=O bonds, respectively [12–14]. However, it is important to note that different interpretations about the nature of these peaks have been found throughout all the consulted bibliography, mostly due to the fact that a great number of organic groups have their XPS C 1s peak in the 285-290 eV range.

In order to explore these changes, fittings of all the XPS C 1s spectra have been performed. These fittings used two peaks for the clean HOPG spectrum: an asymmetrical peak for the sp^2 peak, composed by a Gaussian-Lorentzian sum with a tail modifier (see page 61); and a symmetrical 291 eV peak (FWHM: $\sim$ 5 eV) for the inter-band π-π^* contribution [11]. The asymmetry parameters used for the sp^2 peak were TS=0.13 and TL=170, and they were left as constant for all the fittings; and the G-L parameter for all the peaks was left at 20%.

Figure 5.19 shows example fittings for coverages ranging from the clean substrate to 25 ML,

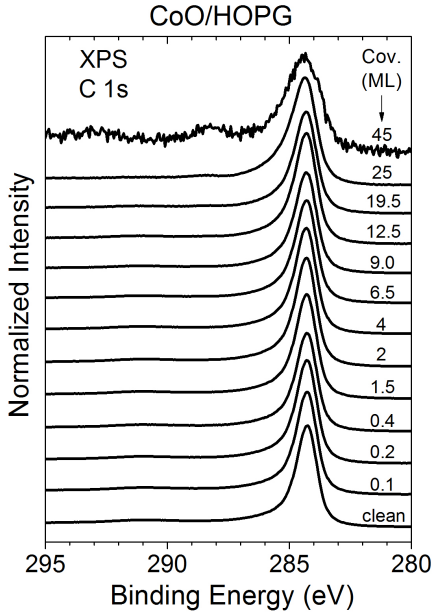

(a) XPS C 1s spectra, as taken

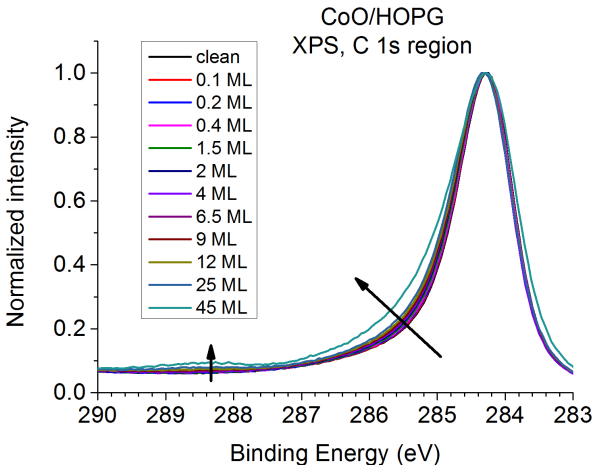

(b) Normalized XPS C 1s spectra

Figure 5.18: XPS C 1s spectra of the growth of cobalt oxides on HOPG made in the GRIN laboratory. Coverage as labelled.

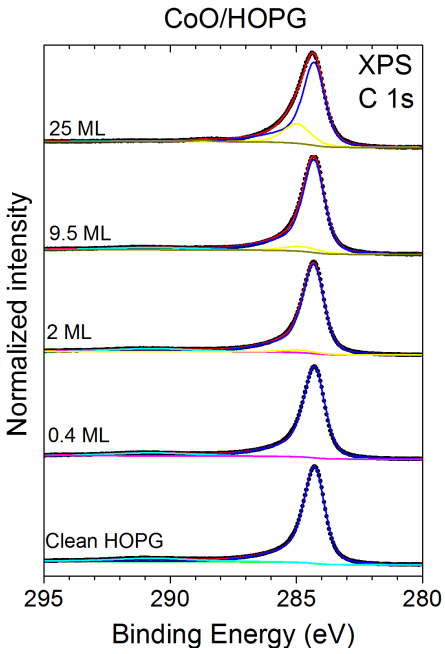

Figure 5.19: Fittings of the XPS C 1s spectra of the clean HOPG substrate and four selected coverages of the growth of CoO on HOPG. Coverages, peaks used and substrates as labelled.

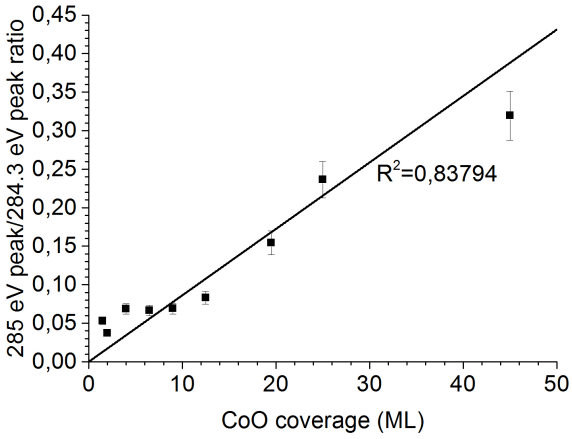

Figure 5.20: Ratio between the intensities of the 284.3 eV and 284.8 eV peaks obtained in the fittings of the XPS C 1s spectra.

Cov. (ML)	Peak 1 (sp^2 peak)			Peak 2			Peak 3 (C-O)			Peak 4 (C=O)		
	BE (eV)	FWHM (eV)	I (a.u.)	BE (eV)	FWHM (eV)	I (a.u.)	BE (eV)	FWHM (eV)	I (a.u.)	BE (eV)	FWHM (eV)	I (a.u.)
0	284.29	0.98	$1.381 \cdot 10^6$	-	-	-	-	-	-	-	-	-
0.1	284.3	0.97	$1.526 \cdot 10^6$	-	-	-	-	-	-	-	-	-
0.2	284.3	0.98	$1.415 \cdot 10^6$	-	-	-	-	-	-	-	-	-
0.4	284.3	0.98	$1.355 \cdot 10^6$	-	-	-	-	-	-	-	-	-
1.5	284.3	0.98	$1.235 \cdot 10^6$	284.87	1.27	65591	-	-	-	-	-	-
2	284.32	0.98	$1.186 \cdot 10^6$	284.87	1.25	43838	-	-	-	-	-	-
4	284.3	0.98	$1.002 \cdot 10^6$	284.87	1.27	68846	-	-	-	-	-	-
6.5	284.29	0.98	$7.962 \cdot 10^5$	284.87	1.25	52887	-	-	-	-	-	-
9	284.31	0.98	$6.592 \cdot 10^5$	284.87	1.25	45398	-	-	-	-	-	-
12.5	284.31	0.98	$5.549 \cdot 10^5$	284.87	1.25	46031	-	-	-	-	-	-
19.5	284.28	0.94	$3.878 \cdot 10^5$	284.87	1.27	59809	288.56	1.51	2432	-	-	-
25	284.3	0.99	$2.113 \cdot 10^5$	285	1.27	49973	288.63	1.51	3595	-	-	-
45	284.35	1.05	11700	285.15	1.27	3738	288.5	1.55	2278	285.65	1.5	532

Table 5.4: Peaks and parameters obtained in the fittings of the XPS C 1s spectra of the growth of cobalt oxides on HOPG.

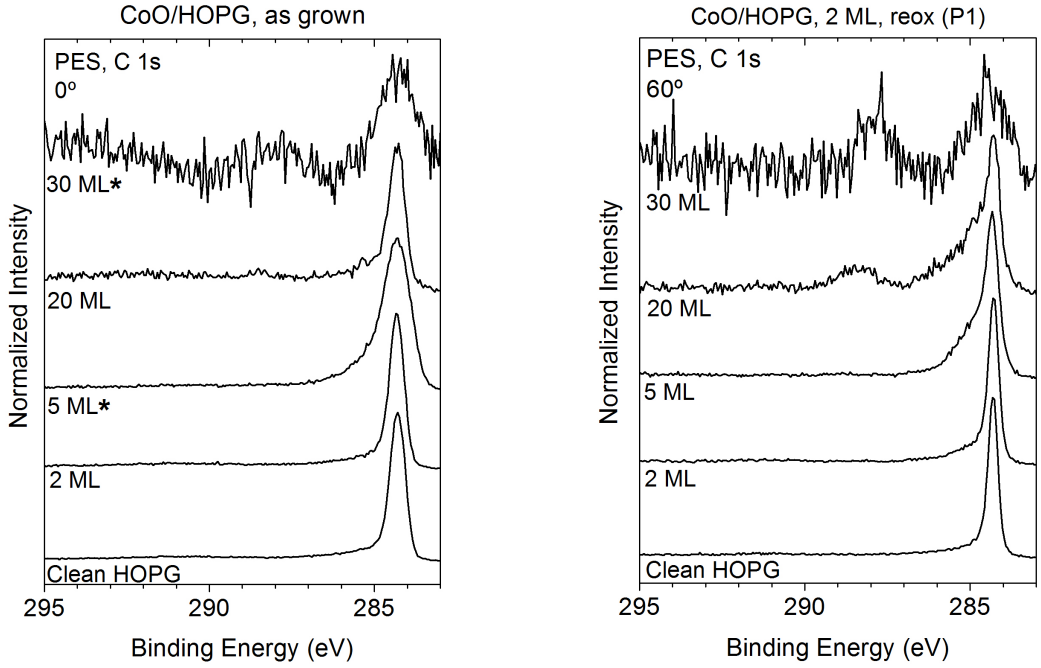

(a) Take-off angle: 0°, $h\nu$=1000 eV and 950 eV (asterisk-marked spectra).

(b) Take-off angle: 60°, $h\nu$=380 eV

Figure 5.21: PES measurements of the C 1s region for the growth of CoO on HOPG. Coverages, take-off angles and $h\nu$ energies as labelled.

and the main parameters obtained for the peak used in these fittings (except for the inter-band π-π^* peak) are displayed at table 5.4. Aside from confirming the appearance of the 285.6 eV and 288.5 eV peaks for coverages larger than 10 ML, they show that the broadening of the main graphite peak is caused by the appearance of a peak at 284.8 eV, which relative intensity with respect to the main sp^2 peak follows an almost linear trend with the coverage (figure 5.20). This contribution is usually assigned in the bibliography to two main sources: C-C bonds with sp^3 hybridization, or C-H bonds [15, 16].

This region was also measured by PES in the growths made at the PM4 beamline of the BESSY synchrotron. The spectra obtained for take-off angles of 0 and 60° are shown in figure 5.21 (the spectra marked with an asterisk have the same resolution loss already commented on subsubsection 5.4.1.2, page 139), and they also show this broadening of the main 284.3 eV peak. The changes in the take-off angle and photon energy yield that this broadening is more pronounced when the sampling depth of the measurement is lowered (for example, it can be easily detected in the 2 ML 60° spectrum, but not on the 2 ML 0° spectrum), which means that it is a superficial feature. The 20 and 30 ML samples also show the 285.6 and 288.5 eV peaks seen in the XPS spectra of the highest coverages grown in the GRIN laboratory. These peaks are more intense in the 60° spectra, which confirms that they have a superficial nature.

As a way to confirm that these peaks match the ones seen in the XPS spectra, the 60° PES C 1s spectra were fitted with the same four peaks used in the XPS C 1s spectra fittings. The energy position of the four peaks used before has been left constant, and their FWHM and intensity

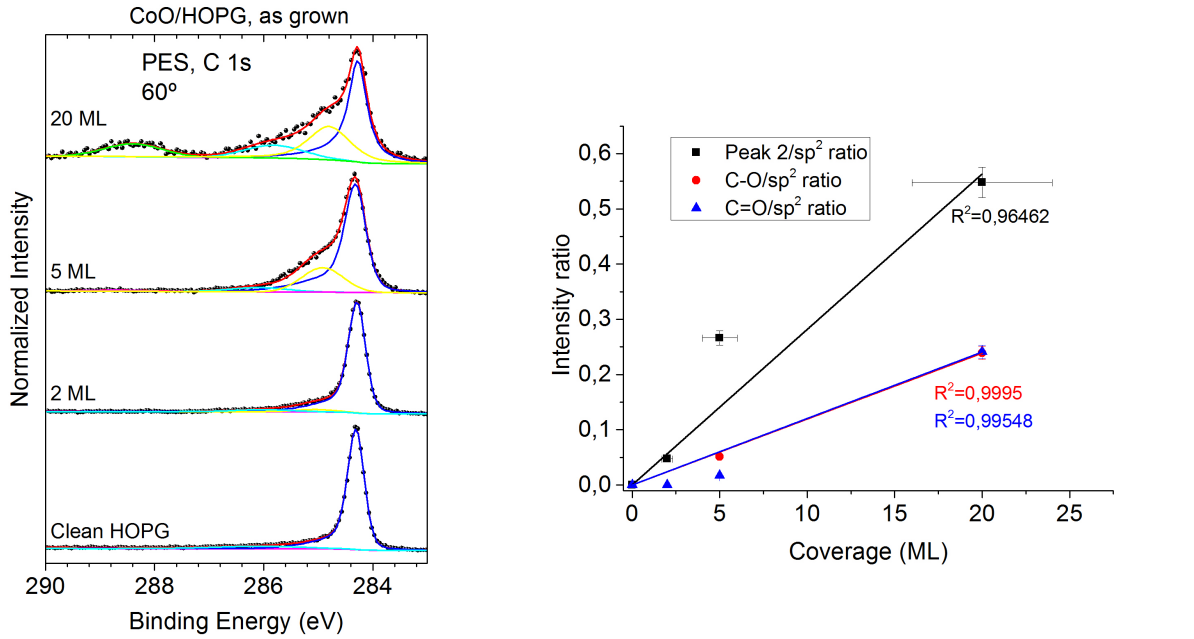

(a) PES fittings

(b) Ratios between the four peaks appeared in the fittings

Figure 5.22: Fittings of the PES measurements of the C 1s region (take-off angle of 60°) for the growth of CoO on HOPG.

Sample	Peak energy (eV)	FWHM (eV)	Area
Clean	284.31	0.36	$1.607 \cdot 10^5$
	286.1	2.02	$1.26 \cdot 10^4$
	290.8	5.1	$1.97 \cdot 10^4$
2 ML	284.3	0.37	$1.104 \cdot 10^5$
	285	0.9	3960
	286	1.27	7104
	291.1	5.1	4396
5 ML	284.3	0.45	$1.21 \cdot 10^5$
	284.85	0.9	$3.32 \cdot 10^4$
	285.9	1.27	$1.22 \cdot 10^4$
	288.7	1.27	1884
20 ML	284.3	0.4	$2.48 \cdot 10^4$
	284.8	0.9	$1.35 \cdot 10^4$
	285.85	1.28	5935
	288.6	1.27	5994

Table 5.5: Peaks and parameters used in the fittings of the PES C 1s spectra (take-off angle: 60°).

have been left free, since these spectra have much higher resolution than those obtained in our laboratory. The Gaussian-Lorentzian parameter of all the peaks was set at 30%. The peak used to simulate the sp^2 contribution is also asymmetric, and its asymmetry parameters have been maintained constant throughout all these fittings (TS=0.1, TL=200); while the rest of the peaks are symmetric. The results of fittings for the 60° spectra are shown in figure 5.22a, and the peak parameters obtained for the four peaks are displayed in table 5.5.

Since the same four peaks seen in the GRIN measurements (and also the 291 eV inter-band π-π^* peak) appear in these fittings, the same peak assignation used before can be made here. The peak at 284.3 eV corresponds to the sp^2 graphite bonds, the 284.8 eV to C-H or sp^3-hybridized C-C bonds, the 285.8 eV to C-O bonds and the 288.6 eV to C=O bonds. The ratio between the 284.8 eV and 284.2 eV (figure 5.22b) yields similar results to the linear trend seen in the GRIN experiments. All the ratios have higher values than those obtained in the fittings of the XPS C 1s spectra, which is another confirmation that all these phenomena are happening only at the surface of the substrate.

5.4.2.2 C 1s XAS spectra

The C 1s XAS for the clean HOPG and the samples grown and measured in-situ are displayed in figure 5.23. For their analysis, we will focus on the clean HOPG spectrum first, and then the rest of the spectra will be commented.

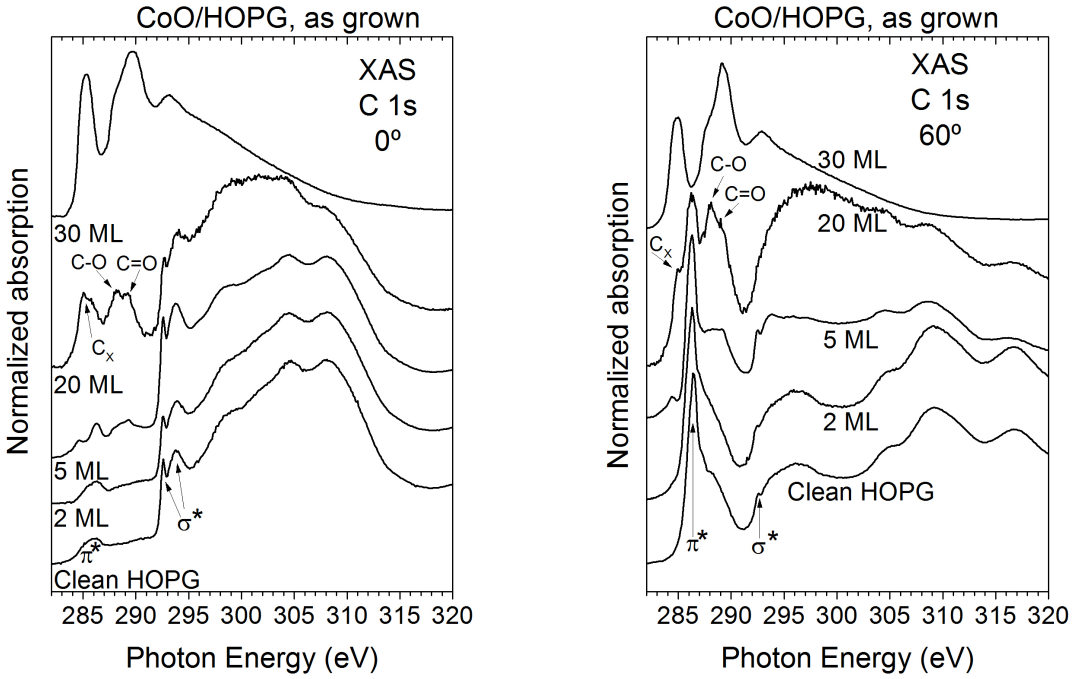

(a) C 1s region, incident angle: 0°.

(b) C 1s, incident angle: 60°

Figure 5.23: XAS C 1s spectra of different coverages of the growth of CoO on HOPG. Incident angles: (a) 0° and (b) 60°.

The bibliography [17–19] usually distinguishes three key features in the C 1s XAS spectrum

of a clean graphite sample: the peak centred at ∼286 eV (called π^*), that corresponds to transitions to the unsaturated C=C bonds above and below the surface plane; and two other peaks (called σ^*), that correspond to transitions between in-plane C-C bonds. The sharper of those peaks is centred at 292.5 eV, and is attributed to a σ^* exciton [20]; while the second one, centered at 293.8 eV, is attributed to another σ^* transition. Higher-order transitions are visible as broader peaks above the energies of these peaks discussed before. Since the beam polarization used in these measurements is linear, the X-ray incidence angle will affect which features are more visible in the XANES spectra: at 0° the in-plane C-C bonds will be more excited, and therefore the σ^* features will be more intense; while at 60° the intra-plane bonds will be the most excited, and the π^* features will be more visible in the spectrum.

The spectra for the clean HOPG substrate (bottom spectra of figures 5.23a and 5.23b) shows these characteristics: sharper π^* features for the 0° measurement, and more intense σ^* features for the 60°. Two new peaks, centred at 288 and 289.2 eV, start growing once the deposition of cobalt oxide begins, being visible on the spectra taken at both angles. The bibliography assign these peaks to C-O and C=O bonds [12, 21, 22], which agrees to the assignation made to the peaks seen in the PES and XPS spectra. Another two peaks (labelled as C_X in the spectra), located at ∼284.5 eV, also grow with the coverage: its assignation is less clear in the bibliography, but they could be related to C-H or other forms of carbon without oxygen bonds [23, 24]. The growth of these peaks with the coverage can be due to two factors: the increase in the adsorbate-substrate interaction, and the smaller depth sampled in the HOPG by the measurement, which would cause superficial effects to be more intense than bulk features. This latter reason can be behind the 30 ML spectra taken (top spectrum of figures 5.23a and 5.23b), which do not show any significant changes for 0 and 60°, and are totally different from the rest.

5.4.3 Summary

All the data presented in this section have led to two main conclusions. The first one is related to the electronic structure of the CoO layers grown on HOPG. A detailed analysis of the XPS Co $2p_{3/2}$ spectra has shown size effects for the CoO ultra-thin films grown at the early stages of growth. These ultra-thin films show a loss of covalence in their bonds as a result of their bidimensional character. The XAS and PES spectra have given us the second major conclusion of this section: there is a strong interaction between the as-grown CoO deposits and the surface of the HOPG substrate. This interaction is causing the distortion of the CoO structure (as evidenced by the anisotropy seen in the Co 2p and O 1s XAS spectra for low coverages), the modification and oxidation of the HOPG surface (the C-O and C=O peaks seen in the XPS, PES and XAS C 1s spectra), and the wetting layer autoassembling seen in the AFM images of the growth. This is not entirely unexpected, though: both metallic cobalt and their oxides are well-known catalysts for carbon oxidation reactions and Fischer-Tropsch processes [25–27], thus some reaction between the CoO deposits and the substrate could be expected.

SECTION 5.5

Nanopatterning on Graphite surfaces promoted by Cobalt oxides

5.5.1 Introduction

In this section, all the results about the reoxidation of CoO samples grown on HOPG will be presented. It will be shown that the main reoxidation process used in this work (Reox-P1 process) promotes the formation of nanochannels, thus leading to the possibility of nanopatterning on the HOPG surface. Since the discovery of the unique physical and chemical properties of graphene, the possibility of fabricating nanostructures by patterning on graphene and graphite surfaces has become a hot research topic due to the multiple applications these materials find in many technological fields [28]. Different from most of the patterning techniques, including lithography [29], plasma etching [30] and electro catalysis using scanning probe microscopes [31, 32], carbon gasification catalysed by metallic nanoparticles in controlled atmosphere at high temperatures has demonstrated to be one of the most efficient methods as cutting tool for graphene [33]. Carbon gasification reactions have been studied using a large variety of metallic nanoparticles and reactant gases such as steam, molecular oxygen, carbon dioxide and hydrogen. For instance, Ci et al. [33] reported the use of Ni nanoparticles and hydrogen for the fabrication of single etch patterns in HOPG at temperatures ranging from 750 to 1100 °C; Severin et al. [34] have used silver nanoparticles and molecular oxygen to produce channelling in graphene at 650 °C; Konishi et al. [35] used Co nanoparticles heated under a gas mixture stream of high purity H_2 (10%) + N_2 (90%) gas at 700 °C; Datta et al. [36] have reported the crystallographic etching of graphene using Fe nanoparticles in H_2 and Ar_2 atmosphere at 900 °C. Moreover, by taking advantage of the ferromagnetic behaviour of the cobalt nanoparticles, Bulut et al. reported a writing method on HOPG surfaces steered by magnetic fields at about 550 °C in air [37]. All these reported methods for channelling formation by carbon gasification are efficient at relatively high temperatures (>600 °C). In general, gasification reactions between carbon and the reactant gas are produced at the carbon-catalyst particles interface (solid/solid/gas reaction), resulting in pitting and deep channelling of the carbon surface with the movement of the catalyst particle along the basal plane [38]. However the mechanisms involved in the reaction of each metallic particles and reactant gases used in these reactions are not completely understood yet.

In this section we will present an effective patterning method on graphite at lower temperatures (400 °C) than those using metallic nanoparticles reported in the literature. Our method uses the cobalt oxide samples grown on HOPG as starting catalyst material, and molecular oxygen as reactant gas. Both the channels produced by this process and the final state of the cobalt oxide overlayers will be characterized by XPS, XAS, RGA, PES and AFM in subsections 5.5.3, 5.5.4 and 5.5.6. It will be shown that, at this temperature, this method is more efficient to produce nano-channelling in graphite using CoO oxide as catalyst than using metallic cobalt: the reasons for this enhanced efficiency will be studied and explained in subsection 5.5.5, and the set of minimum conditions for this nanopatterning will be determined in subsection 5.5.7. Finally, the results of two studies of possible diffusion of Co into the HOPG substrate after this

reoxidation process will be presented in subsection 5.5.8.

5.5.2 Experimental process

The reoxidation of the samples has been performed by two different thermal oxidation methods, called Reox-P1 and Reox-P2. Although the conditions and order of the stages of each process have been described in subsection 2.3.3 (page 50), we will repeat here the most important steps of both processes. The experiments were started with the growth of an 2 ML CoO sample on HOPG. Once the CoO layers were grown, they were submitted to the reoxidation process, which basically consists of exposure at oxygen atmosphere (P_{O_2}=$2 \cdot 10^{-3}$ mbar) and thermal annealing at 400 °C for 1 h. However, in order to distinguish the effect of both, oxygen exposure and thermal annealing, the re-oxidation process was performed in two different ways: for the first process (labelled as Reox-P1), the oxygen exposure was delayed until the substrate temperature reached 400 °C in ultra-high vacuum conditions, approximately in 10 min. In the second process (Reox-P2) the oxygen exposure was started with the sample at room temperature, then reaching 400 °C while it was exposed to the oxygen atmosphere. Also a 3 ML sample of metallic cobalt was grown on HOPG under UHV conditions in order to compare its behaviour when submitted to the re-oxidation process Reox-P1.

The experiments related to this study have been performed in two different ultra-high-vacuum (UHV) chambers, one attached at the analysis chamber of the XPS spectrometer in our laboratory and the other located at the PM4 beamline at the synchrotron BESSY II (Berlin). The majority of the results of the first five subsections are extracted from in-situ measurements (XPS, PES, XAS and RGA results), while the AFM and Raman measurements were made ex-situ. All samples were measured before and after each process.

5.5.3 Chemical analysis of the Co final state

Figure 5.24 shows the Co 2p core-level XPS and XAS spectra of each step of the processes described in the experimental section. It is known that the oxidation state of cobalt catalysts surfaces may vary distinctively in the presence of oxygen as reactant gas [39], therefore the determination of the Co species involved in each of those processes is important to a better understanding of the mechanisms involved in the studied reaction. All the spectra present two main regions, the Co $2p_{3/2}$ and Co $2p_{1/2}$ levels, due to spin-orbit coupling. The Co $2p_{3/2}$ XPS and XAS spectra of the initial 2 ML sample of CoO on HOPG have already been described before, and they are fairly well reproduced by the calculations, when considering a high spin configuration of Co^{2+} ions in octahedral symmetry with a crystal field (10 Dq) of 0.5 eV. This is somewhat smaller than the usual value of 10 Dq for bulk CoO oxide, which is about 1.05 eV [6]. The reduced crystal field, in this case, is consistent with a decrease of coordination of the cobalt atoms in the CoO over-layer, and also coherent with its growth by thermal evaporation at room temperature and with the bi-dimensional character of the CoO wetting layer observed in subsection 5.3.2.

As it has been described in subsection 5.5.2, the next step consisted of annealing the sample at 400 °C for 30 min in UHV, labelled as “heated”. The XPS and XAS spectra change, being

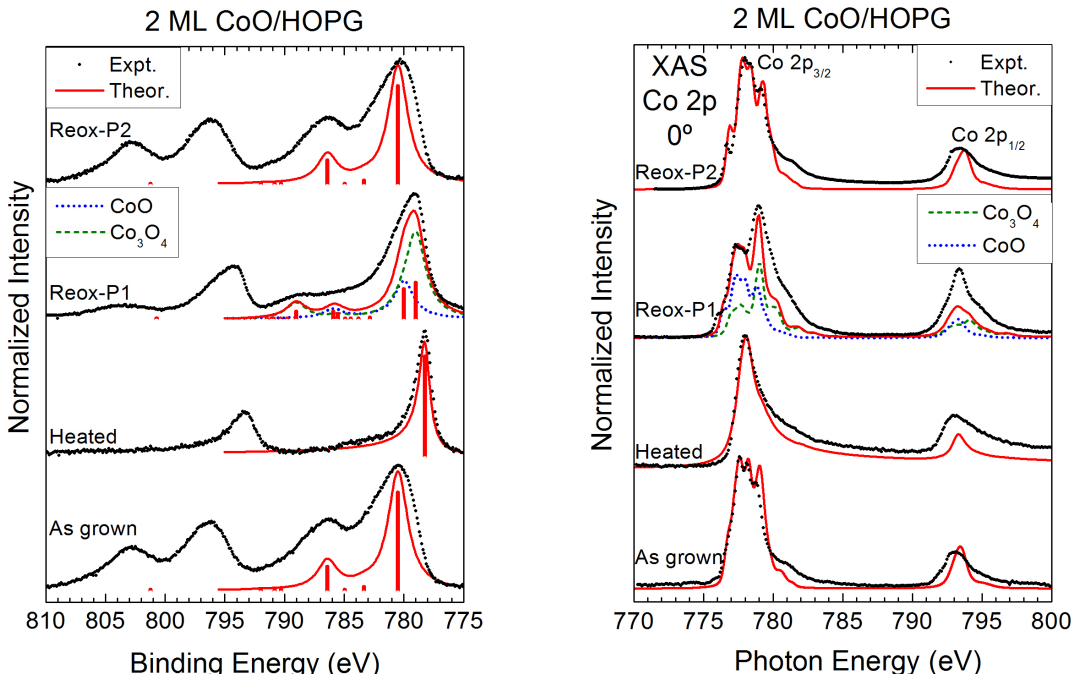

(a) Co 2p XPS spectra (b) Co 2p XAS spectra

Figure 5.24: Experimental (dots) and theoretical (lines) spectra of the Co 2p XPS and XAS spectra of the initial CoO ultra-thin layer as grown (bottom spectra) and submitted to each process (as labelled). For explanation see text.

much narrower than the previous ones, where the satellite in the XPS spectrum (figure 5.24a), as well as the multiplet structure in the XAS spectrum (figure 5.24b) vanish. These spectra are now related to metallic Co, for which the calculations are again in good agreement. Therefore, the results indicate that the first step of the Reox-P1 process reduces the initial CoO overlayer to metallic cobalt previously to the oxygen exposure. This result is consistent with the reducing character of the graphite substrate.

After the complete Reox-P1 process, the XPS and XAS spectra differ from those observed before. The main difference in the XPS spectrum is that the main peak is slightly shifted by 1 eV towards lower binding energies, and the satellite almost disappears, giving rise to two small satellites located at 786 eV and 789 eV. At first, this could indicate that the sample is now in the spinel Co_3O_4 phase. Nevertheless, the XAS spectrum shows again different multiplet structures, which cannot be reproduced solely with a spinel structure. The lower energy structures (777-778 eV) are similar to those observed in the as-grown sample, suggesting that this spectrum corresponds to a mixture of CoO and Co_3O_4 oxides. In fact, both experimental spectra are well reproduced by the calculations of a mixture of around 30% of Co^{2+} in octahedral symmetry (dotted blue curve) and about 70% of spinel Co_3O_4 (dashed green curve). These results show that after the complete Reox-P1 process, the reduced Co particles have been oxidized to Co_3O_4, with a remaining small fraction of CoO. On the other hand, when the initial CoO layer is submitted to the Reox-P2 process, the XPS spectrum is identical to that of the as-grown sample, and the XAS spectrum differs from it in the appearance of a new peak at threshold around 776

eV. The calculations again correspond to a high spin configuration of Co^{2+} ions in octahedral symmetry, but now with a crystal field (10 Dq) of 0.9 eV. The larger crystal field in this case is consistent with the formation of a more ordered and better coordinated CoO layer after Reox-P2 process.

By summarizing the chemical analysis results, the Reox-P1 process reduces the initial CoO layer to metallic cobalt during the first step (heating in UHV) and then oxidises the cobalt atoms located at the near-surface region to the spinel Co_3O_4 oxide upon oxygen exposure at 400 °C. In contrast, the Reox-P2 is not able to reduce the initial CoO layer neither to oxidise to Co_3O_4 maintaining the original oxidation state.

5.5.4 The channelling formation as observed by AFM

Figure 5.25 shows AFM topography images of 2 ML CoO/HOPG samples submitted to the three processes considered, and table 5.6 displays the average dimensions of the clusters found in these samples. Focusing on their shape, dimensions and distribution across the HOPG substrate, it is clear that the as-grown material forms nanoparticles after each of the three processes, which are spread across the terraces and steps of the substrate. These clusters have similar dimensions between each other, and their heights are always bigger than the height of the structures measured in the as-grown CoO samples. The main conclusion that can be extracted from their dimensions and shape is that their morphology is conformed when temperature is applied, and the addition of oxygen does not change it in a significant way.

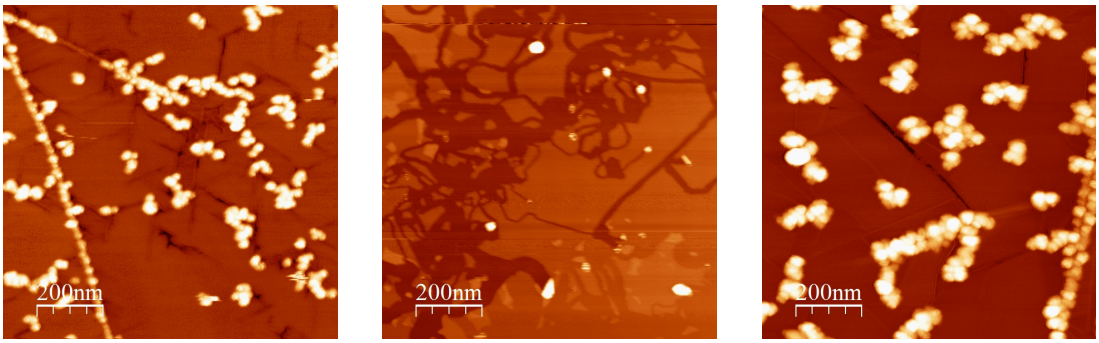

(a) Heated (b) Reox-P1 (c) Reox-P2

Figure 5.25: AFM topography images of 2 ML samples of CoO on HOPG submitted to the three processes considered: (a): heated, (b): Reox-P1, and (c): Reox-P2. Size of the images: 1 µm × 1 µm.

Now we will look at the effects of these processes on the substrate. The images from the heated sample (figure 5.25a) shows the presence of blurred short lines following preferential directions forming angles of 60° and 120° with respect to each other. Similar preferential lines on HOPG and graphene have already been observed during the catalyzed hydrogenation of graphene at temperatures higher than 600 °C with Ni, Co, Fe nanoparticles producing etching of the graphene surface along the crystallographic axes [33, 35, 36].

However, the most striking results come from the images of the samples after the Reox-P1 process (figure 5.25b), which clearly shows multiple nanochannels with trajectories randomly

Process	Width (nm)	Height (nm)
Heated	200±60	8±2
Reox-P1	170±80	8±3
Reox-P2	210±75	11±4

Table 5.6: Mean width and height of the clusters produced in the 2 ML CoO samples after the three processes considered, as seen in the AFM topography images.

distributed along the HOPG surface. The presence of small Co_3O_4 islands at the end of the channels suggests that these particles have moved randomly throughout the HOPG surface activated by temperature and react with the carbon atoms via gasification, leading to the erosion of the surface and producing nano-channel. The width of the channels observed in the topographic images is determined by the lateral size of the Co nanoparticle whereas their depth is always a multiple of 3.35 Å, i.e. the distance between graphite planes [40] (see table 5.7). On the other hand, figure 5.26 shows the AFM image taken in topographic and phase mode from a devastated area of the graphite surface. As the information given by the AFM images taken in phase mode is related to the viscoelasticity of the probed material (see subsection 3.2.1, page 68), it is inferred that the material of the nano-channel is also graphite, confirming the catalytic reaction of carbon gasification. Furthermore, Residual Gas Analysis (RGA) performed with a mass spectrometer (figure 5.27) during the Reox-P1 process indicates the production of CO when the oxygen exposure was initiated, which is another confirmation of the carbon erosion by the clusters. All of these results confirm our previous assumptions about the composition and catalytic origin of these channels.

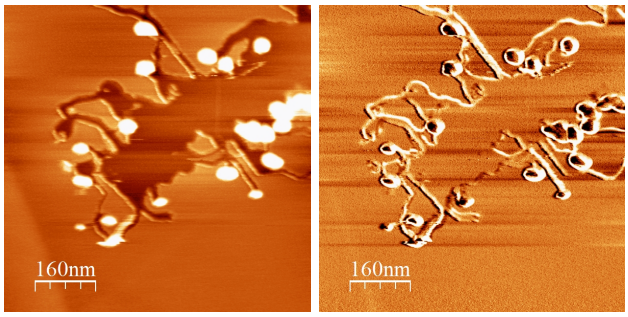

Figure 5.26 AFM topography (left) and phase (right) images of a 2 ML sample of CoO on HOPG after the Reox-P1 process. Size of the images: 800 nm × 800 nm.

Height	Number of planes
0.34±0.02	1.02±0.01
0.68±0.04	2.06±0.03
1.01±0.09	3.03±0.03

Table 5.7 Mean depth of the nanochannels formed on the 2 ML sample of CoO on HOPG after the Reox-P1 process, as seen in the AFM topography images. The HOPG interplanar distance is taken as 3.35 Å [40]

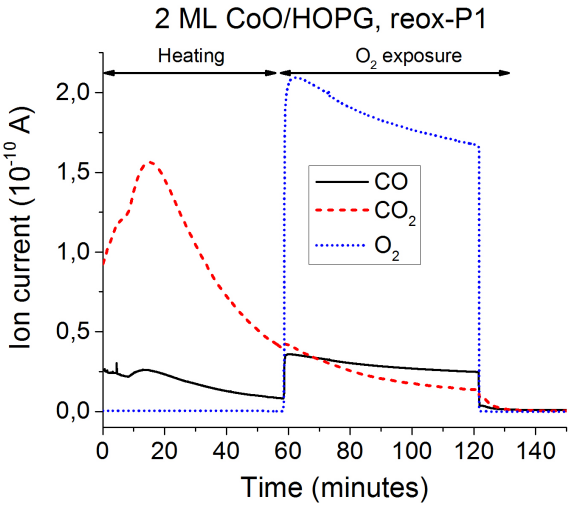

Figure 5.27: RGA recorded during the Reox-P1 process of the initial CoO layer

Another important conclusion comes from the comparison of the Reox-P1 and Reox-P2 images (figures 5.25b and 5.25c): when the re-oxidation process is performed by heating the initial CoO layer under the same oxygen environment (Reox-P2), no formation of nanochannels is observed, however preferential lines following the crystallographic edges are clearly observed. This result is not surprising: the intermediate state of the Reox-P1 process gives metallic Co particles, which are known to produce similar channeling formation when exposed to either oxygen or hydrogen [35, 41–43].

5.5.5 Reduced Co particles versus freshly evaporated Co particles

5.5.5.1 Morphological characterization: AFM

One of the main conclusions extracted from the last subsection is that the reduction of CoO into Co is the most important factor in the nanochannels appearance. In order to test this, and also as a way to compare the efficiency of our method with other experiments, a sample of 3 ML of Co was grown in UHV and submitted in-situ to the Reox-P1 process. Figure 5.28 shows the AFM images of the metallic Co nanoparticles as reduced from the initial CoO layer upon heating at 400 °C (figure 5.28a) and the Co nanoparticles formed by evaporation of metallic cobalt in UHV conditions (figure 5.28c). Table 5.8 displays the dimensions of the clusters seen in the freshly evaporated Co sample before and after the Reox-P1 process.

Two main differences of these Co nanoparticles are observed: firstly, the nanoparticles coming from the reduction of the initial CoO layer are smaller in width (200±60 nm) than those from the cobalt evaporation (100±60 nm). Secondly, the density of Co nanoparticles per unit area resulted from the evaporation is larger than that of the nanoparticles obtained upon reduction of the initial CoO layer, although this difference is obviously due to the larger coverage of the initial evaporated nanoparticles than that of the initial CoO layer. But the main differences are observed in the images of those Co particles after the Reox-P1 process shown in figures 5.28b and 5.28d. Clearly, the nanoparticles formed upon reduction of the initial CoO

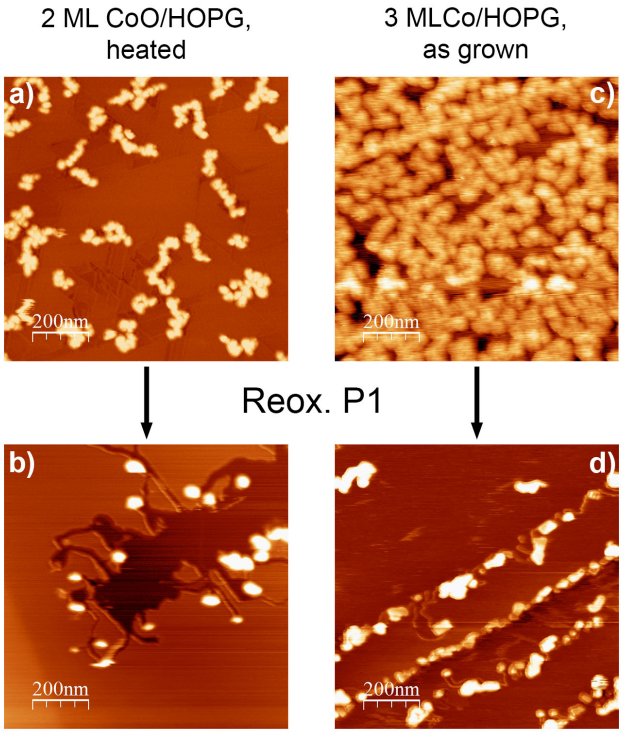

Figure 5.28: 1 µm × 1 µm AFM topography images of a) metallic cobalt nanoparticles as a result of the initial CoO ultra-thin layer submitted to heating at 400 °C in UHV conditions; b) the initial CoO ultra-thin layer submitted to the complete Reox-P1 process; c) 3 ML of evaporated cobalt nanoparticles in UHV; d) evaporated metallic cobalt nanoparticles submitted to the complete Reox-P1 process.

layer efficiently produce nano-channelling, whereas the freshly evaporated Co nanoparticles do not: this experiment directly confirms the enhanced efficiency of our process and the relevance of these results.

Sample	Width (nm)	Height (nm)
3 ML Co/HOPG, as grown	100±60	5±1
3 ML Co/HOPG, after Reox-P1	100±60	9±3

Table 5.8: Mean width and height of the clusters observed in the 3 ML sample of Co on HOPG, before and after the Reox-P1 process.

5.5.5.2 Chemical characterization: XPS and XAS

The results obtained in the last subsubsection suggest that there must be some kind of difference between the nanoparticles coming from the freshly evaporated Co and the reduced

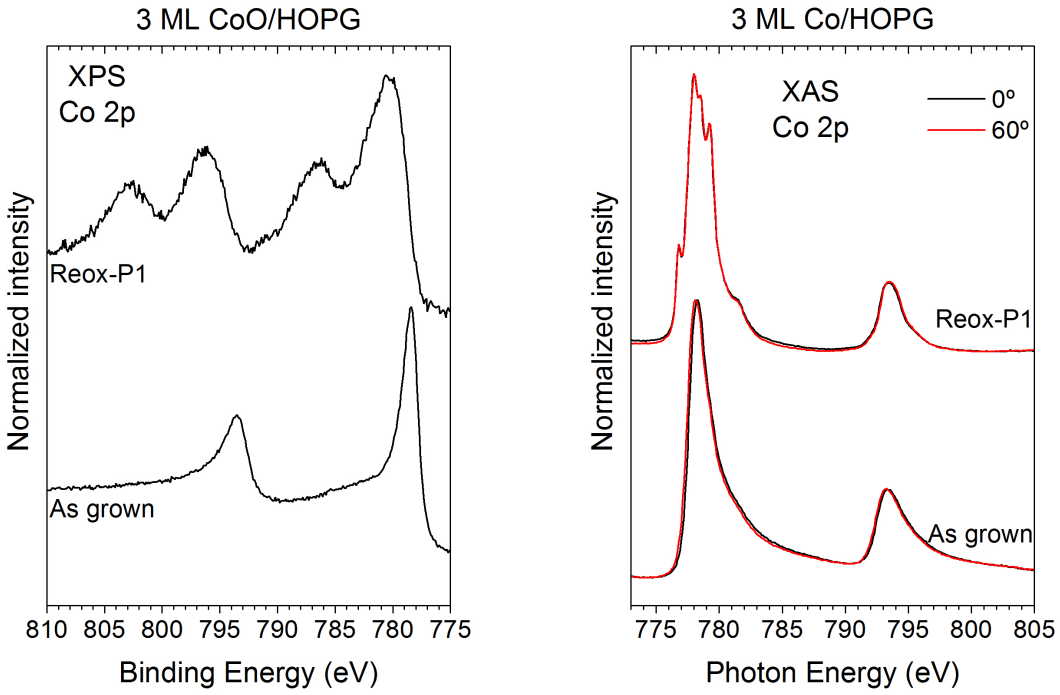

(a) XPS measurements of the Co 2p region.

(b) XAS measurements of the Co 2p region, for sample-beam angles of 0° (black line) and 60° (red line).

Figure 5.29: XPS and XAS Co 2p spectra of the sample with 3 ML of Co on HOPG, before and after the Reox-P1 process.

CoO samples. We have explored possible differences in the electronic structure of these two samples with XPS and XAS. Figure 5.29 shows the XPS and XAS Co 2p spectra of 3 ML samples of Co grown on HOPG before and after the Reox-P1 process. It is seen that the final oxidation state of the evaporated cobalt nanoparticles after the complete Reox-P1 is Co^{2+} (CoO) instead of Co_3O_4. The spectra of the evaporated Co nanoparticles (labelled "as grown") seem to be identical as those of the reduced Co nanoparticles shown in figures 5.24a and 5.24b, whose calculations clearly indicate the presence of metallic cobalt.

Figure 5.30 shows a comparison between the XPS and XAS Co 2p spectra of a heated 2 ML CoO sample and a "as grown" 3 ML Co sample, both grown and treated in UHV conditions. The XAS spectra of both samples (figure 5.30a) do not show any difference between them, and they also do not show any difference when the 0 and 60° spectra are plotted against each other. The only difference appears in the Co 2p XPS spectra (figure 5.30b), in which the binding energy for the reduced Co nanoparticles is slightly shifted by 0.17 eV towards lower binding energies. Two possible explanations can be argued to explain this effect: different relaxation energy of the nanoparticles due to changes in their size, and differences in the local environment of the Co atoms of the nanoparticles. The first hypothesis is not convincing since the difference in size is small (25-50 nm for the reduced nanoparticles versus 50-100 nm for

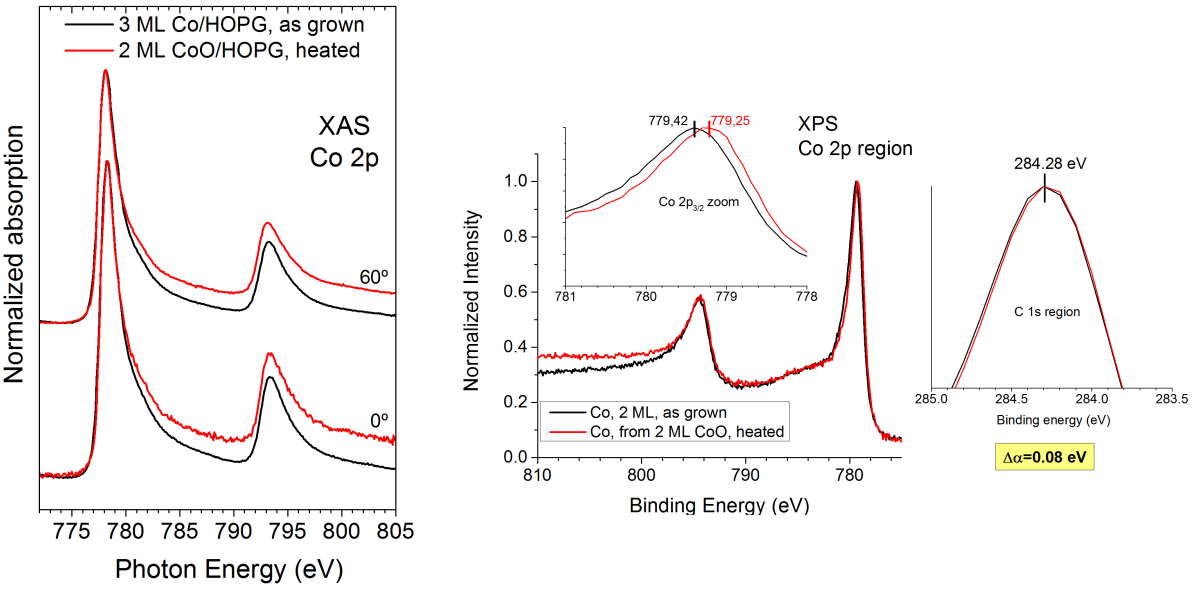

(a) XAS Co 2p spectra.

(b) XPS Co 2p spectra. Insets show zooms of the Co $2p_{3/2}$ and the C 1s regions. $\Delta\alpha$ refers to the Auger parameter.

Figure 5.30: Comparison of the normalized Co 2p XPS and XAS spectra for the as-grown 3 ML of Co on HOPG sample (black line) and the heated 2 ML of CoO on HOPG sample (red line).

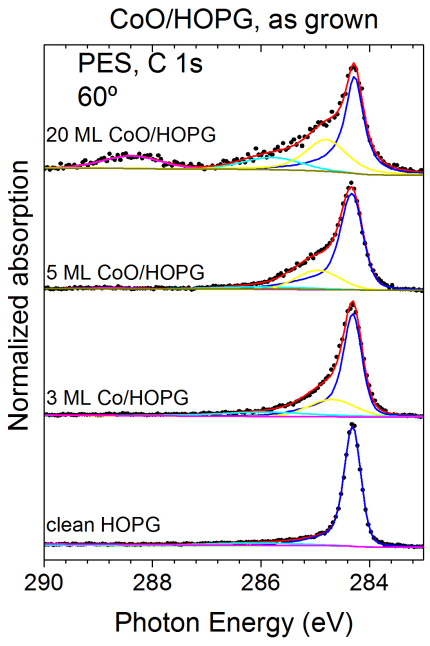

Figure 5.31: PES C 1s spectra and fittings. Samples and coverages as labelled. Take-off angle: 60°, hν=380 eV

Sample	Energy (eV)	FWHM (eV)	Area
Co/HOPG, 2 ML	284.3	0.4	$1.18 \cdot 10^5$
	285	0.95	$3.18 \cdot 10^4$
	285.97	1.31	$2.00 \cdot 10^4$
	291.5	5.1	3333
CoO/HOPG, 5 ML	284.3	0.45	$1.21 \cdot 10^5$
	284.85	0.9	$3.32 \cdot 10^4$
	285.9	1.27	$1.22 \cdot 10^4$
	288.7	1.27	1884
CoO/HOPG, 20 ML	284.3	0.4	$2.48 \cdot 10^4$
	284.8	0.9	$1.35 \cdot 10^4$
	285.85	1.28	5935
	288.6	1.27	5994

Table 5.9: Peaks and parameters used in the fittings of the PES C 1s spectra shown in figure 5.31.

the evaporated nanoparticles) and no quantum size-effects are expected in these relative large nanoparticles. Besides, the binding energy for the smallest nanoparticles should shift towards higher energies as relaxation energy accounts for energy losses of the photoelectrons. The most plausible hypothesis seems to be the second one, i.e. different local environment of the Co nanoparticles.

Aside from these differences in the local environment of the Co nanoparticles, the results obtained in the study of the as-grown CoO samples suggest that the enhanced efficiency of the reduced Co particles could be related to the surface modifications caused by the CoO deposited on the HOPG surface. As a way to prove this, PES measurements of the C 1s region were also made for the 3 ML Co/HOPG sample: the geometry configuration was set to get the most superficial results possible ($h\nu$=380 eV, take-off angle=60°, $\lambda \sim$4 Å). The results of these measurements, fittings for this spectrum, and a comparison with the C 1s PES spectra for 5 and 20 ML samples of CoO grown on HOPG are shown in figure 5.31. The peaks used for these fittings are the same used in the previous PES spectra fittings of the CoO samples grown on HOPG: an asymmetrical peak at 284.2 eV for the C-C sp^2 bonds of the substrate, and symmetrical peaks at 285, 285.8 and 286.5 eV for the rest of the peaks. The parameters obtained for the peaks used in all the spectra displayed in figure 5.31 are shown in table 5.9.

The spectrum of the 2 ML Co/HOPG sample (second spectrum of figure 5.31) also shows a broadening of the main carbon sp^2 peak. This broadening is caused by a peak located at 285 eV, while in the case of the CoO/HOPG samples, it was caused by a peak located at 284.8 eV. Thus, the appearance of this peak suggests the weakening of the sp^2 bonds in graphite by the presence of both Co and CoO. However, the 285.8 and 288.5 eV are not seen in the as grown cobalt sample spectrum. This suggest that the deposited Co is modifying the HOPG surface in a different way, and that it is not weakening the sp^2 bonds of graphite as much as the deposited cobalt oxide. In this picture, the catalytic carbon gasification reaction of the HOPG surface is more efficient for CoO oxide grown on HOPG because of the enhanced weakening of the surface carbon bonds that the CoO provokes. This is also supported by the already displayed XAS O 1s spectra of the as-grown CoO samples (figure 5.16, page 142), which indicate that the O atoms at the interface are interacting with the HOPG surface or, in other words, that the HOPG surface is oxidized by the presence of the oxygen in cobalt oxide at the interface.

5.5.6 Raman study of defects on the HOPG surface

It has been proven that the Reox-P1 process creates channels when applied to a CoO sample grown on HOPG, so it seems logical to think that these channels will have different properties than the rest of the substrate. In order to study the electronic properties of the HOPG surface after these processes, 2 ML CoO samples were submitted to the three processes studied in this section, and measured ex-situ by Raman confocal spectroscopy, with the experimental conditions stated in subsection 3.3.2 (page 72).

Figure 5.32 shows Raman spectra for all the processes tested in this study, as well as spectra from a clean HOPG substrate and a as-grown 2 ML CoO sample, measured both for reference purposes. The Raman spectra displayed have been extracted from the zones marked with crosses in the AFM and optic microscope images, which correspond always to zones with a CoO_x cluster, and a HOPG terrace or step. The AFM integrated in the Raman spectrometer

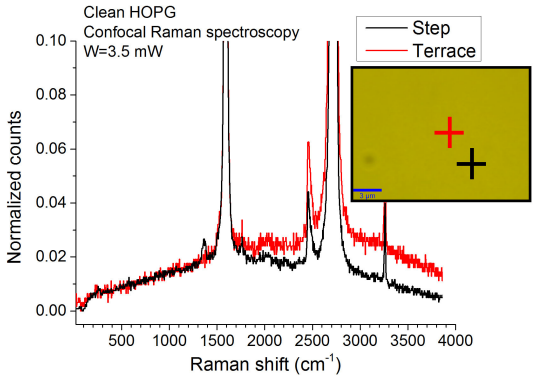

(a) Clean HOPG

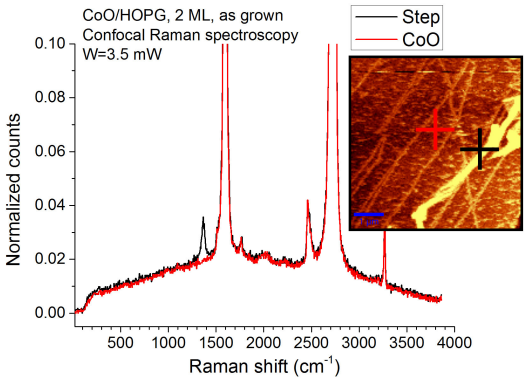

(b) As grown

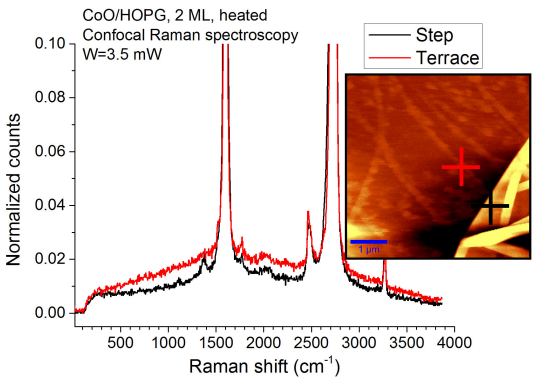

(c) Heated

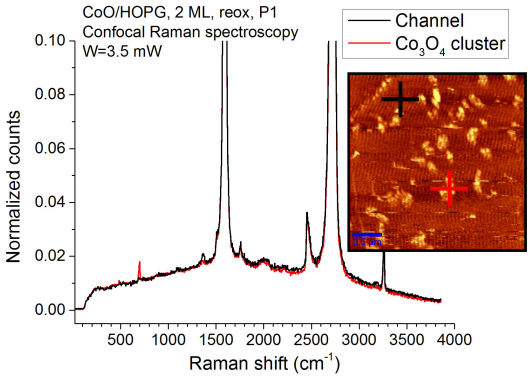

(d) Reox-P1

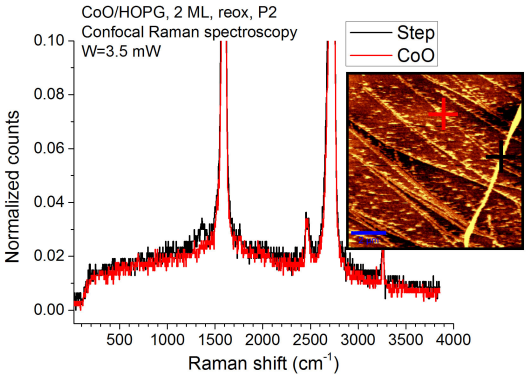

(e) Reox-P2

Figure 5.32: Raman measurements for (a) a clean HOPG sample, (b) as-grown 2 ML of CoO on HOPG, and (c), (d) and (e), 2 ML of CoO on HOPG samples after the three processes considered. The insets show AFM/optic microscope images showing where the spectra were taken: the crosses indicates the precise location where they were measured.

Raman shift (cm^{-1})	Assignation
484 691	CoO [46]
480 522 618 690	Co_3O_4 [46]
1335	Defective carbon (*D* band) [47–49]
1570	Graphite, sp^2 bonds (*G* band) [47–49]

Table 5.10: Most important Raman bands studied in this work.

has less resolution than that used in the rest of the AFM images shown in this work, so all the channels and other structures seen before will not be well resolved in these images.

The most important bands that we are interested for this study are summarized in table 5.10. Aside from the CoO and Co_3O_4 bands, we will look at changes in two of the characteristic HOPG bands, which are called *G* and *D*. The *G* band ($\sim$1570 cm^{-1}) is due to the bond stretching of all pairs of sp^2 atoms in both rings and chains, and it is the most intense of the bands in a HOPG spectrum. The *D* band ($\sim$1335 cm^{-1}) is due to the breathing modes of sp^2 atoms in rings [44, 45], and it only appears when defects are present on the aromatic structure of the graphite honeycomb lattice, like edges or discontinuities. An analysis of the 2*D* band ($\sim$2700 cm^{-1}) is not performed, since its shape and intensity changes strongly with the number of planes analysed, and very subtle changes in the laser focus would lead to big changes in its shape.

All the spectra show the typical HOPG *G*, *D* and 2*D* bands, located roughly at the Raman shift positions mentioned in table 5.10. As expected, the *G* band is always the most intense band of all the spectra, and the *D* band intensity grows when they are taken at a step. The Reox-P1 sample (figure 5.32d) shows the typical Raman bands for the Co_3O_4, but no Co or CoO bands can be seen in the as-grown, heated and Reox-P2 samples (figures 5.32b, 5.32c and 5.32e, respectively). This is expected: the CoO bands are much less intense than the Co_3O_4 bands [50], so no CoO Raman signal can be detected for the low coverages present in the as-grown and Reox-P2 samples. Also no cobalt could possibly be detected in the heated sample, since a metal is infinitely polarizable, and hence it will not yield any Raman signal. Another important result is that these spectra do not show any band that could arise from groups different from those related to HOPG or Co_3O_4, like C-H ($\sim$3000 cm^{-1}), C-O ($\sim$1200 cm^{-1}) or sp^3-bonded carbon ($\sim$2200 cm^{-1}) bands [51]. The C-O or C=O bands are not expected in the Reox-P1 sample, since they did not appear in the XPS and PES spectra, but the absence of these bands in the as-grown sample could be caused by two reasons. One of them is the sampling depth of this technique, which could be too large to be able to resolve such small and superficial contributions. The other reason would be more simple, and in the case of the as-grown sample, could only be applied to the absence of C-H or sp^3-bonded carbon bands: there are no groups like this in the samples.

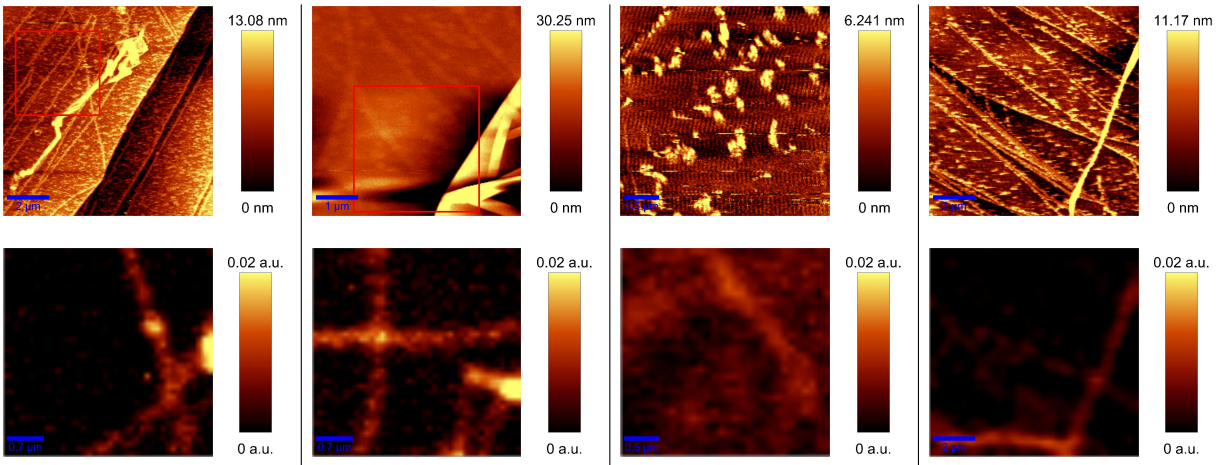

(a) As grown (b) Heated (c) Reox. (P1) (d) Reox. (P2)

Figure 5.33: AFM (top) and Raman images of the D/G band ratio (bottom) for four samples of 2 ML of CoO on HOPG: as grown (a), heated (b), Reox-P1 (c) and Reox-P2 (d). The red squares in the AFM images are the zones mapped with Raman spectroscopy at their respective bottom images. In the case that there is not a red square, it means that the whole image has been mapped. All Raman images have been normalized to the same units for comparison purposes.

The distribution of the D band across the HOPG surface has been studied taking Raman spectra across a whole area and integrating the D and G band in each spectrum. The resulting images have a lateral resolution of 100 nm, and represent the D/G bands ratio, effectively mapping the spatial distribution of the defects. These images are presented in figure 5.33: the AFM images are presented in the top row and the Raman D/G images at the bottom. The AFM images have red squares indicating the precise zone where the Raman images have been extracted. In the cases where the whole area covered by AFM has been used for the Raman image, no red square appears.

The Raman images for the as-grown, heated and Reox-P2 samples (figures 5.33a, 5.33b and 5.33d, respectively) show defects that can be related with pre-existent HOPG features, such as folded planes, edges, steps, etc. However, the image taken after the Reox-P1 process (figure 5.33c) show a much more widespread distribution of the D band across the sample surface. This means that defects have been produced in the surroundings of the cobalt oxide areas, whereas the rest of the images show only the original defects at the steps of the HOPG substrate, confirming that the Reox-P1 process is efficient in the creation of defects in graphite and thus suitable for the creation of nanostructures on its surface, i.e. nanopatterning on the HOPG surface.

Figure 5.34 shows the depth profile (XZ) micro-Raman image taken from a sample submitted to the Reox-P1 process, as well as Raman spectra measured in three areas, as indicated by the crosses. This Raman image is colour-coded, where the intensity of the colour is correlated with the Raman intensity of three different bands: the A_{1g} mode of spinel Co_3O_4 oxide (solid red line), the D band assigned to defects in graphite (dashed blue line) and the G band of the pure graphite substrate (dotted green line). The Raman spectra of the substrate covered by

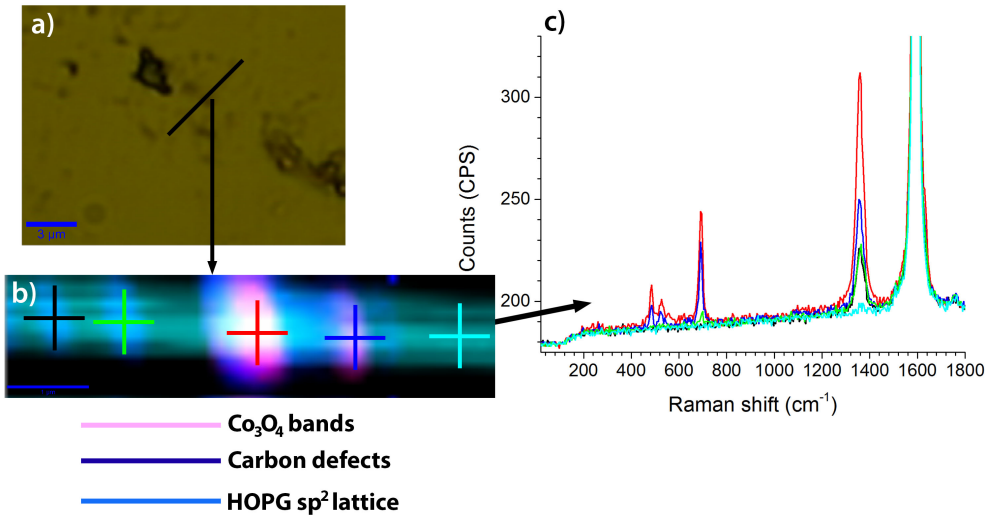

Figure 5.34: a) Optical microscope image of a 2 ML CoO/HOPG sample after the Reox-P1 process. The line marks the zone mapped with Raman in the next image. b) Micro-Raman X-Z image of 2 ML of CoO grown on HOPG submitted to Reox-P1. Crosses indicate the position where the bands shown at the bottom have been measured. c) Carbon Raman bands measured as indicated at image b).

large cobalt oxide islands (solid red cross) show strong defects D band whereas the substrate uncovered (dotted green cross) show no defects. This clearly indicates that the cobalt oxides formed upon Reox-P1 are producing a large amount of defects on the HOPG surface. There are some areas (only blue areas) in which the graphite substrate presents *D* band due to defects but there is not spinel Co_3O_4 oxide. These regions seem to correspond to the channels displayed in AFM, at the end of which the spinel Co_3O_4 oxide is located.

5.5.7 Characterization of the base conditions of the Reox-P1 process

Given all these important results obtained, a characterization of the base conditions necessary for the nanochannels formation is both relevant and important. In order to do this, default conditions for the Reox-P1 process were defined (table 5.11). From this starting point, changes in the CoO coverage, O_2 pressure, O_2 exposure time and annealing temperature were

Parameter	Value
Coverage	2 ML
Heating temperature	400 °C
O_2 exposure time	1 h
O_2 pressure	$2 \cdot 10^{-3}$ mbar

Table 5.11: Default conditions for the Reox-P1 process

explored: only one condition at a time was changed in each series of experiments, leaving the rest as the default values defined in table 5.11. The morphology results will be presented first in each subsubsection, and the electronic characterization will be presented afterwards.

5.5.7.1 CoO coverage

Firstly, we checked the dependence of the nanochannels formation as a function of the coverage. Figure 5.35 shows AFM images for samples with initial CoO coverages of 1, 4 and 20 ML samples submitted to the Reox-P1 process. Nanochannels can be seen for the 1 and 4 ML samples, but not on the 20 ML sample: this sample only shows the Co_3O_4 clusters, which have coalesced and covered all the HOPG substrate. This yields a logical conclusion: we need the right amount of material for the observation of the nanochannels.

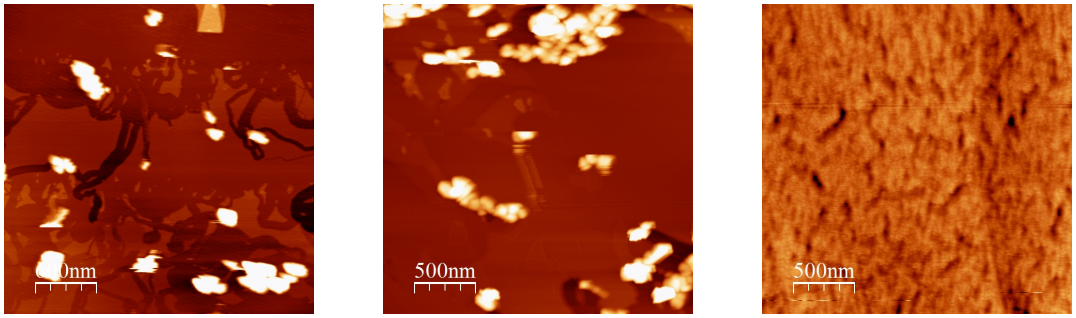

(a) CoO coverage: 1 ML. Image size: 3 μm × 3 μm

(b) CoO coverage: 4 ML. Image size: 2.5 μm × 2.5 μm

(c) CoO coverage: 20 ML. Image size: 2.5 μm × 2.5 μm

Figure 5.35: AFM topography images for samples of CoO on HOPG after Reox-P1, with changes made to the initial CoO coverage. CoO coverage and image size as labelled.

The electronic properties were studied by XPS, PES and XAS. Figure 5.36 shows the in-situ XPS Co $2p_{3/2}$ spectra for coverages ranging from 2 to 20 ML. All the spectra were measured in the same position with respect to the analyser and the X-ray source, and are presented normalized with respect to their minimum value. The spectra show that the final state of the material after the Reox-P1 process is Co_3O_4 for the three samples, which means that the final oxidation state after the process does not depend on the coverage. The intensity of the spectra for the 4 and 20 ML samples do not show a decrease after the Reox-P1 process, but the 2 ML sample shows a loss of intensity.

The 20 ML coverage was also grown and measured in-situ by PES and XAS in the PM4 beamline at BESSY: the results are shown in figures 5.37 and 5.38. They both show similar features as those seen in the study of the 2 ML sample. The C 1s spectra after the Reox-P1 process are closer to the clean HOPG spectra, and all the peaks already studied in the previous chapter disappear (PES) or their intensity is severely diminished (XAS). The XAS spectra show no differences when the beam angle is changed, as in the case of the spectra of the as-grown 20 ML sample. Also, the PES O 1s spectra presents broader peaks after the Reox-P1 process when it is measured with a take-off angle of 60°, which could mean that this spectra has more contributions that those originally considered, although this effect could also be a distortion

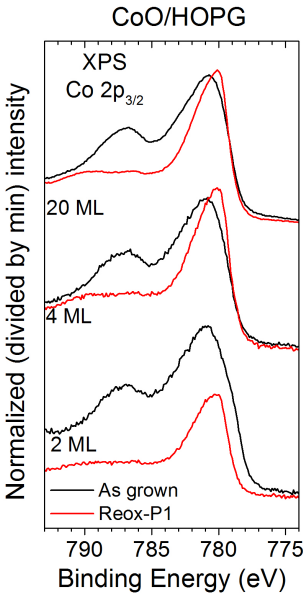

Figure 5.36: XPS Co $2p_{3/2}$ spectra of the 2, 4 and 20 ML samples of CoO on HOPG, before and after the Reox-P1 process.

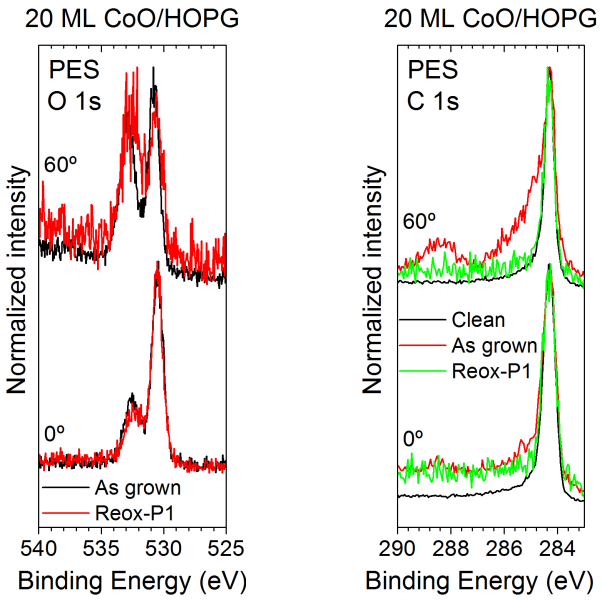

(a) O 1s (b) C 1s

Figure 5.37: PES O 1s and C 1s spectra of the 20 ML sample of CoO on HOPG, before and after the Reox-P1 process. (b) also includes the spectra of the clean HOPG substrate before the deposition of CoO.

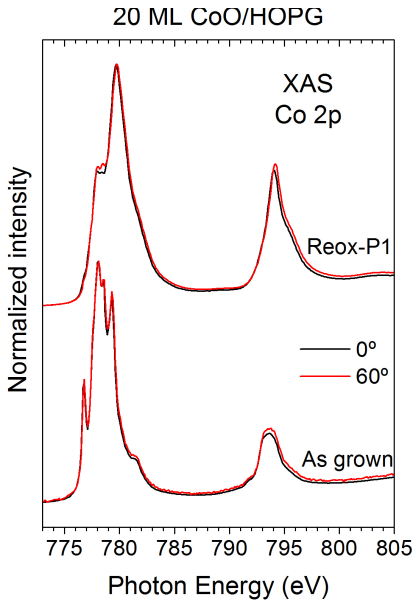

(a) XAS Co 2p spectra, 0 and 60°.

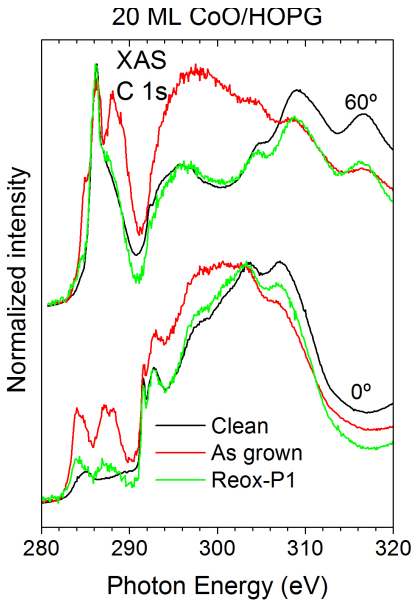

(b) XAS C 1s spectra, 0 and 60°.

Figure 5.38: XAS Co 2p and C 1s spectra for the 20 ML sample of CoO on HOPG, before and after the Reox-P1 process.

caused by the large noise of this spectrum. Nevertheless, these results agree with the Raman results already presented for the Reox-P1 sample: no C-O or C=O bands are observed after the process, and the *D* band will not give a different signal in XPS or XAS, since it only accounts for discontinuities in the graphite planes, and not for different hybridizations or bonds with other elements.

5.5.7.2 Annealing temperature

The next experimental condition tested was the temperature of the treatment, which was changed between 200 and 600 °C, the maximum temperature available in our experimental setup. The AFM measurements for samples with temperatures of 200, 300 and 600 °C are shown in figure 5.39. They show that the nanochannels have been only produced in the 600 °C sample, which allow us to introduce a temperature boundary condition for their appearance in the range between 300 and 400 °C. The 600 °C sample has more channels, pits and areas scratched than the 400 °C one, which means that more temperature further accelerates the attack on the HOPG surface by the CoO_x clusters, something that agrees completely with the catalytic origin of the nanochannels found in the last subsections.

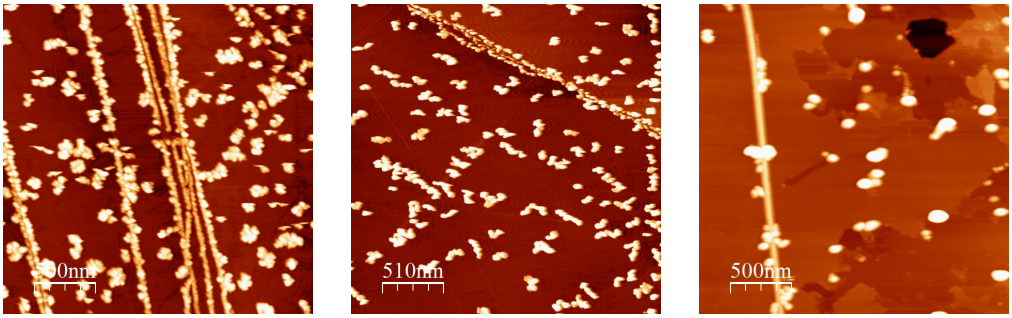

(a) 200 °C, size: 2.5 µm × 2.5 µm (b) 300 °C, size: 2.5 µm × 2.5 µm (c) 600 °C, size: 2.5 µm × 2.5 µm

Figure 5.39: AFM topography images of 2 ML samples of CoO on HOPG after Reox-P1, with changes in the annealing temperature. Range explored: 200-600 °C. Size and temperature as labelled.

The XPS survey and Co 2p spectra of all the temperatures explored are summarized in figure 5.40. They show two main things: CoO instead of Co_3O_4 when the temperature is 600 °C, and a loss on intensity of the Co 2p peak signal that is larger as the temperature increases. The first phenomenon can be studied better if the Co 2p spectra are normalized and plotted against each other: this is presented in figure 5.40b).

This figure shows that, as temperature increases, the intensity of the satellite structure becomes more defined and closer to the CoO satellite structure. Therefore, we can conclude that the reoxidized percentage of material decreases with the temperature, with the 600 °C sample having mostly CoO. This can be expected, since it is known that the Co_3O_4 is not stable at atmospheric pressure for temperatures above 950 °C, and it reduces to CoO [52, 53]. In an atmosphere with an oxygen pressure of five less orders of magnitude, this reduction temperature is expected to be smaller, as the spectrum of the 600 °C sample is showing. Also, the

reducing role of the HOPG substrate and the carbon monoxide produced in these experiments could be related to the decrease of this temperature.

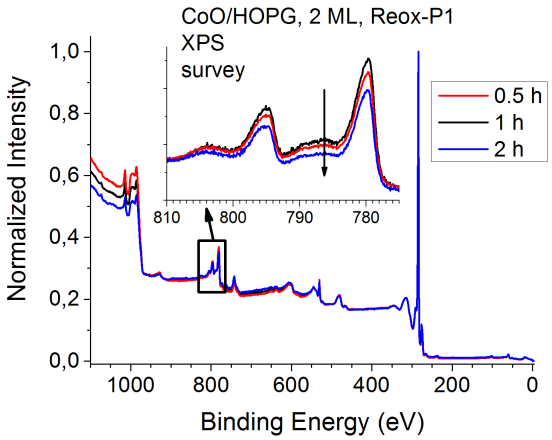

(a) Normalized XPS survey spectra. The inset shows the Co 2p spectra, normalized with respect to the value at 765 eV.

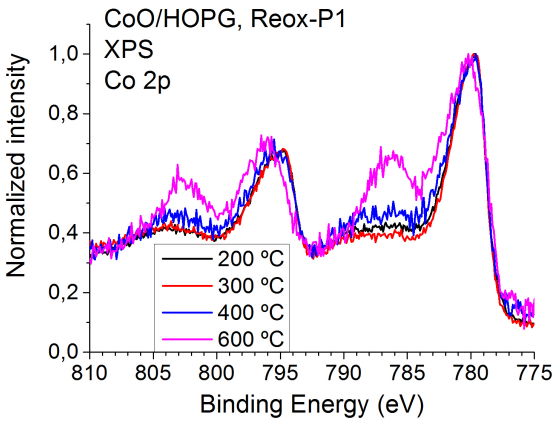

(b) Normalized (0-1) XPS Co 2p spectra.

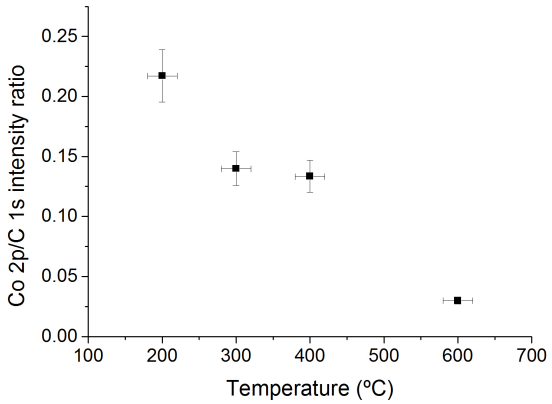

(c) Co 2p/C 1s intensity ratio as a function of the heating temperature.

Figure 5.40: Normalized XPS survey and Co 2p spectra of 2 ML samples of CoO on HOPG after the Reox-P1 process, with changes in the heating temperature. Range explored: 200-600 °C.

The reduction in the Co 2p signal intensity is found to be linear if it is represented against the reoxidation temperature (figure 5.40c). The two main explanations for this loss of intensity are either desorption of CoO_x into the vacuum, or diffusion of Co into the HOPG structure. The possibility of a carbon-based layer deposited on top of the CoO_x clusters was also explored, but it was discarded after considering the XPS spectra displayed in figure 5.36. Indeed, if there was a carbon layer deposited, its origin should be in the scratched carbon from the substrate, but the 4 ML sample, which also showed nanochannels, does not present this loss of intensity in the cobalt peaks.

This leave us with two explanations for this loss of intensity: desorption of CoO_x into the vacuum, or diffusion of Co into the HOPG structure. The vapor pressure of Co is very low for this temperature range (P_{vap} (Co)$\sim 10^{-8}$ mbar for T=1300 °C, for example [54]), so it seems more probable that the cobalt or cobalt oxide is diffusing instead of being desorbed into the vacuum. RBS and GIXRD measurements made in order to measure this diffusion will be presented in section 5.5.8.

5.5.7.3 O_2 exposure time

The next condition changed was the O_2 exposure time, leaving the rest of the experimental conditions as default. The AFM images for samples with exposure times of 0.5 and 2 hours are shown in figure 5.41, and they both show nanochannels. This let us discard the oxygen exposure time as an important factor, at least in the time range explored in this work.

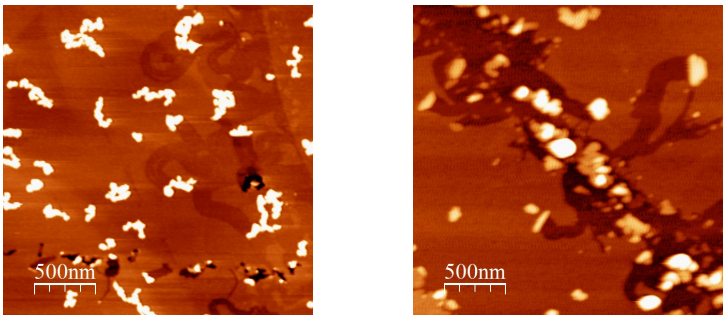

(a) O_2 time: 0.5 h. Image size: 2.5 μm × 2.5 μm.

(b) O_2 time: 2 h. Image size: 2.5 μm × 2.5 μm.

Figure 5.41: AFM topography images of 2 ML samples of CoO on HOPG after Reox-P1, with changes to O_2 exposure time. Range explored: 0.5-2 h. O_2 times and image sizes as labelled.

The XPS spectra (figure 5.42) show a less important decrease of the Co signal with the O_2 exposure time, and almost the same satellite structure intensity for the three samples. This means that the exposition time range explored is not relevant for the final oxidation state of the CoO_x clusters, and that the loss in intensity of the Co peaks increases with time, but at a slower pace.

5.5.7.4 O_2 reoxidation pressure

Changes with the O_2 reoxidation pressure were also studied by XPS and AFM on one sample reoxidized at $2 \cdot 10^{-6}$ mbar. The measurements are summarized in figure 5.43. They show no production of nanochannels, and a final oxidation state of CoO instead of Co_3O_4. This does not mean that the oxidation state after the treatment has to be Co_3O_4 in order to produce nanochannels, since the 600 °C sample had plenty of them, and its final oxidation state was also CoO. But this result imposes another condition for the nanochannels appearance: the oxygen pressure at the O_2 exposure phase must be higher than $2 \cdot 10^{-6}$ mbar.

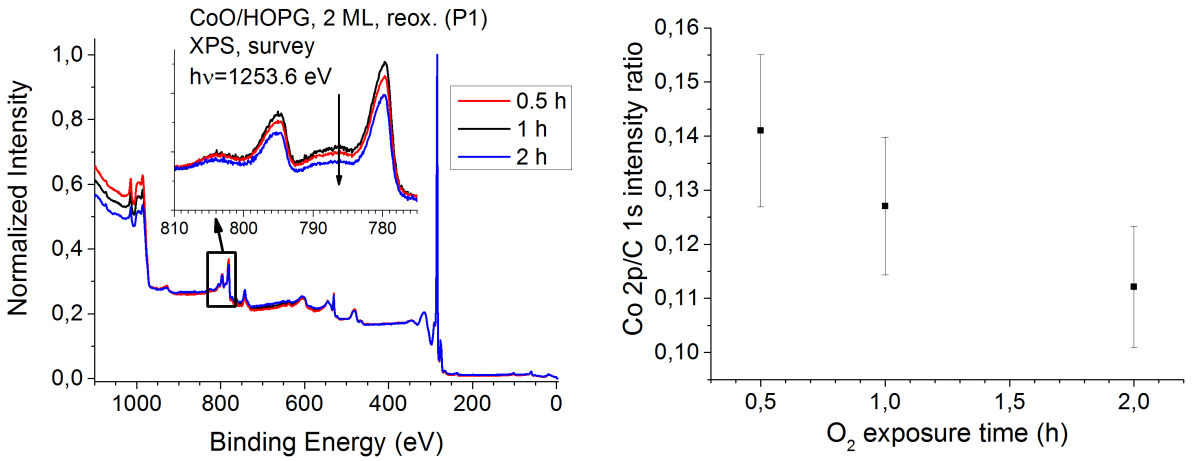

(a) Normalized XPS survey spectra. The inset shows the Co 2p spectra, normalized with respect to the value at 765 eV.

(b) Co 2p/C 1s intensity ratio as a function of the O_2 exposure time.

Figure 5.42: XPS survey and Co 2p spectra of 2 ML samples of CoO on HOPG after Reox-P1, with changes in the O_2 exposure time. Range explored: 0.5-2 h.

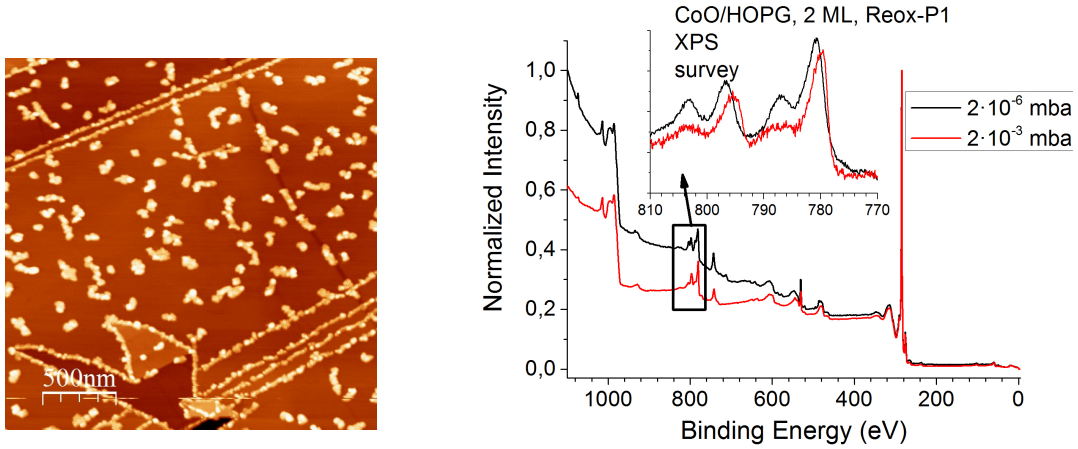

(a) AFM topography image. Size: 2.5 µm × 2.5 µm.

(b) Normalized (0-1) XPS survey spectra of the survey region. Inset shows Co 2p region, normalized with respecct to the value at 760 eV.

Figure 5.43: AFM image and normalized XPS survey and Co 2p spectra of a 2 ML sample of CoO on HOPG after Reox-P1, with changes in the O_2 pressure. Pressure explored: $2 \cdot 10^{-6}$ mbar. AFM image size: as labelled.

5.5.7.5 Summary

The most important conclusions about the minimum conditions for the appearance of the nanochannels can be summarized in these points:

- Maximum CoO coverage: between 4 and 20 ML.
- Minimum temperature: between 300 and 400 °C
- Minimum time: does not seem to be an important parameter, at least in the time range explored (0.5-2 h)
- Minimum O_2 pressure: higher than $2 \cdot 10^{-6}$ mbar

This study is not as complete as it should be, since it omits a lot of points in the ranges explored (specially in the O_2 pressure and exposure time). Nevertheless, it serves as a first approximation about the minimum conditions necessary for the nanochannels appearance, opening ways for future studies, and maybe applications of these interesting results in more applied fields.

This section has also yielded another interesting result: there is a loss of intensity of the Co 2p peaks seen in the 2 ML samples. This loss of intensity increases with the temperature and O_2 exposure time, but it does not appear for larger coverages. The data collected about this intensity loss lead us to think that the reason behind it could be diffusion of Co into the HOPG structure. The reason why this effect is not seen for coverages larger than 2 ML could be that only a low quantity of material is diffusing, so this effect would not be as noticeable for larger coverages in the XPS spectra.

5.5.8 Study of possible diffusion of Cobalt into bulk Graphite

The results obtained in subsubsection 5.5.7.2 suggested that some Co was diffusing through the HOPG substrate after the Reox-P1 process. In this section, the results of the studies made to measure this diffusion will be presented. Two techniques were used for this study: RBS and GIXRD.

5.5.8.1 RBS results (CMAM)

The RBS measurements were made at the Centro de Micro-Análisis de Materiales de Madrid (CMAM), with the configurations and parameters explained in subsection 3.5.2, page 81. For this measurements, four samples were prepared, with their coverage measured by XPS: two of them with 2 ML of CoO, as grown and after the Reox-P1 process; a third one with 30 ML of CoO, and another with 60 ML of CoO after the Reox-P1 process. In both cases, the Reox-P1 process was applied for 4 hours in order to increase the diffusion of Co, so it could be more easily measurable. Two ion energies were used: the low coverage samples were measured with 3035 keV, and the high coverage samples were measured with 1800 keV. As explained in subsection 3.5.2, the 3035 keV energy was chosen to profit from the O resonance, so the sensibility of the measurements of the low coverage samples would be improved. This samples

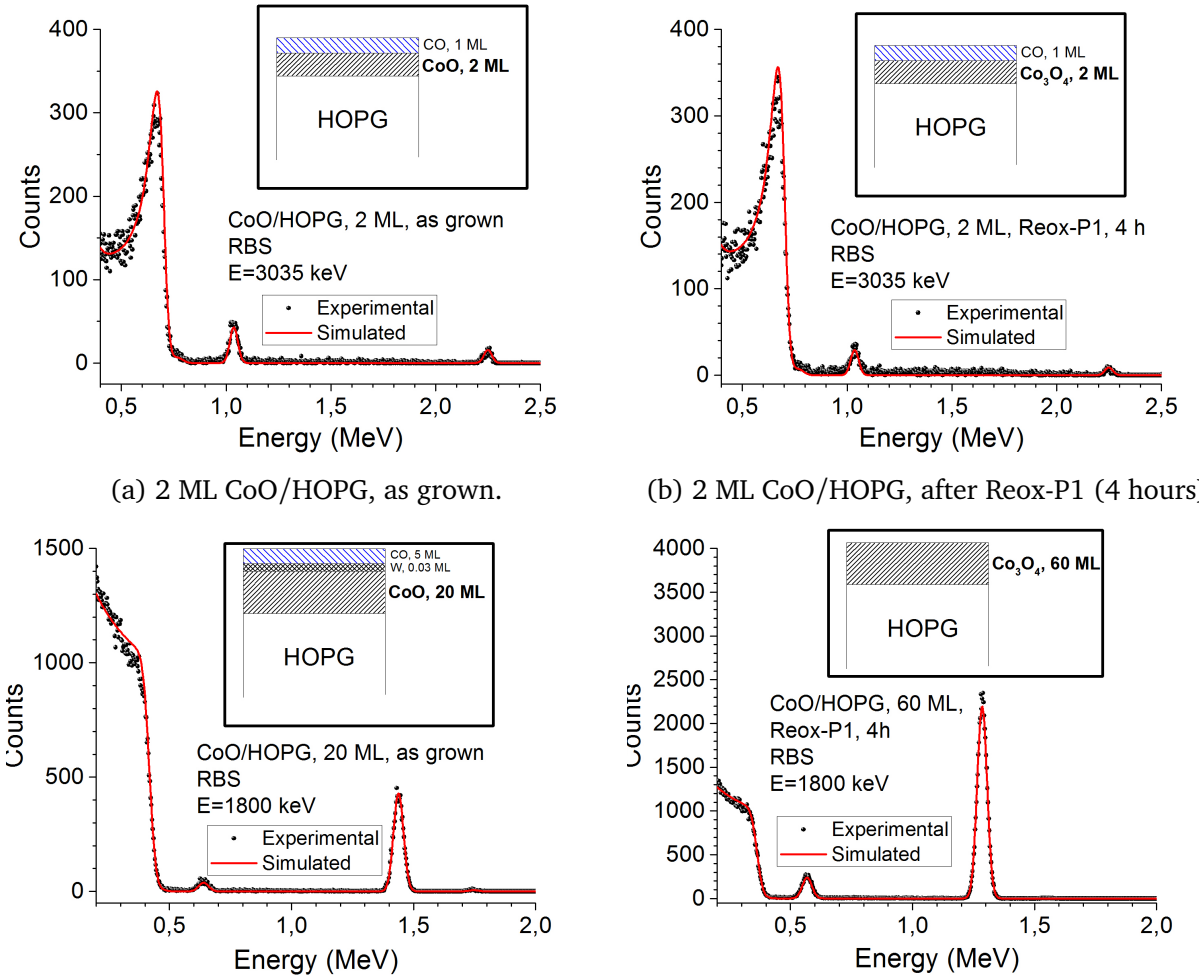

(a) 2 ML CoO/HOPG, as grown.

(b) 2 ML CoO/HOPG, after Reox-P1 (4 hours)

(c) 20 ML CoO/HOPG, as grown.

(d) 60 ML CoO/HOPG, after Reox-P1 (4 h)

Figure 5.44: RBS experimental data and SIMNRA simulations of the four samples studied. The insets show the composition of the layers resulting from the SIMNRA calculations. Coverage and O_2 exposure times as labeled.

Sample	Co/O ratio	Coverage (ML)
2 ML, as grown	1	2
2 ML, after Reox-P1 (1 h)	0.74	1.25
30 ML, as grown	1	30
60 ML, after Reox-P1 (4 h)	0.73	200

Table 5.12: Co/O ratios and coverage values found in the simulations made with SIMNRA of the RBS spectra displayed in figure 5.44.

have been measured ex-situ, so some atmosphere contamination is expected. The experimental data taken, along with the simulations made with the software SIMNRA 6.06, are displayed in figure 5.44.

Table 5.12 shows the Co/O ratios and the total quantity of cobalt oxides deposited as obtained from the SIMNRA calculations of each spectrum. The as-grown samples yield ratios that agree with the growth of CoO, while the Reox-P1 sample ratios are close to the one found in Co_3O_4. The coverage values and composition of the samples are also in the same range as those estimated by XPS, except for the last sample, which coverage is far larger than the initial estimation. Some CO had to be used in order to improve the simulations: this CO is attributed to atmosphere contamination. Also, some W appeared in the 20 ML sample, probably coming from the evaporator. Unfortunately, no diffusion effects (e.g., asymmetries in the Co or O peaks) have been seen in any of the samples studied. A possible reason for this could be that the mean depth resolution of RBS is estimated to be around 5-50 nm [55]. This means that it is possible that the diffusion exists, but this technique does not have enough resolution to measure it.

5.5.8.2 GIXRD (1 0 L) scans (ESRF, SpLine)

Another approach to detect possible diffusion effects is to measure the HOPG interplanar distance of the first layers, and see possible changes with the sampling depth. If these changes exist, they can be related to CoO_x particles located between the HOPG planes, proving the diffusion of Co. As a way to measure this, GIXRD scans along the (1 0 L) direction were performed at the optical branch A of the SpLine beamline at the ESRF synchrotron (Grenoble, France) for different sample-beam angles, ranging from 0 to 5°. All the rest of details about the measurement conditions and the data treatment have been displayed in subsection 3.6.2, page 81. For these measurements, the samples used were the same which AFM and XPS results have already been displayed in section 5.5.7, except for the changes in the O_2 pressure, which could not be completed before this beamtime. The total number of samples can be divided in three groups, depending on which condition of the Reox-P1 process has been changed: changes in the coverage, changes in the O_2 exposure time, and changes in the heating temperature. A clean HOPG sample was also measured for reference purposes.

The interplanar distances measured for all the samples are displayed in figure 5.45: they are represented against the penetration length of the X-rays for the sample-beam angle used in each scan. The main conclusion that can be extracted from these data is that no significant trend is observed in all of them. The reason for this lies in the large attenuation length of the x-rays used in these measurements ($h\nu$=15 keV) , which is represented in figure 5.45d for angles ranging from 0 to 5°. We can see in this figure that once the critical angle is exceeded, the attenuation length increases almost exponentially, so if our diffusion is happening only in the first nanometers of the substrate (as the RBS measurements suggested), we are not going to be able to measure it with this technique.

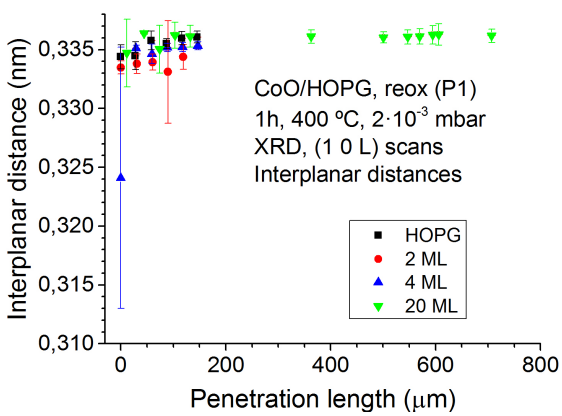

(a) Initial CoO coverage changes.

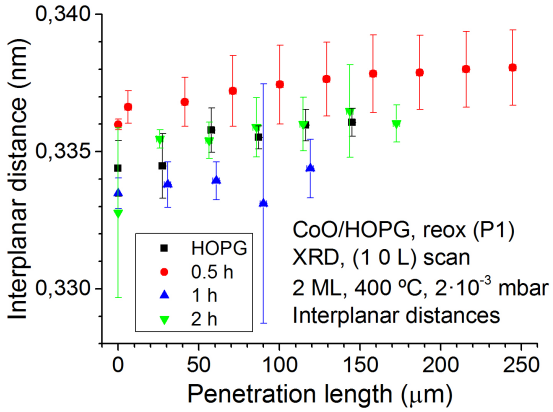

(b) O_2 exposure time changes.

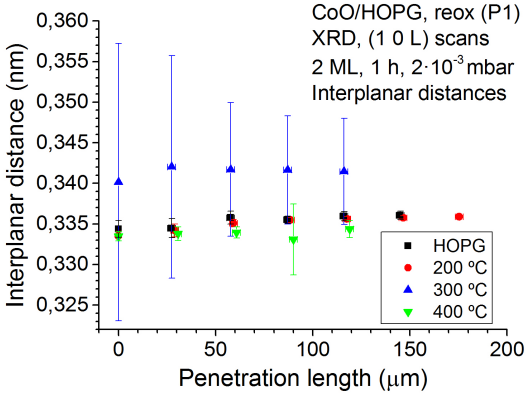

(c) Heating temperature changes.

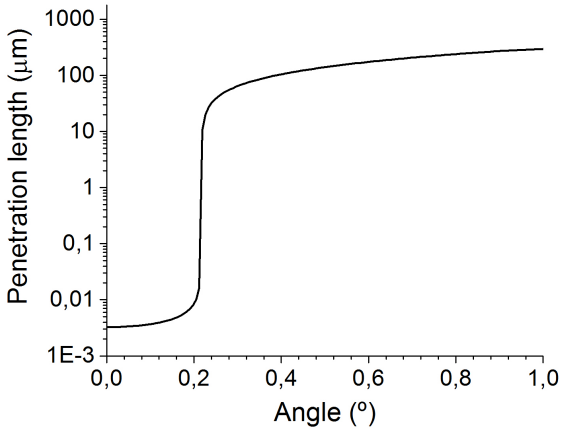

(d) HOPG attenuation length. Data taken from [56]

Figure 5.45: HOPG interplanar distance data obtained from the GIXRD (1 0 L) scans performed to multiple samples of CoO on HOPG after the Reox-P1 process. The HOPG interplanar distance are represented against the X-ray penetration length. In each graph, one condition of the default Reox-P1 conditions has been changed: a) Initial CoO coverage (2, 4 and 20 ML), b) O_2 exposure time (0.5, 1 and 2 hours), and c) heating temperature (200, 300 and 400 °C). The clean HOPG sample is also represented in each graph. d) shows the X-ray penetration length as a function of the beam angle for graphite.

5.5.9 Summary

In this section, the effect of vacuum heating and two reoxidation processes (labelled as Reox-P1 and Reox-P2) over as-grown CoO samples on HOPG have been studied by different techniques. The oxidation state of the cobalt has been shown to be different after each process: Co for the vacuum heating, a mixture of Co_3O_4 and CoO for the Reox-P1, and CoO for the Reox-P2 process. This has been explained in terms of the free energy of the Co oxidation reaction and the order of the stages of each process.

However, the most striking results have been extracted from the morphology of the samples: the Reox-P1 samples show nanochannels with random trajectories scratched across their surface, while the others do not have them. XPS, XAS and Raman spectroscopy measurements have exposed that the reason behind them lies in the order of the Reox-P1 stages, since the vacuum heating phase reduces the CoO clusters to metallic Co. These reduced clusters serve as catalyst for the gasification reaction of the substrate, and the thermal movement of these clusters keeps gasificating the areas where they are moving, scratching the observed channels in their way. The Raman characterization of these samples has determined that these channels are composed of carbon defects, and no C-O, C-H or other kind of bonds have been observed. This gasification catalysed by metallic nanoparticles is a well-known phenomenon, used since the seventies as a way to pattern the surface of graphite, but these results lower the minimum temperature for this process in 200 °C, and also requires less O_2 flow than similar past studies. The reason behind this efficiency lies in the use of CoO as a starting point for the patterning, since freshly evaporated Co samples grown on HOPG have not produced these channels after being exposed to the Reox-P1 process. The hypothesis proposed to explain this different behaviour is based on two related factors. The first one is the different local environment of the reduced Co particles, as seen in the binding energy difference of the Co 2p spectra of both freshly evaporated and reduced (from CoO) Co samples. The second one is the less important modification of the HOPG surface by the freshly evaporated Co on HOPG, as seen in the PES C 1s spectra.

In order to complement this study, the experimental conditions for this nanochannels formation have been characterized, yielding minimum temperature (300-400 °C), O_2 pressure and reoxidation temperature conditions. Other effects, like the different final oxidation state for temperatures around 600 °C, have been discovered along the way. Measurements of the possible diffusion of Co into the HOPG substrate by GIXRD and RBS have been made, but no results have come out of those measurements.

SECTION 5.6

Stability on air conditions

In the last section of this chapter, the results of study of the chemical stability of the as-grown and Reox-P1 samples after being exposed to room conditions will be presented. For the study of the stability of the as-grown CoO samples on HOPG, two coverages (2 and 40 ML) were grown and measured in-situ by XPS, and then they were exposed to room conditions for a week: after that week, they were measured again by XPS. The study of the Reox-P1 samples

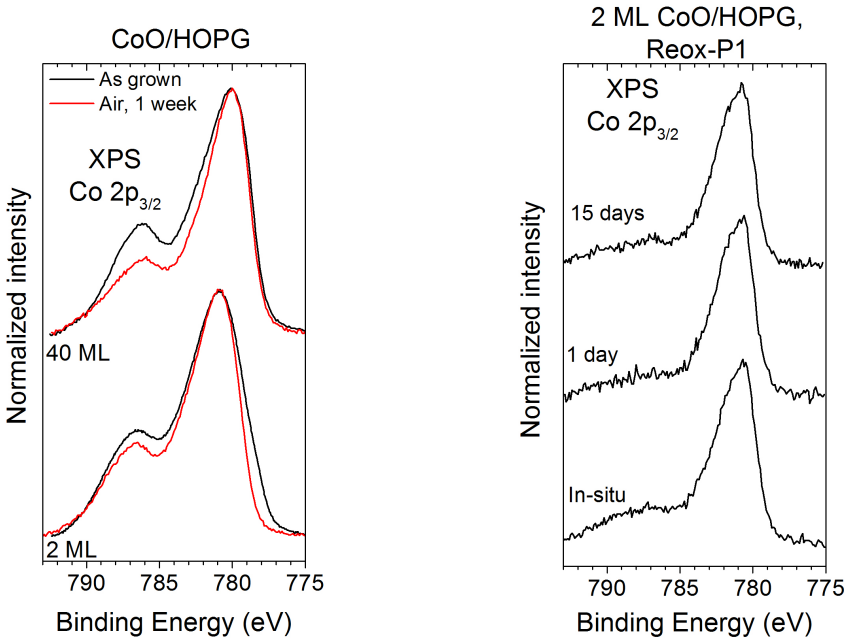

(a) 2 and 40 ML samples of CoO on HOPG, before (black line) and after being exposed to room conditions for 1 week (red line).

(b) 2 ML sample of CoO on HOPG after Reox-P1, measured in situ and after being exposed 1 day and 2 weeks at room conditions.

Figure 5.46: Normalized (0-1) XPS Co $2p_{3/2}$ spectra of CoO samples grown on HOPG, before (a) and after the Reox-P1 process (b). The spectra presented were taken in-situ and after being exposed to room conditions. A Shirley background has been removed on all the spectra. Coverages and air exposure times are indicated in each graph.

stability was started with the growth of a 2 ML CoO/HOPG sample, which was submitted to the Reox-P1 process and measured in situ. Then, it was measured by XPS after being exposed to room conditions for incrementally larger times.

The results of the XPS measurements of the as-grown and Reox-P1 process samples are displayed in figure 5.46. Figure 5.46a shows the as-grown 2 and 40 ML samples, measured as grown and after 1 week at room conditions; and figure 5.46b shows the 2 ML Reox-P1 sample measured as grown and after 1 day and 2 weeks at room conditions.

The spectra of the as-grown samples show a lessening of the satellite structure after being exposed to room conditions. This means that a part of the deposited CoO is being reoxidized to Co_3O_4 by the action of the atmosphere. Meanwhile, the Reox-P1 sample do not show any change after being exposed to room conditions, which means that the Co_3O_4 clusters formed after this process are stable in room conditions.

SECTION 5.7

Conclusions

The main conclusions about all the data presented in this chapter can be separated in two big groups: the data related to the characterization of the growth of CoO in HOPG, and the study and characterization of these samples when reoxidized in controlled conditions.

The growth of cobalt oxides on HOPG has been characterized by multiple spectroscopic and microscopic techniques. It has been seen that the main oxidation state during the growth is CoO, with the appearance of Co_3O_4 for the largest coverages explored (80 ML) and some unoxidized cobalt for the lowest coverages evaporated. The morphology of the growth follows a Stranski-Krastanov mode, with the material first accumulating at the steps, and forming a unit cell thick wetting layer of CoO. Once this wetting layer has been formed, dendritic islands scattered across the terraces grow on it up to coverages of 30 ML. Strong diffusion of the CoO deposits along the HOPG surface has also been observed. This leads to the autoassembling of the CoO clusters following the directions dictated by the honeycomb surface structure of HOPG. The study of possible size and interface effects have yielded similar quantum size effects as the ones seen in the oxide experiments for coverages below 4 ML, and distortions in the octahedron coordination structures. It has also been seen that the HOPG surface is modified by the deposited CoO, and carbon-oxygen bonds appear on the surface of the sample, in the form of C-O and C=O bonds. It has been proposed that this interaction is the reason behind the differences seen in the XAS spectra when the sample-beam angle is changed. These as-grown CoO samples suffers modifications when exposed to atmosphere conditions, with some part of the deposited CoO changing its oxidation state to Co_3O_4.

The characterization of the as-grown CoO samples after being exposed to reoxidizing conditions has yielded a very important result: if the samples are firstly heated in UHV conditions at 400 °C and then exposed to an O_2 pressure of $2 \cdot 10^{-3}$ mbar (process labelled in this work as Reox-P1 process), nanochannels conformed by carbon defects appear scratched on the HOPG surface. The characterization of the stages of these processes has revealed that the UHV heating reduces the deposited CoO into Co, and these cobalt clusters act as catalysers for the gasification reaction of the HOPG substrate. The temperature causes the random movement of this particles across the surface of the substrate, scratching these channels in their path. The oxygen contained in the starting CoO layer seems to play an important role by weakening the bonds of the HOPG surface previously to the re-oxidation process. Although the first step of this process (heating at 400 °C) produce the reduction of the initial CoO layer to cobalt nanoparticles, these particles behave in a different way from those grown directly by evaporation of cobalt. This different behaviour is explained by the defects created by the CoO layer on the HOPG surface previously to the re-oxidation process. The channelling of graphitic surfaces by metallic nanoparticles is well known since the seventies, but our method requires less temperature and oxygen pressure than the usual method reported in the bibliography, and is therefore more efficient. A basic characterization of the minimum conditions of the nanochannels appearance has confirmed the enhanced efficiency of our method when compared to the one reported in the bibliography. The quality of the nano-channels produced by this method could be improved by controlling the amount of the initial CoO layer as well as by magnetic steering of the cobalt

nanoparticles during the reaction: this improvements will surely be explored in future works, given the relevance and importance of these results.

SECTION 5.8

Bibliography

[1] B. V. L'VOV. "Mechanism of carbothermal reduction of iron, cobalt, nickel and copper oxides". *Thermochimica Acta* 360.2 (2000), pp. 109–120. DOI: 10.1016/S0040-6031(00)00540-2.

[2] I. PREDA. "Surface and Interface Effects in NiO". Universidad Autónoma de Madrid, 2008.

[3] I. STRANSKI and L. KRASTANOW. "Abhandlungen der Mathematisch Naturwissenschaftlichen Klasse IIb". *Akademie der Wissenschaften Wien* 146 (1938), pp. 797–810.

[4] R. FOLLATH, F. SENF, and W. GUDAT. "Plane-grating monochromator at BESSY II using collimated light". *Journal of Synchrotron Radiation* 5.3 (May 1998), pp. 769–771. DOI: 10.1107/S090904959800079X.

[5] G. S. KNAPP, B. W. VEAL, H. K. PAN, and T. KLIPPERT. "XANES study of 3d oxides: Dependence on crystal structure". *Solid State Communications* 44.9 (1982), pp. 1343–1345. DOI: 10.1016/0038-1098(82)90889-4.

[6] F. M. F. DE GROOT, M. ABBATE, J. VAN ELP, G. A. SAWATZKY, Y. J. MA, C. T. CHEN, and F. SETTE. "Oxygen 1s and cobalt 2p X-ray absorption of cobalt oxides". *Journal of Physics: Condensed Matter* 5.14 (1993), p. 2277. DOI: 10.1088/0953-8984/5/14/023.

[7] J. G. CHEN. "NEXAFS investigations of transition metal oxides, nitrides, carbides, sulfides and other interstitial compounds". *Surface Science Reports* 30.1-3 (1997), pp. 1–152. DOI: 10.1016/S0167-5729(97)00011-3.

[8] F. M. F. DE GROOT, M. GRIONI, J. C. FUGGLE, J. GHIJSEN, G. A. SAWATZKY, and H. PETERSEN. "Oxygen 1s x-ray-absorption edges of transition-metal oxides". *Phys. Rev. B* 40 (8 Sept. 1989), pp. 5715–5723. DOI: 10.1103/PhysRevB.40.5715.

[9] J. WANG, J. ZHOU, Y. HU, and T. REGIER. "Chemical interaction and imaging of single Co_3O_4/graphene sheets studied by scanning transmission X-ray microscopy and X-ray absorption spectroscopy". *Energy and Environmental Science* 6 (3 2013), pp. 926–934. DOI: 10.1039/C2EE23844F.

[10] M.J. WEBB, P. PALMGREN, P. PAL, O. KARIS, and H. GRENNBERG. "A simple method to produce almost perfect graphene on highly oriented pyrolytic graphite". *Carbon* 49.10 (2011), pp. 3242–3249. DOI: 10.1016/j.carbon.2011.03.050.

[11] H. ESTRADE-SZWARCKOPF. "XPS photoemission in carbonaceous materials: A "defect" peak beside the graphitic asymmetric peak". *Carbon* 42.8-9 (2004), pp. 1713–1721. DOI: 10.1016/j.carbon.2004.03.005.

[12] H. K. JEONG, L. COLAKEROL, M. H. JIN, P. A. GLANS, K. E. SMITH, and Y. H. LEE. "Unoccupied electronic states in graphite oxides". *Chemical Physics Letters* 460.4-6 (2008), pp. 499–502. DOI: 10.1016/j.cplett.2008.06.042.

[13] D. YANG, A. VELAMAKANNI, G. BOZOKLU, S. PARK, M. STOLLER, R. D. PINER, S. STANKOVICH, I. JUNG, D. A. FIELD, C. A. VENTRICE JR., and R. S. RUOFF. "Chemical analysis of graphene oxide films after heat and chemical treatments by X-ray photoelectron and Micro-Raman spectroscopy". *Carbon* 47.1 (2009), pp. 145–152. DOI: 10.1016/j.carbon.2008.09.045.

[14] K. HAUBNER, J. MURAWSKI, P. OLK, L. M. ENG, C. ZIEGLER, B. ADOLPHI, and E. JAEHNE. "The Route to Functional Graphene Oxide". *ChemPhysChem* 11.10 (2010), pp. 2131–2139. ISSN: 1439-764. DOI: 10.1002/cphc.201000132.

[15] B. ROUSSEAU, H. ESTRADE-SZWARCKOPF, A. L. THOMANN, and P. BRAULT. "Stable C-atom displacements on HOPG surface under plasma low-energy argon-ion bombardment". English. *Applied Physics A* 77.3-4 (2003), pp. 591–597. DOI: 10.1007/s00339-002-1538-x.

[16] S. TAKABAYASHI, K. OKAMOTO, T. NAKATANI, H. SAKAUE, and T. TAKAHAGI. "Surface Analysis of Carbon-Hydrogen Bonds in Diamondlike Carbon Films by X-ray Photoelectron Spectroscopy". *Japanese Journal of Applied Physics* 48.9R (2009), p. 092304. DOI: 10.1143/JJAP.48.092304.

[17] J. W. CHIOU, SEKHAR C. RAY, S. I. PENG, C. H. CHUANG, B. Y. WANG, H. M. TSAI, C. W. PAO, H.-J. LIN, Y. C. SHAO, Y. F. WANG, S. C. CHEN, W. F. PONG, Y. C. YEH, C. W. CHEN, L.-C. CHEN, K.-H. CHEN, M.-H. TSAI, A. KUMAR, A. GANGULY, P. PAPAKONSTANTINOU, H. YAMANE, N. KOSUGI, T. REGIER, L. LIU, and T. K. SHAM. "Nitrogen-Functionalized Graphene Nanoflakes (GNFs:N): Tunable Photoluminescence and Electronic Structures". *The Journal of Physical Chemistry C* 116.30 (2012), pp. 16251–16258. DOI: 10.1021/jp303465u.

[18] W. F. POND, C. L. YUEH, Y. D. CHANG, M.-H. TSAI, Y. K. CHANG, Y. Y. CHEN, J. F. LEE, S. L. WEI, C. Y. WEN, L. C. CHEN, K. H. CHEN, I. N. LIN, and H. F. CHENG. "X-ray absorption studies of carbon-related materials". *Journal of Synchrotron Radiation* 8.2 (Mar. 2001), pp. 145–149. DOI: 10.1107/S0909049500019750.

[19] J. A. BRANDES, G. D. CODY, D. RUMBLE, P. HABERSTROH, S. WIRICK, and Y. GELINAS. "Carbon K-edge XANES spectromicroscopy of natural graphite". *Carbon* 46.11 (2008), pp. 1424–1434. DOI: 10.1016/j.carbon.2008.06.020.

[20] R. AHUJA, P. A. BRÜHWILER, J. M. WILLS, B. JOHANSSON, N. MÅRTENSSON, and O. ERIKSSON. "Theoretical and experimental study of the graphite 1s x-ray absorption edges". *Physical Review B* 54 (20 Nov. 1996), pp. 14396–14404. DOI: 10.1103/PhysRevB.54.14396.

[21] S. PARK, D. A. DIKIN, S. B. T. NGUYEN, and R. S. RUOFF. "Graphene Oxide Sheets Chemically Cross-Linked by Polyallylamine". *The Journal of Physical Chemistry C* 113.36 (2009), pp. 15801–15804. DOI: 10.1021/jp907613s.

[22] P. TANG, G. HU, Y. GAO, W. LI, S. YAO, Z. LIU, and D. MA. "The microwave adsorption behavior and microwave-assisted heteroatoms doping of graphene-based nano-carbon materials". *Scientific reports* 4 (2014), p. 5901. DOI: 10.1038/srep05901.

[23] Y. KEBUKAWA, M. E. ZOLENSKY, A. L. D. KILCOYNE, Z. RAHMAN, P. JENNISKENS, and G. D. CODY. "Diamond xenolith and matrix organic matter in the Sutter's Mill meteorite measured by C-XANES". *Meteoritics & Planetary Science* 49.11 (2014), pp. 2095–2103. DOI: 10.1111/maps.12312.

[24] G. D. CODY, E. HEYING, C. M. O. ALEXANDER, L. R. NITTLER, A. L. D. KILCOYNE, S. A. SANDFORD, and R. M. STROUD. "Establishing a molecular relationship between chondritic and cometary organic solids". *Proceedings of the National Academy of Sciences* 108.48 (2011), pp. 19171–19176. DOI: 10.1073/pnas.1015913108.

[25] K. A. PRIOR, K. SCHWAHA, and R. M. LAMBERT. "Surface chemistry of the non-basal planes of cobalt: The structure, stability, and reactivity of Co(10$\bar{1}$2)-CO". *Surface Science* 77.2 (1978), pp. 193–208. DOI: 10.1016/0039-6028(78)90001-8.

[26] G. MELAET, W. T. RALSTON, C. S. LI, S. ALAYOGLU, K. AN, N. MUSSELWHITE, B. KALKAN, and G. A. SOMORJAI. "Evidence of Highly Active Cobalt Oxide Catalyst for the Fischer-Tropsch Synthesis and CO_2 Hydrogenation". *Journal of the American Chemical Society* 136.6 (2014), pp. 2260–2263. DOI: 10.1021/ja412447q.

[27] D. JIANG and S. DAI. "The role of low-coordinate oxygen on Co_3O_4(110) in catalytic CO oxidation". *Physical Chemistry Chemical Physics* 13 (3 2011), pp. 978–984. DOI: 10.1039/C0CP01138J.

[28] M. POLINI, F. GUINEA, M. LEWENSTEIN, H. C. MANOHARAN, and V. PELLEGRINI. "Artificial honeycomb lattices for electrons, atoms and photons". *Nature nanotechnology* 8.9 (2013), pp. 625–633. DOI: 10.1038/nnano.2013.161.

[29] Z. CHEN, Y. M. LIN, M. J. ROOKS, and P. AVOURIS. "Graphene nano-ribbon electronics". *Physica E: Low-dimensional Systems and Nanostructures* 40.2 (2007). International Symposium on Nanometer-Scale Quantum Physics, pp. 228–232. DOI: 10.1016/j.physe.2007.06.020.

[30] S. PANG, H. N. TSAO, X. FENG, and K. MÜLLEN. "Patterned Graphene Electrodes from Solution-Processed Graphite Oxide Films for Organic Field-Effect Transistors". *Advanced Materials* 21.34 (2009), pp. 3488–3491. DOI: 10.1002/adma.200803812.

[31] T. MUHL, J. KRETZ, I. MONCH, C. M. SCHNEIDER, H. BRUCKL, and G. REISS. "Parallel nanolithography in carbon layers with conductive imprint stamps". *Applied Physics Letters* 76.6 (Feb. 2000), pp. 786–788. DOI: 10.1063/1.125895.

[32] S. C. EAGLE and G. K. FEDDER. "Writing nanometer-scale pits in sputtered carbon films using the scanning tunneling microscope". *Applied Physics Letters* 74.25 (June 1999), pp. 3902–3903. DOI: 10.1063/1.124218.

[33] L. CI, Z. XU, L. WANG, W. GAO, F. DING, K. F. KELLY, B. I. YAKOBSON, and P. M. AJAYAN. "Controlled nanocutting of graphene". English. *Nano Research* 1.2 (2008), pp. 116–122. DOI: 10.1007/s12274-008-8020-9.

[34] N. SEVERIN, S. KIRSTEIN, I. M. SOKOLOV, and J. P. RABE. "Rapid Trench Channeling of Graphenes with Catalytic Silver Nanoparticles". *Nano Letters* 9.1 (2009). PMID: 19143507, pp. 457–461. DOI: 10.1021/nl8034509.

[35] S. KONISHI, W. SUGIMOTO, Y. MURAKAMI, and Y. TAKASU. "Catalytic creation of channels in the surface layers of highly oriented pyrolytic graphite by cobalt nanoparticles". *Carbon* 44.11 (2006), pp. 2338–2340. DOI: 10.1016/j.carbon.2006.05.003.

[36] S. S. DATTA, D. R. STRACHAN, S. M. KHAMIS, and A. T .C. JOHNSON. "Crystallographic etching of few-layer graphene". *Nano letters* 8.7 (2008), pp. 1912–1915.

[37] L. BULUT and R. H. HURT. "A Magneto-catalytic Writing Technique for Etching Complex Channel Patterns into Graphenic Carbons". *Advanced Materials* 22.3 (2010), pp. 337–341. DOI: 10.1002/adma.200901932.

[38] C. W. KEEP, S. TERRY, and M. WELLS. "Studies of the nickel-catalyzed hydrogenation of graphite". *Journal of Catalysis* 66.2 (1980), pp. 451–462. DOI: 10.1016/0021-9517(80)90047-0.

[39] S. ZAFEIRATOS, T. DINTZER, D. TESCHNER, R. BLUME, M. HÄVECKER, A. KNOP-GERICKE, and R. SCHLÖGL. "Methanol oxidation over model cobalt catalysts: Influence of the cobalt oxidation state on the reactivity". *Journal of Catalysis* 269.2 (2010), pp. 309–317. DOI: 10.1016/j.jcat.2009.11.013.

[40] W. PISULA, X. FENG, and K. MÜLLEN. "Self-Organization of Nanographenes". *Carbon Nanotubes and Related Structures*. Wiley-VCH Verlag GmbH & Co. KGaA, 2010, pp. 405–453. ISBN: 9783527629930. DOI: 10.1002/9783527629930.ch14.

[41] R. T. K. BAKER, J. A. FRANCE, L. ROUSE, and R. J. WAITE. "Catalytic oxidation of graphite by platinum and palladium". *Journal of Catalysis* 41.1 (1976), pp. 22–29. DOI: 10.1016/0021-9517(76)90196-2.

[42] H. CHANG and A. J. BARD. "Scanning tunneling microscopy studies of carbon-oxygen reactions on highly oriented pyrolytic graphite". *Journal of the American Chemical Society* 113.15 (1991), pp. 5588–5596. DOI: 10.1021/ja00015a012.

[43] M. LUKAS, V. MEDED, A. VIJAYARAGHAVAN, L. SONG, P. M. AJAYAN, K. FINK, W. WENZEL, and R. KRUPKE. "Catalytic subsurface etching of nanoscale channels in graphite". *Nature Communications* 4 (2013), p. 1379. DOI: 10.1038/ncomms2399.

[44] A. C. FERRARI. "Raman spectroscopy of graphene and graphite: Disorder, electron-phonon coupling, doping and nonadiabatic effects". *Solid State Communications* 143.1-2 (2007). Exploring graphene Recent research advances, pp. 47–57. DOI: 10.1016/j.ssc.2007.03.052.

[45] K. SASAKI, Y. TOKURA, and T. SOGAWA. "The Origin of Raman D Band: Bonding and Antibonding Orbitals in Graphene". *Crystals* 3.1 (2013), pp. 120–140. DOI: 10.3390/cryst3010120.

[46] D. GALLANT, M. PÉZOLET, and S. SIMARD. "Optical and Physical Properties of Cobalt Oxide Films Electrogenerated in Bicarbonate Aqueous Media". *The Journal of Physical Chemistry B* 110.13 (2006). PMID: 16570997, pp. 6871–6880. DOI: 10.1021/jp056689h.

[47] M. S. DRESSELHAUS, A. JORIO, A. G. SOUZA FILHO, and R. SAITO. "Defect characterization in graphene and carbon nanotubes using Raman spectroscopy". *Philosophical Transactions of the Royal Society A: Mathematical, Physical and Engineering Sciences* 368.1932 (2010), pp. 5355–5377. DOI: 10.1098/rsta.2010.0213.

[48] A. JORIO. "Raman Spectroscopy in Graphene-Based Systems: Prototypes for Nanoscience and Nanometrology". *ISRN Nanotechnology* (2012), p. 234216. DOI: 10.5402/2012/234216.

[49] L. M. MALARD, M. A. PIMENTA, G. DRESSELHAUS, and M. S. DRESSELHAUS. "Raman spectroscopy in graphene". *Physics Reports* 473.5-6 (2009), pp. 51–87. DOI: 10.1016/j.physrep.2009.02.003.

[50] C. XU, Y. LIU, G. XU, and G. WANG. "Fabrication of CoO nanorods via thermal decomposition of CoC_2O_4 precursor". *Chemical Physics Letters* 366.5-6 (2002), pp. 567–571. DOI: 10.1016/S0009-2614(02)01640-8.

[51] D. LIN-VIEN, N. B. COLTHUP, W. G. FATELEY, and J. G. GRASSELLI. *The handbook of infrared and Raman characteristic frequencies of organic molecules*. Elsevier, 1991. ISBN: 9780080571164.

[52] T. H. MANSOURE. "Direct Fabrication of Cobalt Oxide Nanoparticles Employing Sucrose as a Combustion Fuel". *Journal of Nanoparticles* 2013 (2013), p. 384350. DOI: 10.1155/2013/384350.

[53] H. Y. LIN and Y. W. CHEN. "The mechanism of reduction of cobalt by hydrogen". *Materials Chemistry and Physics* 85.1 (2004), pp. 171–175. DOI: 10.1016/j.matchemphys.2003.12.028.

[54] G. L. WEISSLER, K. MARTON, and R. W. CARLSON. *Vacuum Physics and Technology*. Methods in Experimental Physics. Elsevier Science, 1980. ISBN: 9780080859958.

[55] J. R. TESMER and M. A. NASTASI. *Handbook of modern ion beam materials analysis*. Mrs Symposium Proceedings Series. Materials Research Society, 1995. ISBN: 9781558992542.

[56] MATERIALS SCIENCE DIVISION: THE CENTER FOR X-RAY OPTICS. *X-Ray attenuation length calculator*. Ed. by LAWRENCE BERLEKEY NATIONAL LABORATORY. URL: http://henke.lbl.gov/optical_constants/atten2.html.

Chapter 6

Conclusions, open questions and future research

Five years ago, this work was started with a lot of open questions and challenges, both theoretical and experimental. A lot of those questions have been answered by the end of it, and a good deal of surprising results have been discovered along the way, both enriching the initial goals and opening new lines of work and potential applications for the future. No work is perfect, and as it has been shown in chapters 4 and 5, some questions have not been answered with the results achieved here. This section will summarize the most important results of this thesis, and will outline some of the most important questions that remain unanswered, as well as suggesting some future lines of work related to the results obtained here, as a way to complete and expand the work done in this half a decade.

SECTION 6.1

Main conclusions of this work

The study of the growth and interaction of cobalt oxides grown on the four substrates considered (SiO_2, Al_2O_3, MgO and HOPG) has been done in two different blocks of experiments: those related to the study of the growth of cobalt oxides on the above substrates, and those related to the characterization of these samples after being exposed to different conditions. All the samples have been grown by reactive thermal evaporation of cobalt in a controlled O_2 atmosphere, and the study of the growth has been carried out by successive evaporations of cobalt oxide on these substrates. XPS measurements were performed after each stage, and other in-situ measurements, such as RGA, XANES or PES, were measured depending on the experimental facility used and the specific experiment. The rest of the measurements, such as AFM, EXAFS or Raman, were made ex-situ.

6.1.1 Interaction of Cobalt oxides with other oxide substrates

The chemistry of the growth of cobalt oxides on the three oxide substrates has been measured in-situ with XPS, and the assignation of the oxidations states found during the growths has been supported by theoretical cluster calculations of the XPS Co $2p_{3/2}$ spectra for different Co ions. The main oxidation state found for coverages below 40 ML on the three substrates has been CoO, while Co_3O_4 appears for coverages above this value for the growths on SiO_2 and Al_2O_3, and some unoxidized cobalt has been detected in the first coverages of the growth on SiO_2. According to the literature, Co^{2+} are the usual species formed on all substrates for the growth using Co evaporation, i.e., low energy near equilibrium method, but other higher energy methods such as oxygen plasma assisted can grow $Co^{2+,3+}$ species. The oxidation states found in our experiments have been explained in terms of the free energy diagrams of the cobalt oxidation reaction (the $2Co + O_2 \longrightarrow 2CoO$ reaction has less free energy than the $3Co + 2O_2 \longrightarrow Co_3O_4$ reaction), while it has been suggested that the presence of unoxidized cobalt in the growth on SiO_2 is caused by the different coordination and lattice parameter of the substrate and the CoO (tetrahedral vs. octahedral), although the presence of oxygen vacancies on the SiO_2 surface cannot be discarded without additional experiments. Meanwhile, the study of the morphology of the growths has yielded two different modes: Volmer-Weber (islands) for the growth on SiO_2, and Frank-Van Der Merwe (layer-by-layer) for the growth on

MgO and Al_2O_3. They have been explained in terms of the different coordination and lattice parameter (in the case of the growths on SiO_2 and MgO), and with the help of theoretical DFT calculations of the interface (in the case of the growth on Al_2O_3). These ways of growth have also been confirmed with a detailed analysis combining AFM and XPS-IPSA.

The study of the interface effects have been performed using new theoretical cluster calculations of the XPS Co $2p_{3/2}$ spectra of CoO structures simulating different local environments, which have shown that changes in the relative position and intensity of the shake-up satellite peak (with respect to the main line peak) are related to changes in the different morphologies of the CoO nanostructures formed at the early stages of growth, which depend directly on the crystal structure of the substrates, and lead to changes in the ionic-covalent character of the bonds of those CoO nanostructures. This is a clear divergence with respect to previous studies of other transition metal oxides deposited on these substrates with similar evaporation techniques, which showed that the covalence-ionicity character of the substrates directly influenced the electronic structure of the grown oxide. In the case of the CoO/Al_2O_3 interface, this work has provided an experimental proof of a substrate-overlayer charge transfer theoretically predicted by DFT calculations of this interface.

In the other block of results, the stability of these samples has been tested under large exposure times to room conditions, and after a thermal oxidation annealing. The exposure to room conditions has revealed the growth of cobalt hydroxide and Co_3O_4 over time, confirmed with XPS and XANES measurements. The EXAFS Co 1s spectra have revealed an oxygen excess that cannot be linked to the CoO grown layers, and it has been proposed as the reason behind the oxidation state change seen for coverages above 40 ML in the study of the chemistry of the growth. All of these effects are less important on the samples grown on MgO, being also the only substrate where a small percentage of crystallinity of the CoO deposits has been detected: therefore, it has been concluded that this substrate is the most suitable for the growth of stable ultra-thin CoO layers. This has been explained in terms of their similar crystal structures and almost equal lattice parameters. The study of the samples after the thermal oxidation annealing has confirmed this conclusion, since the samples grown on MgO are also remarkably stable for coverages up to 4 ML. The samples grown on SiO_2 with coverages below 2 ML are also stable after this process: this has been explained in terms of the higher surface energy of the nanoparticles formed in these stages of the growth on SiO_2.

6.1.2 Interaction of Cobalt oxides with graphite

The chemistry of the growth of cobalt oxides on HOPG has been studied in a similar way as the study on oxide substrates. The metallic and reducing character of this surface will give significant differences in their interaction with the cobalt oxides, although the chemistry of the Co species formed are identical as those obtained in oxide substrates. Some unoxidized cobalt has been observed for coverages below 1 ML: the strong diffusion of the CoO adsorbates through the HOPG surface towards the steps as well as the reducing character of graphite seems to be the reason. The morphology of the growth occurs in a Stranski-Krastanov way, with an initial accumulation of material at the steps of the substrate, and the growth of a wetting layer afterwards, which auto-assembles itself along the crystallographic directions of the substrate. Later on, dendritic islands also start growing on top of this layer and on

the previously accumulated material at the steps. This morphology has been confirmed with a combined AFM-XPS-IPSA analysis, which also revealed that the substrate is completely covered for coverages above 20 ML. The study of the CoO interface has been carried out in a similar way as in the case of the growths on oxide substrates), observing the predominance of effects attributable to the wetting layer rather than to the material accumulated at the steps.

The study of the thermal annealing of ultrathin CoO layers on HOPG led us to obtain a patterning method much more efficient to produce nanochannels on the HOPG surface via carbon gasification that the usual methods reported in the literature using metallic transition metal nanoparticles. Those methods are performed at temperatures between 600 and 1000 °C whereas ours works at 400 °C. A detailed XPS, XAS, AFM and micro-Raman analysis led us to conclude that the presence of oxygen, CoO instead of Co, is the key for such high efficiency. Although the initial CoO layer is reduced upon heating to metallic Co nanoparticles, its interaction previous heating produces a weakening of the sigma bonds of the HOPG surface which allows the gasification of the carbon atoms at lower temperatures. We have analysed the differences between the Co nanoparticles reduced from CoO upon heating and freshly evaporated Co nanoparticles, concluding that reduced Co nanoparticles act on a different local environment which has been previously modified by the initial CoO layer. The base conditions for this method have also been determined, being temperatures between 300 and 400 °C and a O_2 pressure between 10^{-6} and 10^{-3} mbar.

SECTION 6.2

Open questions and future lines of work

No work is perfect, and much less one as long and sprawling as a doctoral thesis. While a lot of the phenomena observed have been successfully explained, there are some open questions that have not been answered with the set of data presented, and there is always room for improvement and further development of the explanations presented in this work. In this last section of this thesis a brief outline of the most important open questions and possible lines of work for the future will be presented.

6.2.1 Open questions

- Although some explanations of the oxidation states found after the reoxidation of CoO grown on the four substrates have been given, a more throughout study of this aspect of the reoxidation processes must be made, specifically about the chemistry aspect of it. Our current hypotheses about the chemistry side of these processes will be outlined now, but it is important to corroborate these ideas with adequate experimental work in the future:

  - CoO grown on oxides, after the Reox-P1 process. The reoxidation of the CoO samples on Al_2O_3 is easily explainable by the fact that Al_2O_3 is a very inert substance, with an elevated heat of formation (−1675.7 kJ/mol [1]), and that it do not react with almost any other substances (Al_2O_3 is not reduced by CO even in blast furnaces,

and an electrolytic cell is commonly used for its reduction [2]). The stability found in MgO can be attributed, aside from the crystallinity of the grown samples, to the hygroscopic character of this substrate. Indeed, if the substrate has some initial water on its surface, it will convert to carbon monoxide once the sample is heated, which will reduce the Co_3O_4 via this reaction:

$Co_3O_4 + CO \longrightarrow 3CoO + CO_2$.

The case of the initial stability of the CoO/SiO_2 sample is more elusive. The morphological reasons are still valid, of course, but the possibility of the formation of SiO (another well-known reducing agent) in the heating phase can not be discarded without additional experiments, although the bibliography consulted agrees that the reduction of SiO_2 into SiO in UHV conditions cannot happen without an additional reductive agent, such as graphite or hydrogen [3, 4].

– CoO grown on HOPG, after the three processes. The three different oxidation states found after the three different thermal processes applied to the as-grown samples can also be related to the reactions that the different species can be experimenting. The reduction of CoO into Co in the heating process is due to the apparition of carbon atoms coming from the heating of the HOPG substrate, and the formation of CO because of these atoms reacting with the surrounding O atoms in the residual gas of the chamber. A cascade process occurs, where these four reactions compete at the same time:

$2C + O_2 \longrightarrow 2CO$

$2CoO + C \longrightarrow 2Co + CO_2$

$CoO + C \longrightarrow Co + CO$

$CoO + CO \longrightarrow Co + CO_2$

Three of them reduce the CoO into Co, and two of them introduce more CO into the surroundings, further accelerating the reduction of CoO into Co. The case of the presence of Co_3O_4 and CoO after the Reox-P1 process can also be explained by the same mechanism, but this time the species reduced would be the Co_3O_4 into CoO via the reaction $Co_3O_4 + CO \longrightarrow 3CoO + CO_2$.

- The presence of unoxidized cobalt on the first stages of the growth of CoO on HOPG and SiO_2 has also not been successfully explained. Some suggestions about its origin have been made (different coordinations, O_2 vacancies in the SiO_2 substrate, or the reducting character of the HOPG surface), but a definitive explanation of this needs more experiments.

- Some peaks that appear in the XPS, PES and XAS spectra have not been properly assigned, and more experiments would be necessary for a proper assignation (although some preliminary hypotheses have been presented). This peaks are:

  – The 532.5 eV peak (labelled as O^{II}) seen in the XPS and PES O 1s spectra of the CoO samples grown on HOPG (figures 5.3 and 5.4, pages 129 and 130, respectively). Two probable assignations have been made in this work, but they are not definitive at this point.

  - The 284.8 eV peak seen in the XPS and PES C 1s spectra of the CoO samples grown on HOPG (figures 5.19 and 5.22, pages 143 and 146, respectively).
  - The 284.5 eV peaks seen in the XAS C 1s spectra of the CoO samples grown on HOPG (figure 5.23, page 147).
  - The 285 eV peak seen in the Co sample grown on HOPG (figure 5.31, page 157).

- Theoretical DFT calculations of the CoO/MgO and CoO/SiO_2 interfaces would be important in order to have a deeper understanding of the phenomena described in section 4.3 (page 104).

- The hypothesis made in subsection 5.5.5 about the different structure of the reduced CoO/HOPG samples when compared to the freshly grown Co/HOPG samples could gain more strength from in-situ structural characterization results. An adequate way to achieve this could be EXAFS measurements of the Co 1s region, made in a vacuum system, and ideally with the sample still heated. Other structural techniques that could be applied in-situ, like XRD, could also be helpful, although the expected amorphous structure of these samples could result in unsuccessful measurements.

- More accurate and superficial measurements of the diffusion of Co into the HOPG substrate after the application of the Reox-P1 process to CoO samples grown on HOPG could be performed, in order to determine if it really exists.

- A hypothesis about the nature of the 7710 eV peak seen in the Co 1s XANES spectra of the 3 ML CoO sample on Al_2O_3 after being submitted to room conditions for three months (figure 4.19b, page 111) has been made, but more measurements and experiments are necessary in order to confirm it.

6.2.2 Future lines of work

- One of the most promising lines of work involves controlling the nanopatterning of HOPG promoted by cobalt oxides. There are two important factors for this nanolithography technique to be useful: a careful control of the size and position of the reduced Co clusters after the heating of the sample, and a control of their movement during the O_2 exposition phase of the Reox-P1 process. The second factor has been shown to be achievable with magnetic fields [5], but a good control of the first parameter is a more important challenge. A possible route could be the previous deposition and reduction of CoO using some sort of initial mask, and the removal of that mask in UHV conditions before the O_2 exposure phase. Another route could be the pre-patterning of the substrate surface with other kind of lithography technique, so the initial reduction of CoO would happen preferentially on those zones. A lot of work has to be done for this technique to be useful in industrial environments, but the results shown in this work are relevant enough for this to become a promising research line in the future.

- The remarkable stability of the CoO layers grown on MgO can be useful in the development of magnetic devices, given the antiferromagnetic properties of this material,

and the useful properties of ferromagnetic-antiferromagnetic junctions. Half-magnetic ferromagnetic materials with a similar rock-salt structure are specially suitable to be grown on top of CoO, such as NaO [6], CrTe [7] or Li_3N [8], for example, and novel and interesting devices could be developed with CoO as the antiferromagnetic material.

SECTION 6.3

Bibliography

[1] J. D. COX, DONALD D. WAGMAN, and V. A. MEDVEDEV. *CODATA key values for thermodynamics*. Chem/Mats-Sci/E, 1989. ISBN: 9780891167587.

[2] G. F. SCHRADER and A. K. ELSHENNAWY. *Manufacturing processes and materials*. Society of Manufacturing Engineers, 2000. ISBN: 9780132272711.

[3] B. OZTURK and R.J. FRUEHAN. "The rate of formation of SiO by the reaction of CO or H_2 with silica and silicate slags". English. *Metallurgical Transactions B* 16.4 (1985), pp. 801–806. DOI: 10.1007/BF02667516.

[4] B. G. GRIBOV, K. V. ZINOV'EV, O. N. KALASHNIK, N. N. GERASIMENKO, D. I. SMIRNOV, and V. N. SUKHANOV. "Structure and phase composition of silicon monoxide". English. *Semiconductors* 46.13 (2012), pp. 1576–1579. DOI: 10.1134/S1063782612130093X.

[5] L. BULUT and R. H. HURT. "A Magneto-catalytic Writing Technique for Etching Complex Channel Patterns into Graphenic Carbons". *Advanced Materials* 22.3 (2010), pp. 337–341. DOI: 10.1002/adma.200901932.

[6] F. AHMADIAN. "Half-metallic Ferromagnetism in the Rocksalt and Zincblende NaX (X=O, S, Se, Te, and Po)". English. *Journal of Superconductivity and Novel Magnetism* 25.5 (2012), pp. 1589–1596. DOI: 10.1007/s10948-012-1480-x.

[7] Y. LIU, S. K. BOSE, and J. KUDRNOVSKÝ. "First-principles theoretical studies of half-metallic ferromagnetism in CrTe". *Physical Review B* 82 (9 Sept. 2010), p. 094435. DOI: 10.1103/PhysRevB.82.094435.

[8] G. Y. GAO, K. L. YAO, Z. L. LIU, Y. MIN, J. ZHANG, S. W. FAN, and D. H. ZHANG. "Bulk and surface sp half-metallic ferromagnetism in alkali metal pnictides with rocksalt structure: a first-principles calculation". *Journal of Physics: Condensed Matter* 21.27 (2009), p. 275502. DOI: 10.1088/0953-8984/21/27/275502.

Chapter 6

Conclusiones, preguntas abiertas y futuras líneas de investigación

Este trabajo fue iniciado hace cinco años con una gran cantidad de incógnitas y desafíos, tanto teóricos como experimentales. Muchas de esas preguntas han obtenido respuesta al final de este trabajo, y una gran cantidad de resultados sorprendentes y relevantes han sido descubiertos al mismo tiempo, enriqueciendo las metas iniciales y abriendo nuevas líneas de trabajo y aplicaciones interesantes de estos resultados para el futuro. No existe el trabajo perfecto, y como se ha mostrado en los capítulos 4 y 5 de este trabajo, algunas de estos resultados han quedado sin explicar. En esta sección se resumirán los resultados más importantes de esta tesis, y también se expondrán algunas de las cuestiones que quedan sin respuesta y posibles líneas de investigación para el futuro, de manera que se pueda ampliar y profundizar en el trabajo realizado en este tema durante el último lustro.

SECTION 6.1

Conclusiones principales de este trabajo

El estudio del crecimiento e interacción de óxidos de cobalto con los cuatro sustratos considerados en este trabajo (SiO_2, Al_2O_3, MgO y HOPG) se puede resumir en dos grandes bloques de experimentos: los relacionados con el estudio del crecimiento, y los relacionados con la caracterización de estas muestras después de haber sido sometidas a diferentes condiciones. Todas las muestras han sido crecidas por evaporación térmica de cobalto en una atmósfera controlada de oxígeno, y el estudio del crecimiento se ha realizado mediante evaporaciones sucesivas sobre cada sustrato. Se realizaron medidas in-situ de XPS realizadas después de cada evaporación, y otro tipo de medidas in-situ, como RGA, XANES o PES, fueron realizadas dependiendo del experimento y la instalación en la que fue hecho. El resto de medidas, como las de AFM, EXAFS o Raman, fueron hechas ex-situ.

6.1.1 Interacción de óxidos de cobalto con sustratos de óxidos.

La química del crecimiento de óxidos de cobalto sobre los tres sustratos de óxidos fue realizada con medidas in-situ de XPS, y la asignación de los distintos estados de oxidación encontrados en dichas medidas se ha apoyado en cálculos teóricos de clusters de los espectros XPS del Co $2p_{3/2}$ para distintos iones de cobalto. El estado de oxidación mayoritario encontrado en los crecimientos para recubrimientos menores de 40 ML ha sido CoO, mientras que se ha encontrado Co_3O_4 para recubrimientos por encima de este en los crecimientos sobre SiO_2 y Al_2O_3, y pequeñas cantidades de cobalto sin oxidar para los primeros estadios del crecimiento en SiO_2. La bibliografía consultada establece que las especies de Co^{2+} son las más usuales para este tipo de técnica, pero especies de $Co^{2+,3+}$ pueden ser evaporadas usando otros métodos de evaporación más energéticos, como evaporación de plasma asistida por oxígeno. Los estados de oxidación encontrados en nuestros experimentos han sido explicados gracias a los diagramas de energía libre de la reacción de oxidación del cobalto (la reacción $2Co + O_2 \longrightarrow CoO$ tiene menor energía libre que la reacción $3Co + 2O_2 \longrightarrow Co_3O_4$), y se ha sugerido que la presencia de cobalto sin oxidar es debida a la diferente coordinación del CoO y del SiO_2, aunque la posibilidad de presencia de vacantes de O_2 en la superficie del sustrato de SiO_2 no puede ser descartada sin experimentos adicionales. El estudio de la morfología del crecimiento ha

revelado dos modos de crecimiento distintos: Volmer-Weber (crecimiento en islas) para los primeros estadios del crecimiento sobre SiO_2, y Frank-Van Der Merwe (crecimiento capa a capa) para el crecimiento sobre MgO y Al_2O_3, y para las últimas fases del crecimiento sobre SiO_2. Estas morfologías han sido explicadas en SiO_2 y MgO según los distintos parámetros de red y coordinaciones del CoO y de los sustratos, y con la ayuda de cálculos DFT en el caso del crecimiento sobre Al_2O_3. Estos modos de crecimiento han sido confirmados con un análisis combinando AFM y XPS-IPSA.

El estudio de los efectos de intercara se ha llevado a cabo con cálculos teóricos de clusters del espectro XPS del Co $2p_{3/2}$ para estructuras de CoO con distintos entornos locales. Estos cálculos han mostrado que los cambios en la posición e intensidad relativa del satélite shake-up del espectro (con respecto a la línea principal de fotoemisión) están relacionados con los cambios en la morfología de las nanoestructuras de CoO formadas en las primeras etapas del crecimiento, las cuáles dependen directamente de la estructura cristalina de los sustratos, e inducen cambios en el carácter iónico-covalente de los enlaces de las nanoestructuras de CoO. Esto es una clara diferencia con respecto a estudios previos de óxidos de metales de transición depositados en estos sustratos por técnicas similares, los cuales mostraron que el carácter iónico-covalente de los sustratos influía en la estructura electrónica de las capas de óxidos crecidas sobre ellos. En el caso de la intercara CoO/Al_2O_3, estos ajustes también han proporcionado una prueba experimental de la transferencia de carga sustrato-CoO teóricamente predicha por los cálculos teóricos de DFT de esta intercara.

En el otro bloque de resultados, la estabilidad de estas muestras ha sido probada bajo tiempos grandes de exposición a condiciones atmosféricas, y después de un proceso de oxidación térmica. La exposición a condiciones atmosféricas ha revelado el crecimiento de hidróxido de cobalto y de Co_3O_4 con el tiempo, confirmado tanto por XPS como por XANES. Las medidas EXAFS del Co 1s han revelado un exceso de oxígeno que no puede ser relacionado con este crecimiento de hidróxido o de óxido de cobalto, y se ha propuesto que es la razón detrás del cambio de oxidación visto en el estudio del crecimiento para recubrimientos mayores de 40 ML. Todos estos efectos son menos importantes en las muestras crecidas sobre MgO, además de ser las únicas muestras en el que se ha medido un pequeño porcentaje de cristalinidad, con lo que se ha concluido que este sustrato es el más adecuado para el crecimiento de láminas delgadas estables de CoO. Esto ha sido explicado mediante la similaridad de parámetros de red y estructuras cristalinas de ambos compuestos. El estudio de estas muestras después del proceso de oxidación térmica ha confirmado esta conclusión, dado que las muestras en MgO son estable para recubrimientos iguales o menores a 4 ML. Las muestras crecidas sobre SiO_2 también son estables cuando el recubrimiento es menor de 2 ML: esto ha sido explicado en función de la mayor energía superficial de las nanopartículas formadas en el crecimiento para esos espesores.

6.1.2 Interacción de óxidos de cobalto con HOPG

La química del crecimiento de óxidos de cobalto sobre HOPG ha sido estudiada de manera similar a lo hecho en el crecimiento sobre sustratos de óxidos. El carácter tanto metálico como reductor de este sustrato introducirá cambios importantes en su interacción con el CoO, aunque la química de las especies encontradas en el crecimiento es idéntica a la vista

en el crecimiento sobre sustratos de óxidos. Se ha detectado también algo de cobalto sin oxidar para recubrimientos menores de 1 ML: se han propuesto como razones la difusión de los adsorbatos de CoO a través de la superficie de HOPG y el carácter reductor del sustrato. La morfología del crecimiento se desarrolla en un modo tipo Stranski-Krastanov, con una acumulación inicial del material en los escalones del sustrato, y el crecimiento de una capa mojante en las terrazas, la cual se ordena según las direcciones cristalográficas del sustrato. Posteriormente, se produce el crecimiento de islas con estructuras dendríticas encima de esta capa mojante, y también en las acumulaciones iniciales de material. Estas morfologías han sido confirmadas con análisis combinando AFM y XPS-IPSA, los cuáles han revelado que el cubrimiento completo del sustrato ocurre para recubrimientos de 20 ML. El estudio de la intercara de CoO se ha realizado de manera similar a lo ya hecho en la parte de sustratos de óxidos, y se ha observado la preponderancia de los efectos provenientes de la capa mojante para esos recubrimientos.

El estudio de la oxidación térmica de las muestras de CoO depositadas sobre CoO nos ha permitido obtener un método de nanomarcado de superficies de HOPG mucho más eficiente que los métodos usuales con nanopartículas metálicas reportados en la bibliografía. Estos métodos usan temperaturas de entre 600 y 1000 °C, mientras que el nuestro funciona a 400 °C. Se ha estudiado este proceso mediante XPS, XAS, AFM y espectroscopía micro-Raman, y se ha concluido que la clave de nuestra elevada eficiencia es la presencia de oxígeno (CoO en vez de Co). La capa inicial de CoO es reducida a Co en la fase de calentamiento de nuestro proceso, pero su interacción previa a su aplicación produce un debilitamiento de los enlaces σ de la superficie del HOPG, la cual permite la gasificación de los átomos de carbono a temperaturas más bajas. Hemos analizado las diferencias entre nanopartículas recién evaporadas de Co y las reducidas del CoO original, concluyendo que estas últimas poseen un entorno local distinto, modificado previamente por la capa original de CoO. También se ha realizado una caracterización básica de las condiciones mínimas de este proceso, concluyéndose que son necesarias temperaturas de calentamiento de entre 300 y 400 °C, y una presión de O_2 mínima de entre 10^{-6} y 10^{-3} mbar.

SECTION 6.2

Cuestiones abiertas y futuras líneas de trabajo

No existe el trabajo perfecto, y mucho menos uno tan largo y extenso como una tesis doctoral. Es cierto que muchos de los fenómenos que se han encontrado en estos experimentos han sido explicados, pero aún quedan algunas preguntas que, con los datos que se han obtenido hasta ahora, no pueden ser respondidas adecuadamente; y por supuesto, siempre queda espacio para mejorar estos resultados y desarrollar nuevas vías de investigación y desarrollo basadas en ellos. En esta última sección de la tesis, se expondrán algunas delas cuestiones que quedan sin respuesta al final de esta tesis, y también se comentarán algunas líneas posibles de trabajo para el futuro.

6.2.1 Cuestiones abiertas

- Se han dado algunas explicaciones sobre las razones detrás de los estados de oxidación del CoO crecido sobre los cuatro sustratos después de haber sido sometidas a los tratamientos térmicos, pero sería conveniente realizar un estudio más en profundidad sobre esto, centrándose especialmente en el aspecto más químico de estos procesos. Se expondrán a continuación las hipótesis más recientes que se tienen sobre este tema, aunque es importante corroborarlas en el futuro con experimentos adicionales:

  – CoO crecido sobre óxidos, después del proceso Reox-P1. La reoxidación de CoO a Co_3O_4 cuando el sustrato es Al_2O_3 es fácilmente explicable por el hecho de que el Al_22O_3 es una sustancia con un gran calor de formación ($-1675.7\,kJ/mol$ [1]) y con muy poca reactividad (es una de las pocas sustancias que no es fácilmente reducida por CO incluso en procesos de altos hornos, usándose normalmente una célula electrolítica para ello [2]). Además de la cristalinidad encontrada en las muestras de CoO crecidas sobre MgO, la razón de su estabilidad puede deberse al carácter higroscópico de este sustrato. Si bien es cierto que el sustrato es calentado antes de empezar el crecimiento de CoO, la mínima presencia de H_2O provocará la aparición de CO una vez el sustrato sea calentado, desencadenando la siguiente reacción de reducción de Co_3O_4 a CoO:

    $Co_3O_4 + CO \longrightarrow 3CoO + CO_2$

    El caso de la estabilidad de la muestra de CoO crecida sobre SiO_2 no es tan obvio. Las razones morfológicas dadas en el capítulo 4 siguen siendo válidas, pero la posibilidad de la formación de SiO en la fase de calentamiento no puede ser descartada sin experimentos adicionales, aunque la bibliografía consultada parece estar de acuerdo en que la reducción de SiO_2 a SiO en condiciones de UHV sólo puede suceder cuando se usan agentes reductores adicionales, como grafito o hidrógeno [3, 4].

  – CoO crecido sobre HOPG, después de los tres procesos Los tres estados de oxidación encontrados después de la aplicación de los tres diferentes procesos térmicos a las muestras de CoO crecidas sobre HOPG también pueden ser relacionadas con las reacciones que las diferentes sustancias estarían experimentando. La reducción de CoO a Co después del calentamiento en vacío es debida a la aparición de átomos de carbono provenientes del sustrato de HOPG calentado, y su reacción con los átomos de O del gas residual de la cámara, formando CO. formación de CO. Con ese CO, se produce un proceso en cascada, en el que diferentes reacciones compiten entre sí:

    $2C + O_2 \longrightarrow 2CO$

    $2CoO + C \longrightarrow 2Co + CO_2$

    $CoO + C \longrightarrow Co + CO$

    $CoO + CO \longrightarrow Co + CO_2$

    Tres de ellas reducen el CoO a Co, y dos de ellas introducen más moléculas de CO en las inmediaciones de la muestra, acelerando la reducción de CoO a Co. El caso

de la presencia de Co_3O_4 y CoO después del proceso Reox-P1 también podría ser explicado por este mismo mecanismo, sólo que, en este caso, la sustancia que se reduciría sería el Co_3O_4, mediante la reacción $Co_3O_4 + CO \longrightarrow 3CoO + CO_2$.

- La presencia de cobalto sin oxidar para las primeras etapas del crecimiento de CoO en HOPG y SiO_2 tampoco ha sido suficientemente bien explicado. Se han dado algunas sugerencias sobre su origen (distintas coordinaciones, vacancias de O_2 en el sustrato de SiO_2, o el carácter reductor del sustrato de HOPG), pero son necesarios más experimentos para dar una explicación clara de esto.

- No se han asignado de manera definitiva todos los picos aparecidos en los espectros XPS, PES y XAS, y serían necesarios más experimentos para poder hacer una asignación correcta de ellos. Estos picos son:

  - El pico a 532.5 eV (llamado O^{II}) visto en los espectros XPS y PES de la región del O 1s en las muestras de CoO sobre HOPG (figuras 5.3 and 5.4, páginas 129 y 130, respectivamente).
  - El pico a 284.8 eV visto en los espectros XPS y PES de la región C 1s en las muestras de CoO sobre HOPG (figuras 5.19 and 5.22, páginas 143 y 146, respectivamente).
  - El grupo de picos a 284.5 eV visto en los espectrosXAS de la región C 1s en las muestras de CoO sobre HOPG (figura 5.23, página 147).
  - El pico a 285 eV visto en el espectro PES de la región C 1s en la muestra de Co crecida sobre HOPG (figura 5.31, página 157).

- Son necesarios cálculos teóricos de DFT de las intercaras de CoO/MgO y CoO/SiO_2 para tener una comprensión más profunda de los fenómenos descritos en la subsección 4.3 (página 104).

- La hipótesis hecha en la subsección 5.5.5 sobre la distinta estructura de las muestras reducidas de CoO cuando son comparadas con las muestras de Co recién evaporadas está incompleta sin medidas estructurales in-situ. Una manera adecuada de conseguir esto podría ser medidas EXAFS de la región del Co 1s hechas en un sistema de vacío, y a ser posible aplicando temperatura a la muestra a la vez que se mide. Otras técnicas estructurales, como XRD, también podrían ser útiles, aunque la esperada estructura amorfa de estas muestras podría resultar en medidas no satisfactorias.

- Son necesarias medidas más precisas y superficiales de la difusión de Co cuando se aplica el proceso Reox-P1 a muestras de CoO sobre HOPG, para determinar si, en primer lugar, existe tal difusión.

- Se ha propuesto una hipótesis para explicar el origen del pico visto en el espectro XANES del Co 1s en la muestra de 3 ML de CoO sobre Al_2O_3 expuesta durante tres meses a condiciones de presión atmosférica (figura 4.19b, página 111), pero son necesarios más experimentos y medidas para confirmarla.

6.2.2 Líneas futuras de trabajo

- Una de las líneas de investigación más prometedoras que puede desarrollarse a partir de estos resultados implica el control del nanomarcado de la superficie de los sustratos de HOPG promovido por óxidos de cobalto. Hay dos parámetros críticos para que esta técnica de nanolitografía pueda ser viable: un control preciso del tamaño y posición de los clusters de Co después de la reducción de CoO, y el control del movimiento de estos clusters durante la fase de exposición a O_2 del proceso Reox-P1. Se ha probado que el segundo factor puede controlarse mediante la aplicación de campos magnéticos [5], pero el control adecuado del primer factor es más complejo. Una posible manera de hacerlo podría ser depositando y reduciendo el CoO a través de una máscara, que sería quitada antes de comenzar la fase de exposición a O_2 (todo esto en condiciones de UHV). Otra ruta para conseguir esto podría ser mediante el pre-marcado de la superficie con técnicas de nanolitografía, para que tanto la deposición como la reducción de CoO ocurriera preferentemente en los puntos premarcados. Queda mucho trabajo por delante para que esta técnica pueda ser útil en entornos industriales, pero los resultados presentados en este trabajo son lo suficientemente relevantes como para que pueda ser una línea prometedora de investigación en el futuro.

- La destacable estabilidad y las esperadas propiedades antiferromagnéticas de las muestras de CoO crecidas sobre MgO pueden ser útiles en el desarrollo de dispositivos magnéticos, dadas las propiedades de uniones de materiales ferromagnéticos-antiferromagnéticos. Los materiales más interesantes para este tipo de dispositivos podrían ser los materiales ferromagnéticos "medio-magnéticos" con estructuras de halita, como el NaO [6], el CrTe [7] o el Li_3N [8], que podrían dar lugar a nuevos e interesantes dispositivos magnéticos.

SECTION 6.3

Bibliography

[1] J. D. Cox, Donald D. Wagman, and V. A. Medvedev. *CODATA key values for thermodynamics*. Chem/Mats-Sci/E, 1989. ISBN: 9780891167587.

[2] G. F. Schrader and A. K. Elshennawy. *Manufacturing processes and materials*. Society of Manufacturing Engineers, 2000. ISBN: 9780132272711.

[3] B. Ozturk and R.J. Fruehan. "The rate of formation of SiO by the reaction of CO or H_2 with silica and silicate slags". English. *Metallurgical Transactions B* 16.4 (1985), pp. 801–806. DOI: 10.1007/BF02667516.

[4] B. G. Gribov, K. V. Zinov'ev, O. N. Kalashnik, N. N. Gerasimenko, D. I. Smirnov, and V. N. Sukhanov. "Structure and phase composition of silicon monoxide". English. *Semiconductors* 46.13 (2012), pp. 1576–1579. DOI: 10.1134/S1063782612130093X.

[5] L. BULUT and R. H. HURT. "A Magneto-catalytic Writing Technique for Etching Complex Channel Patterns into Graphenic Carbons". *Advanced Materials* 22.3 (2010), pp. 337–341. DOI: 10.1002/adma.200901932.

[6] F. AHMADIAN. "Half-metallic Ferromagnetism in the Rocksalt and Zincblende NaX (X=O, S, Se, Te, and Po)". English. *Journal of Superconductivity and Novel Magnetism* 25.5 (2012), pp. 1589–1596. DOI: 10.1007/s10948-012-1480-x.

[7] Y. LIU, S. K. BOSE, and J. KUDRNOVSKÝ. "First-principles theoretical studies of half-metallic ferromagnetism in CrTe". *Physical Review B* 82 (9 Sept. 2010), p. 094435. DOI: 10.1103/PhysRevB.82.094435.

[8] G. Y. GAO, K. L. YAO, Z. L. LIU, Y. MIN, J. ZHANG, S. W. FAN, and D. H. ZHANG. "Bulk and surface sp half-metallic ferromagnetism in alkali metal pnictides with rocksalt structure: a first-principles calculation". *Journal of Physics: Condensed Matter* 21.27 (2009), p. 275502. DOI: 10.1088/0953-8984/21/27/275502.

Appendix I. List of publications and communications to congresses

PAPERS IN JOURNALS INCLUDED IN SCI:

- Contributions directly related to this work:
  - **Nanopatterning on highly oriented pyrolytic graphite surfaces promoted by cobalt oxides**. D. Díaz-Fernández, J. Méndez, A. del Campo, R. J. O. Mossanek, M. Abbate, M. A. Rodríguez, G. Domínguez-Cañizares, O. Bomatí-Miguel, A. Gutiérrez, L. Soriano. *Carbon, 85, pp. 89-98 (2015)*
  - **Study of the early stages of growth of Co oxides on oxide substrates**. D. Díaz-Fernández, J. Méndez, F. Yubero, G. Domínguez-Cañizares, A. Gutiérrez and L. Soriano. *Surface and Interface Analysis, 46, pp. 975.979 (2014)*
  - **The growth of cobalt oxides on HOPG and SiO_2 surfaces: A comparative study**. D. Díaz-Fernández, J. Méndez, O. Bomatí-Miguel, F. Yubero, R. J. O. Mossanek, M. Abbate, G. Domínguez-Cañizares, A. Gutiérrez, S. Tougaard, L. Soriano. *Surface Science, 624, pp. 145-153 (2014)*
- Other publications:
  - **Effects of grain refinement and disorder on the electronic properties of nanocrystalline NiO**. G. Domínguez-Cañizares, A. Gutiérrez, J. Chaboy, D. Díaz-Fernández, G.R. Castro, L. Soriano. *Journal of Materials Science, 49, pp 2773-2780 (2014)*
  - **Comparison of different methodologies for obtaining nickel nanoferrites**. R. Galindo, N. Menéndez, P. Crespo, V. Velasco, O. Bomatí-Miguel, D. Díaz-Fernández, P. Herrasti. *Journal of Magnetism and Magnetic Materials, 361, pp 118-125 (2014)*
  - **Effects of Ni vacancies and crystallite size on the O 1s and Ni 2p X-ray absorption spectra of nanocrystalline NiO**. R. J. O. Mossanek, G. Domínguez-Cañizares, A. Gutiérrez, M. Abbate, D. Díaz-Fernández, L. Soriano. *Journal of Physics: Condensed Matter, 25, 495506 (2013)*
  - **Hexagonally arranged NiO nanoporous membranes with varying electrical conductivity**. A. Gutiérrez, G. Domínguez-Cañizares, J.A. Jiménez, I. Preda, D. Díaz-Fernández, F. Jiménez-Villacorta, G.R. Castro, J. Chaboy, L. Soriano. *Applied Surface Science, 276, pp. 832-837 (2013)*

– **X-Ray Absorption Study of the Local Structure at the NiO/Oxide Interfaces**. I. Preda, L. Soriano, D. Díaz-Fernández, G. Domínguez-Cañizares, A. Gutiérrez, G. R. Castro, J. Chaboy. *The Journal of Synchrotron Radiation, vol. 20, pp. 635-640 (2013)*

COMMUNICATIONS TO CONGRESSES:

- Communications directly related to this work:
  - Oral presentations:

    Study of the growth and properties of Cobalt oxide ultra-thin films on different oxide substrates. D. Díaz-Fernández and L. Soriano. *XVII INC Young Researchers Meeting, Miraflores de la Sierra, Spain, 19th December, 2014*.

    Stabilization of ultrathin cobalt oxide films on different oxide substrates. D. Díaz-Fernández, G. Domínguez-Cañizares, A. Gutiérrez, L. Soriano. *EVC 2014, Aveiro, Portugal, 8th-12th September, 2014*. *IVC 2013, NST/SS-1-Or-9, Paris, France, 9th-13th September, 2013*.

    The interaction of Co oxides with graphite surfaces. D. Díaz-Fernández, J. Méndez, A. del Campo, M. A. Rodríguez, G. Domínguez-Cañizares, O. Bomatí-Miguel, A. Gutiérrez, L. Soriano. *Workshop: High Structural and Spatial Resolution using Raman Confocal and Scanning Probe Microscopy, Madrid, Spain, 7th November, 2013*.

    Study of the way of growth of Co oxides on different oxides. D. Díaz-Fernández, G. Domínguez-Cañizares, A. Gutiérrez, L. Soriano. *ECASIA'15, Cagliary, Italy, 13th-18th September, 2013*.

    The interaction of Co oxides with graphite surfaces. D. Díaz-Fernández, J. Méndez, G. Domínguez-Cañizares, A. Gutiérrez, L. Soriano. *IVC 2013, NST/SS-1-Or-9, Paris, France, 9th-13th September, 2013*.

    Interaction of cobalt oxides with graphite surfaces. D. Díaz-Fernández, J. Méndez, R. J. O. Mossanek, M. Abbate, A. del Campo, M. A. Rodríguez, G. Domínguez-Cañizares, O. Bomatí-Miguel, A. Gutiérrez, L. Soriano. *IMDEA 3rd Early Stage Researchers Workshop, Madrid, Spain, 27th-28th June, 2013*.

  - Posters:

    Nano-patterning on graphite by cobalt oxides. D. Díaz-Fernández, J. Méndez, A. del Campo, M. A. Rodríguez, G. Domínguez-Cañizares, O. Bomatí-Miguel, A. Gutiérrez, L. Soriano. *NanoSpain 2014, Madrid, Spain, 11th-14th March, 2014*.

    Interaction of cobalt oxides with graphite surfaces upon annealing and oxygen exposure. D. Díaz-Fernández, J. Méndez, A. del Campo, M. A. Rodríguez, G. Domínguez-Cañizares, O. Bomatí-Miguel, A. Gutiérrez, L. Soriano. *XVI INC Young Researchers Meeting, Miraflores de la Sierra, Spain, 19th December, 2013*.

    Characterization of the growth of cobalt oxides on HOPG and SiO_2 by XPS and AFM: a comparative study. D. Díaz-Fernández, J. Méndez, F. Yubero, O.

Bomatí-Miguel, G. Domínguez-Cañizares, A. Gutiérrez, L. Soriano. *Fuerzas y Tunel 2012, San Lorenzo del Escorial, Spain, 12th-14th September, 2012*.

Characterization of the growth of cobalt oxides on HOPG and other oxides: substrate effects. D. Díaz-Fernández, L. Soriano, J. Méndez, L. Álvarez, F. Yubero. *INC Summer School, Miraflores de la Sierra, Spain, 12th-16th September, 2011*.

- Other communications:
  - **Effect of grain size and disorder on conductive NiO thin films**.
    G. Domínguez-Cañizares, A. Gutiérrez, D. Díaz-Fernández, J. Chaboy, G. R. Castro, J. A. Jiménez, M. Abbate, R. J. O. Mossanek and L. Soriano. *XVI INC Young Researchers Meeting, Miraflores de la Sierra, Spain, 19th December, 2013* (Oral presentation)
  - **Direct evidence of hole states in conducting NiO films observed by X-ray absorption spectroscopy**. A. Gutiérrez, G. Domínguez-Cañizares, D. Díaz-Fernández, L. Soriano. *IVC 2013, TF-6-Or-3, Paris, France, 9th-13th September, 2013* (Oral presentation)
  - **Hole conductivity in NiO thin films**. G. Domínguez-Cañizares, A. Gutiérrez, D. Díaz-Fernández, M. Abbate, R.J.O. Mossanek, L. Soriano. *IMDEA 3rd Early Stage Researchers Workshop, Madrid, Spain, 27th-28th June, 2013* (Oral presentation)
  - **Analysis of empty states in p-type conducting nanostructured NiO thin films with tailored physical properties**. G. Domínguez-Cañizares, A. Gutiérrez, S. Krause, R. Ovsyannikov, M. Abbate, D. Díaz-Fernández, L. Soriano. *NanoSpain 2013, Bilbao, Spain, 23th-26th April, 2013* (Poster)
  - **Effects of microstructure on the electronic states of nanostructured NiO**. G. Domínguez-Cañizares, A. Gutiérrez, J. A. Jiménez, J. Chaboy, G. R. Castro, D. Díaz-Fernández, L. Soriano. *4th Joint BER II and BESSY II User Meeting, Berlin, Germany, 12th-14th December, 2012* (Poster)
  - **Coercivity, morphology and anionic defects in Fe/NiO layers on nanoporous Al_2O_3 membranes**. M. Iglesias, G. Domínguez-Cañizares, E. Navarro, E. Paz, D. Díaz-Fernández, A. Gutiérrez , L. Soriano, M. Alonso, F. Soria, F. Cebollada, J. M. González and F. J. Palomares. *NanoSpain 2011, Bilbao, Spain, 11th-14th April, 2011* (Poster)
  - **Growth and characterization of NiO hexagonally arranged nanoporous membranes**. A. Gutiérrez, I. Preda, G. Domínguez-Cañizares, D. Díaz, L. Soriano. *ICSFS14 International Conference on Solid Films and Surfaces, Dublin, Ireland, 29th June-4th July, 2008* (as D. Díaz) (Oral presentation)
  - **Characterization of the growth of NiO ultra-thin films on some selected oxides: oxide-oxide interface formation**. I. Preda, A. Gutiérrez, G. Domínguez-Cañizares, D. Díaz, L. Soriano. *ICSFS14 International Conference on Solid Films and Surfaces, Dublin, Ireland, 29th June-4th July, 2008* (as D. Díaz) (Oral presentation)